Extraordinary Nonlinear Light Matter Interactions in Low-Dimensional Materials through Nano Manufacturing

Ahmed Raza Khan

Year 2020

A THESIS SUBMITTED FOR THE DEGREE OF DOCTOR OF PHILOSOPHY
OF THE AUSTRALIAN NATIONAL UNIVERSITY

Research School of Electrical, Energy and Materials Engineering
Australian National University, Australia

Ahmed Raza Khan - 2020

Ahmed Raza Khan - July 2020

Declaration

This thesis is an account of the research undertaken in the Nano Electromechanical Systems (NEMS) Laboratory, within Research School of Electrical, Energy and Materials Engineering, at the Australian National University from 2016 to 2020.

This thesis, except explicitly stated in the text, contains no material previously published or written by others.

Ahmed Raza Khan

Year 2020

Dedication

I would like to dedicate my thesis to all those people who are source of my motivation!

- *To my mother Mrs. Shamim Jabbar (late) who died in second year of my PhD studies. She was a constant source of love and inspiration to my life!*
- *To my father Mr. Abdul Jabbar Khan, brother Zahid Raza Khan and wife Sapna Anwar for their continuous support!*
- *To Mr. Abdul Sattar Edhi (late), the great humanitarian, for his service to humanity!*
- *To Dr. Ruth Pfao (late), the iron lady, to treat 50000+ patients of leprosy!*

Acknowledgements

The work presented in this thesis would not have been possible without the support of a number of individuals and organizations and they are gratefully acknowledged below:

- I would like to express my deepest gratitude to my primary supervisor Associate Professor Yuerui Lu, who has the attitude of a genius: he incessantly and compellingly transferred an essence of quest to my research potential. Without his leadership and determined help, this thesis would not have been possible. Specially, his invaluable input in executing the research plan and transforming it into a quality publication is the skill of lift-time I learnt during this work. I am grateful to him for providing me with an abundance of opportunities, resources, sound advice, guidance as well as being willing to have in-depth discussions whenever I approached him for help.

- I wish to express my sincere appreciation to the members of my supervisory panel, Professor Daniel Macdonald and Professor Robert Elliman, for accepting my supervision and opening their laboratory facilities to me.

- I am very grateful to Prof. Yun Liu and Dr. Teng Lu from Department of Chemistry of Australian National University for wonderful research collaboration.

- I would like to thank to my fellow PhD students, faculty members, and administrative staff at the Research School of Electrical, Energy and Materials Engineering of Australian National University for being so wonderful! In this regard, I would like to special thank my current and ex-group fellows, Yi Zhu, Boqing Liu, and Wendi (Marvin) Ma, Ankur Sharma, Kun Liang, Linglong Zhang, Mudassar Nauman, Jiong Yang, and all others for their contribution towards the accomplishment of this thesis. Moreover, I am grateful to Dr. Khu Wu, Dr. Hieu Nguyen, Daryl Webb, Dr. Naeem Shahid and Dr. Kaushal Vora to train me on multiple tools. I want to express my gratitude to Dr. Tieyu Lü for technical help, CAM (Centre of Advanced Microscopy) and ANFF (Australian

National Fabrication Facility) for research facilities, Sheeraz Alvi and Asim Riaz for useful discussions and suggestions, and ANU for awarding me Vice Chancellor Travel Grant 2019.

- I would like to acknowledge also University of Engineering & Technology, Lahore, Pakistan, not only for the financial support granted through scholarship, but also for the cherishing moments during the tenure of my bachelor’s degree as well as during my career as a faculty member.

- I would like to express my most sincere love and thank to my mother (late) and my father as a continuous source of my motivation, support and guidance throughout my life. They always stood by me through thick and thin. My sincere appreciation goes to my brother for his sincere help and guidance. Lastly, I would like to say special thanks to my wife for her patience, support and wonderful company and being on my side even at the most challenging situations during my PhD studies.

Abstract

Low dimensional materials, such as two-dimensional (2D) layered materials, have attracted significant attention over past decades due to their unique electrical and optical properties. Nonlinear optical processes are of great interest for various applications, e.g., microscopy, therapy, optical switches, ultrashort pulsed laser and frequency conversion. This thesis primarily discusses the extraordinary nonlinear light matter interactions in low dimensional materials via nano-manufacturing techniques using structural engineering methods such as strain engineering, folding and thermal variation.

Firstly, strain induced wrinkles and folds in 2D layered materials are achieved using a new fabrication technique through controlling the strain. The improved electrical and optoelectronic characteristics of strain induced wrinkles and folds are explored via atomic force microscopy (AFM), surface potential, current and photo-current measurements for potential applications in optoelectronics devices. Interlayer screening effect is found as the dominant factor causing layer dependent surface potential reduction for both perfect pack layers (flat WS_2) and twisted layers (folded WS_2). Strain is found to tune semi conductive junction properties significantly (~12.5% reduction in Schottky barrier height per % strain) and laser illumination is found to cause further lowering of SBH due to photo generated carriers.

Secondly, nonlinear light matter interactions in 2D layered materials are investigated through optical second harmonic generation (SHG). SHG from twisted layers of folds are found to follow vector superposition principle of SH wave vectors coming from individual layers of fold. As a result, folding angle in trilayer folds is measured accurately through polarization dependent SHG response. Strain dependent SHG quenching and enhancement in the direction parallel and perpendicular respectively to the direction of the compressive strain vector is found in polarization dependent SHG. As a result, a complete strain vector in strain induced wrinkles is measured accurately through polarization dependent SHG which is explained using photoelastic approach for ultrathin TMDs. Band-nesting induced transition (C peak), which can be significantly modulated by strain, is found to highly enhance SHG and is also discussed.

Thirdly, SHG response of layered TMDs is shown highly sensitive to temperature modulation. Temperature dependent SHG is found to show opposite trends for single layer and few odd layers (3L, 5L, 7L, etc) of TMDs. A remarkable temperature dependent SHG enhancement is found in single layer MoSe2 whereas few odd layers show significant temperature dependent SHG reduction. Temperature dependent SHG investigation with other TMDs i.e. MoS2, WS2 and WSe2 shows the similar trend which reveals an important structural characteristic for TMDs.

Finally, an additional study is performed on light matter interactions in 1D Pentacene nano wires which is another class of low dimensional materials. Pentacene nano wires are grown on hBN using vapour deposition approach. Pentacene nanowires show high crystalline features which are explained through Shpol'skii effect.

In sum, this thesis is focused on nonlinear light mater interaction in 2D materials for applications in various optoelectronic and nonlinear photonic devices.

Publications

[1] **Ahmed Raza Khan**, Boqing Liu, Wendi Ma, Linglong Zhang, Ankur Sharma, Yi Zhu, Tieyu Lü and Yuerui Lu, “Direct Measurement of Folding Angle and Strain Vector in Atomically thin WS_2 using Second Harmonic Generation”, ACS Nano, 2020 (in-review)
Preprint: http://arxiv.org/abs/2002.03616

[2] **Ahmed Raza Khan**, Yuerui Lu, “Optical Harmonic Generation in 2D Materials”, 2020 [in-preparation]

[3] **Ahmed Raza Khan**, Boqing Liu, Linglong Zhang, Yi Zhu, Xin He, Lijun Zhang, Tieyu Lü, Yuerui Lu, “Extraordinary Temperature Dependent SHG in Atomically Thin Layers of Transition-Metal Dichalcogenides”, Advanced Optical Materials, 2020, **2000441**, (DOI. 10.1002/adom.202000441)

[4] **Ahmed Raza Khan**§, Teng Lu§, Wendi Ma, Yun Liu, Yuerui Lu, “Tunable Optoelectronic Properties of WS2 using Local Strain Engineering and Folding”, Advanced Electronics Materials, 2020, **1901381**, (DOI: 10.1002/aelm.201901381)

[5] Ankur Sharma§, **Ahmed Raza Khan**§, Yi Zhu, Yuerui Lu, “Quasi-line spectral emissions from high crystalline 1D Organic Nanowires”, Nano-letters, 2019, **19**, 11, 7877-7886, (DOI: 10.1021/acs.nanolett.9b02943)

§ Authors contributed equally to the work

Contents

LIST OF TABLES

List of Figures

1 INTRODUCTION

1.1 Background

Nonlinear light matter interactions is the study of the nonlinear behaviour of material in response to the applied optical field.[1,2] For instance, intensity of second harmonic light from a non-linear medium shows a quadratic scaling behaviour in response to the applied laser light. Non-linear materials play an important role in the field of photonics such as photon generation, imaging and photon manipulation.[3–6], Therefore, these materials are also used in various photonic applications such as lasers[7], waveguides[8–11], optic fibres[12], optical frequency converters,[13,14] optical switches[15,16] and photo detectors.[17–19]

Conventional nonlinear photonic devices are based on bulk materials which belong to non-inversion symmetric crystal classes such as Lithium Niobate ($LiNbO_3$),[20–23] Barium Titanate ($BaTiO_3$), β-BaB_2O_4 (BBO)[24,25] etc. Nonlinear properties of optical materials are highly dependent on phase matching conditions. The dimensionality of optical materials, a key factor for phase matching, thus plays an important role on the efficiency of nonlinear light matter interaction. Conventional non-linear materials, due to phase matching issues, have certain limitations making them unsuitable for future nonlinear photonic devices [26,27]. On the other hand, ultrathin materials, with a thickness far below the optical coherence length, eliminate the requirement for phase matching. As a result, these materials show extraordinary nonlinear light matter interactions causing highly enhanced nonlinear properties[26,28]. Researchers have shown that some 2D materials show strong non-linear optical properties, such as the SHG (second harmonic generation) signals from 2D TMDs are found/predicted to be a few orders of magnitude greater than that of common bulk materials[29–33]. For instance, extraordinary SHG enhancement (10-1000 times) is discovered in monolayer/multilayers of MoS_2,[34,3536] $MoSe_2$,[37] WS_2[38], WSe_2[39] .

In addition, nonlinear properties in 2D layered materials can be tuned using various techniques, such as electric tuning[40], exciton resonances[41], thickness variation[35], valley selection[42], dielectric[43] and nanostructures enhancement[44] which can optimize the performance of nonlinear optical devices. Apart from that, nonlinear interaction of light in 2D materials has potential for various characterization modes, such as layer identification[35], lattice orientation[35], phase variation[28], defects characterization[45–50], piezoelectric and ferroelectric detection[26,51–53], bio imaging[54], etc., thus making optical harmonic generation a powerful characterization tool for 2D materials. Furthermore, optical harmonic generation in 2D materials pave the way for various applications in device making and bio-imaging.

1.2 Non-linear light matter interactions

When an electric field strength **E** is applied to a nonlinear material, the polarization **P** of that material system takes the form of power series expansion and can be expressed as;[2,6]

$$\boldsymbol{P(t) = \chi^1 E(t) + \chi^2 E(t)^2 + \chi^3 E(t)^3 \ldots\ldots \chi^n E(t)^n} \qquad (1.1)$$

The χ^1 term is called the linear optical process whereas χ^n terms with $n \geq 2$ are called nonlinear optical processes. Specifically, χ^2 is the second order non-linear susceptibility, χ^3 is the third order non-linear susceptibility and so on.[1]We refer the terms $\boldsymbol{\chi^2 E(t)}$ and $\boldsymbol{\chi^3 E(t)}$ as the second-order and third-order nonlinear polarization[2] respectively whereas the terms with n≥4 are termed as higher order nonlinear polarization. Eq. (1.1) shows if optical field is quite strong or non-linear susceptibility of the material is large enough then higher-order (n≥2) terms in Eq. (1.1) become obvious which give rise non-linear optical behaviour.[19]

Nonlinear light matter interactions include the optical harmonic generation (OHG) processes which show nonlinear polarization behaviour (i.e n is not equal to 1).

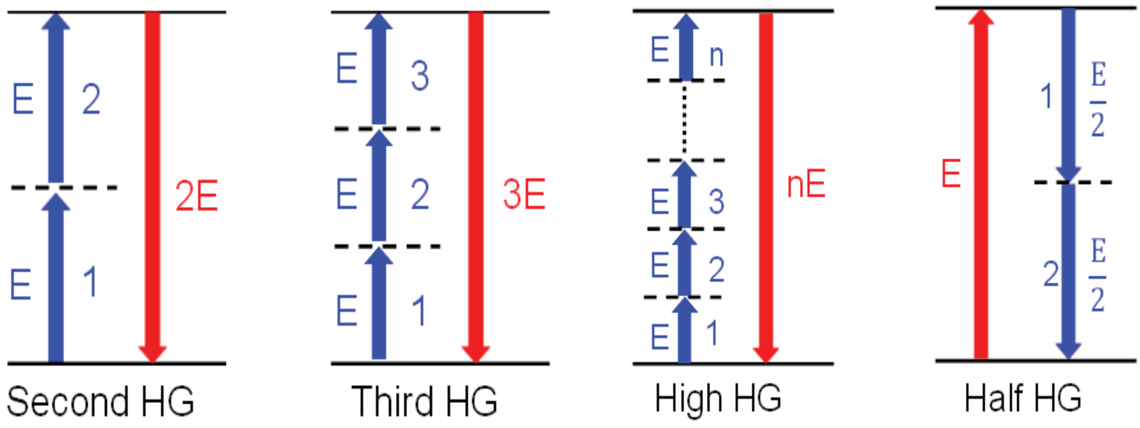

Figure 1.1 | Fundamentals of optical harmonic generation (HG).
Schematic diagram of different types of optical harmonic generation processes including second, third, high and half harmonic generation.

Optical harmonic generation processes include second harmonic generation (SHG), third harmonic generation (THG) and high harmonics generation (HHG) processes which are discussed as follow;

1.2.1 Second harmonic generation

Second Harmonic Generation (SHG) is a second-order (n=2) nonlinear optical process, in which two photons of same frequency ω merge into a single photon with double frequency 2ω[31,34,37,38,55–60], as shown in **Figure 1.1.** SHG response of the material depends on loss of inversion symmetry, lattice orientation, saturable absorption, frequency of the applied optical field.[26] For instance, 1L TMDs, with lack of inversion symmetry and good phase matching, show strong SHG response. Even layers of TMDs and graphene, on the other hand, show weak SHG response due to their centrosymmetric nature.[35] The potential applications of SHG effect in 2D materials include ultrashort pulsed laser, photonic circuits, GHz technology, material characterization such as determination of lattice orientation.[35,39]

1.2.2 Third harmonic generation

Third Harmonic Generation (THG) is a third-order (n=3) nonlinear optical process, in which three photons of same frequency ω merge into a single photon with triple frequency 3ω, as shown in **Figure 1.1.**[58] In contrast to SHG, THG response of the material does not depends on intrinsic crystal symmetry. Therefore, Graphene, despite its centrosymmetric structure shows strong THG response whereas it has weak SHG response.[61–64] THG effect is 2D materials has potential applications in bio imaging[65,66], photonics devices.[67] and materials' characterization[66,68] such as identification of layer number[58], grain boundaries detection[49], crystallographic orientation determination.[69]

1.2.3 High harmonic generation

High Harmonic Generation (THG) is high-order ($n\geq4$) nonlinear optical process, in which four or more photons of same frequency ω merge into a single photon with nω frequency, as shown in **Figure 1.1.** Even harmonic generation processes are sensitive to intrinsic crystal symmetry whereas odd harmonic generation processes do not depend on intrinsic crystal symmetry.[70] Traditionally, HHG is observed in various bulk crystals such as ZnO[71], Si[72] and GaSe[73], liquid phases[74] and the rare-gas phases such as Ar and Ne.[75–79] Theoretical analysis shows that HHG is linked with electron dynamics within the materials. Therefore, strong many-body interaction, electronic properties and reduced interlayer screening make 2D materials an ideal platform to observe high harmonic generation processes. For example, In 1L MoS_2, higher order harmonics between 6th and 13th generation and its polar response was demonstrated using an intense mid-IR excitation (0.3 eV).[70] HHG has important implications in atto-second physics and ultra-short pulse generation.[80]

Table 1.1 SHG properties of 2D materials

Group	Material	Second order susceptibility "pm/V" [1] (wavelength)		Fabrication	Thickness	Substrate
		Experimental	Simulations			
Graphene		90 (650 nm)[81] Zero (650 nm)[81] Zero (650 nm)[81] Zero (650 nm)[81]	- - - -	Exfoliation Exfoliation Exfoliation Exfoliation	3L (ABA) [2] 3L (ABC) [3] 1L 2L	SiO_2 SiO_2 SiO_2 SiO_2
h-BN		20.6(415 nm) [82] 30 (450 nm)[35] -	- - 20-210 (192-700 nm)[26]	Exfoliation Exfoliation -	1L 1L 1L	SiO_2 SiO_2 -
TMDs [4]	**MoS_2**	40 (680 nm)[37] 120 (435 nm)[34] 29.5 (440 nm)[34] 20-550 (460-700 nm)[82] 43 (620 nm)[83] - - -	- - - - - - 70-200 (516-775 nm)[33] 123-200 (387 nm–443 nm)[34] 112 – 150 (387 nm–443 nm)[34]	CVD Exfoliation Exfoliation Exfoliation CVD - - -	1L 1L 3L 1L 1L 1L 3L 1L	SiO_2 Quartz Quartz SiO_2 SiO_2 - - -
	WS_2	500 (440 nm)[84] 80-670 (460-700 nm)[82] 4500 (415 nm)[38]	- - 200-1150 (300 nm-620 nm)[38]	CVD Exfoliation Exfoliation	1L 1L 1L	SiO_2 SiO_2 SiO_2
	$MoSe_2$	50 (810 nm)[37] 7800 (775 nm)[43]	- -	CVD Exfoliation	1L 1L	SiO_2 Si waveguide
	WSe_2	100 (775 nm)[39] 19 (775 nm)[39] 60 (738 nm)[85]	- - -	Exfoliation Exfoliation Exfoliation	1L 5L 1L	SiO_2 SiO_2 SiO_2
	$MoTe_2$	2500 (775 nm)[86]	-	Exfoliation	1L	SiO_2
Group III–VI	**GaS**	-	71 (800 nm)[87]	-	1L	-
	GaSe	2400 (605 nm)[88] 1700 (675 nm)[88] 700 (800 nm) [88] 18 (780 nm)[89] 86 (700 nm)[90] - - - - -	- - - - - - 75 (800 nm)[87] 84 (605 nm)[87] 88 (675 nm)[87] 18.2 (865 nm)[89] 32.4 (865 nm)[87]	Exfoliation Exfoliation Exfoliation Exfoliation Exfoliation - - - - -	1L 1L 1L Bulk Few L 1L 1L 1L 1L 14L	SiO_2 SiO_2 SiO_2 Si SiO_2 - - - - -
	GaTe	1.15 (780 nm)[91] - -	- 180 (800 nm)[87] 184.3 (780 nm)[87]	Exfoliation - -	Few L 1L Few L	SiO_2 - -
	InSe	- (530 nm)[92] -	- 150 - 650 (275 – 1550 nm)[93]	Exfoliation -	ML [5] 1L	Quartz -
Group IV–VI	**GeSe**	- -	7368 (939 nm)[26] 500-10000 (620-1550 nm)[94]	- -	1L 1L	- -
	GeS	-	200-8000 (443-1550 nm)[94]	-	1L	-
	SnSe	-	200-10000 (620-1550 nm)[94]	-	1L	-
	SnS	-	550-7800 (550-1550 nm)[94]	-	1L	-
Other Materials	**In_2Se_3** **Bi_2Se_3** **SiC** **ZnO** **GaN**	- - - - -	208.8 (420 nm)[95] - (410 nm)[96] 141 (313nm)[97] 14.4 (413 nm)[97] 33.6 (290 nm)[97]	- - - - -	ML 6–40 nm 1L 1L 1L	- - - - -

[1] Non-linear susceptibility units are displayed in pm/V.
[2] ABA (Bernal stacked)
[3] ABC (Rhombohedral)

[4] The values TMDs mentioned are for 2H phase of TMDs.
[5] Multilayers

Table 1.2 THG properties of 2D materials

Group	Material	Third order susceptibility [1] (wavelength)		Fabrication	Thickness	Substrate
		Experimental	Theoretical			
Graphene		1.9 (432nm)[62]	-	CVD	1L	SiO_2
BP		1.4 (519nm)[98]	-	Exfoliation	29L	SiO_2
TMDs	MoS_2	2.4 (520nm)[36]	-	Exfoliation	1L	SiO_2
	WS_2	2.4 (430nm)[99]	-	CVD	1L	SiO_2
	WSe_2	1.3 (517nm)[39] 1.3 (517nm)[39] 1.16 (517nm)[39]	- - -	Exfoliation Exfoliation Exfoliation	1L 5L Bulk	SiO_2 SiO_2 SiO_2
Group III–VI	GaTe	2000 (520nm)[91]	-	Exfoliation	Few L	SiO_2
	GaSe	1700(520nm)[89]	-	Exfoliation	9-14L	SiO_2

[1] Non-linear susceptibility units are displayed in $\times 10^{-19}$ m^2V^{-2}.

1.2.4 Low frequency generation

Low frequency generation or sub frequency generation refer to spontaneous parametric down conversion (SPDC) processes such as half harmonics ($n=1/2$). Half harmonic generation is a nonlinear optical process, in which a photon of fundamental frequency ω splits into two photons $\omega/2$ frequency each, as shown in **Figure 1.1a.** Half-harmonic generation in bulk materials such as Gallium Phosphide (GaP)[100] and Gallium Arsenide (GaAs)[101–103] is demonstrated over broadband mid-infrared frequency generation. Inversion symmetry breaking in ultra-thin 2D materials not only causes improved second harmonics, it can also result in spontaneous parametric down conversion (SPDC) such as half harmonics. For example, Hatef et. al.[104] observed exciting half harmonic emission response at 1560nm (IR) in 1L MoS_2 using 780nm laser excitation beam showing maximum non-linear susceptibility (χ) around 1000pm/V. Half HG process is used in generation of mid-infrared and near-infrared waves, photonic devices such as optical parametric oscillators and modulators.[105]

1.3 Low-dimensional materials

Low dimensional materials have increased research interest soon after he discovery of Graphene in 2004 due to their interesting properties. For instance, Graphene (2D) is a superconductor with excellent electrical and mechanical properties which is totally different from Graphite (3D bulk form).[106] Therefore, low dimensional materials[107–111] have got tremendous attention and are mainly classified into three types (**Figure 1.2**).

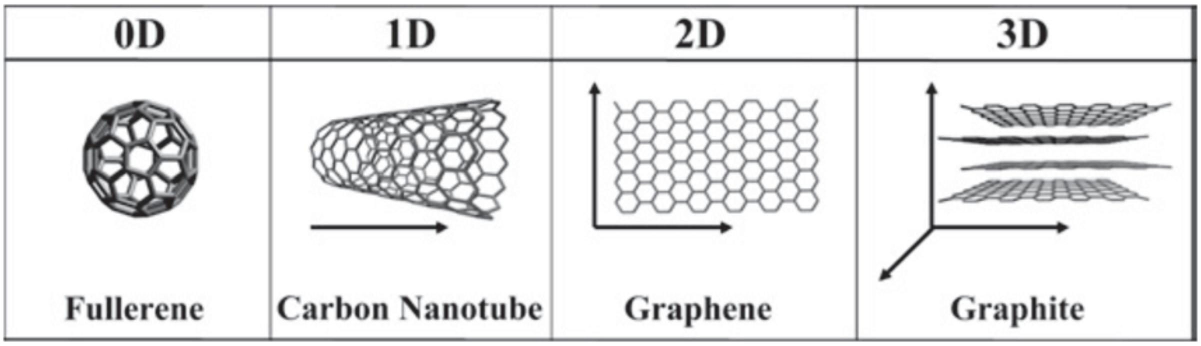

Figure 1.2 | Classifications of low dimensional materials.
Reproduced with permission. Copyright 2016, Springer Link Publications.[112]

1.3.1 Zero-dimensional (0D) materials

In 0D materials, all of the three dimensions are in the nano metric range.[106] For example, nano particles, nano powders, quantum dots, etc.[113–115] Recently, significant progress has been made in the field of 0D materials. A rich variety of physical and chemical methods have been developed for fabricating 0D materials with well-controlled dimensions. Recently, 0D materials such as particle quantum dots, core–shell quantum dots, hollow spheres and nano lenses have been synthesized by several research groups [116–124]. Moreover, they have been extensively studied in light emitting diodes (LEDs)[125,126], solar cells[127], field effect transistors[128], and lasers[115,129].

1.3.2 One-dimensional (1D) materials

In 1D materials, two dimensions are in the nano metric range and third dimension remains large.[106] These structures have shape like rods. For instance. nano tubes, nano rods, nano wires etc.[130,131] It is generally believed that 1D materials are ideal systems for exploring a large number of novel phenomena at the nanoscale and investigating the size and dimensionality dependence of functional properties. For instance, carbon nano-tubes (CNT) have shown interesting dimensional, electrical and optical properties. In the past decade, 1D materials such as nanowires, nanorods, nanotubes, nanobelts, nanoribbons have attracted an increasing interest due to their potential applications in nanoelectronics, photonics and biomedical applications.[115,131–137]

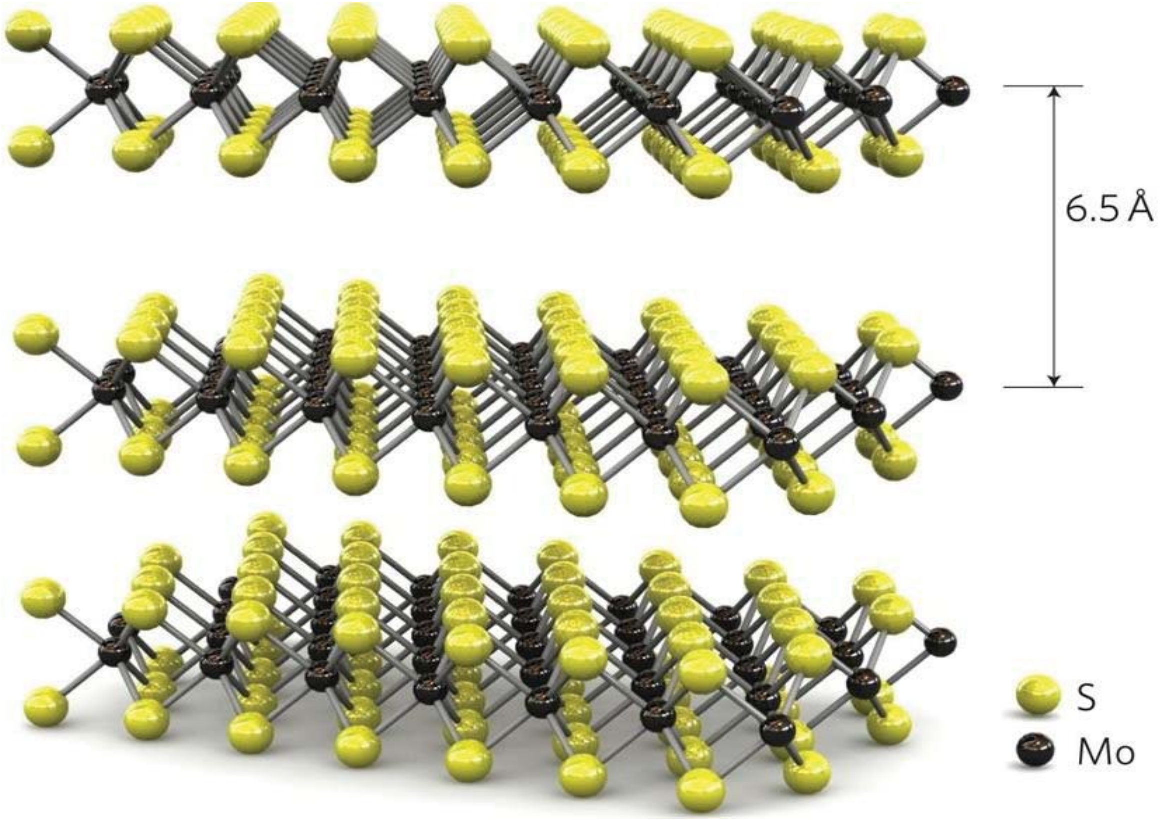

Figure 1.3 | Schematic plot of MoS2, a typical member of TMDs.
Reproduced with permission[138]. Copyright 2011, Nature Publishing Group.

1.3.3 Two-dimensional (2D) materials

In 2D Materials, only one dimension is in the nano metric range whereas other two dimensions remain large.[106] For instance, nano thin films, nano coating, nano layers, etc.[139–141] Soon after the discovery of graphene, 2D layered materials have gained huge interest.[142,143] 2D layered materials typically consist of covalently bonded atomic layers that are weakly bonded together by Van der Waals forces and can be isolated into single or few atoms thick nanosheets.[106] A variety of techniques including mechanical exfoliation, liquid exfoliation, and chemical vapor deposition (CVD) have been employed to synthesize 2D materials.[130,144–147] Apart from graphene, scientists and researchers have found some new 2D layered materials with interesting features such as transition metal dichalcogenides (TMDs), Phosphorene, etc.[146,148]

2D TMDs (MoS_2, WS_2, $MoSe_2$, WSe_2, etc) represent a large family of layered materials in which atoms are covalently bonded in a single layer and different layers are stacked together by weak Van der Waals interaction (**Figure 1.3**). TMDs exhibit tuneable band gaps that can undergo a transition from an indirect band gap in bulk crystals to a direct band gap in monolayer nanosheets.[146] Therefore, TMDs have thus emerged as an exciting class of atomically thin semiconductors for a new generation of electronic and optoelectronic devices.

1.4 Synthesis of Low Dimensional Materials

Low dimensional materials are synthesized using two techniques: top-down exfoliation (mechanical or solution exfoliation) and bottom-up growth (vapor deposition, pulsed laser deposition, or wet chemical method). Mechanical exfoliation and vapour deposition are the most common synthesis methods for low dimensional materials which are described as follow;

Mechanical Exfoliation. This method uses micromechanical cleavage of bulk crystals to get low dimensional materials. This technique is commonly used to get 2D layered materials, such as monolayer and multilayer of TMD. In 2004, a team from the University of Manchester prepared monolayer graphene from graphite using scotch tape method. In this technique, a scotch tape is placed on the bulk crystals and subsequently removed. The scotch tape, with tiny flakes coming off the bulk material, is pressed against the surface of a substrate. On removing the scotch tape, tiny flakes are deposited on the substrate. Even though mechanical exfoliation provides high quality deposition of tiny flakes, however, this process is not a scalable production method suitable for industries [145,149–152].

Liquid phase exfoliation. Liquid phase exfoliation is another effective way for preparing high-quality layered materials. For this method, there are several critical stages: oxidation treatment, ion intercalation/exchange, and surface passivation of solvents. It is one of the most used layered material preparation methods in photonic device applications. This is because it has many advantages, such as simplicity, efficiency, low cost, high scalability, and standardized production process [149]–[152].

Vapour deposition. Physical or chemical vapour deposition is one of most common methods to synthesize low dimensional materials. Chemical vapour deposition is a common bottom-up method to prepare nanomaterials on fixed substrates through the reaction of precursors at high temperatures. Physical vapour deposition is a well-known technique to fabricate nanomaterials on fixed substrates through the vapour deposition of a single material at high temperature. Moreover, pulsed laser deposition has also attracted wide attention[153].

1.5 Motivation and Thesis synopsis

Low dimensional materials show great potential for optoelectronic applications. Recently, enormous attention is given to explore the non-linear properties of low dimensional materials.[26] They show strong non-linear optical properties, due to their unique layer dependent optical properties and good phase matching. [29–33] Non-linear optical interaction has potential applications in various photonic applications such as lasers[7], waveguides[8–11], optic fibres[12], optical frequency converters,[13,14] optical switches[15,16] and photo detectors.[17–19] Nano manufacturing techniques such as local strain engineering, and homo-structures/folding, etc provide functional control over critical optoelectronic properties of low dimensional materials. For instance, strain engineering is shown to reduce the carrier effective mass and modify the valley structure, thus leading to an increase in its career mobility in atomically thin MoS_2.[154–161] Homo-structures and folding are shown to tailor electron and phonon properties.[162] Thermal variation, in addition, is shown to alter optoelectronic properties such as bandgap modulation[163], variation in phonon modes[164–167], tuning in carrier mobility[168]. Ultra-thin TMDs are particularly well-suited experimental platform for this purpose due to their high flexibility and deformability. Here, we aim to explore nonlinear light matter interactions in 2D materials through nanomanufacturing techniques using structural engineering such as strain engineering, folding, thermal modulation.

Chapter 2 will highlight the optical harmonic generation processes in 2D materials. In this regard, the role of optical harmonic generation is highlighted for various types of characterizations in 2D materials, such as layer identification, lattice orientation, phase variation, defects characterization, piezoelectric and ferroelectric detection, etc. Then, the main approaches to tune optical harmonic generation in 2D maters are discussed, such as gate tuning, exciton resonances, etc. Finally, several potential applications of optical harmonic generation processes in 2D materials, such as photonic devices, imaging and sensing, etc., are discussed.

Chapter 3 will discuss local strain engineering and folding as effective nonmanufacturing technique to tune optoelectronic properties of 2D materials. Local strain engineering and folding in 1-3L WS_2 will be achieved using a new fabrication technique. Layer dependent surface potential measurements will be done for both folded layers and naturally stacked layers in 1-3L WS_2. Dark current and photo current measurements in strained and folded WS_2 will be done to explore the effect of straining and folding on optoelectronic properties.

Chapter 4 will talk over nonlinear light matter interaction in folded and strained WS_2 evaluated through SHG (second harmonic generation). Polarization-dependent SHG as a single tool is used to probe folding angle (stacking angle between the individual layers of the fold) and strain vector precisely in atomically thin tungsten disulphide (WS_2). Trilayers fold are found to show extraordinary SHG enhancement with folding angle modulation which is explained using vector superposition of SH wave vectors coming from the individual layers of the folds. Strain is shown sensitive to strain vector. Strained TMDs are studied using polarization dependent SHG which allowed us to find the local strain vector accurately using photoelastic effect. SHG, sensitive to band-nesting induced transition (C-peak), is shown to be significantly modulated through strain modification.

Chapter 5 will focus the temperature dependent SHG investigation in thin Layers of TMDs. Layer dependent SHG response in TMDs is found sensitive to temperature modulation showing opposite trends for single layer and few odd layers (3L, 5L, 7L, etc) of TMDs. SHG, as a powerful and sensitive approach, is used to investigate thermal variation in ultrathin TMDs.

Chapter 6 discusses an additional study performed on light matter interactions in 1D Pentacene wires which is another low dimensional class of the materials. Pentacene nano wires are grown on hBN (hexagonal Boron Nitride) using vapour deposition approach. Pentacene nanowires show high crystalline features which are studied through photoluminescence spectroscopy.

Finally, Chapter 7 will give an overall conclusion of this dissertation, and prospects for future work in this field will also be discussed.

Chapter 1 References

(1) Halina, A. *Introduction to Laser Spectroscopy*; Elsevier, **2005**.

(2) Boyd, R. W.; Masters, B. R. Nonlinear Optics, Third Edition. *J. Biomed. Opt.* **2009**, *14* (2), 029902.

(3) Shen, Y. R. Basic Theory of Surface Sum-Frequency Generation. *J. Phys. Chem. C* **2012**, *116* (29), 15505–15509.

(4) Shen, Y. R. Surface Properties Probed by Second-Harmonic and Sum-Frequency Generation. *Nature* **1989**, *337* (6207), 519–525.

(5) Stijns, E.; Thienpont, H. Fundamentals of Photonics. In *Optical and Digital Image Processing*; Wiley-VCH Verlag GmbH & Co. KGaA: Weinheim, Germany, **2011**; pp 25–48.

(6) Agrawal, G. P. *Applications of Nonlinear Fiber Optics*; Elsevier, **2008**.

(7) Keller, U. Recent Developments in Compact Ultrafast Lasers. *Nature*. **2003**, pp 831–838.

(8) Lin, Q.; Painter, O. J.; Agrawal, G. P. Nonlinear Optical Phenomena in Silicon Waveguides: Modeling and Applications. *Opt. Express* **2007**, *15* (25), 16604.

(9) *Nonlinear Optical Effects and Materials*; Günter, P., Ed.; Springer Series in Optical Sciences; Springer Berlin Heidelberg: Berlin, Heidelberg, **2000**; Vol. 72.

(10) Koos, C.; Jacome, L.; Poulton, C.; Leuthold, J.; Freude, W. Nonlinear Silicon-on-Insulator Waveguides for All-Optical Signal Processing. *Opt. Express* **2007**, *15* (10), 5976.

(11) Tong Ph.D, X. C. *Advanced Materials for Integrated Optical Waveguides*; Springer Series in Advanced Microelectronics; Springer International Publishing: Cham, **2014**; Vol. 46.

(12) Stegeman, G. I.; Stolen, R. H. Waveguides and Fibers for Nonlinear Optics. *J. Opt. Soc. Am. B* **1989**, *6* (4), 652.

(13) Absil, P. P.; Hryniewicz, J. V.; Little, B. E.; Cho, P. S.; Wilson, R. A.; Joneckis, L. G.; Ho, P.-T. Wavelength Conversion in GaAs Micro-Ring Resonators. *Opt. Lett.* **2000**, *25* (8), 554.

(14) Hong, C. K.; Mandel, L. Theory of Parametric Frequency down Conversion of Light. *Phys. Rev. A* **1985**, *31* (4), 2409–2418.

(15) Chang, D. E.; Vuletić, V.; Lukin, M. D. Quantum Nonlinear Optics - Photon by Photon. *Nat. Photonics* **2014**, *8* (9), 685–694.

(16) Champagne, B.; Plaquet, A.; Pozzo, J. L.; Rodriguez, V.; Castet, F. Nonlinear Optical Molecular Switches as Selective Cation Sensors. *J. Am. Chem. Soc.* **2012**, *134* (19), 8101–8103.

(17) Eichler, H. J.; Eichler, J.; Lux, O. Photodetectors. In *Springer Series in Optical Sciences*; **2018**; Vol. 220, pp 381–396.

(18) Piels, M.; Ramaswamy, A.; Bowers, J. E. Nonlinear Modeling of Waveguide Photodetectors. *Opt. Express* **2013**, *21* (13), 15634.

(19) McGurn, A. Nonlinear Optics. In *Springer Series in Optical Sciences*; **2018**; Vol. 213, pp 461–490.

(20) Sohler, W.; Hu, H.; Ricken, R.; Quiring, V.; Vannahme, C.; Herrmann, H.; Büchter, D.; Reza, S.; Grundkötter, W.; Orlov, S.; et al. Integrated Optical Devices in Lithium Niobate. *Opt. Photonics News* **2008**, *19* (1), 24.

(21) Lawrence, M. Lithium Niobate Integrated Optics. *Reports Prog. Phys.* **1993**, *56* (3), 363–429.

(22) Guarino, A.; Poberaj, G.; Rezzonico, D.; Degl’Innocenti, R.; Günter, P. Electro–Optically Tunable Microring Resonators in Lithium Niobate. *Nat. Photonics* **2007**, *1* (7), 407–410.

(23) Wang, C.; Zhang, M.; Chen, X.; Bertrand, M.; Shams-Ansari, A.; Chandrasekhar, S.; Winzer, P.; Lončar, M. Integrated Lithium Niobate Electro-Optic Modulators Operating at CMOS-Compatible Voltages. *Nature*. **2018**, pp 101–104.

(24) Xiong, C.; Pernice, W. H. P.; Ngai, J. H.; Reiner, J. W.; Kumah, D.; Walker, F. J.; Ahn, C. H.; Tang, H. X. Active Silicon Integrated Nanophotonics: Ferroelectric BaTiO3 Devices. *Nano Lett.* **2014**, *14* (3), 1419–1425.

(25) George, N. A. Enhancement of Nonlinear Optical Properties of BaTiO_3 Nanoparticles by the Addition of Silver Seeds: Comment. *Opt. Express* **2017**, *25* (15), 18056.

(26) Wang, H.; Qian, X. Giant Optical Second Harmonic Generation in Two-Dimensional Multiferroics. *Nano Lett.* **2017**, *17* (8), 5027–5034.

(27) Schiek, R.; Pertsch, T. Absolute Measurement of the Quadratic Nonlinear Susceptibility of Lithium Niobate in Waveguides. *Opt. Mater. Express* **2012**, *2* (2), 126.

(28) Zhao, M.; Ye, Z.; Suzuki, R.; Ye, Y.; Zhu, H.; Xiao, J.; Wang, Y.; Iwasa, Y.; Zhang, X. Atomically Phase-Matched Second-Harmonic Generation in a 2D Crystal. *Light Sci. Appl.* **2016**, *5* (8), e16131–e16131.

(29) Yadav, V.; Roy, S.; Singh, P.; Khan, Z.; Jaiswal, A. 2D MoS 2 -Based Nanomaterials for Therapeutic, Bioimaging, and Biosensing Applications. *Small* **2019**, *15* (1), 1803706.

(30) Bhimanapati, G. R.; Lin, Z.; Meunier, V.; Jung, Y.; Cha, J.; Das, S.; Xiao, D.; Son, Y.; Strano, M. S.; Cooper, V. R.; et al. Recent Advances in Two-Dimensional Materials beyond Graphene. *ACS Nano*. **2015**, pp 11509–11539.

(31) Kumar, N.; Najmaei, S.; Cui, Q.; Ceballos, F.; Ajayan, P. M.; Lou, J.; Zhao, H. Second Harmonic Microscopy of Monolayer MoS2. *Phys. Rev. B* **2013**, *87* (16), 161403.

(32) Wagoner, G. A.; Persans, P. D.; Van Wagenen, E. A.; Korenowski, G. M. Second-Harmonic Generation in Molybdenum Disulfide. *J. Opt. Soc. Am. B* **1998**, *15* (3), 1017.

(33) Trolle, M. L.; Seifert, G.; Pedersen, T. G. Theory of Excitonic Second-Harmonic Generation in Monolayer MoS_2 *Phys. Rev. B* **2014**, *89* (23), 235410.

(34) Malard, L. M.; Alencar, T. V.; Barboza, A. P. M.; Mak, K. F.; de Paula, A. M. Observation of Intense Second Harmonic Generation from MoS_2 Atomic Crystals. *Phys. Rev. B* **2013**, *87* (20), 201401.

(35) Li, Y.; Rao, Y.; Mak, K. F.; You, Y.; Wang, S.; Dean, C. R.; Heinz, T. F. Probing Symmetry Properties of Few-Layer MoS_2 and h-BN by Optical Second-Harmonic Generation. *Nano Lett.* **2013**, *13*, 3329–3333.

(36) Woodward, R. I.; Murray, R. T.; Phelan, C. F.; Oliveira, R. E. P. de; Runcorn, T. H.; Kelleher, E. J. R.; Li, S.; Oliveira, E. C. de; Fechine, G. J. M.; Eda, G.; et al. Characterization of the Second- and Third-Order Nonlinear Optical Susceptibilities of Monolayer MoS_2 Using Multiphoton Microscopy. *2D Mater.* **2016**, *4* (1), 011006.

(37) Le, C. T.; Clark, D. J.; Ullah, F.; Senthilkumar, V.; Jang, J. I.; Sim, Y.; Seong, M. J.; Chung, K. H.; Park, H.; Kim, Y. S. Nonlinear Optical Characteristics of Monolayer MoSe2. *Ann. Phys.* **2016**, *528* (7–8), 551–559.

(38) Janisch, C.; Wang, Y.; Ma, D.; Mehta, N.; Elías, A. L.; Perea-López, N.; Terrones, M.; Crespi, V.; Liu, Z. Extraordinary Second Harmonic Generation in Tungsten Disulfide Monolayers. *Sci. Rep.* **2014**, *4* (c), 1–5.

(39) Rosa, H. G.; Ho, Y. W.; Verzhbitskiy, I.; Rodrigues, M. J. F. L.; Taniguchi, T.; Watanabe, K.; Eda, G.; Pereira, V. M.; Gomes, J. C. V. Characterization of the Second- and Third-Harmonic Optical Susceptibilities of Atomically Thin Tungsten Diselenide. *Sci. Rep.* **2018**, *8* (1), 10035.

(40) Klein, J.; Wierzbowski, J.; Steinhoff, A.; Florian, M.; Rösner, M.; Heimbach, F.; Müller, K.; Jahnke, F.; Wehling, T. O.; Finley, J. J.; et al. Electric-Field Switchable Second-Harmonic Generation in Bilayer MoS 2 by Inversion Symmetry Breaking. *Nano Lett.* **2017**, *17* (1), 392–398.

(41) Wang, G.; Marie, X.; Gerber, I.; Amand, T.; Lagarde, D.; Bouet, L.; Vidal, M.; Balocchi, A.; Urbaszek, B. Giant Enhancement of the Optical Second-Harmonic Emission of <math Display="inline"> <mrow> <msub> <mrow> <mi>WSe</Mi> </Mrow> <mrow> <mn>2</Mn> </Mrow> </Msub> </Mrow> </Math> Monolayers by Laser Excitation at Exciton Resonances. *Phys. Rev. Lett.* **2015**, *114* (9), 097403.

(42) Fouladi-Oskouei, J.; Shojaei, S. Quantum-Enhanced Tunable Spin-Valley Dependent Excitonic Second Harmonic Generation in Molybdenum Disulfide Quantum Dots. *Mater. Res. Express* **2019**, *6* (12), 126204.

(43) Chen, H.; Corboliou, V.; Solntsev, A. S.; Choi, D.-Y.; Vincenti, M. A.; de Ceglia, D.; de Angelis, C.; Lu, Y.; Neshev, D. N. Enhanced Second-Harmonic Generation from Two-Dimensional MoSe2 on a Silicon Waveguide. *Light Sci. Appl.* **2017**, *6* (10), e17060–e17060.

(44) Liu, S.; Sinclair, M. B.; Saravi, S.; Keeler, G. A.; Yang, Y.; Reno, J.; Peake, G. M.; Setzpfandt, F.; Staude, I.; Pertsch, T.; et al. Resonantly Enhanced Second-Harmonic Generation Using III–V Semiconductor All-Dielectric Metasurfaces. *Nano Lett.* **2016**, *16* (9), 5426–5432.

(45) Rosa, H. G.; Junpeng, L.; Gomes, L. C. V.; Rodrigues, M. J. L. F.; Haur, S. C.; Gomes, J. C. V. Second-Harmonic Spectroscopy for Defects Engineering Monitoring in Transition Metal Dichalcogenides. *Adv. Opt. Mater.* **2018**, *6* (5), 1701327.

(46) Le, C. T.; Clark, D. J.; Ullah, F.; Jang, J. I.; Senthilkumar, V.; Sim, Y.; Seong, M.-J.; Chung, K.-H.; Kim, J. W.; Park, S.; et al. Impact of Selenium Doping on Resonant Second-Harmonic Generation in Monolayer MoS 2. *ACS Photonics* **2017**, *4* (1), 38–44.

(47) Hristu, R.; Stanciu, S. G.; Tranca, D. E.; Polychroniadis, E. K.; Stanciu, G. A. Identification of Stacking Faults in Silicon Carbide by Polarization-Resolved Second Harmonic Generation Microscopy. *Sci. Rep.* **2017**, *7* (1), 4870.

(48) Kim, C.-J.; Brown, L.; Graham, M. W.; Hovden, R.; Havener, R. W.; McEuen, P. L.; Muller, D. A.; Park, J. Stacking Order Dependent Second Harmonic Generation and Topological Defects in h -BN Bilayers. *Nano Lett.* **2013**, *13* (11), 5660–5665.

(49) Karvonen, L.; Säynätjoki, A.; Huttunen, M. J.; Autere, A.; Amirsolaimani, B.; Li, S.; Norwood, R. A.; Peyghambarian, N.; Lipsanen, H.; Eda, G.; et al. Rapid Visualization of Grain Boundaries in Monolayer MoS2 by Multiphoton Microscopy. *Nat. Commun.* **2017**, *8* (1), 15714.

(50) Yin, X.; Ye, Z.; Chenet, D. A.; Ye, Y.; O'Brien, K.; Hone, J. C.; Zhang, X. Edge Nonlinear Optics on a MoS2 Atomic Monolayer. *Science (80-.).* **2014**, *344* (6183), 488–490.

(51) Wu, W.; Wang, L.; Li, Y.; Zhang, F.; Lin, L.; Niu, S.; Chenet, D.; Zhang, X.; Hao, Y.; Heinz, T. F.; et al. Piezoelectricity of Single-Atomic-Layer MoS2 for Energy Conversion and Piezotronics. *Nature* **2014**, *514* (7523), 470–474.

(52) Cui, C.; Xue, F.; Hu, W.-J.; Li, L.-J. Two-Dimensional Materials with Piezoelectric and Ferroelectric Functionalities. *npj 2D Mater. Appl.* **2018**, *2* (1), 18.

(53) Liu, F.; You, L.; Seyler, K. L.; Li, X.; Yu, P.; Lin, J.; Wang, X.; Zhou, J.; Wang, H.; He, H.; et al. Room-Temperature Ferroelectricity in CuInP2S6 Ultrathin Flakes. *Nat. Commun.* **2016**, *7* (1), 12357.

(54) Wu, P.-C.; Hsieh, T.-Y.; Tsai, Z.-U.; Liu, T.-M. In Vivo Quantification of the Structural Changes of Collagens in a Melanoma Microenvironment with Second and Third Harmonic Generation Microscopy. *Sci. Rep.* **2015**, *5* (1), 8879.

(55) Seyler, K. L.; Schaibley, J. R.; Gong, P.; Rivera, P.; Jones, A. M.; Wu, S.; Yan, J.; Mandrus, D. G.; Yao, W.; Xu, X. Electrical Control of Second-Harmonic Generation in a WSe2 Monolayer Transistor. *Nat. Nanotechnol.* **2015**, *10* (5), 407–411.

(56) Jiang, T.; Liu, H.; Huang, D.; Zhang, S.; Li, Y.; Gong, X.; Shen, Y.-R.; Liu, W.-T.; Wu, S. Valley and Band Structure Engineering of Folded MoS2 Bilayers. *Nat. Nanotechnol.* **2014**, *9* (10), 825–829.

(57) Shinde, S. M.; Dhakal, K. P.; Chen, X.; Yun, W. S.; Lee, J.; Kim, H.; Ahn, J.-H. Stacking-Controllable Interlayer Coupling and Symmetric Configuration of Multilayered MoS2. *NPG Asia Mater.* **2018**, *10* (2), e468–e468.

(58) Säynätjoki, A.; Karvonen, L.; Rostami, H.; Autere, A.; Mehravar, S.; Lombardo, A.; Norwood, R. A.; Hasan, T.; Peyghambarian, N.; Lipsanen, H.; et al. Ultra-Strong Nonlinear Optical Processes and Trigonal Warping in MoS 2 Layers. *Nat. Commun.* **2017**, *8* (1), 2005–2009.

(59) Momma, K.; Izumi, F. VESTA 3 for Three-Dimensional Visualization of Crystal, Volumetric and Morphology Data. *J. Appl. Crystallogr.* **2011**, *44* (6), 1272–1276.

(60) Hsu, W.-T.; Zhao, Z.-A.; Li, L.-J.; Chen, C.-H.; Chiu, M.-H.; Chang, P.-S.; Chou, Y.-C.; Chang, W.-H. Second Harmonic Generation from Artificially Stacked Transition Metal Dichalcogenide Twisted Bilayers. *ACS Nano* **2014**, *8* (3), 2951–2958.

(61) Wang, Y.; Tokman, M.; Belyanin, A. Second-Order Nonlinear Optical Response of Graphene. *Phys. Rev. B* **2016**, *94* (19), 195442.

(62) Jiang, T.; Huang, D.; Cheng, J.; Fan, X.; Zhang, Z.; Shan, Y.; Yi, Y.; Dai, Y.; Shi, L.; Liu, K.; et al. Gate-Tunable Third-Order Nonlinear Optical Response of Massless Dirac Fermions in Graphene. *Nat. Photonics* **2018**, *12* (7), 430–436.

(63) Hong, S.-Y.; Dadap, J. I.; Petrone, N.; Yeh, P.-C.; Hone, J.; Osgood, R. M. Optical Third-Harmonic Generation in Graphene. *Phys. Rev. X* **2013**, *3* (2), 021014.

(64) Trivedi, R.; Khankhoje, U. K.; Majumdar, A. Cavity-Enhanced Second-Order Nonlinear Photonic Logic Circuits. *Phys. Rev. Appl.* **2016**, *5* (5), 054001.

(65) Yelin, D.; Silberberg, Y. Laser Scanning Third-Harmonic Generation Microscopy in Biology. In *Molecular Crystals and Liquid Crystals Science and Technology Section B: Nonlinear Optics*; **2000**; Vol. 24, pp 267–270.

(66) Weigelin, B.; Bakker, G. J.; Friedl, P. Third Harmonic Generation Microscopy of Cells and Tissue Organization. *J. Cell Sci.* **2016**, *129* (2), 245–255.

(67) Corcoran, B.; Monat, C.; Grillet, C.; Moss, D. J.; Eggleton, B. J.; White, T. P.; O'Faolain, L.; Krauss, T. F. Green Light Emission in Silicon through Slow-Light Enhanced Third-Harmonic Generation in Photonic-Crystal Waveguides. *Nat. Photonics* **2009**, *3* (4), 206–210.

(68) Barad, Y.; Eisenberg, H.; Horowitz, M.; Silberberg, Y. Nonlinear Scanning Laser Microscopy by Third Harmonic Generation. *Appl. Phys. Lett.* **1997**, *70* (8), 922–924.

(69) Autere, A.; Ryder, C. R.; Säynätjoki, A.; Karvonen, L.; Amirsolaimani, B.; Norwood, R. A.; Peyghambarian, N.; Kieu, K.; Lipsanen, H.; Hersam, M. C.; et al. Rapid and Large-Area Characterization of Exfoliated Black Phosphorus Using Third-Harmonic Generation Microscopy. *J. Phys. Chem. Lett.* **2017**, *8* (7), 1343–1350.

(70) Liu, H.; Li, Y.; You, Y. S.; Ghimire, S.; Heinz, T. F.; Reis, D. A. High-Harmonic Generation from an Atomically Thin Semiconductor. *Nat. Phys.* **2017**, *13* (3), 262–265.

(71) Ghimire, S.; DiChiara, A. D.; Sistrunk, E.; Agostini, P.; DiMauro, L. F.; Reis, D. A. Observation of High-Order Harmonic Generation in a Bulk Crystal. *Nat. Phys.* **2011**, *7* (2), 138–141.

(72) Vampa, G.; Ghamsari, B. G.; Siadat Mousavi, S.; Hammond, T. J.; Olivieri, A.; Lisicka-Skrek, E.; Naumov, A. Y.; Villeneuve, D. M.; Staudte, A.; Berini, P.; et al. Plasmon-Enhanced High-Harmonic Generation from Silicon. *Nat. Phys.* **2017**, *13* (7), 659–662.

(73) Hohenleutner, M.; Langer, F.; Schubert, O.; Knorr, M.; Huttner, U.; Koch, S. W.; Kira, M.; Huber, R. Real-Time Observation of Interfering Crystal Electrons in High-Harmonic Generation. *Nature* **2015**, *523* (7562), 572–575.

(74) Luu, T. T.; Yin, Z.; Jain, A.; Gaumnitz, T.; Pertot, Y.; Ma, J.; Wörner, H. J. Extreme–Ultraviolet High–Harmonic Generation in Liquids. *Nat. Commun.* **2018**, *9* (1), 3723.

(75) Wang, G.; Jin, C.; Le, A.-T.; Lin, C. D. Influence of Gas Pressure on High-Order-Harmonic Generation of Ar and Ne. *Phys. Rev. A* **2011**, *84* (5), 053404.

(76) Sayrac, M.; Kolomenskii, A. A.; Strohaber, J.; Schuessler, H. A. High Harmonic Generation in Ne and H_2 Gas Mixtures. *J. Opt. Soc. Am. B* **2015**, *32* (12), 2400.

(77) Ghimire, S.; Reis, D. A. High-Harmonic Generation from Solids. *Nat. Phys.* **2019**, *15* (1), 10–16.

(78) Vampa, G.; Brabec, T. Merge of High Harmonic Generation from Gases and Solids and Its Implications for Attosecond Science. *J. Phys. B At. Mol. Opt. Phys.* **2017**, *50* (8), 083001.

(79) Krause, J. L.; Schafer, K. J.; Kulander, K. C. High-Order Harmonic Generation from Atoms and Ions in the High Intensity Regime. *Phys. Rev. Lett.* **1992**, *68* (24), 3535–3538.

(80) Krausz, F.; Ivanov, M. Attosecond Physics. *Rev. Mod. Phys.* **2009**, *81* (1), 163–234.

(81) Shan, Y.; Li, Y.; Huang, D.; Tong, Q.; Yao, W.; Liu, W.-T.; Wu, S. Stacking Symmetry Governed Second Harmonic Generation in Graphene Trilayers. *Sci. Adv.* **2018**, *4* (6), eaat0074.

(82) Stiehm, T.; Schneider, R.; Kern, J.; Niehues, I.; Michaelis de Vasconcellos, S.; Bratschitsch, R. Supercontinuum Second Harmonic Generation Spectroscopy of Atomically Thin Semiconductors. *Rev. Sci. Instrum.* **2019**, *90* (8), 083102.

(83) Clark, D. J.; Senthilkumar, V.; Le, C. T.; Weerawarne, D. L.; Shim, B.; Jang, J. I.; Shim, J. H.; Cho, J.; Sim, Y.; Seong, M.-J.; et al. Strong Optical Nonlinearity of CVD-Grown MoS_2 Monolayer as Probed by Wavelength-Dependent Second-Harmonic Generation. *Phys. Rev. B* **2014**, *90* (12), 121409.

(84) Fan, X.; Jiang, Y.; Zhuang, X.; Liu, H.; Xu, T.; Zheng, W.; Fan, P.; Li, H.; Wu, X.; Zhu, X.; et al. Broken Symmetry Induced Strong Nonlinear Optical Effects in Spiral WS 2 Nanosheets. *ACS Nano* **2017**, *11* (5), 4892–4898.

(85) Seyler, K. L.; Schaibley, J. R.; Gong, P.; Rivera, P.; Jones, A. M.; Wu, S.; Yan, J.; Mandrus, D. G.; Yao, W.; Xu, X. Electrical Control of Second-Harmonic Generation in a WSe2 Monolayer Transistor. *Nat. Nanotechnol.* **2015**, *10* (5), 407–411.

(86) Beams, R.; Cançado, L. G.; Krylyuk, S.; Kalish, I.; Kalanyan, B.; Singh, A. K.; Choudhary, K.; Bruma, A.; Vora, P. M.; Tavazza, F.; et al. Characterization of Few-Layer 1T′ MoTe 2 by Polarization-Resolved Second Harmonic Generation and Raman Scattering. *ACS Nano* **2016**, *10* (10), 9626–9636.

(87) Hu, L.; Huang, X.; Wei, D. Layer-Independent and Layer-Dependent Nonlinear Optical Properties of Two-Dimensional GaX (X = S, Se, Te) Nanosheets. *Phys. Chem. Chem. Phys.* **2017**, *19* (18), 11131–11141.

(88) Zhou, X.; Cheng, J.; Zhou, Y.; Cao, T.; Hong, H.; Liao, Z.; Wu, S.; Peng, H.; Liu, K.; Yu, D. Strong Second-Harmonic Generation in Atomic Layered GaSe. *J. Am. Chem. Soc.* **2015**, *137* (25), 7994–7997.

(89) Karvonen, L.; Säynätjoki, A.; Mehravar, S.; Rodriguez, R. D.; Hartmann, S.; Zahn, D. R. T.; Honkanen, S.; Norwood, R. A.; Peyghambarian, N.; Kieu, K.; et al. Investigation of Second- and Third-Harmonic Generation in Few-Layer Gallium Selenide by Multiphoton Microscopy. *Sci. Rep.* **2015**, *5* (1), 10334.

(90) Allakhverdiev, K. R.; Yetis, M. Ö.; Özbek, S.; Baykara, T. K.; Salaev, E. Y. Effective Nonlinear GaSe Crystal. Optical Properties and Applications. *Laser Phys.* **2009**, *19* (5), 1092–1104.

(91) Susoma, J.; Karvonen, L.; Säynätjoki, A.; Mehravar, S.; Norwood, R. A.; Peyghambarian, N.; Kieu, K.; Lipsanen, H.; Riikonen, J. Second and Third Harmonic Generation in Few-Layer Gallium Telluride Characterized by Multiphoton Microscopy. *Appl. Phys. Lett.* **2016**, *108* (7), 073103.

(92) Deckoff-Jones, S.; Zhang, J.; Petoukhoff, C. E.; Man, M. K. L.; Lei, S.; Vajtai, R.; Ajayan, P. M.; Talbayev, D.; Madéo, J.; Dani, K. M. Observing the Interplay between Surface and Bulk Optical Nonlinearities in Thin van Der Waals Crystals. *Sci. Rep.* **2016**, *6* (1), 22620.

(93) Attaccalite, C.; Palummo, M.; Cannuccia, E.; Grüning, M. Second-Harmonic Generation in Single-Layer Monochalcogenides: A Response from First-Principles Real-Time Simulations. *Phys. Rev. Mater.* **2019**, *3* (7), 074003.

(94) Raj Panday, S.; Fregoso, B. M. Strong Second Harmonic Generation in Two-Dimensional Ferroelectric IV-Monochalcogenides. *J. Phys. Condens. Matter* **2017**, *29* (43), 43LT01.

(95) Lin, J.; Fang, Z.; Tao, H.; Li, Y.; Huang, X.; Ding, K.; Huang, S.; Zhang, Y. Indium Selenide Monolayer: A Two-Dimensional Material with Strong Second Harmonic Generation. *CrystEngComm* **2018**, *20* (18), 2573–2582.

(96) Glinka, Y. D.; Babakiray, S.; Johnson, T. A.; Holcomb, M. B.; Lederman, D. Resonance-Type Thickness Dependence of Optical Second-Harmonic Generation in Thin Films of the Topological Insulator <math> <mrow> <mi Mathvariant="normal">B</Mi> <msub> <mi Mathvariant="normal">i</Mi> <mn>2</Mn> </Msub> <mi Mathvariant="normal">S</Mi> <m. *Phys. Rev. B* **2015**, *91* (19), 195307.

(97) Attaccalite, C.; Nguer, A.; Cannuccia, E.; Grüning, M. Strong Second Harmonic Generation in SiC, ZnO, GaN Two-Dimensional Hexagonal Crystals from First-Principles Many-Body Calculations. *Phys. Chem. Chem. Phys.* **2015**, *17* (14), 9533–9540.

(98) Youngblood, N.; Peng, R.; Nemilentsau, A.; Low, T.; Li, M. Layer-Tunable Third-Harmonic Generation in Multilayer Black Phosphorus. *ACS Photonics* **2017**, *4* (1), 8–14.

(99) Liang, J.; Wang, J.; Zhang, Z.; Su, Y.; Guo, Y.; Qiao, R.; Song, P.; Gao, P.; Zhao, Y.; Jiao, Q.; et al. Universal Imaging of Full Strain Tensor in 2D Crystals with Third-Harmonic Generation. *Adv. Mater.* **2019**, *31* (19).

(100) Sorokin, E.; Marandi, A.; Schunemann, P. G.; Fejer, M. M.; Byer, R. L.; Sorokina, I. T. Efficient Half-Harmonic Generation of Three-Optical-Cycle Mid-IR Frequency Comb around 4 Mm Using OP-GaP. *Opt. Express* **2018**, *26* (8), 9963.

(101) Smolski, V. O.; Yang, H.; Gorelov, S. D.; Schunemann, P. G.; Vodopyanov, K. L. Coherence Properties of a 26–75 Mm Frequency Comb Produced as a Subharmonic of a Tm-Fiber Laser. *Opt. Lett.* **2016**, *41* (7), 1388.

(102) Smolski, V. O.; Vasilyev, S.; Schunemann, P. G.; Mirov, S. B.; Vodopyanov, K. L. Subharmonic GaAs OPO Pumped by a Cr:ZnS Laser with an Instantaneous Bandwidth 3.6–5.6 Mm. In ***2016** International Conference Laser Optics (LO)*; IEEE, 2016; pp R1-18-R1-18.

(103) Smolski, V. O.; Vasilyev, S.; Schunemann, P. G.; Mirov, S. B.; Vodopyanov, K. L. Cr:ZnS Laser-Pumped Subharmonic GaAs Optical Parametric Oscillator with the Spectrum Spanning 36–56 Mm. *Opt. Lett.* **2015**, *40* (12), 2906.

(104) Dinparasti Saleh, H.; Vezzoli, S.; Caspani, L.; Branny, A.; Kumar, S.; Gerardot, B. D.; Faccio, D. Towards Spontaneous Parametric down Conversion from Monolayer MoS2. *Sci. Rep.* **2018**, *8* (1), 3862.

(105) Marandi, A. Half-Harmonic Generation: Enabling Photonic Solutions for Molecular Sensing and Non-Classical Computing. In *Nonlinear Optics (NLO)*; OSA: Washington, D.C., **2019**; Vol. Part F134-, p NM1A.3.

(106) Mohamed, E. F. Nanotechnology: Future of Environmental Air Pollution Control. *Environ. Manag. Sustain. Dev.* **2017**, *6* (2), 429.

(107) Pakdel, A.; Zhi, C.; Bando, Y.; Golberg, D. Low-Dimensional Boron Nitride Nanomaterials. *Mater. Today* **2012**, *15* (6), 256–265.

(108) Tang, Q.; Zhou, Z. Graphene-Analogous Low-Dimensional Materials. *Prog. Mater. Sci.* **2013**, *58* (8), 1244–1315.

(109) Dresselhaus, M. S.; Dresselhaus, G.; Sun, X.; Zhang, Z.; Cronin, S. B.; Koga, T. Low-Dimensional Thermoelectric Materials. *Phys. Solid State* **1999**, *41* (5), 679–682.

(110) Plechinger, G.; Schrettenbrunner, F. X.; Eroms, J.; Weiss, D.; Schüller, C.; Korn, T. Low-Temperature Photoluminescence of Oxide-Covered Single-Layer MoS 2. *Phys. Status Solidi - Rapid Res. Lett.* **2012**, *6* (3), 126–128.

(111) Tian, H.; Tice, J.; Fei, R.; Tran, V.; Yan, X.; Yang, L.; Wang, H. Low-Symmetry Two-Dimensional Materials for Electronic and Photonic Applications. *Nano Today* **2016**, *11* (6), 763–777.

(112) Machado, F. M.; Fagan, S. B.; da Silva, I. Z.; de Andrade, M. J. Carbon Nanoadsorbents. In *Carbon Nanostructures*; **2015**; pp 11–32.

(113) Zhou, H.; Lee, J. Nanoscale Hydroxyapatite Particles for Bone Tissue Engineering. *Acta Biomater.* **2011**, *7* (7), 2769–2781.

(114) Kiani, M. A.; Mousavi, M. F.; Rahmanifar, M. S. Synthesis of Nano- and Micro-Particles of LiMn2O4: Electrochemical Investigation and Assessment as a Cathode in Li Battery. *Int. J. Electrochem. Sci.* **2011**.

(115) Tiwari, J. N.; Tiwari, R. N.; Kim, K. S. Zero-Dimensional, One-Dimensional, Two-Dimensional and Three-Dimensional Nanostructured Materials for Advanced Electrochemical Energy Devices. *Prog. Mater. Sci.* **2012**, *57* (4), 724–803.

(116) Heck, C.; Prinz, J.; Dathe, A.; Merk, V.; Stranik, O.; Fritzsche, W.; Kneipp, J.; Bald, I. Gold Nanolenses Self-Assembled by DNA Origami. *ACS Photonics* **2017**, *4* (5), 1123–1130.

(117) Ning, C.-Z. Semiconductor Nanolasers and the Size-Energy-Efficiency Challenge: A Review. *Adv. Photonics* **2019**, *1* (01), 1.

(118) Vasudevan, D.; Gaddam, R. R.; Trinchi, A.; Cole, I. Core–Shell Quantum Dots: Properties and Applications. *J. Alloys Compd.* **2015**, *636*, 395–404.

(119) Tomić, S.; Vukmirović, N. *Handbook of Optoelectronic Device Modeling and Simulation*; Piprek, J., Ed.; CRC Press: Boca Raton, FL : CRC Press, Taylor & Francis Group, [2017] |, **2017**.

(120) Dabbousi, B. O.; Rodriguez-Viejo, J.; Mikulec, F. V.; Heine, J. R.; Mattoussi, H.; Ober, R.; Jensen, K. F.; Bawendi, M. G. (CdSe)ZnS Core−Shell Quantum Dots: Synthesis and Characterization of a Size Series of Highly Luminescent Nanocrystallites. *J. Phys. Chem. B* **1997**, *101* (46), 9463–9475.

(121) Shen, L.; Yu, L.; Wu, H. Bin; Yu, X.-Y.; Zhang, X.; Lou, X. W. Formation of Nickel Cobalt Sulfide Ball-in-Ball Hollow Spheres with Enhanced Electrochemical Pseudocapacitive Properties. *Nat. Commun.* **2015**, *6* (1), 6694.

(122) Jena, P. V.; Galassi, T. V.; Roxbury, D.; Heller, D. A. Review—Progress toward Applications of Carbon Nanotube Photoluminescence. *ECS J. Solid State Sci. Technol.* **2017**, *6* (6), M3075–M3077.

(123) Bacon, M.; Bradley, S. J.; Nann, T. Graphene Quantum Dots. *Part. Part. Syst. Charact.* **2014**, *31* (4), 415–428.

(124) Chakraborty, C.; Vamivakas, N.; Englund, D. Advances in Quantum Light Emission from 2D Materials. *Nanophotonics* **2019**, *8* (11), 2017–2032.

(125) Yang, Y.; Zheng, Y.; Cao, W.; Titov, A.; Hyvonen, J.; Manders, J. R.; Xue, J.; Holloway, P. H.; Qian, L. High-Efficiency Light-Emitting Devices Based on Quantum Dots with Tailored Nanostructures. *Nat. Photonics* **2015**, *9* (4), 259–266.

(126) Sun, Q.; Wang, Y. A.; Li, L. S.; Wang, D.; Zhu, T.; Xu, J.; Yang, C.; Li, Y. Bright, Multicoloured Light-Emitting Diodes Based on Quantum Dots. *Nat. Photonics* **2007**, *1* (12), 717–722.

(127) Rühle, S.; Shalom, M.; Zaban, A. Quantum-Dot-Sensitized Solar Cells. *ChemPhysChem* **2010**, *11* (11), 2290–2304.

(128) Hetsch, F.; Zhao, N.; Kershaw, S. V.; Rogach, A. L. Quantum Dot Field Effect Transistors. *Mater. Today* **2013**, *16* (9), 312–325.

(129) Baker, S. N.; Baker, G. A. Luminescent Carbon Nanodots: Emergent Nanolights. *Angew. Chemie Int. Ed.* **2010**, *49* (38), 6726–6744.

(130) Shehzad, K.; Xu, Y.; Gao, C.; Duan, X. Three-Dimensional Macro-Structures of Two-Dimensional Nanomaterials. *Chem. Soc. Rev.* **2016**, *45* (20), 5541–5588.

(131) Sharma, A.; Khan, A.; Zhu, Y.; Halbich, R.; Ma, W.; Tang, Y.; Wang, B.; Lu, Y. Quasi-Line Spectral Emissions from Highly Crystalline One-Dimensional Organic Nanowires. *Nano Lett.* **2019**, *19* (11), 7877–7886.

(132) Zhao, Z.; Tian, J.; Sang, Y.; Cabot, A.; Liu, H. Structure, Synthesis, and Applications of TiO 2 Nanobelts. *Adv. Mater.* **2015**, *27* (16), 2557–2582.

(133) Pan, Z. W. Nanobelts of Semiconducting Oxides. *Science (80-.).* **2001**, *291* (5510), 1947–1949.

(134) PEREZJUSTE, J.; PASTORIZASANTOS, I.; LIZMARZAN, L.; MULVANEY, P. Gold Nanorods: Synthesis, Characterization and Applications. *Coord. Chem. Rev.* **2005**, *249* (17–18), 1870–1901.

(135) Zhang, Q.; Yu, Z.; Du, P.; Su, C. Carbon Nanomaterials Used as Conductive Additives in Lithium Ion Batteries. *Recent Pat. Nanotechnol.* **2010**, *4* (2), 100–110.

(136) Pastorin, G. *Carbon Nanotubes: From Bench Chemistry to Promising Biomedical Applications*; 2011.

(137) Kosynkin, D. V.; Higginbotham, A. L.; Sinitskii, A.; Lomeda, J. R.; Dimiev, A.; Price, B. K.; Tour, J. M. Longitudinal Unzipping of Carbon Nanotubes to Form Graphene Nanoribbons. *Nature* **2009**, *458* (7240), 872–876.

(138) Radisavljevic, B.; Radenovic, A.; Brivio, J.; Giacometti, V.; Kis, A. Single-Layer MoS2 Transistors. *Nat. Nanotechnol.* **2011**, *6* (3), 147–150.

(139) Jimenez-Solomon, M. F.; Song, Q.; Jelfs, K. E.; Munoz-Ibanez, M.; Livingston, A. G. Polymer Nanofilms with Enhanced Microporosity by Interfacial Polymerization. *Nat. Mater.* **2016**, *15* (7), 760–767.

(140) Benameur, M. M.; Radisavljevic, B.; Héron, J. S.; Sahoo, S.; Berger, H.; Kis, A. Visibility of Dichalcogenide Nanolayers. *Nanotechnology* **2011**, *22* (12), 125706.

(141) Lin, J.; Chen, H.; Fei, T.; Zhang, J. Highly Transparent Superhydrophobic Organic–Inorganic Nanocoating from the Aggregation of Silica Nanoparticles. *Colloids Surfaces A Physicochem. Eng. Asp.* **2013**, *421*, 51–62.

(142) Xia, F.; Wang, H.; Xiao, D.; Dubey, M.; Ramasubramaniam, A. Two-Dimensional Material Nanophotonics. *Nat. Photonics* **2014**, *8* (12), 899–907.

(143) Manzeli, S.; Ovchinnikov, D.; Pasquier, D.; Yazyev, O. V.; Kis, A. 2D Transition Metal Dichalcogenides. *Nat. Rev. Mater.* **2017**, *2* (8), 17033.

(144) Cai, M.; Thorpe, D.; Adamson, D. H.; Schniepp, H. C. Methods of Graphite Exfoliation. *J. Mater. Chem.* **2012**, *22* (48), 24992.

(145) Yi, M.; Shen, Z. A Review on Mechanical Exfoliation for the Scalable Production of Graphene. *J. Mater. Chem. A* **2015**, *3* (22), 11700–11715.

(146) Lv, R.; Robinson, J. A.; Schaak, R. E.; Sun, D.; Sun, Y.; Mallouk, T. E.; Terrones, M. Transition Metal Dichalcogenides and beyond: Synthesis, Properties, and Applications of Single- and Few-Layer Nanosheets. *Acc. Chem. Res.* **2015**, *48* (1), 56–64.

(147) Jeon, J.; Jang, S. K.; Jeon, S. M.; Yoo, G.; Jang, Y. H.; Park, J.-H.; Lee, S. Layer-Controlled CVD Growth of Large-Area Two-Dimensional MoS 2 Films. *Nanoscale* **2015**, *7* (5), 1688–1695.

(148) Cho, K.; Yang, J.; Lu, Y. Phosphorene: An Emerging 2D Material. *Journal of Materials Research*. 2017, pp 2839–2847.

(149) Hadef, F. An Introduction to Nanomaterials; **2018**; pp 1–58.

(150) Cao, G. *NANOSTRUCTURES AND NANOMATERIALS - Synthesis, Properties and Applications*; Imperial College Press: London, **2004**.

(151) Benjamin, S.; Sharma, S.; Ameta, R. *Microwave-Assisted Organic Synthesis*; Ameta, S. C., Punjabi, P. B., Ameta, R., Ameta, C., Eds.; Apple Academic Press, **2014**.

(152) Novoselov, K. S.; Jiang, D.; Schedin, F.; Booth, T. J.; Khotkevich, V. V.; Morozov, S. V.; Geim, A. K. Two-Dimensional Atomic Crystals. *Proc. Natl. Acad. Sci.* **2005**, *102* (30), 10451–10453.

(153) Liu, B.; Abbas, A.; Zhou, C. Two-Dimensional Semiconductors: From Materials Preparation to Electronic Applications. *Adv. Electron. Mater.* **2017**, *3* (7), 1700045.

(154) Amorim, B.; Cortijo, A.; de Juan, F.; Grushin, A. G.; Guinea, F.; Gutiérrez-Rubio, A.; Ochoa, H.; Parente, V.; Roldán, R.; San-Jose, P.; et al. Novel Effects of Strains in Graphene and Other Two Dimensional Materials. *Phys. Rep.* **2016**, *617*, 1–54.

(155) Liu, J.; Sun, X.; Pan, D.; Wang, X.; Kimerling, L. C.; Koch, T. L.; Michel, J. Tensile-Strained, n-Type Ge as a Gain Medium for Monolithic Laser Integration on Si. *Opt. Express* **2007**, *15* (18), 11272.

(156) Roldán, R.; Castellanos-Gomez, A.; Cappelluti, E.; Guinea, F. Strain Engineering in Semiconducting Two-Dimensional Crystals. *J. Phys. Condens. Matter* **2015**, *27* (31), 313201.

(157) Dhakal, K. P.; Roy, S.; Jang, H.; Chen, X.; Yun, W. S.; Kim, H.; Lee, J.; Kim, J.; Ahn, J. H. Local Strain Induced Band Gap Modulation and Photoluminescence Enhancement of Multilayer Transition Metal Dichalcogenides. *Chem. Mater.* **2017**, *29* (12), 5124–5133.

(158) Chai, Y.; Su, S.; Yan, D.; Ozkan, M.; Lake, R.; Ozkan, C. S. Strain Gated Bilayer Molybdenum Disulfide Field Effect Transistor with Edge Contacts. *Sci. Rep.* **2017**, *7* (1), 41593.

(159) Shen, T.; Penumatcha, A. V.; Appenzeller, J. Strain Engineering for Transition Metal Dichalcogenides Based Field Effect Transistors. *ACS Nano* **2016**, *10* (4), 4712–4718.

(160) Quereda, J.; Palacios, J. J.; Agräit, N.; Castellanos-Gomez, A.; Rubio-Bollinger, G. Strain Engineering of Schottky Barriers in Single- and Few-Layer MoS 2 Vertical Devices. *2D Mater.* **2017**, *4* (2), 021006.

(161) Robinson, B. J.; Giusca, C. E.; Gonzalez, Y. T.; Kay, N. D.; Kazakova, O.; Kolosov, O. V. Structural, Optical and Electrostatic Properties of Single and Few-Layers MoS 2 : Effect of Substrate. *2D Mater.* **2015**, *2* (1), 015005.

(162) Peng, J.; Chung, P. W.; Dubey, M.; Namburu, R. R. Tunable Electron and Phonon Properties of Folded Single-Layer Molybdenum Disulfide. *Nano Res.* **2018**, *11* (3), 1541–1553.

(163) Choi, B. K.; Kim, M.; Jung, K.-H.; Kim, J.; Yu, K.-S.; Chang, Y. J. Temperature Dependence of Band Gap in MoSe2 Grown by Molecular Beam Epitaxy. *Nanoscale Res. Lett.* **2017**, *12* (1), 492.

(164) Thripuranthaka, M.; Kashid, R. V.; Sekhar Rout, C.; Late, D. J. Temperature Dependent Raman Spectroscopy of Chemically Derived Few Layer MoS 2 and WS 2 Nanosheets. *Appl. Phys. Lett.* **2014**, *104* (8), 081911.

(165) Sahoo, S.; Gaur, A. P. S.; Ahmadi, M.; Guinel, M. J.-F.; Katiyar, R. S. Temperature-Dependent Raman Studies and Thermal Conductivity of Few-Layer MoS 2. *J. Phys. Chem. C* **2013**, *117* (17), 9042–9047.

(166) Sinha, S.; Sathe, V.; Arora, S. K. Temperature Dependent Raman Investigations of Few-Layered WS2 Nanosheets. *Solid State Commun.* **2019**, *298*, 113626.

(167) Mobaraki, A.; Sevik, C.; Yapicioglu, H.; Çakır, D.; Gülseren, O. Temperature-Dependent Phonon Spectrum of Transition Metal Dichalcogenides Calculated from the Spectral Energy Density: Lattice Thermal Conductivity as an Application. *Phys. Rev. B* **2019**, *100* (3), 035402.

(168) M, T.; Late, D. J. Temperature Dependent Phonon Shifts in Single-Layer WS 2. *ACS Appl. Mater. Interfaces* **2014**, *6* (2), 1158–1163.

2 OPTICAL HARMONIC GENERATION IN 2D MATERIALS

Recently, optical harmonic generation has been shown as a powerful technique to understand the characteristics of 2D materials. Apart from that, 2D materials offer an exciting platform to tune optical harmonic generation for various nonlinear device applications. Here, the first section of this chapter will discuss different types of characterization modes in 2D materials using optical harmonic generation whereas second section of this chapter will discuss optical harmonic generation tuning in 2D materials.

2.1 Characterization of 2D materials using optical harmonic generation

In order to better understand the features of 2D materials, analytical tools for nano-scale characterization are required. Optical techniques offer a non-invasive, simple and quick way to characterize the layered TMD. Here we show that optical harmonic generation is a simple, easy and quick way to identify various characteristics of 2D layered number such as layer identification[1], lattice symmetry and orientation[2], twisting angles[3], strain direction and intensity[4,5], piezo and ferro-electric response[6,7] which make optical harmonic generation a powerful technique for 2D materials characterization.

2.1.1 Layer Identification, symmetry breaking and preservation

2D layered materials such as TMD, graphene, BP, etc show exciting layer dependent properties which are important for both scientific knowledge and device fabrication.[8,9] Therefore, researchers and device makers need an accurate and quick tool for layer identification for various applications. Optical harmonic generation provides an efficient way of characterization to address these concerns. SHG and even order harmonics generation processes are sensitive to crystal inversion symmetry.[10,11] For instance, even layers of 2H TMDs do not show SHG response due to centrosymmetric nature in contrary to odd layers of TMDs which show significant SHG response as shown in **Figure 2.1a.**[1] In a study, SHG investigation on layer dependent WS_2 and WSe_2 showed a gradual reduction in SHG intensity with an increase in layer number, whereas, the even layer number do not show any SHG response due to inversion symmetric structure.[12] SHG, therefore, can be used to distinguish between even and odd layers of 2H TMDs by exploiting this principle.[2] Moreover, SHG response is found to decrease with an increase in odd layer number for 2H MoS_2 making SHG to predict the odd layer number dependent on intensity variation in 2H phase of MoS_2.

Even though, SHG can predict odd layer number in 2H phase of TMDs, however, SHG cannot identify the change of even layer number.[9] Recently, THG and odd multi-harmonic generation have provided useful results for layer identification for 2H TMDCs.[1,13] For instance, Antti et. al.[1] demonstrated that Third harmonic generation (THG) intensity increases three folds as layer number increases (**Figure 2.1a**) making THG as a useful tool for layer identification. 3R phase of TMDs reveal a broken inversion symmetric structure[14] due to parallel placed layers i.e opposite to the case of 2H TMDs (TMDs layers show anti-parallel stacking between the adjacent layers). Therefore, SHG response is found to follow quadratic layer dependent rise in SHG. i.e $SHG_{nL} = n^2 (SHG_{1L})$ **(Figure 2.1b).**[15]

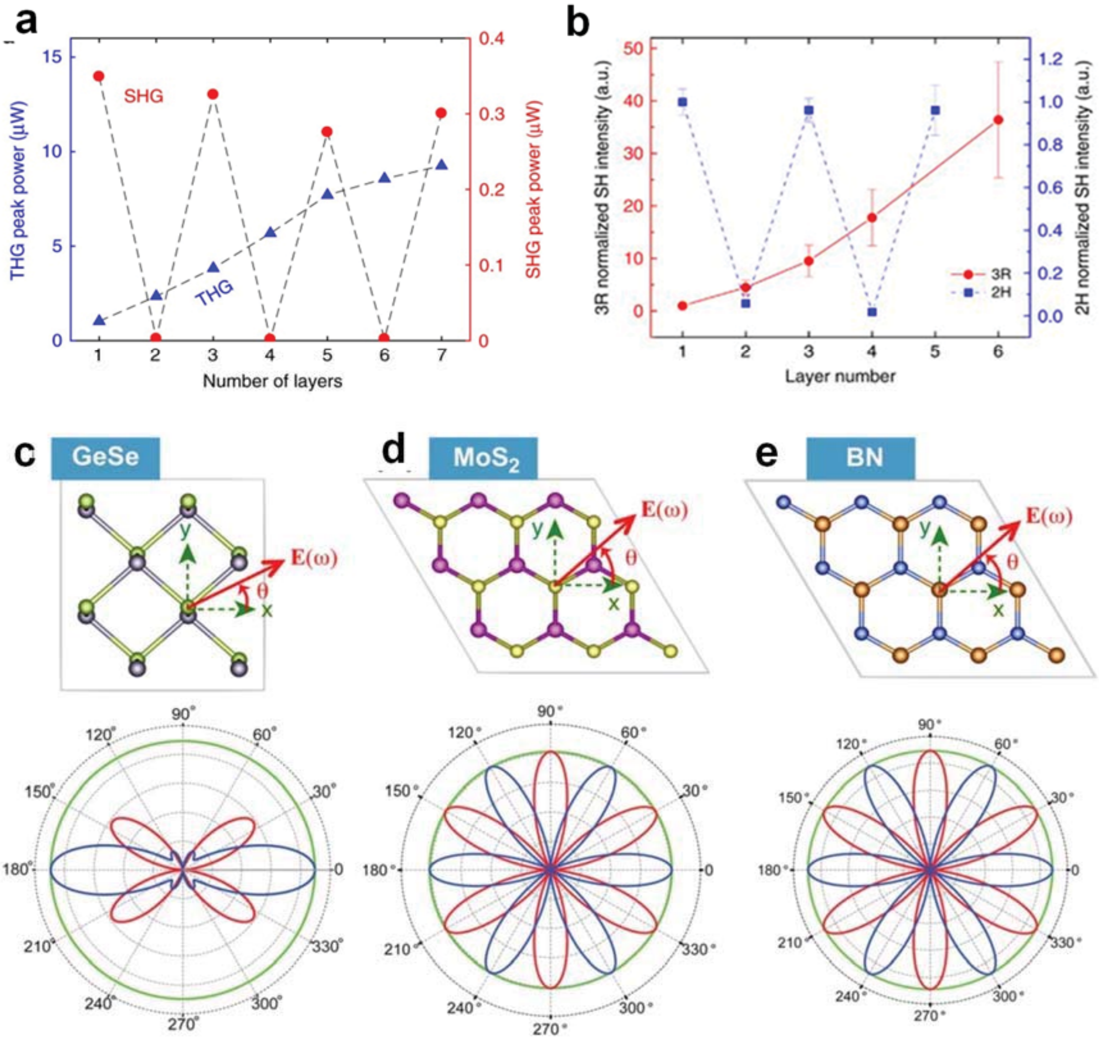

Figure 2.1 | Characterization of layer dependence and crystal orientation of 2D materials using optical harmonic generation

(a) Layer dependent SHG and THG in 2H MoS_2. Reproduced with permission.[1] Copyright 2017, Nature Publishing Group. **(b)** Layer dependent SHG in 2H and 3R phases of MoS_2. Reproduced with permission.[15] Copyright 2016, Nature Publishing Group. **(c)** Polarization dependent SHG susceptibilities in GeSe, (d) MoS_2, and (e) BN. Red (blue) line indicates the polarization component of the SHG response parallel (perpendicular) to the polarization $E(\omega)$ of the incident electric field. θ is the rotation angle between $E(\omega)$ and the crystal lattice (i.e., the *x*-axis here for all three 2D materials). Reproduced with permission.[6] Copyright 2017, ACS Publishing Group.

Apart from TMDs, layer dependent SHG has also been investigated for layered III-VI such as GaSe.[16] ε-GaSe is a non-centrosymmetric structure (space group D^1_{3h}) which is reported to show layer dependent SHG enhancement. Interestingly, the SHG response of nL GaSe above 5L shows a quadratic dependence, whereas thinner flakes show a cubic dependence. This variation between the two SHG behaviours is ascribed to the weak stability of non-centrosymmetric ε-GaSe in thin flakes.[16]

2.1.2 Crystal orientation

Crystal orientation determination is important to optimize the device performance and fundamental research because a variation in lattice orientation can lead to modulation in optoelectronics properties.[3] Conventional optical techniques such as PL or Raman spectroscopy either make this task impossible or difficult to implement. However, polarization-dependent SHG, sensitive to lattice symmetry, is an accurate optical tool to determine the lattice orientation in non-inversion symmetric materials such as 1L TMDs.[14] Polarization dependent SHG is done by using a polarizer between the sample and the detector, parallel or perpendicular to the linearly polarized beam from the pump. The sample is rotated to build a relation between sample rotation and SHG intensity and this orientation dependent SHG is analysed to determine the lattice orientation.[2] For example, Yilei et. al.[2] experimentally determined the MoS_2 lattice orientation direction using polarization dependent SHG. 1L MoS_2 belongs to D_{3h} symmetry group, which gives one independent nonvanishing element of the nonlinear response: $\chi^2_{xxx} = -\chi^2_{xxx} = -\chi^2_{xyy} = -\chi^2_{yyx} = -\chi^2_{yxy}$. Additionally, 6-fold rotational SHG symmetry is reflected from the hexagonal lattice symmetry (D_{3h}) of 1L MoS_2 and hBN.[2] For 1L MoS_2, maximum (minimum) SHG intensity is found along arm chair (zigzag) direction for parallel (perpendicular) polarization which implies the dependence of two polarization SHG components (parallel and perpendicular) on the sample (MoS_2) orientation as under;[2]

$$I_{(parallel)} = I_0\cos^2(3\varphi) \qquad (1)$$

$$I_{(perpendicular)} = I_0\sin^2(3\varphi) \qquad (2)$$

Where I_0 is the maximum SHG intensity and φ is the angle between the polarization of the laser beam and mirror plane in the lattice structure as indicated in **Figure 2.1c-e**. Similar way of polarization dependent SHG is adopted to determine the lattice orientation of odd layers of other 2H TMDs as well.[3,17]

Other D_{3h} symmetry class members such as 3R TMDCs[14], hBN[2], graphene[18], GaSe[19] are found to show a similar six-fold SHG polar plot. InSe is found to show a six-fold SHG polar plot due to its hexagonal structure with symmetry class C_{3v}.[20] Polarization dependent SHG Group IV monochalcogenides (GeSe, GeS, SnSe, SnS) with C_{2v} symmetry class are predicted to show a four-fold SHG plot for perpendicular polar plot (**Figure 2.1e**).[6] The current results indicate SHG as a powerful probe which can be extended to probe the lattice orientation for other 2D materials.

2.1.3 Defects characterization

Defect engineering in 2D materials is a topic of intense research[21] because this technique is frequently used to tune the properties of materials in device making industry. Therefore, defects characterization is important not only to control quality assurance in device fabrication but also it offers a key to understand the material's structure.[22] Optical harmonic generation is highly sensitive to the structural configuration; therefore, OHG is expected to characterize the various types of defects in 2D materials. Researchers have used OHG successfully to probe vacancy defects[22], doping concentration[22], material impurity and doping[23], stacking faults[24,25], grain boundary[26], poly-crystallinity[27], etc. For instance, SHG was successfully employed to check the crystallinity in CVD grown polycrystalline MoS_2.[27] One of the parameter to determine the quality of 2D structure is crystallinity. Single crystal is the purest form of the crystal structure without grain boundary whereas polycrystalline structure develops grain boundaries oriented at different orientations. Because polarization dependent SHG is sensitive to the lattice orientation[2], therefore, it can quickly determine the grain boundaries and polycrystallinity in 2D materials. In this context, SHG was successfully employed to identify the grain and grain boundaries in polycrystalline MoS_2.[27]

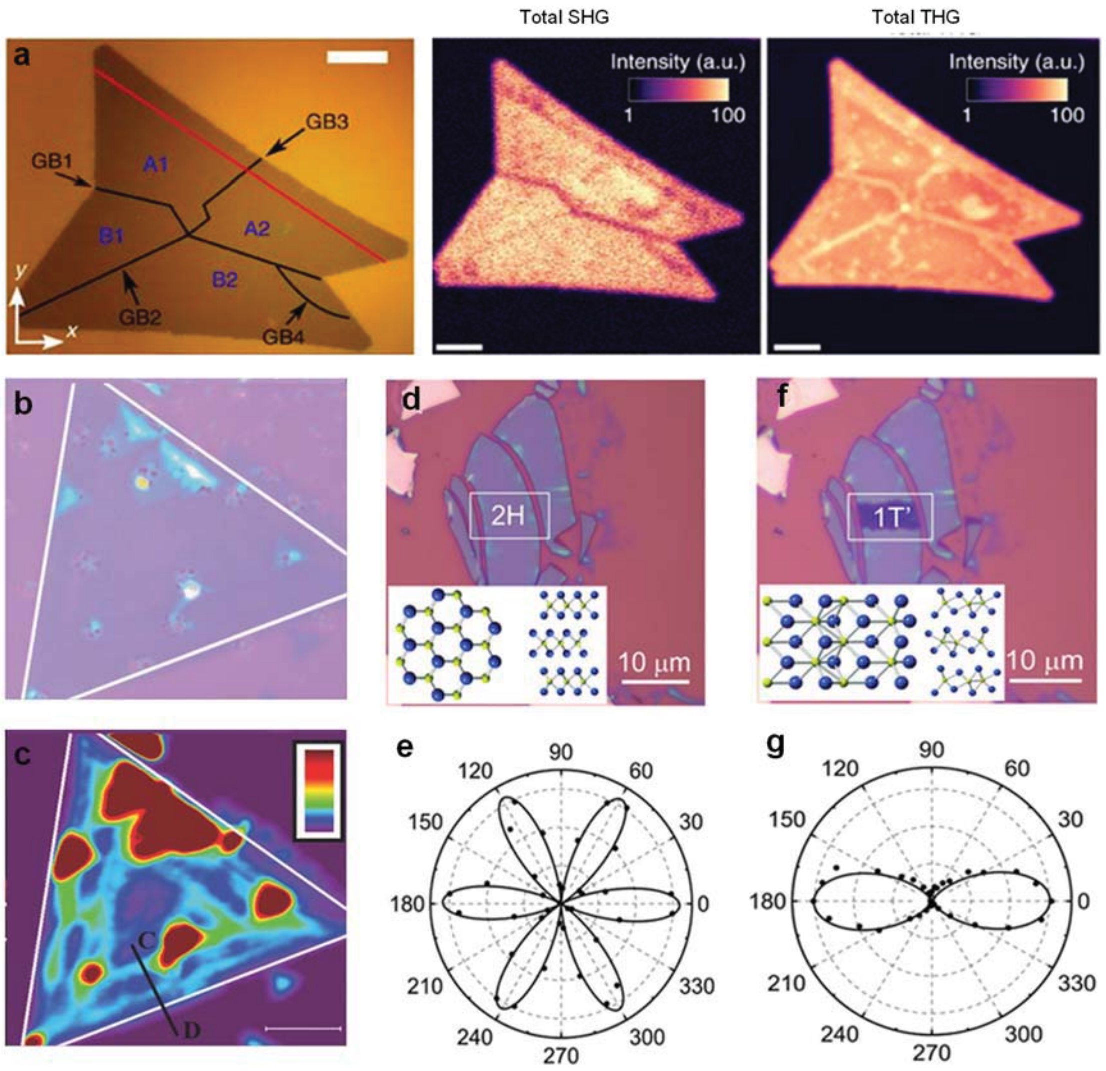

Figure 2.2 | Identification of defects and phase variation using optical harmonic generation. **(a)** Optical image with marked grains (A1, A2, B1 and B2) and grain boundaries (GB1, GB2, GB3 and GB4), experimental total SHG image, experimental total THG image. Reproduced with permission.[26] Copyright 2017, Nature Publishing Group. **(b)** Optical image of 1L WS_2 flake with defects. **(c)** SHG mapping image showing the defect density (scale bar = 10 μm). Reproduced with permission.[22] Copyright 2018, Wiley Library. **(d)** Optical microscope image of a mechanically exfoliated 2H-$MoTe_2$ (Inset shows the lattice structure of 2H- $MoTe_2$) and **(e)** Polarization dependent SHG plot from the few-layer 2H- $MoTe_2$ before laser irradiation **(f)** Optical microscope image of 1T'-$MoTe_2$ after laser irradiation. 2H-$MoTe_2$ phase converts to 1T'-$MoTe_2$ as a result of laser irradiation. (Inset shows the lattice structure of 1T'- $MoTe_2$) and **(g)** Polarization dependent SHG plot from the few-layer 1T'-$MoTe_2$ after laser irradiation. Reproduced with permission.[28] Copyright 2018, Wiley Library.

In another study[26], chemical treatment of polycrystalline MoS_2 resulted into the significant enhancement of SHG and THG on grain boundaries (due to more absorption) making them a sensitive probe for distinguishing grain boundaries as shown in **Figure 2.2a**. THG is found much more sensitive than PL and Raman, moreover, it is found four orders of magnitude faster tool than PL, Raman for sample imaging. These characteristics make optical harmonic generation a powerful tool for high-volume and large-size sample characterization.[26]In another study, SHG is effectively used to monitor sulphur vacancy defects in monolayer WS_2.[22] SHG signal is found to vary according to the density of defects in the material which can be used to distinguish between lower and higher defective regions (**Figure 2.2b-c)**. DFT calculations showed that Sulphur vacancy defects create mid-gap states in the band structure of 1L WS_2 leading to SHG enhancement up to 2 orders of magnitude in defective regions. Because SHG is sensitive to exciton resonances and bandgap modulation, SHG is expected as an effective probe to find the doping concentration as well. In this context, Boron doping on Si/SiO_2 substrate surface is characterized through a decrease in SHG intensity which can be further employed to find the doping concentration[29] and depth[30]. SHG is further used to find the impurity defects and metallic contamination in the materials.[31–33] Apart from that roughness, dislocations are also identified using SHG succefully.[34] Polarization dependent SHG provide a quick and easy way to monitor the artificial stacking, therefore, it is effectively used to find the different types of stacking faults, For instance, Hristuet. al.[24] identified the hexagonal and cubic stacking faults in silicon carbide using polarization dependent SHG. Yuwei et. al. [18] effectively used SHG to differentiate rhombohedral (ABC) stacking faults in trilayer Graphene. Polarization dependent SHG is effectively employed to find the bilayer, trilayer, quadlaer and pentlayer stacking in 2D TMDs.[35] Moreover, Polar SHG technique is shown to successfully suggest the structural variation of layers stacking.[17,35] Optical second harmonic generation imaging represents a viable solution for characterizing structural defects such as stacking faults, dislocations and double positioning boundaries. In this regard, X-ray diffraction and optical second harmonic rotational anisotropy were successfully used to confirm the growth of the cubic polytypic structure and the detailed structure of the defects for cubic silicon carbide layers.[34] These results show OHG a fast and non-invasive investigation method to identify the defects and certify the structures for suitable quality.

2.1.4 Phase variation

Historically, SHG was used to find the phase transition in thick structures.[36] SHG was also used as a tool to identify the temperature dependent phase variation.[37] Recently, SHG has been effectively employed to detect phase variation in 2D materials.[28] For instance, 2H and 1T' are two different phases of $MoTe_2$ showing giant differences in physical properties, symmetry properties and bandgap. Researchers have shown phase transition in $MoTe_2$ using electrostatic doping. 1T' phase is an inversion symmetric phase whereas odd layers of 2H phase show no inversion symmetry.[38–40] SHG signal is found to vanish as a result of doping-induced phase transition into centrosymmetric 1T' phase. On the other hand, giant SHG intensity was observed with phase transition into 2H phase of 1L $MoTe_2$. Moreover, the polarized SHG is an added tool to distinguish phase variations through polar plot variations as shown in **Figure 2.2d-g**. In contrary to the six-fold pattern observed for 2H phase (D_{3h} symmetry), two-fold pattern was found in 1T' with C_s^1 symmetry group.[28]

Similarly, SHG was effectively employed to identify 2H and 3R phases in MoS_2.[86] Monolayers of both 2H and 3R phases of MoS_2 contain alternating M and S atoms in hexagonal arrays. However, each layer in 2H phase is anti-parallel to the adjacent layer whereas adjacent layers are parallel to each other in 3R phase.[2,14] Therefore, even layers of 2H phase being symmetric do not show SHG signal whereas each layer of 3R phase show SHG either odd or even with $SHG_{nL} = n^2 * SHG_{1L}$, where n =number of layers.[15] Apart from TMDs, Tuwei et. al.[18] used SHG effectively to differentiate ABA stacked trilayer Graphene from ABC stacked Graphene. In another study, SHG is used to find the temperature dependent phase variation in $YBa_2Cu_3O_y$.[41] SHG, as an effective tool, may be applied to identify phase transitions for other 2D materials.

2.1.5 Piezoelectric and ferroelectric detection

Lack of inversion symmetry in the materials causes uneven charge distribution leading to interesting properties such as piezoelectricity, paraelectricity and ferroelectricity. 2D piezoelectric and ferroelectric materials are the focus of much research efforts due to their potential applications in energy harvesting, electromechanical and electronic devices.[7,42–44] SHG, a frequency-doubling process, can only occur in materials that lack inversion symmetry, making SHG a sensitive tool for the characterization of piezoelectric and ferroelectric materials.[44] Because even harmonics process show sensitivity to inversion symmetry, they are expected to detect piezoelectricity and ferroelectricity in 2D materials.[45] Specifically, SHG has been widely used for the investigation of piezoelectricity[7] and ferroelectricity[6,46] in 2D materials. Even though, there are other setups available for piezoelectricity and ferroelectricity detection, however, optical SHG is an easy, non-destructive and quick alternative for 2D materials. Various researchers have been reported on SHG investigation for piezoelectric and ferroelectric materials. For instance, piezoelectricity in layer dependent MoS2 is investigated through SHG by Wenzhou et. al.[7] and it is showed that odd layers of TMDs show piezoelectricity due to loss of inversion symmetry whereas even layers, symmetric structures, do not show piezoelectricity. In another study, multiferroicity is evaluated in GeSe (group IV monochalcogenide), 1L MoS_2 and hBN using SHG susceptibility. The strength of SHG susceptibility in GeSe monolayer is calculated to be 1 order of magnitude higher than that in monolayer MoS_2, and 2 orders of magnitude higher than that in monolayer hexagonal BN.[6] Apart from in-plane piezoelectricity, angle-dependent polarized SHG technique can be used to characterize stable out-of-plane 2D ferroelectrics such as In_2Se_3.[47,48] Sample was first rotated to the SHG extinction point, where the In-Se bond direction is normal to both the incident and detecting direction (i.e parallel polarization). Excitation beam is tilted to investigate the out-of-plane response. Beam tilted angle dependent SHG intensity ratio between I_p (p-polarized, out of plane) and I_s (s-polarized, in-plane) is found to increase symmetrically with tilted incidence angle and agreed well with the model of response from out-of-plane dipole to vertical electrical oscillation field **(Figure 2.3a)**. As the tilt angle increases, SHG intensity varies. With this method, out-of-plane polarization in ferroelectric materials was initially checked in In_2Se_3.[47] SHG scanning can be used to reveal the ferroelectric domain structure of the sample, provided that the domain sizes are larger than the effective resolution of the image scan. In this regard, visualization of domain structure in 2D In_2Se_3 was done by SHG and piezo response mapping **(Figure 2.3b-c)**.[47,49] SHG mapping of In_2Se_3 flake shows intensity contrast in different regions corresponding to domains with different dipole strength that matched well with the piezo response mapping. [47] Moreover, SHG mapping is used to examine the electrical poling behaviour in ferroelectric In_2Se_3. **(Figure 2.3d-e)**.[47] The SHG intensity and the corresponding ferroelectric ordering remains robust as a four layer In_2Se_3 sample on SiO_2=Si substrate was heated from room temperature to 600 K. It then dropped sharply to about one-sixth of the initial value when the temperature further increased to 700 K, indicating the disappearance of spontaneous polarization and the structural transition to a centrosymmetric phase **(Figure 2.3f)**. The theoretical limit of the lateral image resolution using this technique corresponds to roughly half the wavelength of the incident light.[50] Moreover, SHG is also used to determine the Curie temperature of 2D ferroelectric $CuInP_2S_6$ flakes.[46] Apart from that, SHG was also used to investigate the temperature dependent ferroelectric to centrosymmetric phase transition for In_2Se_3.[47]

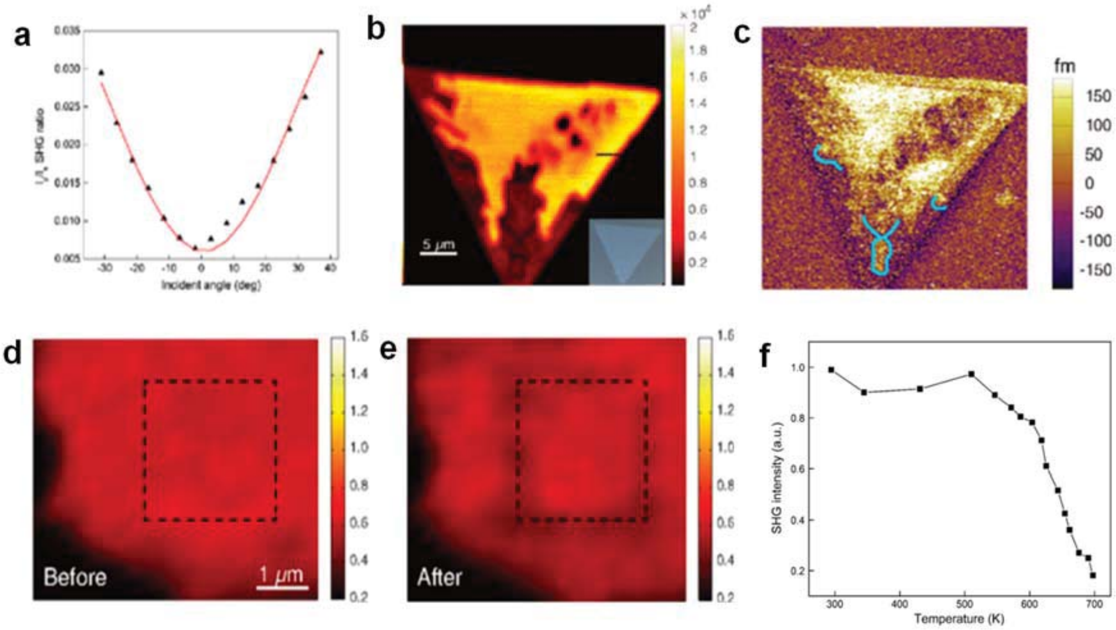

Figure 2.3 | Investigation of piezoelectricity and ferroelectricity in 2D Layered materials using SHG **(a)** Out-of-plane dipole probed by angle resolved polarization selective SHG where beam tilted angle dependent SHG intensity ratio between I_p (p-polarized) and I_s (s-polarized) increases symmetrically with tilted incidence (black triangular) and agrees well with the model of response from out-of-plane dipole to vertical electrical oscillation field, indicating the ratio (13.6:1) between in-plane and out of plane second-order susceptibility at 1080 nm pump (red curve). **(b)** Visualization of domain structure in 2D In_2Se_3 by SHG and **(c)** piezo response mapping, SHG mapping of In_2Se_3 flake shows intensity contrast in different regions corresponding to domains with different dipole strength that match well with the piezo response mapping in (h). The inset is the optical image of the same sample. **(d)** SHG mapping before and **(e)** after the electrical reversed poling. The mapping show dark lines at the boundary of the patterned area resulting from destructive interference, which indicates the reversal of in-plane crystal orientation and corresponding nonlinear optical polarization after reversed electrical poling. **(f)** Observation of temperature-dependent ferroelectric to centrosymmetric phase transition. The SHG intensity and the corresponding ferroelectric ordering remains robust as a four-layer In_2Se_3 sample on SiO_2=Si substrate was heated from room temperature to 600 K. It then dropped sharply to about one-sixth of the initial value when the temperature further increased to 700 K, indicating the disappearance of spontaneous polarization and the structural transition to a centrosymmetric phase. Reproduced with permission.[47] Copyright 2018, APS Physics.

2.2 Tuning of optical harmonic generation in 2D layered materials

Tailoring of optical harmonic generation is important for optimized device performance. However, the nonlinear susceptibilities that give rise to such phenomena are often challenging to tune in each material and, so far, dynamical control of optical nonlinearities remain confined to research laboratories as a spectroscopic tool. Researchers have reported various ways to tune nonlinear interaction in 2D materials which are stated in the following text.

Table 2.1 Typical techniques for SHG tuning

SHG tuning techniques	Material	Optical Harmonic generation	Thickness	Fabrication	Substrate	OHG Tuning values	Laser excitation
Exciton tuning	MoS_2 [51]	SHG	1L	Exfoliation	quartz	8.2 times (C-Exciton)	890 nm
	MoS_2 [51]	SHG	3L	Exfoliation	quartz	6.5 times (C-Exciton)	854 nm
	MoS_2[52]	SHG	1L	Exfoliation	SiO_2	10 times (C-Exciton)	900 nm
	WS_2 [53]	SHG	5L	Exfoliation	SiO_2	5 times (C-Exciton)	900 nm
	$MoSe_2$ [54]	SHG	1L	Exfoliation	SiO_2	5 times (A-Exciton)	1600nm
	$MoSe_2$ [54]	SHG	1L	Exfoliation	SiO_2	1.3 times (B-Exciton)	1400 nm
	MoS_2 [54]	SHG	1L	Exfoliation	SiO_2	4.3 times (A-Exciton)	690 nm
	MoS_2 [54]	SHG	1L	Exfoliation	SiO_2	4.3 times (B-Exciton)	610 nm
	WSe_2[55]	SHG	1L	Exfoliation	SiO_2	4.2 times (A-Exciton)	1410 nm
Gate tuning	WSe_2[55]	SHG	1L	Exfoliation	SiO_2	3.75 times (10%/V), -80 V to 80 V	1490 nm 980 nm
	MoS_2[52]	SHG	2L	Exfoliation	SiO_2	60 times (-20V to 120V)	2100 nm
	Graphene[56]	THG	1L	Exfoliation	SiO_2	30 times (0 to -0.6 eV E_F [2])	1018 nm
	CdS[57]	SHG	ML [1]	PVD	SiO_2	0 to 151 pmV^{-1} (200% V^{-1})	810 nm
	MoS_2[58]	SHG	2L	Exfoliation	SiO_2	25 times (12V to -15V)	1305 nm
	Graphene[59]	SHG	1L	-	-	0 to 30 pmV^{-1} (0 to 1.5 eV chemical potential)	
Stacking symmetry	MoS_2[3]	SHG	Stacked 2L	Stacking of CVD layers	SiO_2	0 to 4 times ((0^o to 60^o stacking angle)	810 nm
	MoS_2[35]	SHG	4L	Stacking of CVD layers	SiO_2	~1 to 16 times (ABAB to AAAA stacking)	1040nm
	MoS_2[35]	SHG	5L	Stacking of CVD layers	SiO_2	~1 to 25 times (ABABA to AAAAA stacking)	1040 nm
	Graphene[18]	SHG	3L	Exfoliation	SiO_2	0 to 90 pmV^{-1} (ABC to ABA stacking)	1300 nm
Valley tuning	MoS_2[60]	SHG	QD [4]	-	-	(0 to ~10^7 pm/V)	1033 nm

[1] Multilayer
[2] E_F is fermi energy
[3] Molecular Beam Epitaxy
[4] Quantum dots

2.2.1 Exciton effect

1L-TMDs have strongly bound excitons that modify their linear optical properties.[61–64] The exciton resonances are also expected to affect their nonlinear optical responses which is demonstrated by various researches.[65,66] For example, in 1L MoS_2, significant enhancement in SHG and THG is found when in resonance with A-exciton[67] and the similar trend is noted for SHG investigation with WS_2.[68] This giant enhancement makes 2D materials the potential applicant for future nonlinear devices. Pairing of electrons and holes is enhanced due to the strong Coulomb interaction, reduced dielectric screening and strong quantum confinement in 2D limit materials leading to strongly bound excitons. Excitons in 2D TMDs are found to exist at room temperature due to strong binding energy up to hundreds of meV.[69] The strong exciton effects in 2D materials due to large density of states increase the efficiency of generating optical harmonic generation. For instance, an enhancement by up to 3 orders of magnitude of the SHG efficiency was recorded in monolayer WSe_2 when the incoming electromagnetic wave is in resonance with the energy of 1s A-exciton.[70]

Similarly, 1L and 3L MoS_2 show considerable SHG enhancement in resonances with A, B and C excitons as shown in **Figure 2.4a**.[51] SHG peaks for the A and B features originate from the direct optical transitions at the K-K' and SHG peaks for the C feature originate from Γ-point of the Brillouin zone. A significant enhancement of $\chi^{(2)}$ sheet MoS2 is observed with spectral positions very well matched with the C peak in the linear absorption spectra (~2.8 eV for monolayers and ~2.7 eV for tri-layers). It suggests that the resonance enhancement of SHG is originated from the increased density of electronic states at Γ-point allowing increased optical transitions.[51] The different resonant position between the monolayers and the tri-layers is thus a consequence of the different energy gaps at the Γ point of the Brillouin zone, a modification of the electronic structure from quantum confinement in reduced sample thickness. While the SHG from trilayer $\chi^{(2)}$ sheet MoS_2 is consistently smaller than that of the monolayer for photon energies above the C resonance, it becomes slightly larger than that of the monolayer at lower photon energies.[51] Because large density of states at the exciton resonances increases electron-hole interaction to multiply second harmonic generation, investigation for many body effects on nonlinear optical behaviour needs further investigation.

Valley polarization is an important way to tune one photon PL emission in TMDs which is controlled by valley selection rules for one-photon case for K(−K) valley of Brillouin zone. Similarly, valley polarization obeys selection rules for two photon case of SHG emission. Xiao et. al.[68] demonstrated nonlinear optical selection rules for SHG based on valley exciton locking while studying optical transitions for monolayer WS_2. It is demonstrated that optical transitions under σ^+ pumping at 1s state generate SHG photons of reverse σ^- spin state and vice verca. In a study on 1L MoS_2, Seyler et. al.[71] showed σ^+(σ^-) excitation photons are absorbed to emit σ^-(σ^+) SHG photons as shown in **Figure 2.4b-c**. Xiao et. al. further demonstrated that SHG and TPA (two photon absorption) selection rules are different, such as, SHG is in resonance with the *s* states whereas TPA to *s* states is parity forbidden in 1L WS_2, in its place, TPA shows transitions to 2*p* states in 1L WS_2.[68] In another study, spin-valley dependent excitonic tuning is used to tune SHG (0 to ~10^7 pmV^{-1}).[60] The second harmonic generation valley selection rules has potential implications for optical switches.

2.2.2 Doping effect and gate tuning

Gate voltage is found to tune linear optical properties due to modulation in fermi level.[72–75] For instance, PL intensity of 2D TMDCs is tuned using gate voltage.[21] This electro-optic modulation has potential applications in photonic devices such as optical switching and communications.[55] Similarly, gate tuning is expected to alter nonlinear optical properties of 2D materials for potential applications in nonlinear devices.

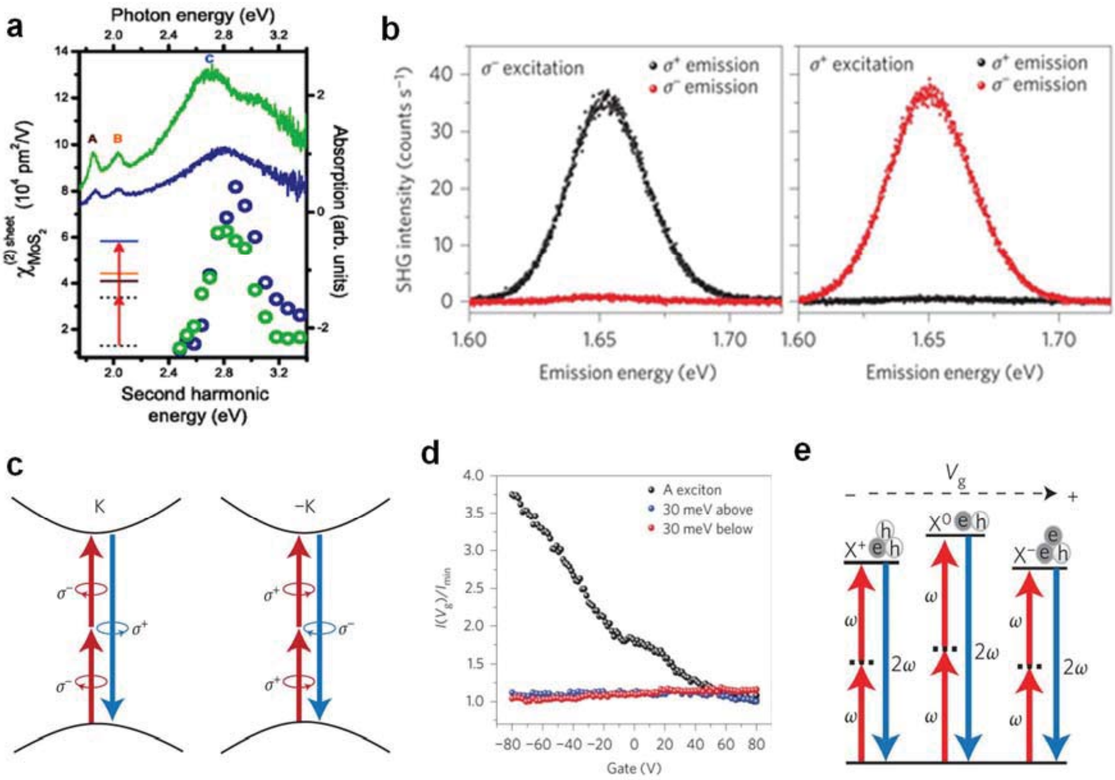

Figure 2.4 | SHG modulation via exciton resonances and gate tuning

(a) Second-order susceptibility, left scale, of a sheet of MoS_2 for monolayer (blue circles) and trilayer (green circles) samples as a function of pump-laser energy, with measured linear absorption (right scale) spectra of monolayer (blue line) and trilayer (green line) with the labelled optical transitions. Inset: Diagram of the second-harmonic enhancement in monolayer MoS_2 where the two-photon energy is in resonance with the C absorption peak. Reproduced with permission.[51] Copyright 2013, APS Physics. (**b**) Circular polarization-resolved SHG response showing the generation of counter-circular SHG. **(c)** Interband valley optical selection rules for SHG. **(d)** Normalized peak intensity of SHG as a function of gate voltage with two-photon excitation energy above, below and resonant with the A exciton. **(e)** Illustration of gate-dependent exciton- and trion-enhanced SHG. Reproduced with permission.[71] Copyright 2015, Nature Publishing Group Valley-selective tuning

In this context, Seyleret. al.[55] observed second-harmonic generation tuneability by over an order of magnitude at low temperature and nearly a factor of four at room temperature through electrostatic doping in 1L WSe_2 based field-effect transistor. Firstly, a significant tuning in SHG spectra is found when SHG is in resonance with the A exciton (~1.76eV) as shown in **Figure 2.4d**.[55] Secondly, gate voltage modulation shows significant SHG tuning at A exciton. SHG response increases (a factor of four) over 100V of shift in gate voltage. This gate dependent SHG tuning is attributed to be arisen from strong exciton charging effects in monolayer semiconductors as shown in **Figure 2.4e**.[55]

Gate voltage is also used to break the inversion symmetry in 2L WSe_2 leading to an enhancement in SHG (532nm wavelength). SHG from 2L WSe_2 is reported to be off-resonant (hence free from PL background). This unusual process takes place only when the gate polarity causes charge accumulation rather than depletion. This enhanced SHG due to asymmetry behaviour is attributed to the presence of mobile charges on the d-shells of W, a unique characteristic of only TMD materials.[76] In another study on bilayer MoS_2[52], gate voltage is used to break the inversion symmetry of bilayer MoS_2 leading to 60 times enhancement in SHG by applying a strong electric field (= +2.6 $MVcm^{-1}$) for SHG emission at $E_{2\omega} = 2.49$ eV. This strong tuning arises from the tuneable interlayer coupling due to the strong electric field applied perpendicular to the basal plane of the crystal which is free from the effect of exciton effect.[52] Apart from 2D TMDCs, symmetry breaking is also observed in centrosymmetric 1L Graphene via doping. SHG is widely tuned by carrier doping or chemical potential, being sharply enhanced at Fermi-edge resonances with its highest strength comparable to the electric dipole-allowed SHG in non-centrosymmetric 2D materials but vanishing at the charge neutral point that manifests the electron-hole symmetry of massless Dirac fermions.[59] Electro-optic modulation in Graphene is also manifested for third-harmonic generation. THG efficiency in graphene is increased by almost one order of magnitude by controlling the Fermi energy over a broad range of wavelength. Gate tuned third-harmonic enhancement is achieved over an ultra-broad bandwidth, suitable for optical communications and signal processing.[71] Although gate tuning of SHG is well known, however, role of charging effects of excitons still need investigations which can potentially be utilized in various applications such as gate tuneable switches and frequency converters.[56,59]

2.2.3 Stacking symmetry

Loss of crystal inversion symmetry results in exciting properties such as piezoelectricity, ferroelectricity, dichroism, improved career mobility, optoelectronic properties and giant SHG response.[7,77,78] A variation in crystal inversion symmetry is achieved using stacking angle modulation in 2D layered materials. Stacking angle modulation in folds, homo-structures and hetero-structures can lead to extraordinary SHG tuning.[3,53]

In a study on stacked MoS_2 layers[35], the 2L, 3L, 4L and 5L with AA, AAA, AAAA and AAAAA stacking order respectively is found to obey; $I^{SH}{}_n = I_o n^2$; where n = number of layers, Io = SHG intensity of a single layer and ; $I^{SH}{}_n$ = cumulative SHG from n layers with 0 degree stacking angle. Moreover, 3R structures with 0^o degree stacking angle variation between adjacent layers is also found to obey[15]; $I^{SH}{}_n = I_o n^2$. Hsu et. al.[3] investigated twisted bilayers for homo and hetero-structures for variable angles (2^o, 16^o, 30^o, 37^o and 54^o) and found superposition principle to be valid for SH wave vectors.

2.3 Chapter summary

Low dimensional materials, as an excellent platform to observe and tune optical harmonic generation, have many potential applications in nonlinear optical devices, sensing and imaging, characterization, etc. Nano manufacturing using structural engineering techniques such as folding, straining, thermal modulation, etc are shown to significantly tune the optical properties of the materials. Using these nano manufacturing techniques, nonlinear optical behaviour in 2D materials will be explored in next chapters with potential applications in optoelectronic and nonlinear photonic devices.

Chapter 2 References

[1] A. Säynätjoki, L. Karvonen, H. Rostami, A. Autere, S. Mehravar, A. Lombardo, R. A. Norwood, T. Hasan, N. Peyghambarian, H. Lipsanen, K. Kieu, A. C. Ferrari, M. Polini, Z. Sun, *Nat. Commun.* **2017**, *8*, 2005.

[2] Y. Li, Y. Rao, K. F. Mak, Y. You, S. Wang, C. R. Dean, T. F. Heinz, *Nano Lett.* **2013**, *13*, 3329.

[3] W.-T. Hsu, Z.-A. Zhao, L.-J. Li, C.-H. Chen, M.-H. Chiu, P.-S. Chang, Y.-C. Chou, W.-H. Chang, *ACS Nano* **2014**, *8*, 2951.

[4] L. Mennel, M. M. Furchi, S. Wachter, M. Paur, D. K. Polyushkin, T. Mueller, *Nat. Commun.* **2018**, *9*, 516.

[5] J. Liang, J. Zhang, Z. Li, H. Hong, J. Wang, Z. Zhang, X. Zhou, R. Qiao, J. Xu, P. Gao, Z. Z. Z. Z. Z. Liu, Z. Z. Z. Z. Z. Liu, Z. Sun, S. Meng, K. Liu, D. Yu, *Nano Lett.* **2017**, *17*, 7539.

[6] H. Wang, X. Qian, *Nano Lett.* **2017**, *17*, 5027.

[7] W. Wu, L. Wang, Y. Li, F. Zhang, L. Lin, S. Niu, D. Chenet, X. Zhang, Y. Hao, T. F. Heinz, J. Hone, Z. L. Wang, *Nature* **2014**, *514*, 470.

[8] S. Raj Panday, B. M. Fregoso, *J. Phys. Condens. Matter* **2017**, *29*, 43LT01.

[9] Y. Z. You Zheng, C. L. Changyong Lan, Z. Z. Zhifei Zhou, X. H. Xiaoying Hu, T. H. Tianying He, C. L. Chun Li, *Chinese Opt. Lett.* **2018**, *16*, 020006.

[10] D. C. Hanna, *Opt. Laser Technol.* **1985**, *17*, 104.

[11] Y. Wang, J. Xiao, S. Yang, Y. Wang, X. Zhang, *Opt. Mater. Express* **2019**, *9*, 1136.

[12] H. Zeng, G.-B. Liu, J. Dai, Y. Yan, B. Zhu, R. He, L. Xie, S. Xu, X. Chen, W. Yao, X. Cui, *Sci. Rep.* **2013**, *3*, 1608.

[13] Y. S. You, G. Ndabashimiye, H. Liu, Y. Li, T. F. Heinz, D. A. Reis, S. Ghimire, *Opt. InfoBase Conf. Pap.* **2017**, *Part F82-C*, 1.

[14] J. Shi, P. Yu, F. Liu, P. He, R. Wang, L. Qin, J. Zhou, X. Li, J. Zhou, X. Sui, S. Zhang, Y. Zhang, Q. Zhang, T. C. Sum, X. Qiu, Z. Liu, X. Liu, *Adv. Mater.* **2017**, *29*, 1701486.

[15] M. Zhao, Z. Ye, R. Suzuki, Y. Ye, H. Zhu, J. Xiao, Y. Wang, Y. Iwasa, X. Zhang, *Light Sci. Appl.* **2016**, *5*, e16131.

[16] W. Jie, X. Chen, D. Li, L. Xie, Y. Y. Hui, S. P. Lau, X. Cui, J. Hao, *Angew. Chemie Int. Ed.* **2015**, *54*, 1185.

[17] T. Jiang, H. Liu, D. Huang, S. Zhang, Y. Li, X. Gong, Y.-R. Shen, W.-T. Liu, S. Wu, *Nat. Nanotechnol.* **2014**, *9*, 825.

[18] Y. Shan, Y. Li, D. Huang, Q. Tong, W. Yao, W.-T. Liu, S. Wu, *Sci. Adv.* **2018**, *4*, eaat0074.

[19] X. Zhou, J. Cheng, Y. Zhou, T. Cao, H. Hong, Z. Liao, S. Wu, H. Peng, K. Liu, D. Yu, *J. Am. Chem. Soc.* **2015**, *137*, 7994.

[20] S. Deckoff-Jones, J. Zhang, C. E. Petoukhoff, M. K. L. Man, S. Lei, R. Vajtai, P. M. Ajayan, D. Talbayev, J. Madéo, K. M. Dani, *Sci. Rep.* **2016**, *6*, 22620.

[21] J. Pei, J. Yang, R. Xu, Y.-H. Zeng, Y. W. Myint, S. Zhang, J.-C. Zheng, Q. Qin, X. Wang, W. Jiang, Y. Lu, *Small* **2015**, *11*, 6384.

[22] H. G. Rosa, L. Junpeng, L. C. V. Gomes, M. J. L. F. Rodrigues, S. C. Haur, J. C. V. Gomes, *Adv. Opt. Mater.* **2018**, *6*, 1701327.

[23] C. T. Le, D. J. Clark, F. Ullah, J. I. Jang, V. Senthilkumar, Y. Sim, M.-J. Seong, K.-H. Chung, J. W. Kim, S. Park, S. H. Rhim, G. Kim, Y. S. Kim, *ACS Photonics* **2017**, *4*, 38.

[24] R. Hristu, S. G. Stanciu, D. E. Tranca, E. K. Polychroniadis, G. A. Stanciu, *Sci. Rep.* **2017**, *7*, 4870.

[25] C.-J. Kim, L. Brown, M. W. Graham, R. Hovden, R. W. Havener, P. L. McEuen, D. A. Muller, J. Park, *Nano Lett.* **2013**, *13*, 5660.

[26] L. Karvonen, A. Säynätjoki, M. J. Huttunen, A. Autere, B. Amirsolaimani, S. Li, R. A. Norwood, N. Peyghambarian, H. Lipsanen, G. Eda, K. Kieu, Z. Sun, *Nat. Commun.* **2017**, *8*, 15714.

[27] X. Yin, Z. Ye, D. A. Chenet, Y. Ye, K. O'Brien, J. C. Hone, X. Zhang, *Science (80-.).* **2014**, *344*, 488.

[28] Y. Song, R. Tian, J. Yang, R. Yin, J. Zhao, X. Gan, *Adv. Opt. Mater.* **2018**, *6*, 1.

[29] H. Park, J. Qi, Y. Xu, K. Varga, S. M. Weiss, B. R. Rogers, G. Lüpke, N. Tolk, *Phys. Status Solidi Basic Res.* **2010**, *247*, 1997.

[30] A. Bonda, S. Uba, L. Uba, *Appl. Phys. Lett.* **2014**, *105*, 191608.

[31] Bongim Jun, R. D. Schrimpf, D. M. Fleetwood, Y. V. White, R. Pasternak, S. N. Rashkeev, F. Brunier, N. Bresson, M. Fouillat, S. Cristoloveanu, N. H. Tolk, *IEEE Trans. Nucl. Sci.* **2004**, *51*, 3231.

[32] M. L. Alles, R. Pasternak, X. Lu, N. H. Tolk, R. D. Schrimpf, D. M. Fleetwood, R. P. Dolan, R. W. Standley, *IEEE Trans. Semicond. Manuf.* **2007**, *20*, 107.

[33] I. V. Kityk, B. Marciniak, A. Mefleh, *J. Phys. D. Appl. Phys.* **2001**, *34*, 1.

[34] R. Hristu, S. G. Stanciu, D. E. Tranca, A. Matei, G. A. Stanciu, *Sci. Rep.* **2015**, *4*, 5258.

[35] S. M. Shinde, K. P. Dhakal, X. Chen, W. S. Yun, J. Lee, H. Kim, J.-H. Ahn, *NPG Asia Mater.* **2018**, *10*, e468.

[36] L. L. Kulyuk, I. V. Kravetsky, *Jpn. J. Appl. Phys.* **1993**, *32*, 749.

[37] M. N. Ahamad, A. Vasudevarao, V. Gopalan, H. Jain, K. B. R. Varma, *J. Non. Cryst. Solids* **2009**, *355*, 1517.

[38] O. Rubel, *Phys. Rev. B* **2018**, *97*, 224101.

[39] A. Krishnamoorthy, L. Bassman, R. K. Kalia, A. Nakano, F. Shimojo, P. Vashishta, *Nanoscale* **2018**, *10*, 2742.

[40] Y. Li, K.-A. N. Duerloo, K. Wauson, E. J. Reed, *Nat. Commun.* **2016**, *7*, 10671.

[41] L. Zhao, C. A. Belvin, R. Liang, D. A. Bonn, W. N. Hardy, N. P. Armitage, D. Hsieh, *Nat. Phys.* **2017**, *13*, 250.

[42] T. Y. Kim, S. K. S. W. Kim, S. K. S. W. Kim, *Nano Converg.* **2018**, *5*, 1.

[43] J. Briscoe, S. Dunn, *Nano Energy* **2014**, *14*, 15.

[44] C. Cui, F. Xue, W.-J. Hu, L.-J. Li, *npj 2D Mater. Appl.* **2018**, *2*, 18.

[45] H. Liu, Y. Li, Y. S. You, S. Ghimire, T. F. Heinz, D. A. Reis, *Nat. Phys.* **2017**, *13*, 262.

[46] F. Liu, L. You, K. L. Seyler, X. Li, P. Yu, J. Lin, X. Wang, J. Zhou, H. Wang, H. He, S. T. Pantelides, W. Zhou, P. Sharma, X. Xu, P. M. Ajayan, J. Wang, Z. Liu, *Nat. Commun.* **2016**, *7*, 12357.

[47] J. Xiao, H. Zhu, Y. Wang, W. Feng, Y. Hu, A. Dasgupta, Y. Han, Y. Wang, D. A. Muller, L. W. Martin, P. Hu, X. Zhang, *Phys. Rev. Lett.* **2018**, *120*, 227601.

[48] Y. Zhou, D. Wu, Y. Zhu, Y. Cho, Q. He, X. Yang, K. Herrera, Z. Chu, Y. Han, M. C. Downer, H. Peng, K. Lai, *Nano Lett.* **2017**, *17*, 5508.

[49] J. Nordlander, G. De Luca, N. Strkalj, M. Fiebig, M. Trassin, *Appl. Sci.* **2018**, *8*, 570.

[50] S. A. Denev, T. T. A. Lummen, E. Barnes, A. Kumar, V. Gopalan, *J. Am. Ceram. Soc.* **2011**, *94*, 2699.

[51] L. M. Malard, T. V. Alencar, A. P. M. Barboza, K. F. Mak, A. M. de Paula, *Phys. Rev. B* **2013**, *87*, 201401.

[52] J. Klein, J. Wierzbowski, A. Steinhoff, M. Florian, M. Rösner, F. Heimbach, K. Müller, F. Jahnke, T. O. Wehling, J. J. Finley, M. Kaniber, *Nano Lett.* **2017**, *17*, 392.

[53] A. R. Khan, B. Liu, W. Ma, L. Zhang, A. Sharma, Y. Zhu, T. Lü, Y. Lu, **2020**.

[54] C. T. Le, D. J. Clark, F. Ullah, V. Senthilkumar, J. I. Jang, Y. Sim, M. J. Seong, K. H. Chung, H. Park, Y. S. Kim, *Ann. Phys.* **2016**, *528*, 551.

[55] K. L. Seyler, J. R. Schaibley, P. Gong, P. Rivera, A. M. Jones, S. Wu, J. Yan, D. G. Mandrus, W. Yao, X. Xu, *Nat. Nanotechnol.* **2015**, *10*, 407.

[56] G. Soavi, G. Wang, H. Rostami, D. G. Purdie, D. De Fazio, T. Ma, B. Luo, J. Wang, A. K. Ott, D. Yoon, S. A. Bourelle, J. E. Muench, I. Goykhman, S. Dal Conte, M. Celebrano, A. Tomadin, M. Polini, G. Cerullo, A. C. Ferrari, *Nat. Nanotechnol.* **2018**, *13*, 583.

[57] M.-L. Ren, J. S. Berger, W. Liu, G. Liu, R. Agarwal, *Nat. Commun.* **2018**, *9*, 186.

[58] J. Lee, K. F. Mak, J. Shan, *Nat. Nanotechnol.* **2016**, *11*, 421.

[59] Y. Zhang, D. Huang, Y. Shan, T. Jiang, Z. Zhang, K. Liu, L. Shi, J. Cheng, J. E. Sipe, W.-T. Liu, S. Wu, *Phys. Rev. Lett.* **2019**, *122*, 047401.

[60] J. Fouladi-Oskouei, S. Shojaei, *Mater. Res. Express* **2019**, *6*, 126204.

[61] K. F. Mak, K. He, C. Lee, G. H. Lee, J. Hone, T. F. Heinz, J. Shan, *Nat. Mater.* **2013**, *12*, 207.

[62] K. He, N. Kumar, L. Zhao, Z. Wang, K. F. Mak, H. Zhao, J. Shan, *Phys. Rev. Lett.* **2014**, *113*, 026803.

[63] T. Cheiwchanchamnangij, W. R. L. Lambrecht, *Phys. Rev. B* **2012**, *85*, 205302.

[64] A. Ramasubramaniam, *Phys. Rev. B* **2012**, *86*, 115409.

[65] G. Wang, X. Marie, I. Gerber, T. Amand, D. Lagarde, L. Bouet, M. Vidal, A. Balocchi, B. Urbaszek, *Phys. Rev. Lett.* **2015**, *114*, 097403.

[66] M. Grüning, C. Attaccalite, *Phys. Rev. B* **2014**, *89*, 081102.

[67] N. K. Balla, M. O'Brien, N. McEvoy, G. S. Duesberg, H. Rigneault, S. Brasselet, D. McCloskey, *ACS Photonics* **2018**, *5*, 1235.

[68] J. Xiao, Z. Ye, Y. Y. Wang, H. Zhu, Y. Y. Wang, X. Zhang, *Light Sci. Appl.* **2015**, *4*, e366.

[69] A. Sharma, H. Yan, L. Zhang, X. Sun, B. Liu, Y. Lu, *Acc. Chem. Res.* **2018**, *51*, 1164.

[70] H. G. Rosa, Y. W. Ho, I. Verzhbitskiy, M. J. F. L. Rodrigues, T. Taniguchi, K. Watanabe, G. Eda, V. M. Pereira, J. C. V. Gomes, *Sci. Rep.* **2018**, *8*, 10035.

[71] K. L. Seyler, J. R. Schaibley, P. Gong, P. Rivera, A. M. Jones, S. Wu, J. Yan, D. G. Mandrus, W. Yao, X. Xu, *Nat. Nanotechnol.* **2015**, *10*, 407.

[72] T. Sohier, E. Ponomarev, M. Gibertini, H. Berger, N. Marzari, N. Ubrig, A. F. Morpurgo, *Phys. Rev. X* **2019**, *9*, 031019.

[73] S. Mouri, Y. Miyauchi, K. Matsuda, *Nano Lett.* **2013**, *13*, 5944.

[74] J. S. Ross, S. Wu, H. Yu, N. J. Ghimire, A. M. Jones, G. Aivazian, J. Yan, D. G. Mandrus, D. Xiao, W. Yao, X. Xu, *Nat. Commun.* **2013**, *4*, 1474.

[75] C. Cong, J. Shang, Y. Wang, T. Yu, *Adv. Opt. Mater.* **2018**, *6*, 1700767.

[76] H. Yu, D. Talukdar, W. Xu, J. B. Khurgin, Q. Xiong, *Nano Lett.* **2015**, *15*, 5653.

[77] H. Zhu, Y. Wang, J. Xiao, M. Liu, S. Xiong, Z. J. Wong, Z. Ye, Y. Ye, X. Yin, X. Zhang, *Nat. Nanotechnol.* **2015**, *10*, 151.

[78] A. R. Khan, T. Lu, W. Ma, Y. Lu, Y. Liu, *Adv. Electron. Mater.* **2020**, *6*, 1901381.

3 FOLDING AND STRAIN ENGINEERING IN 2D MATERIALS

3.1 Introduction

Tuning the optoelectronic properties of semiconductors is important for device fabrication and fundamental science.[1] Researchers have used various ways to tune the optoelectronic properties such as strain engineering,[2,3] doping,[4,5] defect engineering,[6] etc. Particularly, local strain engineering provides an effective and straightforward way to tune the optoelectronic properties of semiconductors such as bandgap, carrier mobility, binding energy of excitons,[2,3,7] which has therefore been broadly used to improve the device performance such as enhancement of solar cell efficiencies and generation of single photon emitters.[8–12]

Two-dimensional (2D) atomic crystals such as 2D transition metal dichalcogenides (TMDC) monolayers are an ideal platform to study strain engineering because they can withstand strain greater than 10%.[13] In addition, they can be folded or wrapped due to their high flexibility, making them promising candidates for stretchable and flexible electronics.[13–15] Using strain engineering of 2D TMDCs, researchers have successfully tuned optoelectronic properties.[16,17] For example, Desai *et. al.* showed considerable photoluminescence (PL) enhancement on atomically thin tungsten diselenide (WSe_2) upon strain application.[18] Strain effect is used to increase the career mobility of ultrathin

MoS_2, thus leading to an improvement in the performance of MoS_2 based field effect transistor (FET).[19]

Local strain engineered in 2D TMDs is typically achieved through stretching of a flexible substrate.[20] This method involves the exfoliation of 2D material on a pre-stretched flexible substrate followed by the formation of strained wrinkles after the release of the stretched substrate.[3] The wrinkles in ultra-thin TMDs easily fall down to form folds due to their low bending rigidity.[20] Therefore, wrinkles formation in thick TMDs (layer $\geq$ 3) is only reported.[3,20] The excitons in thick wrinkles are reported to funnel towards the middle of the wrinkle's region; therefore, the wrinkles can change the local confinement potential of excitons.[3] Wrinkles are also reported to show exciting bandgap modification in atomically thin MoS_2[3]. PL measurements on 3-5L wrinkles indicate that band gap energy decreases significantly as uniaxial strain increases. The experimental measurements showed ~45.2meV per % strain reduction in indirect bandgap whereas ~32meV per % strain reduction is found in direct bandgap (k-k' valley transition). This significant bandgap shift was also proved for wrinkles using tight-binding model.[3] The change of optical and electrical properties in strain induced wrinkles has also been observed with other 2D materials as well.[21–23] Several studies have reported the strain dependent bandgap reduction ~27-46 meV/(strain%)[7,24,25] in monolayer WS_2."

Here, we have developed a new method, mechanical buckling of flexible substrate, to create both wrinkles and folds simultaneously in 1-3L WS_2 by successfully controlling the strain. The Kelvin probe force microscope (KPFM) and conductive atomic force microscope (CAFM) are used for surface potential mapping and current mapping, respectively. A layer dependent reduction in surface potential is found due to the dominant interlayer screening effect irrespective of the layers' orientation. The current mappings demonstrate strain tuning of semi conductive junction properties of strain induced wrinkles. This behavior is explained using Thermionic model which suggests 1.6% strain on wrinkle nanostructures reduce 20% of Schottky barrier height (SBH). Photo- Conductive Atomic Force Microscope (PCAFM investigation reveals that the SBH can be further lowered due to photo-enhanced current. Our results demonstrate an important advance towards controlling the properties of atomically thin WS_2 via strain induced wrinkling and folding. Moreover, these techniques could be applied to other 2D materials[26–35] and heterostructures[36–39] for applications in quantum optics, nanophotonics and optoelectronics.

3.2 Fabrication of folds and strain induced wrinkles

We employed mechanical buckling of the flexible substrate to achieve both wrinkles and folds simultaneously in 1-3L WS_2. The details of the fabrication method are shown in **Figure 3.1a**. (i) The WS_2 flakes are exfoliated on a pre-buckled Gel polymer film. (ii) After exfoliation, the buckled Gel film is released causing compressive forces on the exfoliated WS_2 flakes. The compressive forces generate big and tiny wrinkles. (iii) The big wrinkles are formed in the direction perpendicular to the compressive forces (x-direction) and they fall down to form folds, (iv) whereas the tiny wrinkles are generated in the direction parallel to the compressive forces (y-direction). The tiny wrinkles maintain their wrinkles like curvature which is explained later. In the text, the terms of big wrinkles and folds are used interchangeable. Without the specific notation, winkles present tiny wrinkles. A 3D schematic of the folds and wrinkles' formation after mechanical buckling is shown in **Figure 3.1b**. The buckled WS_2 sample is transferred onto a Si/SiO_2/gold electrode substrate.[40,41] Phase shifting interferometry (PSI)[27,29,42–44] is employed to identify the layer number of the WS_2 flakes **(Figure A5.1)**.

It is unambiguous that big wrinkles are formed perpendicular to the compressive forces (antiparallel red arrows) as depicted in optical image of buckled WS_2 **(Figure 3.1c).** Intriguingly, along with big wrinkles, some tiny wrinkles are also detected, and their alignment is almost perpendicular to the big wrinkles as revealed by AFM topography (**Figure 3.1d)**. The width of the tiny wrinkles (100-190 nm) is much smaller than that of the big wrinkles, which is the possible reason why there is no trace of tiny wrinkles under the optical microscope. The inserted plot (red rectangle) of **Figure 3.1d** gives detailed height profiles of both big and tiny wrinkles which indicate that the height of big wrinkles is much smaller than the tiny wrinkles. Moreover, height profile of tiny wrinkles presents a sharp peak-shaped cross-section in contrary to big wrinkles which present an almost rectangular shaped cross-section. According to this profile, we assume that big wrinkles form folds whereas tiny wrinkles are the wrinkles maintaining their curvature.

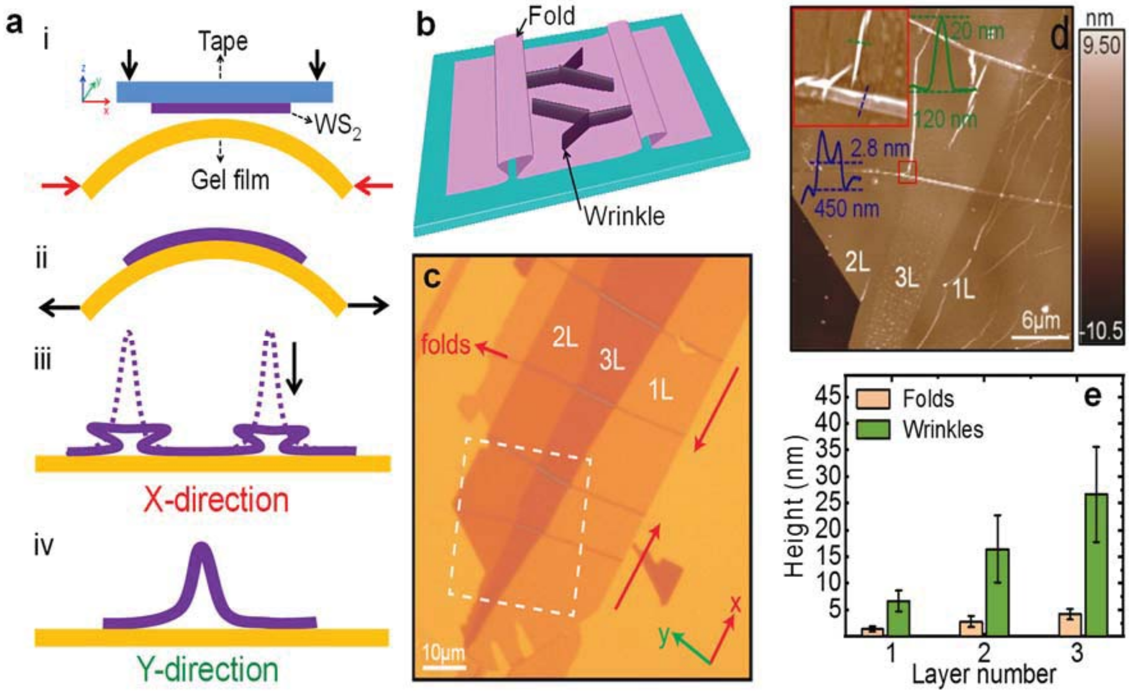

Figure 3.1 | Creation of wrinkles and folds in 1-3L WS_2.
(a) Schematic diagram of the fabrication process for wrinkles and folds formation in atomically thin WS_2. (i) An elastomeric substrate (Gel film) is buckled prior depositing WS_2 flakes using a tape. (ii) The buckled substrate is released causing compressive forces which create big and tiny wrinkles perpendicular and parallel respectively, to the direction of forces (X-direction). (iii) Big wrinkles fall down to form folds (X-

direction view) (iv) whereas tiny wrinkles retain their shape (Y-direction view). **(b)** A 3D image of strained sample showing wrinkles and folds, different colours for the wrinkles and the folds are used for clear visibility. **(c)** Optical microscopic image of 1-3L strained WS_2 sample fabricated by the method described above; folds are created perpendicular to the direction of the compressive forces, two anti-parallel arrows (red colour) indicate the direction of the compressive force.**(d)** AFM topography image of the region marked by the white dashed rectangle in (c) whereas inset image is the zoom-in view of the small red rectangle. Inset image shows AFM measurement of the wrinkle (20 nm height and 120nm width) and fold (2.8 nm height and 450nm width) in green and blue colours respectively. **(e)** The layer dependence of wrinkles and height differences for folds measured on 1L, 2L and 3L. The histogram shows the AFM height measurements, with variation in measurements indicated by the error bars. The orange and green rectangles indicate the height measurements for folds and wrinkles respectively.

Figure 3.1e plots the height difference between the big/tiny wrinkle and corresponded flat regions. For the big wrinkles, the height differences measured on 1L, 2L and 3L samples are 1.4 ± 0.5, 2.8 ± 0.5 and 4.2 ± 1 nm, respectively. These values match the height of 2L, 4L and 6L samples very well as the thickness of single layer is evaluated around 0.7 nm, which agrees well with the reported value.[45] Therefore, the big wrinkles can be regarded as the bi-folded samples. *E.g.*, the big wrinkle on the 1L sample can be considered as bi-folded single layer (1L+1L+1L) samples and its height is in good consistency with the pristine 3L sample. In a previous work on MoS_2[3], the appearance of the fold regions is possibly ascribed to the collapsing of the large wrinkles caused by the buckling-induced delamination. Such wrinkle to fold transition is also observed on monolayers of graphene and TMDC by researchers in the past.[20,46–48] It is worthy to note that the tiny wrinkles appear in the centre of the nano-flakes and therefore, their height values present large deviations. However, their deformation is relatively small, and they maintain their wrinkles' like curvature. The maximum uniaxial strain ε is accumulated on top of the winkles and can be estimated as; [3]

$$\varepsilon \sim \pi^2 h\delta/(1-\nu^2)\lambda^2 \qquad (1)$$

where ν is the Poisson's ratio (ν =2.2 for WS_2[49]), h is the thickness of the flake, and δ and λ are the height and width of the wrinkle which were measured using atomic force microscopy (AFM). The relationship shows that the height of the wrinkles increases with the strain applied. For the wrinkles' profile on 2L WS_2 given in **Figure 3.1d** (green color), strain ε can be estimated as 2% where $h = 1.4$nm, δ=20nm, $\lambda = 120$nm.

Wrinkling requires a minimum value of strain to initiate the wrinkles formation. As the strain increases, the height of the wrinkles increases. After a critical strain level (ε_f), wrinkles cannot maintain their curvature and collapse forming folds **(Figure A5.2c)**. Critical strain level is dependent on layer thickness and elastic modulus of ultra-thin WS_2 film (See section S3 for more details). As layer number increases, ε_f increases and fold formation in higher layer number decreases. Therefore, wrinkle to fold transition is dominant in small layer number (1L > 2L > 3L) due to their low critical strain (ε_f). Moreover, it can also be found that wrinkles' average height increases as layer number increases (3L > 2L > 1L) which can be attributed to increasing critical strain level (ε_f) in higher layer number showing more capability to maintain wrinkles' curvature **(Figure 3.1e).** Additionally, the width of the folds also showed an increase as layer number increases which ranges 180-400 nm, 250-450 nm and 350-500 nm for 1L, 2L and 3L respectively.

3.3 Surface potential measurements

With intentional manufacturing, we have obtained different local features (flat, fold and wrinkles) in 1-3L WS_2. As varying the local stacking and strain states of the WS_2 samples, the electronic structures are expected to be tuned. KPFM is a useful tool to map the surface potential at the nano-meter scale. In KPFM, an AC bias is applied to a conductive tip to produce an electrical force which is minimized when contact potential difference or surface potential between tip and sample is compensated by an applied DC bias. In principle, the contact potential difference (V_{CPD}) is originated from the different work functions between the tip and sample, which can be expressed as follows;[50,51]

$$V_{CPD} = \frac{\Phi_{tip} - \Phi_{sample}}{-e} \qquad (2)$$

Where Φ_{tip} and Φ_{sample} are work functions of the tip and the sample and e is the electronic charge. However, many factors such as trapped charges, tip damage and permanent dipoles between the sample and tip will impact the results. Therefore, KPFM usually gives an accurate measurement of the potential difference rather than the absolute value. The surface potential mapping is carried out for the flat, folded, wrinkled regions of 1-3L WS_2. The typical morphology and surface potential images are presented in **Figure 3.2a-d.** The potential measured on different layers presents evident contrast. Combining the morphology mapping, in the 1L, 2L and 3L samples, the surface potential in fold regions is unambiguously lower than the flat regions for the similar layer number. However, no clear features are obtained for wrinkles in surface potential mapping which can be ascribed to the small size (width~100-190nm) of wrinkles making it to be difficult to be resolved. In order to conduct quantitative analysis on folded regions, the surface potential values are calculated by fitting the histograms collected from different domains **(Figure A5.3).** The offsets (**Figure 3.2b** and **3.2d**) exhibit a small divergence, therefore, the surface potential of flat 3L sample is considered as the reference to make the measured values comparable. As shown in **Figures 3.2e** and **3.2f**, the surface potential of flat and folded regions decreases linearly with an increase in layer number. The differences between each layer are ~23 mV and 9.5 mV for flat and folded regions, respectively. Taking the KPFM set-up into the consideration, work function increases as layer number increases which is consistent with the previous studies on layer dependent work function of flat MoS_2.[52,53] The layer-dependent work function can be explained by the dominant interlayer screening effect reported for both graphene and MoS_2.[54–56] Geometrically, the layer number of folded regions is comparable with the pristine 3L, 6L and 9L samples while the twisted stacking will result in the change of the interlayer coupling in comparison with the perfect packing samples. Intriguingly, no distinct difference is obtained between the surface potential of bi-folded 1L and flat 3L samples, indicating the interlayer screening effect is dominant in WS_2 folds irrespective of the layer orientation.

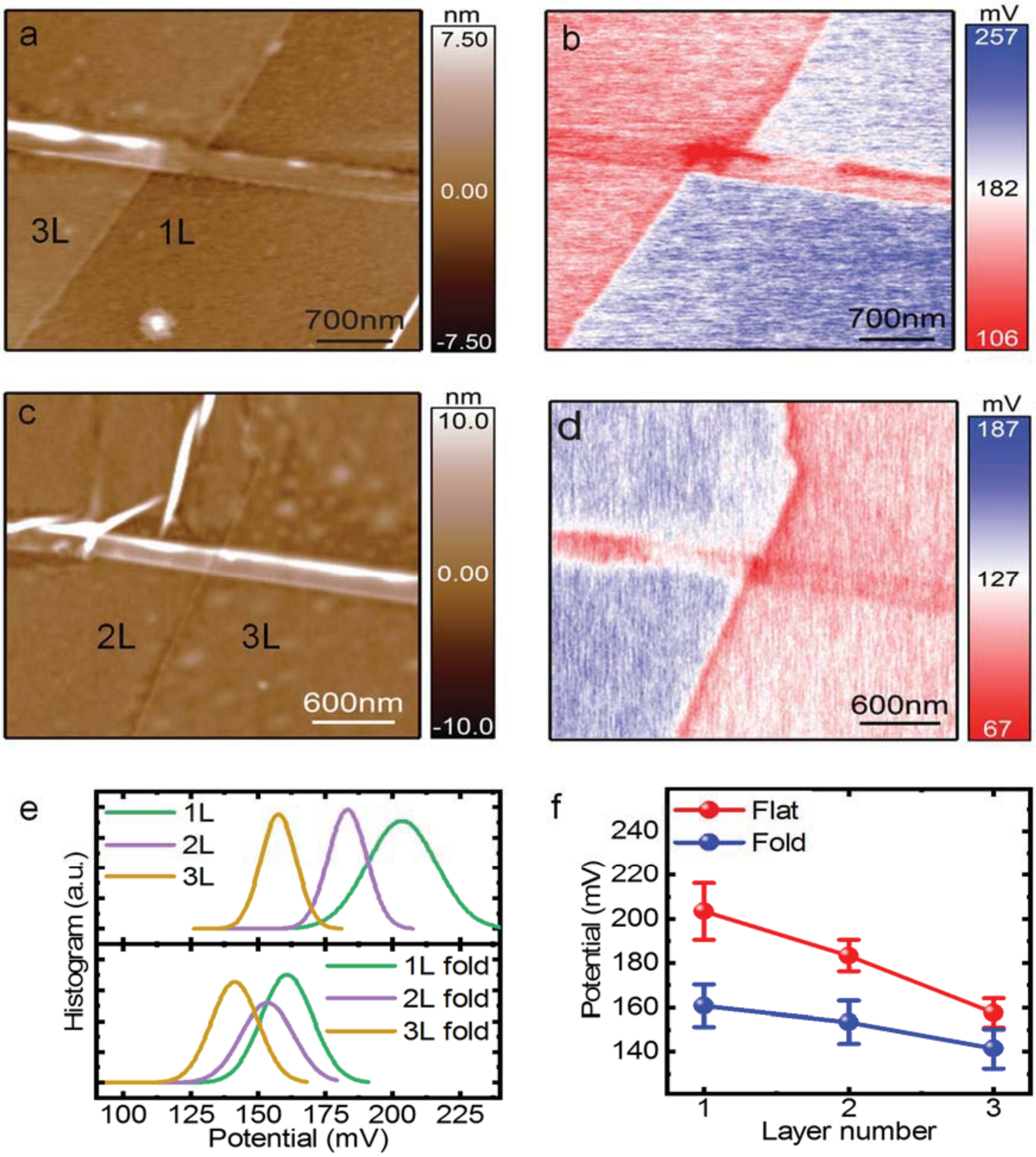

Figure 3.2 | Layer-dependent surface potential of folds in 1-3L WS_2.
(**a**) AFM topography image, showing the flat, folded and wrinkled regions on 1L and 3L.(**b**) Surface potential mapping of (a). **(c)** AFM topography image, showing the flat, folded and wrinkled regions on 2L and 3L. **(d)** Surface potential image of the region shown in (c) **(e)** Surface potential histogram of 1-3L flat WS_2 (upper panel) and 1-3L fold WS_2 (lower panel). **(f)** Surface potential of 1-3Lflat WS_2 (red) and 1-3L fold WS_2 (blue), with variation in the readings is indicated by the error bars.

3.4 Dark carrier transport

The charge transport behaviour is important characteristic for the semi conductive device performance. This section will focus on charge transportation for flat, folded and winkled regions. A schematic of the set-up for the conductive and photoconductive atomic force microscopy (CAFM and PCAFM) is shown in **Figure 3.3a**. The CAFM tip acts as the top electrode and gold is the bottom electrode. In dark condition (no light), the current mappings of AFM topographic image (red rectangle) are done under 4V and 10V bias (**Figure 3.3b-c)**. No evident current is detected overall under 4V except some traces at the wrinkled regions. With increasing the bias to 10V, the wrinkles exhibit significant enhancement of electrical current flow and current reaches around 400 pA. The local *I-V* curves on different regions are measured to further investigate the electronic properties as shown in **Figure 3.3d**. At the low bias, the current measured at flat, folded and wrinkled regions exhibit nearly insulating behaviour while the diode-like characteristics are obtained by gradually increasing the bias. Schottky barrier height (SBH), Φ_b, measured at wrinkled regions is lower than those measured at flat and folded regions which will be explained later. The distance to the bottom gold electrode is similar (~20 µm) for three regions. Therefore, we can assume the obtained *I-V* behaviours are mainly determined by the metal tip-semiconductor contact resistance. Due to the difference between the tip work function and electron affinity of WS_2, Schottky barrier is formed at the interface. **Figure 3.3e** illustrates the equilibrium case of Schottky barrier between CAFM tip and WS_2 (flat and wrinkle). It is evident SBH represented by Φ_b ($\Phi_b = \Phi_{tip} - \chi$, where χ is the WS_2 electron affinity), is the determinant factor for the current flow.[57,58]

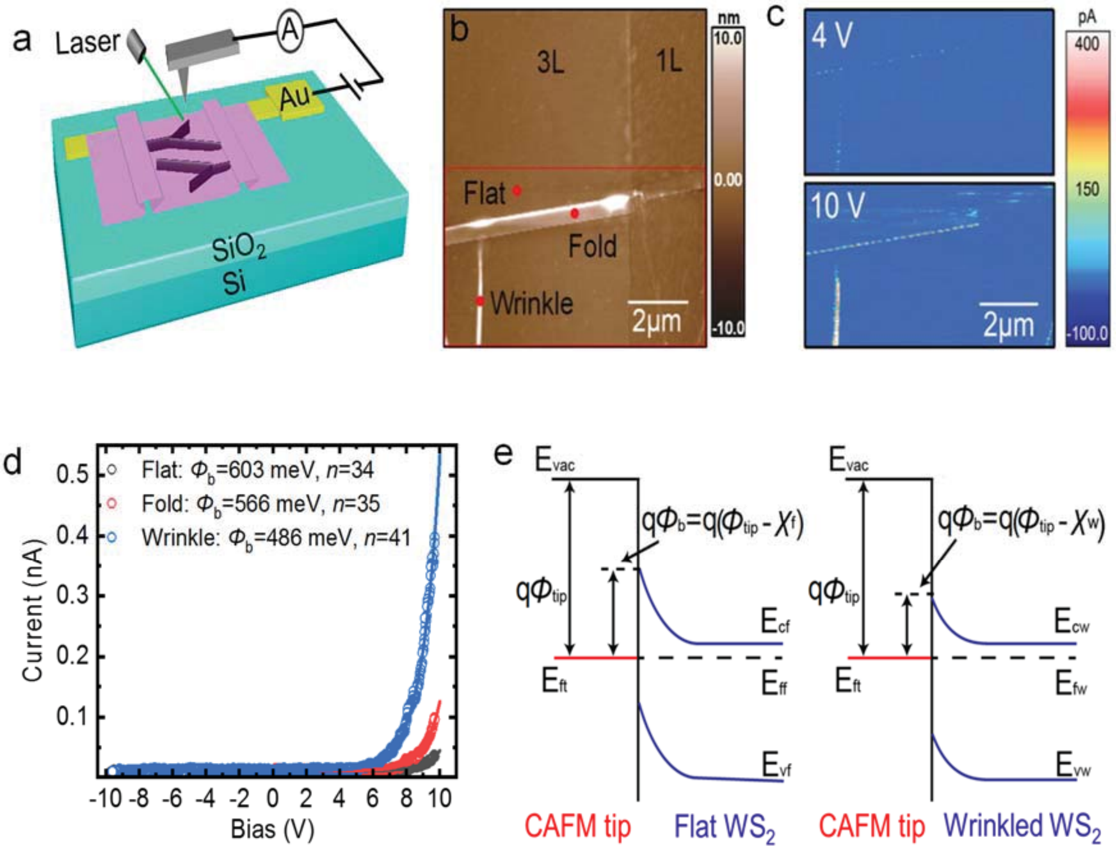

Figure 3.3 | Current mapping of wrinkles in atomically thin WS_2 by conductive AFM imaging.

(a) A schematic of conductive AFM configuration for carrier transport measurements. Strained sample is transferred onto a gold electrode and the voltage is applied on the sample under forward bias. **(b)** AFM topography image, showing the flat, folded and wrinkled regions. **(c)** Current mapping of the region marked by red rectangle in (b) under bias voltages of 4V and 10V, **(d)** A current-voltage (*I*-*V*) curve for flat, fold and wrinkle indicated by red dots in (b) under (-10 to +10V) bias voltage, Schottky barrier height (Φ_b) for flat = 603 meV, fold = 566 meV and wrinkle = 486 meV is calculated using thermionic model. The corresponding strain for the wrinkle is calculated to be 1.6%. **(e)** Energy band diagram for CAFM tip-WS_2 (flat) and CAFM tip-WS_2 (wrinkled) junction. Φ_{tip} is the CAFM tip work function, E_{vac} is the reference vacuum level, q is the charge, Φ_b is the barrier height, χ_f and χ_w are electron affinity for flat and wrinkle WS_2 respectively, E_{ft}, E_{ff} and E_{fw} are the Fermi level of the tip, flat and wrinkle WS_2 respectively. E_{vf} and E_{cf} are valence and conduction band levels of flat WS_2 whereas E_{vw} and E_{cw} are valence and conduction band levels of wrinkle WS_2.

Li et al.[55] performed a C-AFM study on ultrathin MoS_2 using a conductive tip and successfully explained the characteristics of the resulting junction in the forward bias regime using thermionic emission model. Therefore, the current under forward bias can be described by the thermionic emission model over the Schottky barrier as under [59];

$$I = A_{tip}A^{*}T^{2}e^{-\frac{q\phi_B}{kT}}e^{\frac{q(V-IR)}{nkt}} \qquad (3)$$

where A_{tip} is the tip-sample contact area, $A^{*}=4\pi qk^{2}m_{\mathrm{eff}}/h^{3}$ is the Richardson constant with effect mass for electrons ~ $0.3m_e$ for WS_2 [60], h is the Planck constant, T is the temperature which equals ~ 300 K, q is the elementary charge and Φ_B is the SBH, k is Boltzmann constant, R is the resistance in the circuit, and n is the ideality factor. Since the current value is quite small (< 500 pA), the voltage drops across the Schottky barrier (V-IR) is almost equal to the applied bias.

The fitting parameters for the three curves are displayed in **Figure 3.3d**. The large ideality factor, $n = 34$, 35 and 41 for flat, fold and wrinkle suggests the thermionic emission model requires careful consideration while Φ_b fitted for the flat sample is around 603 meV, which is close to the recently reported Φ_b =590 meV between the Pt-coated tip and WS_2 nanoflake.[61] The fitting results suggest different I-V characteristics collected from flat, folded and wrinkled regions are originated from the different SBH formation at the metal-semiconductor interface. A large reduction of Φ_b (~486 meV) is obtained for the wrinkled WS_2 junction as compared to the flat WS_2 junction whereas the strain is calculated to be 1.6% on the wrinkle using equation (1). Previously, researchers have reported strain induced bandgap reduction in ultrathin WS_2[7,62] which can be attributed to lowering of SBH in wrinkled WS_2. The bandgap generally decreases with increasing the thickness in 2D TMDs semiconductors.[63,64] Therefore, we find a reduction in SBH of tip-WS_2 (fold) junction which is in good agreement with a previous study showing SBH reduction with increasing the thickness of MoS_2 in MoS_2-metal contact.[65] However, it is still worthy to note that the folding of 2D materials could change the stacking orders among the layers, thereby tuning interlayer coupling and band structures[48].

3.5 Photo carrier transport

In the previous sections, we successfully demonstrated strain engineering and folding as powerful tools to tune the electronic properties. Strain engineering and folding are also expected to tune optoelectronic properties. In this context, the current mappings of the topographic image (red rectangle in **Figure 3.3b)** are carried out under dark (no light) and light condition for direct comparison. It is evident that current flow under illumination is enhanced for all the regions (flat, fold and wrinkle). However, wrinkled regions present the strongest contrast compared with other two regions. *I-V* junction characteristics of flat, folded and wrinkled region under illumination are presented to further explore this behaviour **(Figure 3.4b)**. Here, *I-V* curves present rectifying characteristics with 5V forward bias under illumination whereas no obvious current responses were obtained for three regions using the same applied voltage under the dark condition. Furthermore, a small photocurrent is detectable under the zero voltage bias, which might be arisen from the tiny photo-response compared with the instrumental current threshold (~10 pA) or small work function difference between the top and bottom electrodes (Pt/Ir tip and Au). Enhancement of the electrical current under illumination might have a close relationship with the photo-generated carriers. As the *I-V* curves still exhibit diode-like features, it can be proposed that the current flowing in the circuit is mainly decided by the metal/semiconductor contact resistance. Through adopting the thermionic model, either increasing the temperature or decreasing the SBH can intensify the current. Both current mapping and time-resolved photo-response under the repeated on-off light irradiation indicate the hysteresis, which is normally due to the thermal effect, is not obvious in flat WS_2 samples (**Figure A5.5-A5.6**). To further investigate the impacts of photo-generated carriers on SBH, the surface potential under the light irradiation is shown in **Figure 3.4c**. It is obvious that the surface potentials on both flat and folded regions exhibit an abrupt increase when the incident laser is on. **Figure 3.4d** shows the surface potential variation as a function of the incident laser power measured in the same region. The detailed surface potential images can be found in **Figure A5.7**. For both the flat and folded regions, the biggest variation occurs when the laser is switched on, which indicates that the surface potential change mainly originates from the photoexcitation rather than the thermal excitation.

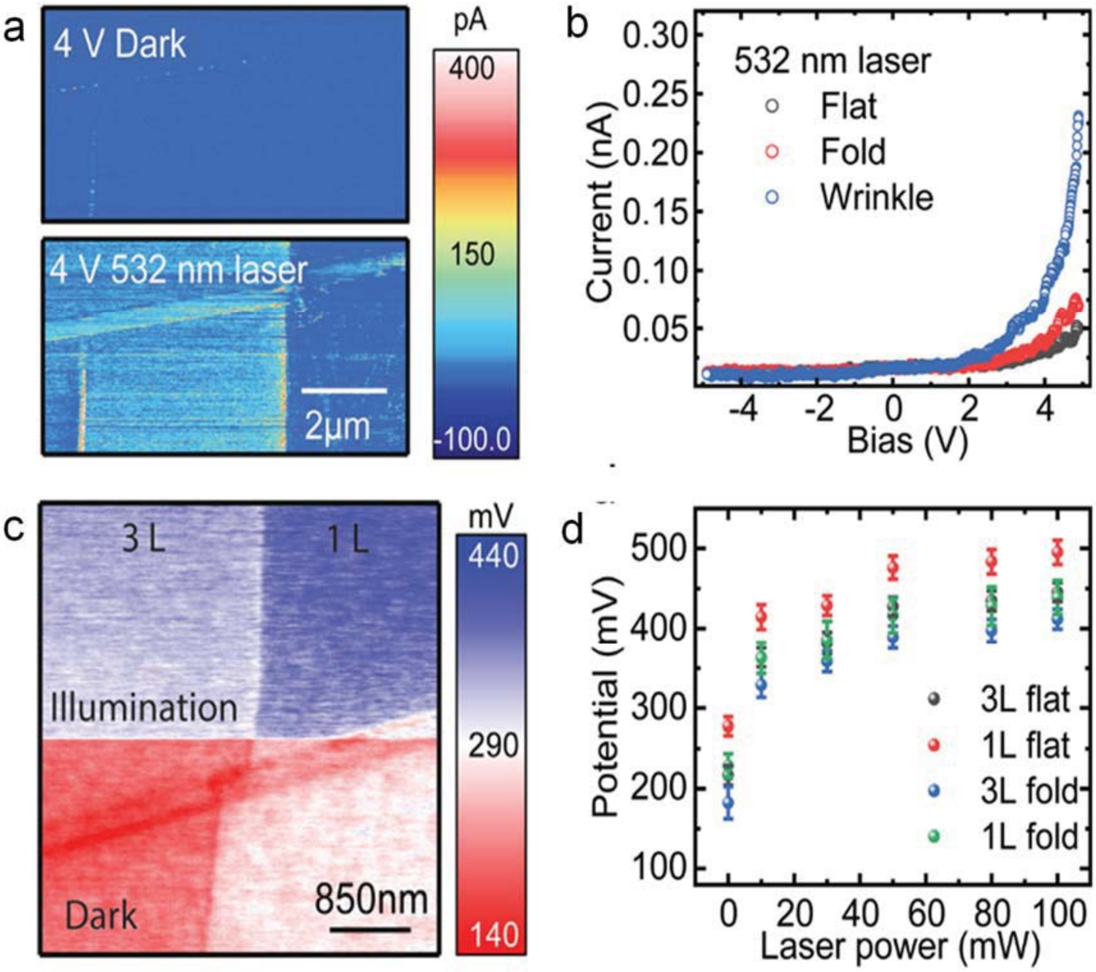

Figure 3.4 | Differentiation of wrinkled and folded nano-structures by photo-conductive AFM. **(a)** Current mapping (of the region marked by red rectangle in Figure 3.3c) under dark (no light) and light (60 mW) at forward biased voltage of 4V; **(b)** Current-voltage (*I*-*V*) curve showing photocurrent response for flat, fold and wrinkle under excitation from a 532nm laser with 60 mW power density. **(c)** Surface potential mapping of 1L and 3L under dark (no light) and light (60 mW) **(d)** Laser power dependent surface potential (mV) response of 1 & 3L flat and fold under excitation from a 532nm laser with 60 mW power density. Error bars indicate the variation in measurements.

According to the KPFM set-up, the increase of surface potential is a consequence of accumulated positive charges on the surface or the appearance of upward dipole-moment.[66] Both effects can bend the band structure of WS_2 samples, lowering the SBH. Therefore, the photo-enhanced current is attributed to lowering the SBH by the photo-generated current.

3.6 Chapter summary

In summary, we have successfully demonstrated the fabrication of both fold and wrinkle nanostructures simultaneously in 1-3L WS_2 by controlling strain. It is found that the interlayer screening effect is the dominant factor in layer dependent surface potential measurements. Therefore, we find layer dependent surface potential reduction for both perfect pack and twisted layers of ultrathin WS_2. The current mappings demonstrate strain tuning of semi conductive junction properties of strain induced wrinkles. This behaviour is explained using Thermionic model, which suggests 20% reduction in Schottky barrier height through 1.6% strain on wrinkle. Photo- Conductive Atomic Force Microscope (PCAFM) investigation reveals further lowering of SBH due to photo generated carriers. Our technique offers a route to local strain engineering in ultra-thin materials, opening many applications in diverse fields such as electronics, quantum optics, optoelectronics and surface science.

Chapter 3 References

(1) Santos, E. J. G.; Kaxiras, E. Electrically Driven Tuning of the Dielectric Constant in MoS2 Layers. *ACS Nano* **2013**, *7* (12), 10741–10746.

(2) Quereda, J.; Palacios, J. J.; Agräit, N.; Castellanos-Gomez, A.; Rubio-Bollinger, G. Strain Engineering of Schottky Barriers in Single- and Few-Layer MoS 2 Vertical Devices. *2D Mater.* **2017**, *4* (2), 021006.

(3) Castellanos-Gomez, A.; Roldán, R.; Cappelluti, E.; Buscema, M.; Guinea, F.; Van Der Zant, H. S. J.; Steele, G. A. Local Strain Engineering in Atomically Thin MoS2. *Nano Lett.* **2013**, *23* (11), 534.

(4) Du, Y.; Liu, H.; Neal, A. T.; Si, M.; Ye, P. D. Molecular Doping of Multilayer Mos2 Field-Effect Transistors: Reduction in Sheet and Contact Resistances. *IEEE Electron Device Lett.* **2013**, *34* (10), 1328–1330.

(5) Fontana, M.; Deppe, T.; Boyd, A. K.; Rinzan, M.; Liu, A. Y.; Paranjape, M.; Barbara, P. Electron-Hole Transport and Photovoltaic Effect in Gated MoS2 Schottky Junctions. *Sci. Rep.* **2013**, *3* (1), 1634.

(6) Pei, J.; Gai, X.; Yang, J.; Wang, X.; Yu, Z.; Choi, D.-Y.; Luther-Davies, B.; Lu, Y. Producing Air-Stable Monolayers of Phosphorene and Their Defect Engineering. *Nat. Commun.* **2016**, *7* (1), 10450.

(7) Wang, L.; Kutana, A.; Yakobson, B. I. Many-Body and Spin-Orbit Effects on Direct-Indirect Band Gap Transition of Strained Monolayer MoS2 and WS2. *Ann. Phys.* **2014**, *526* (9), L7–L12.

(8) Kern, J.; Niehues, I.; Tonndorf, P.; Schmidt, R.; Wigger, D.; Schneider, R.; Stiehm, T.; Michaelis de Vasconcellos, S.; Reiter, D. E.; Kuhn, T.; et al. Nanoscale Positioning of Single-Photon Emitters in Atomically Thin WSe2. *Adv. Mater.* **2016**, *28* (33), 7101–7105.

(9) Palacios-Berraquero, C.; Kara, D. M.; Montblanch, A. R. P.; Barbone, M.; Latawiec, P.; Yoon, D.; Ott, A. K.; Loncar, M.; Ferrari, A. C.; Atatüre, M. Large-Scale Quantum-Emitter Arrays in Atomically Thin Semiconductors. *Nat. Commun.* **2017**, *8* (1), 15093.

(10) Branny, A.; Kumar, S.; Proux, R.; Gerardot, B. D. Deterministic Strain-Induced Arrays of Quantum Emitters in a Two-Dimensional Semiconductor. *Nat. Commun.* **2017**, *8* (1), 15053.

(11) Feng, J.; Qian, X.; Huang, C.-W.; Li, J. Strain-Engineered Artificial Atom as a Broad-Spectrum Solar Energy Funnel. *Nat. Photonics* **2012**, *6* (12), 866–872.

(12) Li, H.; Contryman, A. W.; Qian, X.; Ardakani, S. M.; Gong, Y.; Wang, X.; Weisse, J. M.; Lee, C. H.; Zhao, J.; Ajayan, P. M.; et al. Optoelectronic Crystal of Artificial Atoms in Strain-Textured Molybdenum Disulphide. *Nat. Commun.* **2015**, *6* (1), 7381.

(13) Mennel, L.; Furchi, M. M.; Wachter, S.; Paur, M.; Polyushkin, D. K.; Mueller, T. Optical Imaging of Strain in Two-Dimensional Crystals. *Nat. Commun.* **2018**, *9* (1), 516.

(14) Bertolazzi, S.; Brivio, J.; Kis, A. Stretching and Breaking of Ultrathin MoS 2. *ACS Nano* **2011**, *5* (12), 9703–9709.

(15) Akinwande, D.; Petrone, N.; Hone, J. Two-Dimensional Flexible Nanoelectronics. *Nat. Commun.* **2014**, *5* (1), 5678.

(16) Dhakal, K. P.; Roy, S.; Jang, H.; Chen, X.; Yun, W. S.; Kim, H.; Lee, J.; Kim, J.; Ahn, J. H. Local Strain Induced Band Gap Modulation and Photoluminescence Enhancement of Multilayer Transition Metal Dichalcogenides. *Chem. Mater.* **2017**, *29* (12), 5124–5133.

(17) Shen, T.; Penumatcha, A. V.; Appenzeller, J. Strain Engineering for Transition Metal Dichalcogenides Based Field Effect Transistors. *ACS Nano* **2016**, *10* (4), 4712–4718.

(18) Desai, S. B.; Seol, G.; Kang, J. S.; Fang, H.; Battaglia, C.; Kapadia, R.; Ager, J. W.; Guo, J.; Javey, A. Strain-Induced Indirect to Direct Bandgap Transition in Multilayer WSe 2. *Nano Lett.* **2014**, *14* (8), 4592–4597.

(19) Chai, Y.; Su, S.; Yan, D.; Ozkan, M.; Lake, R.; Ozkan, C. S. Strain Gated Bilayer Molybdenum Disulfide Field Effect Transistor with Edge Contacts. *Sci. Rep.* **2017**, *7* (1), 41593.

(20) Castellanos-Gomez, A.; van der Zant, H. S. J.; Steele, G. A. Folded MoS2layers with Reduced Interlayer Coupling. *Nano Res.* **2014**, *7* (4), 1–7.

(21) Hattab, H.; N'Diaye, A. T.; Wall, D.; Klein, C.; Jnawali, G.; Coraux, J.; Busse, C.; Van Gastel, R.; Poelsema, B.; Michely, T.; et al. Interplay of Wrinkles, Strain, and Lattice Parameter in Graphene on Iridium. *Nano Lett.* **2012**, *12* (2), 678–682.

(22) Meng, L.; Su, Y.; Geng, D.; Yu, G.; Liu, Y.; Dou, R.-F.; Nie, J.-C.; He, L. Hierarchy of Graphene Wrinkles Induced by Thermal Strain Engineering. *Appl. Phys. Lett.* **2013**, *103* (25), 251610.

(23) Quereda, J.; San-Jose, P.; Parente, V.; Vaquero-Garzon, L.; Molina-Mendoza, A. J.; Agraït, N.; Rubio-Bollinger, G.; Guinea, F.; Roldán, R.; Castellanos-Gomez, A. Strong Modulation of Optical Properties in Black Phosphorus through Strain-Engineered Rippling. *Nano Lett.* **2016**, *16* (5), 2931–2937.

(24) He, X.; Li, H.; Zhu, Z.; Dai, Z.; Yang, Y.; Yang, P.; Zhang, Q.; Li, P.; Schwingenschlogl, U.; Zhang, X. Strain Engineering in Monolayer WS 2 , MoS 2 , and the WS 2 /MoS 2 Heterostructure. *Appl. Phys. Lett.* **2016**, *109* (17), 173105.

(25) Zhang, Q.; Chang, Z.; Xu, G.; Wang, Z.; Zhang, Y.; Xu, Z. Q.; Chen, S.; Bao, Q.; Liu, J. Z.; Mai, Y. W.; et al. Strain Relaxation of Monolayer WS2 on Plastic Substrate. *Adv. Funct. Mater.* **2016**, *26* (47), 8707–8714.

(26) Neupane, G. P.; Ma, W.; Yildirim, T.; Tang, Y.; Zhang, L.; Lu, Y. 2D Organic Semiconductors, the Future of Green Nanotechnology. *Nano Mater. Sci.* **2019**, *1* (4), 246–259.

(27) Pei, J.; Yang, J.; Yildirim, T.; Zhang, H.; Lu, Y. Many-Body Complexes in 2D Semiconductors. *Adv. Mater.* **2019**, *31* (2), 1706945.

(28) Cho, K.; Yang, J.; Lu, Y. Phosphorene: An Emerging 2D Material. *Journal of Materials Research*. 2017, pp 2839–2847.

(29) Xu, R.; Yang, J.; Zhu, Y.; Yan, H.; Pei, J.; Myint, Y. W.; Zhang, S.; Lu, Y. Layer-Dependent Surface Potential of Phosphorene and Anisotropic/Layer-Dependent Charge Transfer in Phosphorene-Gold Hybrid Systems. *Nanoscale* **2016**, *8*, 129–135.

(30) Vogl, T.; Lecamwasam, R.; Buchler, B. C.; Lu, Y.; Lam, P. K. Compact Cavity-Enhanced Single-Photon Generation with Hexagonal Boron Nitride. *ACS Photonics* **2019**, *6* (8), 1955–1962.

(31) Vogl, T.; Doherty, M. W.; Buchler, B. C.; Lu, Y.; Lam, P. K. Atomic Localization of Quantum Emitters in Multilayer Hexagonal Boron Nitride. *Nanoscale* **2019**, *11* (30), 14362–14371.

(32) Vogl, T.; Campbell, G.; Buchler, B. C.; Lu, Y.; Lam, P. K. Fabrication and Deterministic Transfer of High-Quality Quantum Emitters in Hexagonal Boron Nitride. *ACS Photonics* **2018**, *5* (6), 2305–2312.

(33) Vogl, T.; Lu, Y.; Koy Lam, P. Room Temperature Single Photon Source Using Fiber-Integrated Hexagonal Boron Nitride. *J. Phys. D. Appl. Phys.* **2017**, *50* (29), 295101.

(34) Ahmed, T.; Kuriakose, S.; Abbas, S.; Spencer, M. J. S.; Rahman, M. A.; Tahir, M.; Lu, Y.; Sonar, P.; Bansal, V.; Bhaskaran, M.; et al. Multifunctional Optoelectronics via Harnessing Defects in Layered Black Phosphorus. *Adv. Funct. Mater.* **2019**, *29* (39), 1–12.

(35) Lu, J.; Yang, J.; Carvalho, A.; Liu, H.; Lu, Y.; Sow, C. H. Light-Matter Interactions in Phosphorene. *Acc. Chem. Res.* **2016**, *49* (9), 1806–1815.

(36) Zhang, L.; Sharma, A.; Zhu, Y.; Zhang, Y.; Wang, B.; Dong, M.; Nguyen, H. T.; Wang, Z.; Wen, B.; Cao, Y.; et al. Efficient and Layer-Dependent Exciton Pumping across Atomically Thin Organic–Inorganic Type-I Heterostructures. *Adv. Mater.* **2018**, *30* (40), 1803986.

(37) Tebyetekerwa, M.; Zhang, J.; Liang, K.; Duong, T.; Neupane, G. P.; Zhang, L.; Liu, B.; Truong, T. N.; Basnet, R.; Qiao, X.; et al. Quantifying Quasi-Fermi Level Splitting and Mapping Its Heterogeneity in Atomically Thin Transition Metal Dichalcogenides. *Adv. Mater.* **2019**, *31* (25), 1900522.

(38) Zhang, L.; Yan, H.; Sun, X.; Dong, M.; Yildirim, T.; Wang, B.; Wen, B.; Neupane, G. P.; Sharma, A.; Zhu, Y.; et al. Modulated Interlayer Charge Transfer Dynamics in a Monolayer TMD/Metal Junction. *Nanoscale* **2019**, *11* (2), 418–425.

(39) Liu, Y.; Shivananju, B. N.; Wang, Y.; Zhang, Y.; Yu, W.; Xiao, S.; Sun, T.; Ma, W.; Mu, H.; Lin, S.; et al. Highly Efficient and Air-Stable Infrared Photodetector Based on 2D Layered Graphene-Black Phosphorus Heterostructure. *ACS Appl. Mater. Interfaces* **2017**, *9* (41), 36137–36145.

(40) Yang, J.; Wang, Z.; Wang, F.; Xu, R.; Tao, J.; Zhang, S.; Qin, Q.; Luther-Davies, B.; Jagadish, C.; Yu, Z.; et al. Atomically Thin Optical Lenses and Gratings. *Light Sci. Appl.* **2016**, *5* (3), e16046–e16046.

(41) Castellanos-Gomez, A.; Buscema, M.; Molenaar, R.; Singh, V.; Janssen, L.; Van Der Zant, H. S. J.; Steele, G. A. Deterministic Transfer of Two-Dimensional Materials by All-Dry Viscoelastic Stamping. *2D Mater.* **2014**, *1* (1), 11002.

(42) Pei, J.; Yang, J.; Xu, R.; Zeng, Y.-H.; Myint, Y. W.; Zhang, S.; Zheng, J.-C.; Qin, Q.; Wang, X.; Jiang, W.; et al. Exciton and Trion Dynamics in Bilayer MoS 2. *Small* **2015**, *11* (48), 6384–6390.

(43) Yang, J.; Wang, Z.; Yu, Z.; Lu, Y. Manipulating Optical Beam Flow Fronts in 2D Materials. *SPIE Newsroom* **2016**.

(44) Rose, A.; Smith, D. R. Overcoming Phase Mismatch in Nonlinear Metamaterials [Invited]. *Opt. Mater. Express* **2011**, *1* (7), 1232.

(45) Zhang, Y.; Zhang, Y.; Ji, Q.; Ju, J.; Yuan, H.; Shi, J.; Gao, T.; Ma, D.; Liu, M.; Chen, Y.; et al. Controlled Growth of High-Quality Monolayer WS 2 Layers on Sapphire and Imaging Its Grain Boundary. *ACS Nano* **2013**, *7* (10), 8963–8971.

(46) Deng, S.; Berry, V. Wrinkled, Rippled and Crumpled Graphene: An Overview of Formation Mechanism, Electronic Properties, and Applications. *Mater. Today* **2016**, *19* (4), 197–212.

(47) Zang, J.; Ryu, S.; Pugno, N.; Wang, Q.; Tu, Q.; Buehler, M. J.; Zhao, X. Multifunctionality and Control of the Crumpling and Unfolding of Large-Area Graphene. *Nat. Mater.* **2013**, *12* (4), 321–325.

(48) Jiang, T.; Liu, H.; Huang, D.; Zhang, S.; Li, Y.; Gong, X.; Shen, Y.-R.; Liu, W.-T.; Wu, S. Valley and Band Structure Engineering of Folded MoS2 Bilayers. *Nat. Nanotechnol.* **2014**, *9* (10), 825–829.

(49) Brau, F.; Damman, P.; Diamant, H.; Witten, T. A. Wrinkle to Fold Transition: Influence of the Substrate Response. *Soft Matter*. 2013, pp 8177–8186.

(50) Melitz, W.; Shen, J.; Kummel, A. C.; Lee, S. Kelvin Probe Force Microscopy and Its Application. *Surface Science Reports*. 2011, pp 1–27.

(51) Nonnenmacher, M.; O'Boyle, M. P.; Wickramasinghe, H. K. Kelvin Probe Force Microscopy. *Appl. Phys. Lett.* **1991**, *58* (25), 2921–2923.

(52) Choi, S.; Shaolin, Z.; Yang, W. Layer-Number-Dependent Work Function of MoS2 Nanoflakes. *J. Korean Phys. Soc.* **2014**, *64*, 1550–1555.

(53) Kaushik, V.; Varandani, D.; Mehta, B. R. Nanoscale Mapping of Layer-Dependent Surface Potential and Junction Properties of CVD-Grown MoS2 Domains. *J. Phys. Chem. C* **2015**, *119* (34), 20136–20142.

(54) Lee, N. J.; Yoo, J. W.; Choi, Y. J.; Kang, C. J.; Jeon, D. Y.; Kim, D. C.; Seo, S.; Chung, H. J. The Interlayer Screening Effect of Graphene Sheets Investigated by Kelvin Probe Force Microscopy. *Appl. Phys. Lett.* **2009**, *95* (22), 222107.

(55) Li, Y.; Xu, C. Y.; Zhen, L. Surface Potential and Interlayer Screening Effects of Few-Layer MoS 2 Nanoflakes. *Appl. Phys. Lett.* **2013**, *102*, 143110.

(56) Castellanos-Gomez, A.; Cappelluti, E.; Roldán, R.; Agraït, N.; Guinea, F.; Rubio-Bollinger, G. Electric-Field Screening in Atomically Thin Layers of MoS2: The Role of Interlayer Coupling. *Adv. Mater.* **2013**, *25* (6), 899–903.

(57) Rudan, M. *Physics of Semiconductor Devices*; 2015.

(58) Henisch, H. K. Metal-Semiconductor Schottky Barrier Junctions and Their Applications. *Proc. IEEE* **2008**, *74* (6), 894.

(59) Choi, J. H. J.; Zhang, H.; Choi, J. H. J. Modulating Optoelectronic Properties of Two-Dimensional Transition Metal Dichalcogenide Semiconductors by Photoinduced Charge Transfer. *ACS Nano* **2016**, *10* (1), 1671–1680.

(60) Hill, H. M.; Rigosi, A. F.; Rim, K. T.; Flynn, G. W.; Heinz, T. F. Band Alignment in MoS2/WS2 Transition Metal Dichalcogenide Heterostructures Probed by Scanning Tunneling Microscopy and Spectroscopy. *Nano Lett.* **2016**, *16* (8), 4831–4837.

(61) Nowakowski, K.; Van Bremen, R.; Zandvliet, H. J. W.; Bampoulis, P. Control of the Metal/WS 2 Contact Properties Using 2-Dimensional Buffer Layers. *Nanoscale* **2019**, *11* (12), 5548–5556.

(62) Amin, B.; Kaloni, T. P.; Schwingenschlögl, U. Strain Engineering of WS2, WSe2, and WTe2. *RSC Adv.* **2014**, *4* (65), 34561–34565.

(63) Ruppert, C.; Aslan, O. B.; Heinz, T. F. Optical Properties and Band Gap of Single- and Few-Layer MoTe2 Crystals. *Nano Lett.* **2014**, *14* (11), 6231–6236.

(64) Zhao, Z. Y.; Liu, Q. L. Study of the Layer-Dependent Properties of MoS2 Nanosheets with Different Crystal Structures by DFT Calculations. *Catal. Sci. Technol.* **2018**, *8* (7), 1867–1879.
(65) Kwon, J.; Lee, J. Y.; Yu, Y. J.; Lee, C. H.; Cui, X.; Hone, J.; Lee, G. H. Thickness-Dependent Schottky Barrier Height of MoS2 Field-Effect Transistors. *Nanoscale* **2017**, *9* (18), 6151–6157.
(66) Mai, H.; Lu, T.; Li, Q.; Liu, Z.; Li, Y.; Kremer, F.; Li, L.; Withers, R. L.; Wen, H.; Liu, Y. Above-Band Gap Photoinduced Stabilization of Engineered Ferroelectric Domains. *ACS Appl. Mater. Interfaces* **2018**, *10* (15), 12781–12789.

4 SHG OF FOLDS AND STRAIN INDUCED WRINKLES

4.1 Introduction

Structural engineering of 2D materials provide an exciting platform to tailor the material's properties through modification in lattice structure. As discussed, both strain engineering and folding provide an effective way to tune optoelectronic properties and improve the performance of optoelectronic devices, therefore, there is a need of full assessment of local strain vector and folding parameters to utilize their full potential.

Conventionally, determination of both strain amplitude and direction requires combination of multiple tools. For instance, researchers use atomic force microscopy (AFM) to measure the strain amplitude on strain induced wrinkles[1] whereas electron/neutron microscopy is used to determine the relation of strain direction to lattice structure.[2] Recently, optical second-harmonic generation (SHG) has been shown to probe the crystallographic orientation, lattice symmetry and stacking order of non-inversion symmetric 2D materials such as odd layers of TMDs, hBN, Group IV monochalcogenides, etc.[3–6] Because SHG intensity is very sensitive to the structural configurations of 2D materials; it is, in principle, feasible to employ SHG to monitor folding and straining in 2D materials.

Here, we have used polarization dependent SHG as a single tool to probe folding angle and strain vector precisely in atomically thin tungsten disulphide (WS_2). Trilayer folds with 60° folding angle are found to show 9 times SHG enhancement as compared to 1L

WS_2 due to the vector superposition of SH wave vectors coming from the individual layers of the folds. We find strain dependent SHG quenching and enhancement, parallel and perpendicular respectively to the direction of the compressive strain vector. However, strain angle dependent total SHG (without polarizer) remains constant which allows us to find the local strain vector accurately using photoelastic effect. We find SHG to be very sensitive to C-exciton and can be tuned through strain modification. Our results show SHG is a powerful tool to pro be both folding angle and strain vector in atomically thin TMDs.

4.2 Differentiation of folds and wrinkles by SHG

In this work, we have used mechanical buckling of the flexible substrate to obtain folds[7] (1-3L) and strained wrinkles[1] (5-6L) in atomically thin WS_2. The details of the fabrication method are shown in **Figure 4.1a** and given in methods section and **A6.1-2** in supplementary information. Optical microscopic images of folds (1-3L) are shown in **Figure 4.1b**. Odd layers i.e 1L, 3L and 5L show SHG signal due to non-centrosymmetric structure whereas even layer numbers do not show SHG signal due to centrosymmetric structure which is consistent with the previous studies.[6] Interestingly, a significant higher SHG response (~2-3 times) from folded regions is observed as compared to flat regions as shown in **Figure 4.1c**. Power dependent SHG on flat, folded and wrinkles regions is performed to confirm if the photons collected are SH photons. The corresponding SHG signal intensity is drawn with excitation power on a log scale. A fitted value ~ 2 on logscale for power vs SHG intensity confirms the collected photons as SH photons[13–15] (**Figure A6.2**).

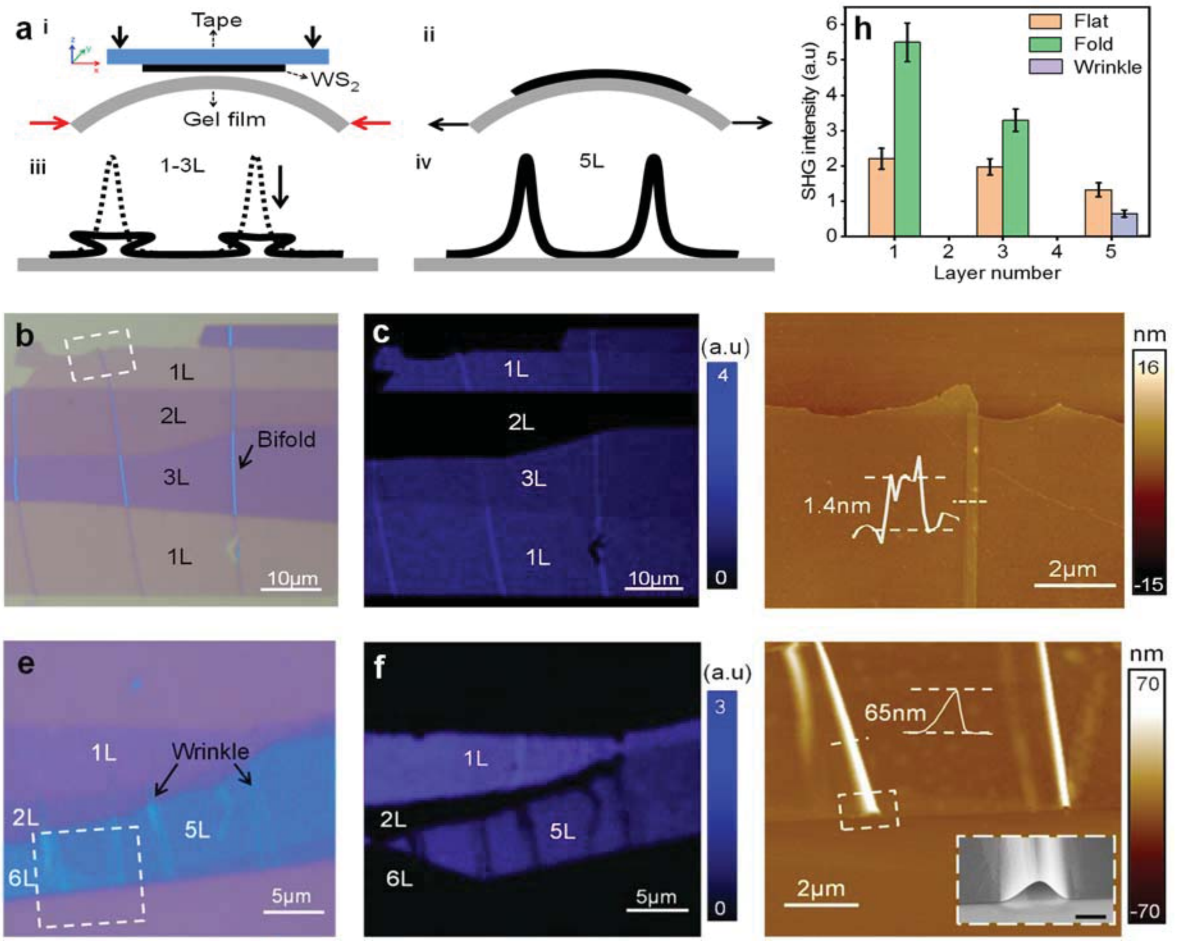

Figure 4.1 | Differentiation of wrinkles and folds by SHG
(a) Schematic diagram of the fabrication process of buckled WS_2 sample. (b) Optical microscopic image of 1-3L WS_2 sample fabricated by the process described in (a), showing the formation of folds due to collapse of wrinkles. (c) AFM (Atomic force microscopy) topography image of the region marked by the white dashed rectangle in (b) (d) Optical microscopic image of 5-6L buckled WS_2 sample showing strained wrinkles on 5L and 6L. (e) SHG intensity mapping of the region shown in Figure 4.1(b). The mapping shows SHG enhancement on 1L and 3L folded regions. (f) SHG intensity mapping of the region shown in Figure 4.1(e). The SHG mapping shows reduction in SHG on 5L wrinkles. (g) AFM topography image of the region marked by the white dashed rectangle in (e). Inset shows SEM (Scanning Electron Microscopy) of the wrinkle's profile (h) A stat-plot showing the SHG response for flat, folded (1L & 3L) and strained wrinkled (5L) regions for ultrathin WS_2. Histogram shows the SHG intensity response, with uncertainties indicated by the error bars. The light brown, green and light blue rectangles indicate the SHG intensity measurements for flat, folded and wrinkled regions respectively. All the measurements are taken at 900nm laser excitation.

Atomic Force Microscopic (AFM) investigation shows that the height differences measured on the 1L, 2L and 3L folds of WS_2 are found to be 1.4 ± 0.5, 2.8 ± 0.5 and 4.2 ± 1 nm respectively (**Figure 4.1d and Figure A6.3**). These values match the height of 2L, 4L and 6L WS_2 very well as the thickness of single layer is evaluated around 0.7

nm[16], which confirms the bifold formation (such as trilayer fold or 1L+1L+1L on 1L WS_2) in 1-3L WS_2. SHG investigation of 5L wrinkles shows a drop in SHG as compared to flat 5L (**Figure 4.1f)** which will be explained later. AFM investigation of 4-6L wrinkles reveals a rapid increase in the height (~50-70nm) as shown in **Figure 4.1g and Figure S3**. The wrinkle like curvature in Scanning electron microscopy (SEM) examination confirms that wrinkles maintain their curvature in $\geq$4L in WS_2. **(Figure 4.1g)**Phase Shifting Interferometry (PSI) is employed to identify the layer number.[8–12] We have used 900nm laser excitation confocal light microscope for second harmonic generation (SHG) mapping (450nm) of flat and folded regions of 1-3L WS_2 as shown in **Figure 4.1c** (see methods section **Appendix A2** for more details).

4.3 SHG investigation of folds

In the previous section, we showed SHG enhancement on folds. The SH response from the fold can be modeled by the vector superposition of all the layers of the fold which is explained here. Let's consider the case of trilayer fold (1L+1L+1L) on 1L WS_2. Opening up of 1L fold shows that the top layer of the fold (designated as L_1 in **Figure 4.2a**) is parallel to the bottom layer (L_3), which implies arm chair direction of L_1 (shown as the black line bisecting the hexagonal WS_2 and black triangle in L_1) is parallel to the armchair direction of L_3 (green bisecting line), whereas armchair direction of the mid layer L_2 (blue bisecting line) of the fold makes an angle of 180° with the arm chair direction of L_1 and L_3. 1L WS_2 belongs to D_{3h} symmetry, therefore, it shows a six-fold polar SH response as under[6];

$$I_{//}(2\omega) \propto cos^2 3\varphi \qquad (1)$$

where $I_{//}(2\omega)$ is the SHG intensity for parallel polarization (i.e polarizer is parallel to the direction of polarization component of incident laser) and φ is the azimuthal angle between the polarized incident laser and the armchair direction.[5,6] SHG intensity becomes maximum when the incident laser polarization is parallel to the armchair direction.[6] For our folding case, $I_{L1} = I_{L3} \propto \cos^2 3\varphi_1$ and $I_{L2} \propto \cos^2 3(\varphi_1 + 180 + \theta_f)$ where $I_{L1}(2\omega)$, $I_{L2}(2\omega)$, and $I_{L3}(2\omega)$ are the SHG wave vector responses from L_1, L_2 and L_3 of the fold. Hsu. et. al.[3] reported that SH wave vector from two stacked layers (I_s) under parallel polarization can be found by the vector superposition of SH wave vectors from two individual layers as under;

$$I_{s_{//}}(2\omega) \propto I_a + I_b + 2\sqrt{(I_a * I_b)}\, \cos 3(\theta) \qquad (2)$$

where θ is the stacking angle between the armchair directions of a and b. Thus, SHG response from the fold can be solved by the vector superposition of the SHG response coming from the individual layers of the fold i.e $I_{L1}(2\omega)$, $I_{L2}(2\omega)$ and $I_{L3}(2\omega)$ as shown in **Figure 4.2b**.

In case of our trilayer fold, this can be done by the vector addition of two entities first ($I_{L1}(2\omega)$ and $I_{L2}(2\omega)$) to find their resultant $I_{L12}(2\omega)$ where $\theta = 180 + \theta_f$) and then adding this resultant vector i.e $I_{L12}(2\omega)$ to the third entity vector ($I_{L3}(2\omega)$) to get the overall resultant vector $I_{Lf}(2\omega)$ where $I_{Lf}(2\omega)$ is SH wave vector from the fold. φ_1 is the azimuthal angle between incident laser polarization component and armchair direction of $I_{L1}(2\omega)$ whereas $3\varphi_P$ is the phase shifting angle between $I_{L1}(2\omega)$ and $I_{Lf}(2\omega)$ as demonstrated in **Figure 4.2b**.

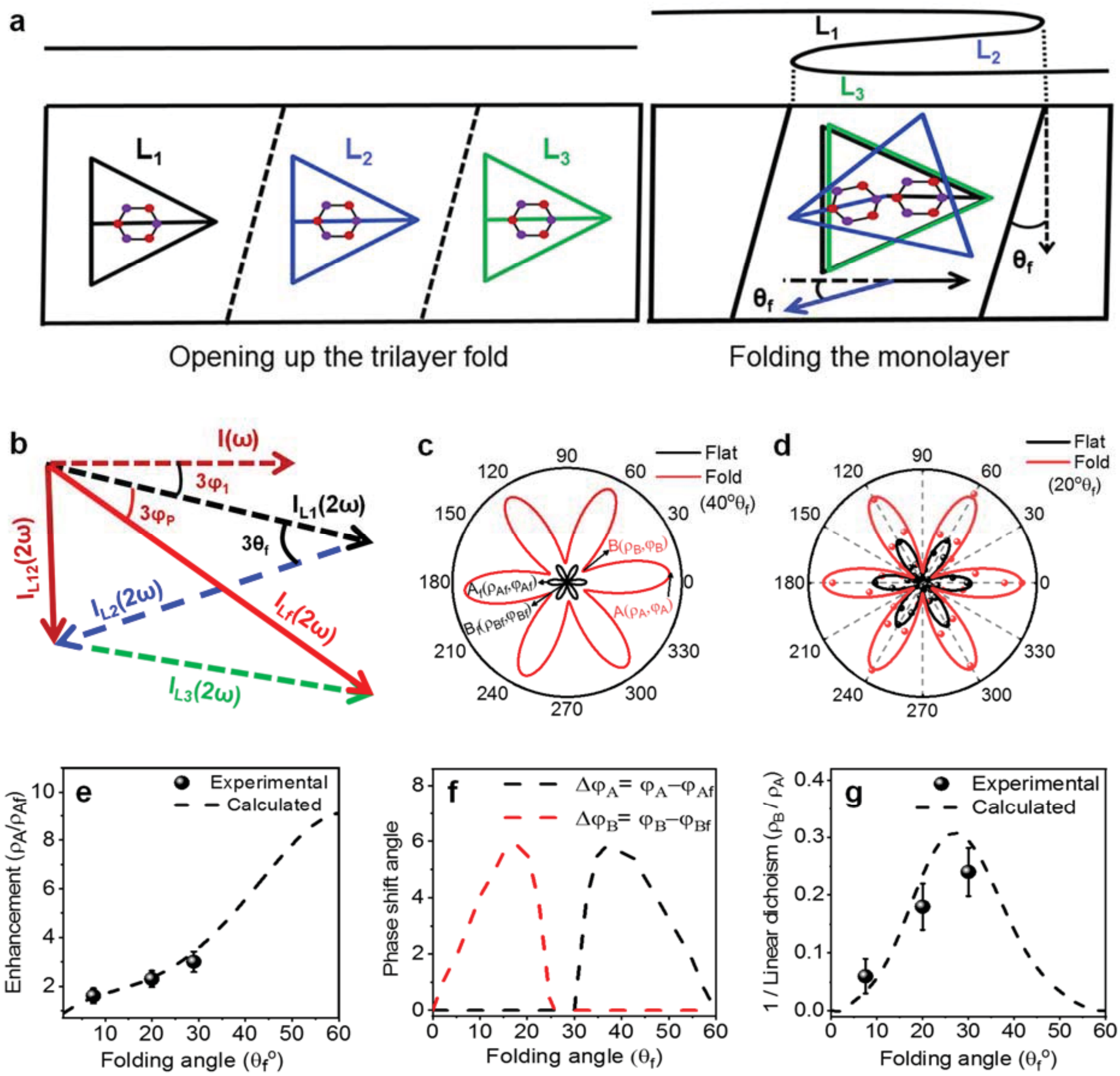

Figure 4.2 | Engineering SHG through folding of atomically thin TMDs.
(a) A schematic illustration for the stacking of layers in a trilayer fold (*1L+1L+1L*). The top (layer 1) and bottom layer (layer 3) are parallel to each other, whereas armchair direction of mid layer (layer 2) makes an angle of (180+θ_f) with the armchair direction of top and bottom layer. [The lines (black, blue and green) bisecting the triangles (black, blue and green) show the armchair direction] (b) Vector superposition of the SH fields from the layer of the fold, where $I_{L1}(2\omega)$ (black line), $I_{L2}(2\omega)$ (blue line) and $I_{L3}(2\omega)$ (green line) are the SH wave vectors from L_1, L_2 and L_3 respectively, $I(\omega)$ (brown line) is the laser wave vector and $I_{Lf}(2\omega)$ is the resultant SH wave vector from the fold. $3\varphi_1$ is the phase shifting angle between input linearly polarized laser and $I_{L1}(2\omega)$ whereas $3\varphi_P$ is the phase shifting angle between $I_{L1}(2\omega)$ and $I_{Lf}(2\omega)$. (c) Calculated SHG $I_{II}(2\omega)$ polar response for 1L flat and fold (40°θ_f). A(ρ_A, φ_A) is the maximum SHG (ρ_A) amplitude point for the fold with φ_A (degrees) angle from 0° whereas B(ρ_B, φ_B) is the minimum SHG (ρ_B) amplitude point for the fold with φ_B (degrees) angle from 0°. A_f (ρ_{Af}, φ_{Af}) and B_f (ρ_{Bf}, φ_{Bf}) represent the maximum and minimum point of the flat region. (d) Experimental investigation of polarization resolved SHG $I_{||}(2\omega)$ intensity pattern for 1L flat and folded WS_2. Continuous lines are the fitted plots, whereas symbols are experimental data points. (e) The folding angle dependence of SHG phase shift angle (degrees) (f) The folding angle dependence of SHG enhancement for fold, where enhancement= ρ_A / ρ_{Af}. (g) The folding angle dependence of (Linear dichrisom)$^{-1}$ where (Linear dichrisom)$^{-1}$ = ρ_B / ρ_A. Dashed line is the

calculated response whereas spherical symbols are the experimental data points. Error bars represent the range of error in the measured values.

Using the above scheme, the angular SHG response of folded region [$I_{Lf}(2\omega)$] with θ_f = 40° is calculated as shown in **Figure 4.2c** where $A(\rho_A, \varphi_A)$ is the maximum amplitude point of SHG (ρ_A) for the fold with φ_A (degrees) angle from horizontal (0°) whereas $B(\rho_B, \varphi_B)$ is the minimum SHG (ρ_B) amplitude point for the fold with φ_B (degrees) angle from horizontal. $A_f(\rho_{Af}, \varphi_{Af})$ and $B_f(\rho_{Bf}, \varphi_{Bf})$ represent the maximum and minimum points of the flat region. Here, φ_{Af} and φ_{Bf} represent AC (armchair) direction at 0° and ZZ (zigzag) direction at 30° because we are using parallel polarization for SHG.

In order to experimentally investigate the polarization dependent SHG response of folded region, we put a polarizer in between sample and spectrometer in such a position that the polarization component of the SH radiation is parallel to the polarization state of the incident laser (900nm)i.e parallel polarization of SHG (see methods section for more details). We get an enhanced (~2.6) SHG polar response from the folded region (θ_f = 20°) along the armchair direction as demonstrated in **Figure 4.2d** (See supplementary section **S4** for folding angle determination). As folding angle is expected to tune SHG intensity coming from the fold, we calculate SHG enhancement factor = ρ_A/ρ_{Af} as indicated by the dashed line as shown in **Figure 4.2e.** The calculated angular SHG response shows 1 to 9 times SHG enhancement as θ_f goes from 0° to 60°. The experimental results are found in good agreement with the calculated values which shows the validity of our model predictions. Phase shifting angle of folded region is the angular variation in waveform of folded region w.r.t flat region. This measurement can be important in order to optimize the device performance. We, therefore, calculate the phase shifting angles as follow; (i) $\Delta\varphi_A = \varphi_A - \varphi_{Af}$ and (ii) $\Delta\varphi_B = \varphi_B - \varphi_{Bf}$. A maximum phase shift of 6° is found at 20° and 40° for $\Delta\varphi_B$ and $\Delta\varphi_B$ respectively as shown in **Figure 4.2f.** However, phase shifting angles are too small to be detected accurately within the resolution limit of our experimental setup. An anisotropy response of SHG intensity is expected to be influenced by folding angle, therefore, we are interested to calculate (linear dichroism (LD))$^{-1}$ = ρ_{B} / ρ_{A} which shows a maximum value of 0.3 at 30^{o} θ_f as shown in **Figure 4.2g.** Experimental investigation shows good agreement with the model prediction. The above results thus establish SHG as a powerful technique to monitor folds in atomically thin WS_2.

4.4 SHG investigation of strained wrinkles

In the previous section, we showed that the wrinkles on 5L do not collapse and maintain their wrinkles' like curvature; therefore, SHG response of wrinkles is expected to be influenced by the local strain vector. In this context, we run polarization-dependent SHG on the flat and winkled regions (P_1 and P_2) of 5L WS_2 (**Figure 4.3a-4.3c)** using pump 830nm laser which is initially aligned with the armchair direction of the flat region. Similar to 1L, we get a uniform six-fold SHG polar pattern from flat 5L WS_2 due to D_{3h} symmetry (**Figure 4.3a)**.

On the other hand, we get a distortion in SHG polar pattern on strain induced wrinkles (P_1 and P_2) as shown in **Figure 4.3b-c.** In order to understand SHG polar pattern evolution for strain induced wrinkles, we consider photoelastic effect, an established approach,[17] for the explanation of SHG polar pattern evolution under strain. Let's take the case of odd layer WS_2 (D_{3h} symmetry) under uniaxial strain ε along the horizontal direction as depicted in **Figure 4.3d**.

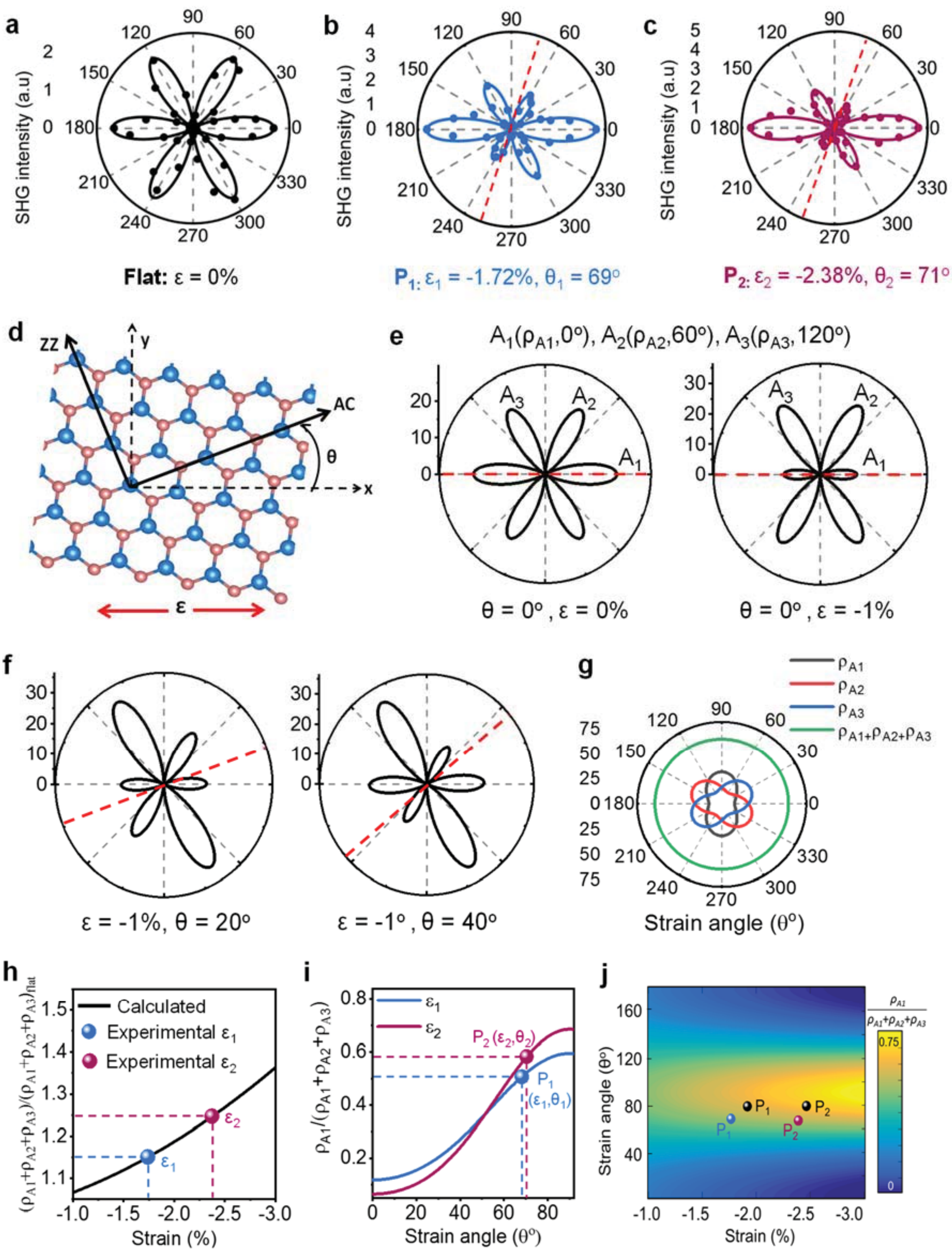

Figure 4.3 | Determination of strain vector by angle resolve SHG

(a) Experimental investigation of polarization resolved SHG intensity $I_{ll}(2\omega)$ pattern for for flat (b) P_1 wrinkle (c) P_2 wrinkle of 5L WS_2. Continuous lines are the fitted plots, whereas symbols are experimental data points. Red dashed line indicates the direction of strain. Determination of strain amplitude and direction is given in the following figures. (d) A schematic illustration to show the uniaxial strain ε applied along the horizontal direction with θ° strain angle between strain direction and AC (armchair) direction. Tensile strain and compressive strain are indicated by positive and negative signs respectively. ZZ: zigzag.

(e) Calculated polar response of SHG intensity $I_{ll}(2\omega)$ for WS_2 at the strain levels of 0% and -1% (0° strain angle). $A_1(\rho_{A1},0^o)$, $A_2(\rho_{A2},60^o)$ and $A_3(\rho_{A3},120^o)$ are three points with SHG intensity of ρ_{A1}, ρ_{A2} and ρ_{A3} in 0°, 60° and 120° direction with respect to horizontal direction. SHG intensity reduces and increases in the direction along and perpendicular to the compressive strain vector. (f) Calculated SHG I_{ll} (2ω) polar response of WS_2 at strain angles of 20° and 40° (ε= -1%). (g) Calculated strain angle dependent $\rho_{A1}, \rho_{A2}, \rho_{A3}$ and $\rho_{A1}+\rho_{A2}+\rho_{A3}$ (ε= -1%) (h) Strain dependent calculated ratio of $\rho_{A1}+\rho_{A2}+\rho_{A3}$ and $(\rho_{A1}+\rho_{A2}+\rho_{A3})_{\text{flat}}$ i.e $(\rho_{A1}+\rho_{A2}+\rho_{A3}) / (\rho_{A1}+\rho_{A2}+\rho_{A3})_{\text{flat}}$, $\varepsilon_1 = -1.72\%$ (blue sphere) and $\varepsilon_2 = -2.38\%$ (plum sphere) represent two strain values extracted from P_1 and P_2 wrinkles' SHG polar plots shown in Figure 4.3a-c where $(\rho_{A1}+\rho_{A2}+\rho_{A3}) / (\rho_{A1}+\rho_{A2}+\rho_{A3})_{\text{flat}} = 1.15$ and 1.25 for P_1 and P_2. (i) Strain angle (θ°) dependent calculated $\rho_{A1} / (\rho_{A1}+\rho_{A2}+\rho_{A3})$ for ε_1 (blue line) and ε_2 (plum line). $\theta_1 = 69^o$ (blue sphere) and $\theta_2 = 71^o$ (plum sphere) represent strain angles extracted from P_1 and P_2 SHG polar plots where $\rho_{A1} / (\rho_{A1}+\rho_{A2}+\rho_{A3}) = 0.51$ (P_1) and 0.58 (P_2). (j) SHG contour map showing strain (%) and strain angle (θ°) of P_1 (blue sphere) and P_2 (plum sphere) wrinkles extracted from SHG polar plots solely. The measured strain and strain angle using combination of AFM and SHG are displayed as black spheres for the comparison.

Strain angle (θ^o) is defined as the angle between strain direction and AC (armchair) direction. The parallel polarized SHG intensity "$I_{//}(2\omega)$" under uniaxial strain ε for D_{3h} symmetry class considering photoelastic effect, is;[17]

$$I_{//}(2\omega) \propto \frac{1}{4}\left(A\cos(3\varphi) + B\cos(2\theta + \varphi)\right)^2 \qquad (3)$$

where $A = (1 - v)(p_1 + p_2)(\varepsilon_{xx} + \varepsilon_{yy}) + 2\chi_o$ and $B = (1 + v)(p_1 - p_2)(\varepsilon_{xx} - \varepsilon_{yy})$, p_1 and p_2 are the photoelastic coefficients, ε_{xx} and ε_{yy} are the values of the strain(%) along x and y direction where tensile strain and compressive values are taken as positive and negative respectively, v is the Poisson ratio, φ is the polarization angle and χ_0 is the nonlinear susceptibility parameter of the unstrained crystal lattice. Because the wrinkles' formation occurs due to the inward compressive forces, therefore, the polar SHG response is calculated for 0% and -1% strain amplitude (at θ=0°) using Poisson ratio of $v_{(WS_2)} = 0.22$[18], $p_1 = 0.75$ nm/V/%[19], $p_2 = -0.97$ nm/V/%[19] and $\chi_0 = 4.5$ nm/V[20] (**Figure 4.3e**).

SHG quenching and enhancement is found in the direction parallel and perpendicular respectively to the strain direction. The quenching and enhancement in their respective directions increase with the strain amplitude. The pattern's distortion is associated with the direction of compressive strain vector as demonstrated for variable strain angles (20°, 40°) in **Figure 4.3f**. If $A_1(\rho_{A1},0^o)$, $A_2(\rho_{A2},60^o)$ and $A_3(\rho_{A3},120^o)$ represent three points with SHG intensity of ρ_{A1}, ρ_{A2} and ρ_{A3} along three AC directions $\varphi = 0^o$, 60^o and 120^o respectively **(Figure 4.3e)**, we find an invariable total SHG intensity $(\rho_{A1}+\rho_{A2}+\rho_{A3})$ irrespective of the strain angle **(Figure 4.3g)**. As the total SHG intensity $(\rho_{A1}+\rho_{A2}+\rho_{A3})$ remains constant for each value of strain angle, we can use this finding to calculate strain dependent $(\rho_{A1}+\rho_{A2}+\rho_{A3})/(\rho_{A1}+\rho_{A2}+\rho_{A3})_{\text{flat}}$ to extract $\varepsilon_1 = -1.72\%$ and $\varepsilon_2 = -2.38\%$ from SHG polar plots of P_1 and P_2 wrinkles **(Figure 4.3h)**. Hereafter, we calculate strain angle dependent $\rho_{A1} / (\rho_{A1}+\rho_{A2}+\rho_{A3})$ for ε_1 and ε_2 values as shown in **Figure 4.3i** to extract $\theta_1 = 69^o$ and $\theta_2 = 71^o$ from SHG polar plots. The extracted values are displayed in a contour plot **(Figure 4.3j)**. Extracted values of strain angle are very close to each other because the wrinkles (on the same sample) are parallel to each other. Using the extracted values of strain vector, we find that SHG polar plots **(Figures 4.3b-c)** fit well to photoelastic behaviour and degree of distortion relates well with the extracted values of strain vector. In order to validate our model calculations, we use AFM and polarization dependent SHG to measure the strain ε_{xx} (%) and the strain angle (θ^o) respectively for the selected wrinkles (See section S6 and S7 for more details). The measured values (black spheres in **Figure 4.3j**) show good agreement with the extracted measurements from SHG polar plots using the scheme given in **Figure 4.3a-i**. Conventionally, the strain direction and amplitude measurements require the combination of multiple tools, such as AFM and polarization dependent SHG are required for these measurements in our case. However, SHG as a single powerful tool has the potential to probe strain amplitude and direction in 2D materials.

4.5 Wavelength dependent SHG of folds and wrinkles

SHG response is expected to be influenced by variation in laser wavelength, therefore, we run laser excitation wavelength dependence ($810 \leq \lambda \leq 950$nm) on the flat, folded and wrinkled regions of ultrathin WS_2 (**Figure 4.4a-c**). Here, we find SHG peak centered at 870-880nm laser wavelength (or 435-440nm of SHG wavelength) in wavelength dependent SHG for 1L flat region (**Figure 4.4b**). The peak position is attributed to the resonance phenomenon due to the presence of C-exciton.[13,21] (**Figure 4.4d**). Wavelength dependent SHG response of 1L folds shows SHG enhancement at all the wavelengths scanned (**Figure 4.4b**). Recently, SHG is found highly sensitive towards strain according to the recent research.[22] This sensitive behavior is shown by significant (49%) SHG quenching per 1% strain in atomically thin $MoSe_2$.[22] Such highly sensitive behavior is also reported for MoS_2.[17] However, no study is reported on the origin of such sensitivity of SHG towards strain in 2D TMDs. Wavelength dependent SHG of strain induced 5L wrinkles show a remarkable blue shift in exciton resonance SHG peak (**Figure 4.4c**). This shift in SHG peak position appears to be dependent on strain amplitude. The shift in SHG peak position is attributed to the strain dependent shift in C-exciton resonance which is consistent with the literature.[23]

In order to further explain the origin of this shift, we employed first-principles density functional theory (DFT) using simulation code Abinit to calculate the strain dependent wavelength dependent second order non-linear susceptibility $I\chi$ ($-2\omega, \omega, \omega$) of 5L WS_2 (See Methods section **Appendix A2** for more details). Tensile strain causes red shifting of SHG peak whereas compressive strain results in blue shifting of SHG peak position. The simulation results show a remarkable shift in SHG peak position (in resonance with C-exciton) upon strain (%) as shown in **Figure 4.4e-f** which is ~ 12.5 nm / Strain (%).

The experimental measurements show a shift ~ 15 nm / Strain (%) which agrees well with the simulation results. Hence, wavelength dependent SHG clarifies the origin of resonance enhanced SHG peak shift in strain induced wrinkles thus provides another way to characterize fold and wrinkle nanostructures.

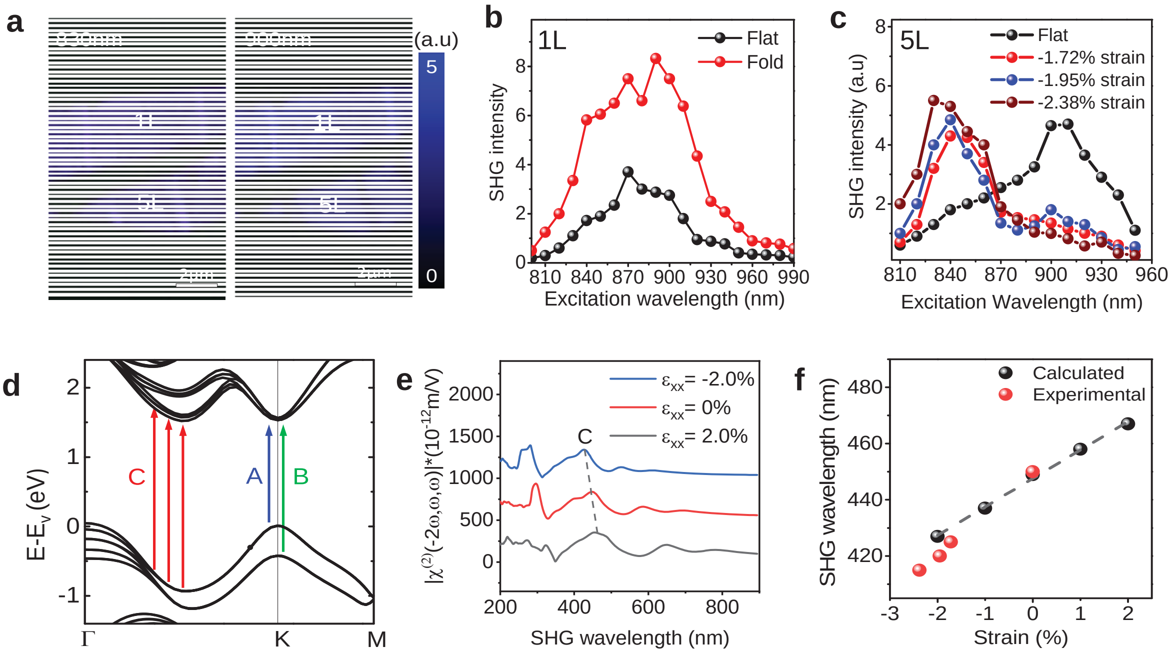

Figure 4.4 | Differentiation of folds and wrinkles through wavelength dependent SHG
(a) SHG intensity mapping of 1L folds and 5L wrinkles for 830 nm and 900 nm. 1L folds show an enhancement on both the excitation wavelengths scanned whereas WS_2 wrinkles show an enhancement and reduction in SHG intensity at 830 nm and 900nm respectively. (b) Excitation wavelength dependent SHG intensity of folded and flat regions of 1L WS_2. Folds show an enhancement at all the wavelengths scanned. (c) Excitation wavelength dependent SHG of flat and strain induced (-1.72%, -1.95% and -2.38%) wrinkled regions of 5L WS_2. SHG peak blue shifts with the compressive strain. (d) The band structure of 5L WS2 with the label of C calculated by the DFT. The arrows indicate the transition in A, B and the band nesting (C) (e) The wavelength dependent second order non-linear susceptibility ($I\chi$) spectra of 5L WS2 for three Strain (-2%, 0%, 2%) levels. Spectra are vertically shifted by 500nm and 1000nm for improved visibility. The C-exciton resonance enhanced SHG peak position is indicated by C. (f) The strain dependent SHG peak wavelength (in resonance with C exciton). Black colour and red colour spheres represent calculated and experiments values respectively. Black dashed line is the linear fit of the calculated values.

4.6 Chapter summary

In summary, we have shown SHG as a sensitive and powerful tool to investigate the folding angle and strain angle accurately in 2D WS_2. Here, for the first time, we use polarization dependent SHG technique to measure folding angle and strain vector in atomically thin tungsten disulphide (WS_2). Trilayer folds are found to show 9 times SHG enhancement due to the vector superposition of SH wave vectors coming from the individual layers of the fold with 60^o folding angle. We find strain dependent SHG quenching and enhancement in the direction parallel and perpendicular respectively to the direction of the compressive strain vector. However, despite a variation in strain angle, total SHG remains constant which allow us to find the local strain vector using photoelastic approach. We also demonstrate that band-nesting induced transition (C peak) can highly enhance SHG, which can be significantly modulated by strain. Our results present an important advance, with applications in nonlinear optical devices.

Chapter 4 References

(1) Castellanos-Gomez, A.; Roldán, R.; Cappelluti, E.; Buscema, M.; Guinea, F.; Van Der Zant, H. S. J.; Steele, G. A. Local Strain Engineering in Atomically Thin MoS2. *Nano Lett.* **2013**, *23* (11), 534.

(2) Liu, Z.; Amani, M.; Najmaei, S.; Xu, Q.; Zou, X.; Zhou, W.; Yu, T.; Qiu, C.; Birdwell, A. G.; Crowne, F. J.; et al. Strain and Structure Heterogeneity in MoS2 Atomic Layers Grown by Chemical Vapour Deposition. *Nat. Commun.* **2014**, *5* (1), 5246.

(3) Hsu, W.-T.; Zhao, Z.-A.; Li, L.-J.; Chen, C.-H.; Chiu, M.-H.; Chang, P.-S.; Chou, Y.-C.; Chang, W.-H. Second Harmonic Generation from Artificially Stacked Transition Metal Dichalcogenide Twisted Bilayers. *ACS Nano* **2014**, *8* (3), 2951–2958.

(4) Shinde, S. M.; Dhakal, K. P.; Chen, X.; Yun, W. S.; Lee, J.; Kim, H.; Ahn, J.-H. Stacking-Controllable Interlayer Coupling and Symmetric Configuration of Multilayered MoS2. *NPG Asia Mater.* **2018**, *10* (2), e468–e468.

(5) Wang, H.; Qian, X. Giant Optical Second Harmonic Generation in Two-Dimensional Multiferroics. *Nano Lett.* **2017**, *17* (8), 5027–5034.

(6) Li, Y.; Rao, Y.; Mak, K. F.; You, Y.; Wang, S.; Dean, C. R.; Heinz, T. F. Probing Symmetry Properties of Few-Layer MoS2 and h-BN by Optical Second-Harmonic Generation. *Nano Lett.* **2013**, *13*, 3329–3333.

(7) Castellanos-Gomez, A.; van der Zant, H. S. J.; Steele, G. A. Folded MoS2 Layers with Reduced Interlayer Coupling. *Nano Res.* **2014**, *7* (4), 572–578.

(8) Pei, J.; Yang, J.; Xu, R.; Zeng, Y.-H.; Myint, Y. W.; Zhang, S.; Zheng, J.-C.; Qin, Q.; Wang, X.; Jiang, W.; et al. Exciton and Trion Dynamics in Bilayer MoS 2. *Small* **2015**, *11* (48), 6384–6390.

(9) Pei, J.; Yang, J.; Yildirim, T.; Zhang, H.; Lu, Y. Many-Body Complexes in 2D Semiconductors. *Adv. Mater.* **2019**, *31* (2), 1706945.

(10) Xu, R.; Yang, J.; Zhu, Y.; Yan, H.; Pei, J.; Myint, Y. W.; Zhang, S.; Lu, Y. Layer-Dependent Surface Potential of Phosphorene and Anisotropic/Layer-Dependent Charge Transfer in Phosphorene-Gold Hybrid Systems. *Nanoscale* **2016**, *8*, 129–135.

(11) Yang, J.; Wang, Z.; Yu, Z.; Lu, Y. Manipulating Optical Beam Flow Fronts in 2D Materials. *SPIE Newsroom* **2016**.

(12) Rose, A.; Smith, D. R. Overcoming Phase Mismatch in Nonlinear Metamaterials [Invited]. *Opt. Mater. Express* **2011**, *1* (7), 1232.

(13) Malard, L. M.; Alencar, T. V.; Barboza, A. P. M.; Mak, K. F.; De Paula, A. M. Observation of Intense Second Harmonic Generation from MoS2atomic Crystals. *Phys. Rev. B - Condens. Matter Mater. Phys.* **2013**, *87* (20), 1–5.

(14) Le, C. T.; Clark, D. J.; Ullah, F.; Senthilkumar, V.; Jang, J. I.; Sim, Y.; Seong, M. J.; Chung, K. H.; Park, H.; Kim, Y. S. Nonlinear Optical Characteristics of Monolayer MoSe2. *Ann. Phys.* **2016**, *528* (7–8), 551–559.

(15) Shi, J.; Yu, P.; Liu, F.; He, P.; Wang, R.; Qin, L.; Zhou, J.; Li, X.; Zhou, J.; Sui, X.; et al. 3R MoS 2 with Broken Inversion Symmetry: A Promising Ultrathin Nonlinear Optical Device. *Adv. Mater.* **2017**, *29* (30), 1701486.

(16) Zhang, Y.; Zhang, Y.; Ji, Q.; Ju, J.; Yuan, H.; Shi, J.; Gao, T.; Ma, D.; Liu, M.; Chen, Y.; et al. Controlled Growth of High-Quality Monolayer WS 2 Layers on Sapphire and Imaging Its Grain Boundary. *ACS Nano* **2013**, *7* (10), 8963–8971.

(17) Mennel, L.; Furchi, M. M.; Wachter, S.; Paur, M.; Polyushkin, D. K.; Mueller, T. Optical Imaging of Strain in Two-Dimensional Crystals. *Nat. Commun.* **2018**, *9* (1), 516.

(18) Liu, K.; Yan, Q.; Chen, M.; Fan, W.; Sun, Y.; Suh, J.; Fu, D.; Lee, S.; Zhou, J.; Tongay, S.; et al. Elastic Properties of Chemical-Vapor-Deposited Monolayer MoS 2 , WS 2 , and Their Bilayer Heterostructures. *Nano Lett.* **2014**, *14* (9), 5097–5103.

(19) Mennel, L.; Paur, M.; Mueller, T. Second Harmonic Generation in Strained Transition Metal Dichalcogenide Monolayers: MoS 2 , MoSe 2 , WS 2 , and WSe 2. *APL Photonics* **2019**, *4* (3), 034404.

(20) Janisch, C.; Wang, Y.; Ma, D.; Mehta, N.; Elías, A. L.; Perea-López, N.; Terrones, M.; Crespi, V.; Liu, Z. Extraordinary Second Harmonic Generation in Tungsten Disulfide Monolayers. *Sci. Rep.* **2014**, *4* (c), 1–5.

(21) Zhu, B.; Chen, X.; Cui, X. Exciton Binding Energy of Monolayer WS2. *Sci. Rep.* **2015**, *5* (1), 9218.

(22) Liang, J.; Zhang, J.; Li, Z.; Hong, H.; Wang, J.; Zhang, Z.; Zhou, X.; Qiao, R.; Xu, J.; Gao, P.; et al. Monitoring Local Strain Vector in Atomic-Layered MoSe2 by Second-Harmonic Generation. *Nano Lett.* **2017**, *17* (12), 7539–7543.

(23) Frisenda, R.; Drüppel, M.; Schmidt, R.; Michaelis de Vasconcellos, S.; Perez de Lara, D.; Bratschitsch, R.; Rohlfing, M.; Castellanos-Gomez, A. Biaxial Strain Tuning of the Optical Properties of Single-Layer Transition Metal Dichalcogenides. *npj 2D Mater. Appl.* **2017**, *1* (1), 10.

5 TEMPERATURE DEPENDENT SECOND HARMONIC GENERATION IN ULTRATHIN TMDS

5.1 Introduction

Temperature is found to alter optoelectronic properties such as bandgap modulation[1], variation in phonon modes[2–5], tuning in carrier mobility[6] in 2D TMDs. Therefore, it is important to investigate the layer dependent thermal variation in 2D TMDs in order to better control and optimize the performance of electronic devices. As discussed, optical second-harmonic generation (SHG) is sensitive lattice symmetry[7], lattice variation[8] and strain direction and intensity[9–11] in 2D layered materials. Thermal variation causes significant structural variation in 2D materials, thus making SHG a potentially useful and powerful tool to investigate temperature changes in 2D materials. Here, we show SHG a highly sensitive tool to investigate the thermal variation in ultrathin TMDs. An opposite SHG response is found for single layer and few odd layers (3L, 5L, 7L, etc) of TMDs. A remarkable SHG enhancement (25.8%) is found in single layer $MoSe_2$ with rise in temperature. On the other hand, few odd layers show considerable temperature dependent SHG quenching for 3L (-55.2%), 5L(-31.02%) and 7L(-18.4%) of MoSe2. Other TMD materials i.e. MoS_2, WS_2 and WSe_2 show the similar trend which reveals an important structural characteristic for TMDs. Non-linear susceptibility calculations considering thermal expansion behaviour for single layer and few layers TMD explains the layer dependent temperature dependent SHG behaviour, which shows good agreement with the experimental findings. Our results show SHG a powerful and sensitive probe to monitor thermal variation in layered TMDs.

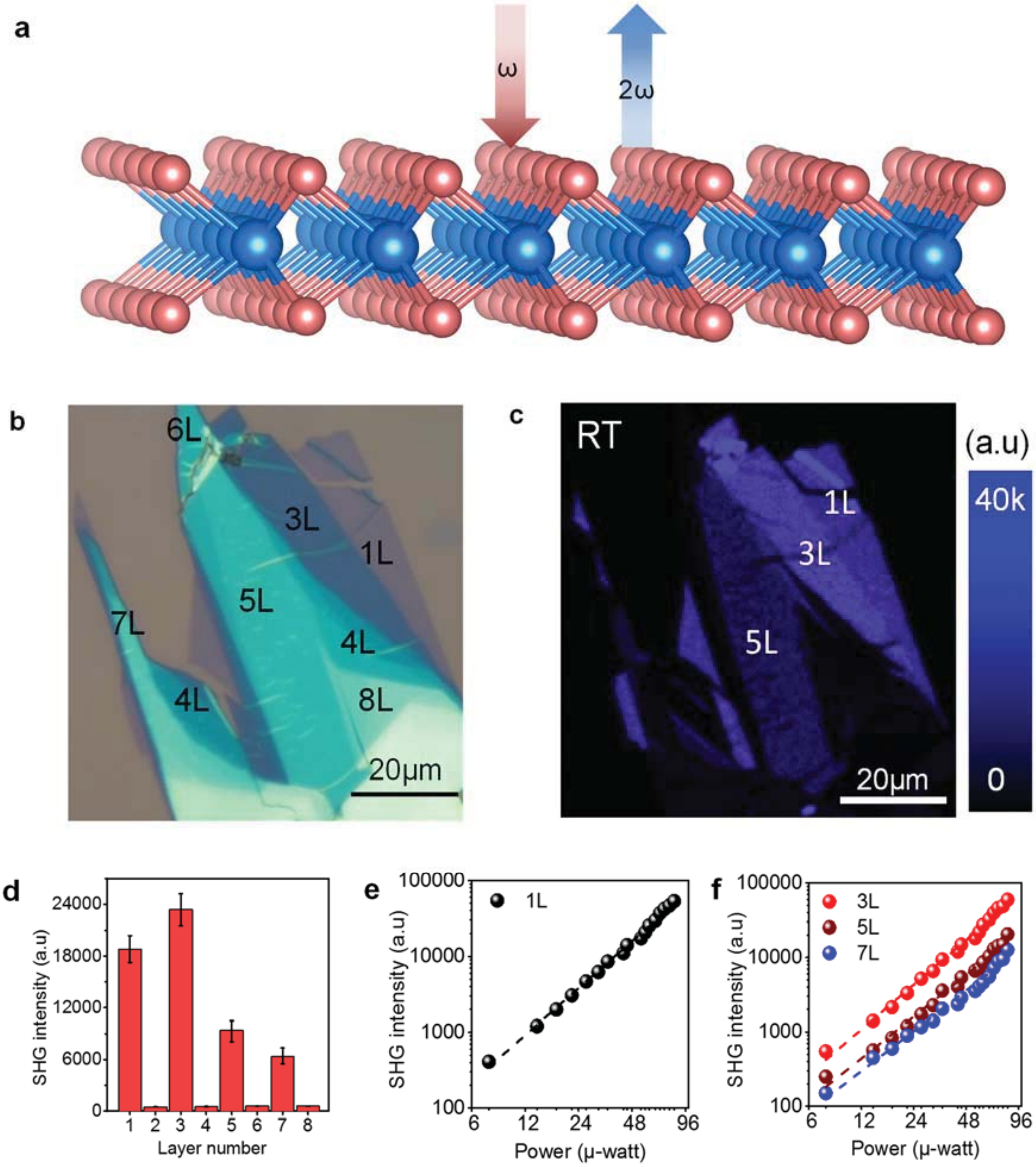

Figure 5.1 | Layer Dependent Second Harmonic Generation in $MoSe_2$.
(a) Schematic illustration of the SHG process, two photons of the same frequency ω merge into a single photon with double frequency 2ω. (b) Optical microscopic Image of 1-8L $MoSe_2$ for Second Harmonic Generation (SHG) mapping. (c) SHG image of (b) showing the layer dependent SHG response (laser excitation: 900nm). (d) Column chart showing layer dependent SHG response of 1-8L $MoSe_2$. Histogram shows the SHG intensity response, with variation in measurements is indicated by the error bars. (e) Power

dependent SHG of 1L and (f) 3L, 5L and 7L. (Note: All the SHG measurements are taken at 900nm laser excitation.)

5.2 Layer dependent SHG in Molybdenum selenide

In our experiment, few-layered $MoSe_2$ flakes are mechanically exfoliated onto a Si/SiO2 (275 nm) chip substrate using a scotch tape as indicated in[12–14]. $MoSe_2$ layers are identified by their colour contrast on an optical microscope as shown in **Figure 5.1b**. Variable colours contrast indicate height variation. Phase-shifting interferometry (PSI)[15–20] is used to identify the layer number of ultrathin $MoSe_2$ as shown in **Figure A5.1a and A5.1b**. Confocal light microscope (Zeiss 780) with 900 nm laser excitation is employed for Second Harmonic Generation (SHG) (see **Annexure A3** section for more details). SHG mapping of 1-8L $MoSe_2$ at room temperature (RT) is done in order to check the layer dependent SHG response as shown in **Figure 5.1c.**

Even layers of $MoSe_2$ belong to the centrosymmetric D_{3d} space group, whereas odd layer number belongs to the non-centrosymmetric D_{3h} space group, therefore, we get SHG signal from odd layer number, i.e. 1L, 3L,5L and 7L and we do not get SHG response from even layer number, i.e. 2L, 4L, 6L and 8L (**Figure 5.1d**), consistent with the previous studies[7,9,21,22] which show SHG a sensitive probe to lattice symmetry. As SHG shows quadratic scaling behavior[23–26], therefore, power dependent SHG measurements are performed for all the odd layers (1L, 3L, 5L and 7L) in order to confirm the existence of SH photons. The corresponding SHG signal responses for each odd layer were drawn with excitation power on a log scale[27] as shown in **Figure 5.1e** and **Figure 5.1f**. The obtained slope values ~2.0 confirm the SHG.

5.3 Temperature dependent SHG in layered Molybdenum selenide

In order to determine the temperature dependent SHG behaviour, temperature controller equipped with liquid Nitrogen and heating source is used to tune the temperature of the sample (for more details see Methods section **Appendix A3**). SHG intensity mappings are performed at variable temperature settings ranging from -130°C to 110°C for 1-8L $MoSe_2$ using 900 nm laser excitation as shown in **Figure 5.2a-c**.

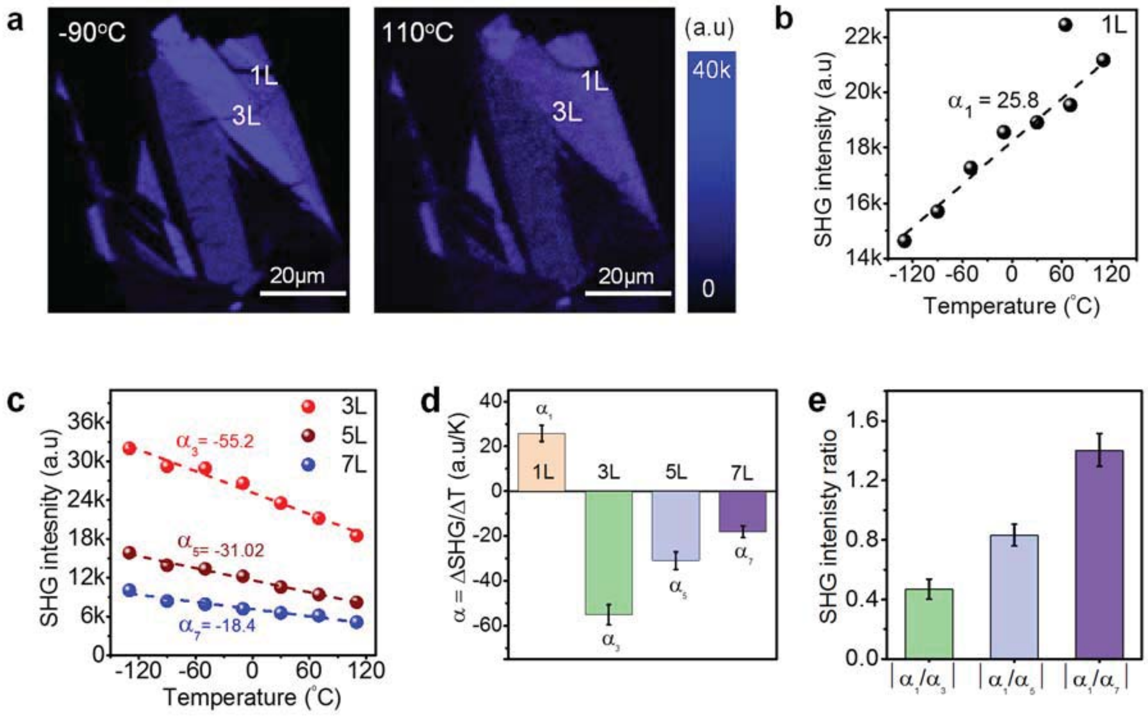

Figure 5.2 | Temperature Dependent SHG of Layered $MoSe_2$.
(a) Second Harmonic mapping of 1-8L $MoSe_2$ sample at -90°C and 110°C. (b) Temperature dependent SHG response of 1L and (c) 3L, 5L, 7L where dashed lines indicate the linear fits and α_1, α_3, α_5 and α_7 indicate the slopes of the linear fit dashed lines for 1L, 3L, 5L and 7L. (d) Layer dependent temperature dependent SHG slope values (α_1, α_3, α_5 and α_7). The variation in the measurements is indicated by the error bars. (e) SHG slope ratios (α_1/α_3), (α_1/α_5) and (α_1/α_7) for $MoSe_2$. (All the SHG measurements are taken at 900nm laser excitation.)

Even layers of $MoSe_2$ do not show SHG response at all scanned temperatures. Interestingly, single layer and few odd layers of $MoSe_2$ show opposite temperature dependent SHG behaviour. SHG intensity of 1L $MoSe_2$ increases with the temperature whereas few odd layers of $MoSe_2$ i.e. 3L, 5L and 7L show the opposite trend. The measured temperature dependence of SHG fits linearly and α_1, α_3, α_5, α_7 represent the slopes of the linear fitted lines for 1L, 3L, 5L and 7L. The measurements show $\alpha_1=25.8\pm3.5$ (brown), $\alpha_3=-55.2\pm4.5$ (green), $\alpha_5 = -31.02\pm4$ (blue) and $\alpha_7 = -18.2\pm3$ (purple) for $MoSe_2$ as shown in **Figure 5.2d** (variation in values is indicated by the error bars). SHG slopes ratios α_1/α_3 (green), α_1/α_5 (blue) and α_1/α_7 (purple) are shown in **Figure 5.2e** which show the increasing trend of α_1/α_n as layer number "n" increases.

5.4 Temperature dependent SHG in other TMDs

The temperature dependent SHG investigation indicates SHG is sensitive to thermal variation in $MoSe_2$. In order to find the temperature dependent SHG behaviour with other layer dependent TMDs, we perform temperature dependent layer dependent SHG measurements for layer dependent WSe_2, WS_2, and MoS_2 at the same laser excitation i.e. 900 nm (**Figure 5.3a-e**). SHG mappings indicate that temperature dependent SHG for others TMDs shows the similar behaviour like thermal investigation in $MoSe_2$. For instance, SHG response of 1L WSe_2 increases with the temperature whereas 3L WSe_2 show a decreasing SHG response (**Figure 5.3a-b**). Similarly, SHG intensity for higher few layers i.e. 5L, 7L decreases with the rise in temperature. Layer dependent WS_2 (**Figure 5.3c-d**) and MoS_2 (**Figure 5.3e**) show the similar trend. Here, we find the temperature dependent SHG slope values as under; $\alpha_1 = 63.12 \pm 7.00$, $\alpha_3 = -33.22 \pm 5.16$, $\alpha_5 = -29.74 \pm 4.98$ for WS_2, $\alpha_1 = 18.29 \pm 2.91$, $\alpha_3 = -25.72 \pm 3.93$, $\alpha_5 = -21.51 \pm 4.07$, $\alpha_7 = -14.02 \pm 3.28$ for WSe_2 and $\alpha_1 = 93.03 \pm 8.91$, $\alpha_3 = -57.99 \pm 6.84$, $\alpha_5 = -52.89 \pm 6.46$, $\alpha_7 = -43.97 \pm 4.22$ for MoS_2 (**Figure 5.3f).**

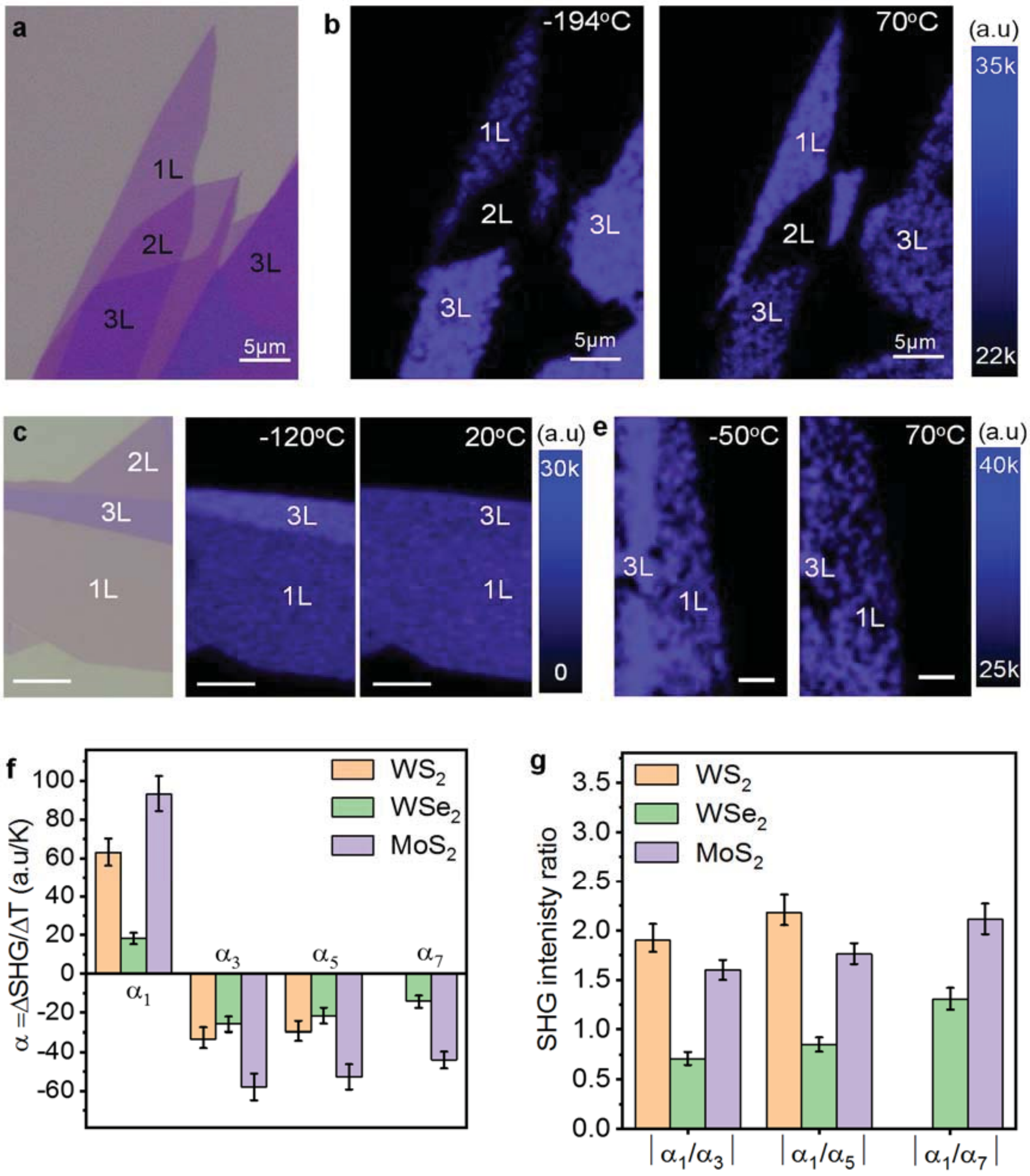

Figure 5.3 | Temperature Dependent SHG of other layered transition metal dichalcogenides (TMDs). (a) Optical microscope image of 1-3L WSe_2 sample used for SHG mapping. (b) Temperature dependent SHG mapping of WSe_2 at -194°C and 70 °C. (c) Optical microscope image of 1-3L WS_2 sample. (d) Temperature dependent SHG mapping of WS_2 sample at -120 °C and 20 °C. (e) Temperature dependent SHG mapping of the sample at -50°C and 70 °C. (Note: All Scale bars indicates 5 µm length, laser excitation = 900nm) (f) Layer dependent temperature dependent SHG slope values (α) for WS_2, WSe_2 and MoS_2. (g) SHG slope ratios for WSe_2, WSe_2 and $MoSe_2$. A variation in measurements is indicated by the error bars.

Temperature dependent SHG slope ratios (1L to 3L, 5L, 7L) indicate $\alpha_1/\alpha_3 = 1.9 \pm 0.165$, $\alpha_1/\alpha_5 = 2.18 \pm 0.18$ for WS_2, $\alpha_1/\alpha_3 = 0.71 \pm 0.068$, $\alpha_1/\alpha_5 = 0.85 \pm 0.075$ and $\alpha_1/\alpha_7 = 1.304$

± 0.115 for WSe_2, and $\alpha_1/\alpha_3 = 1.6 \pm 0.1$, $\alpha_1/\alpha_5 = 1.76 \pm 0.11$ and $\alpha_1/\alpha_7 = 2.11 \pm 0.16$ for MoS_2 as shown in **Figure 5.3g** which shown similar temperature dependent SHG behaviour for other TMDs. As Temperature dependent SHG behaviour for other TMDs is found similar and SHG response is sensitive to variation in lattice structure, SHG behaviour indicates an important structural characteristic for TMDs. Therefore, we explore the thermal expansion behaviour of TMDs to understand and explain the temperature dependent SHG in TMDs layers.

5.5 Simulations

The optical field of the SHG is proportional to the nonlinear optical susceptibility; therefore, the relation between SHG intensity and crystal lattice can be shown by calculating second order nonlinear susceptibility considering thermal expansion in layer dependent TMDs. In this regard, we employ first-principles density functional theory (DFT)[30] using simulation code Abinit to calculate the second order non-linear susceptibility $\mathbf{I\chi}$ (-2ω, ω, ω).[27]

Exchange-correlation function within the local density approximation (LDA)[31] and a k-point sampling for the Brillouin zone (BZ) integration are used . An energy cut-off of 52Ry for the plane-wave basis and a k-point sampling of 30×30×1 is applied in the simulation. A vacuum layer thicker than 10 Å is added to avoid the mirror interaction. Dynamical stability of the crystal structures is confirmed by phonon dispersion from density functional perturbation theory calculations. We speculate that thermal expansion behaviour in TMD layers might lead to the opposite SHG responses in 1L and few odd layers of TMDs. Few layers and bulk TMDs, with weak Van der Waals forces (X-X) between vertically stacked layers, show higher thermal expansion than 1L TMDs in interlayer direction.[32] Therefore, we consider Van der Waals gap during thermal expansion behaviour in few odd layers of TMDs. In 1L MoS_2, Vertical lattice parameter is represented by "***d***" or (S-Mo-S) bond length and horizontal lattice parameter is represented by "***a***" 1L MoS_2 (TMD) as shown in **Figure 5.4a.** Lattice parameters increase with the rise in temperature. Thermal expansion of the vertical lattice parameter (***d***) is reported to be greater than thermal expansion of horizontal lattice parameter **(*a*)**[33]. Therefore, we have calculated the second order non-linear susceptibility **I**χ (-2ω, ω, ω) (mV) of 1L MoS_2 for three cases; (i) free 1L MoS_2, (ii) 4% increase in ***d*** (iii) 1% increase in ***a***. DFT calculations show that non-linear susceptibility (***I****χ***)** decreases as horizontal lattice parameter **(*a*)** increases whereas non-linear susceptibility (***I****χ***)** shows an enhancement with increase in ***d*** **(Figure 5.4b)** which explains the SHG enhancement with temperature in 1L TMDs.

Few layers in TMDs are under the influence of interlayer attraction forces from other layers which are of Van der Waals' type.[34–37] Therefore, in comparison with 1L, few layers and bulk TMDs are reported with comparatively higher out-of-plane expansion coefficient as compared to in-plane expansion coefficient.[32,33] This directional dependence thermal expansion behaviour can lead to variable lattice symmetries for 1L and few odd layers of TMDs showing us the opposite SHG behaviour for 1L and few layers TMDs. This interlayer attraction due to S-S bond length is represented by Van der Waals' gap d_2 as shown in **Figure 5.4c.** On the other hand, d_1 indicates the vertical intralayer attraction due to S-M-S bond length. Van der Waals forces of attraction are considered weak forces of attraction as compared to intralayer forces of attraction, therefore, $\mathbf{d_2}$ is expected to increase considerably greater than $\mathbf{d_1}$ with temperature increase. We have calculated the second order non-linear susceptibility **I**χ (-2ω, ω, ω) (mV) for few layers of MoS_2 for three cases; (i) free few layer MoS_2, (ii) 4% increase in d_1 (iii) 8% increase in d_2. Non-linear susceptibility calculations show that **I**χ (-2ω, ω, ω) decreases as $\boldsymbol{d_2}$ increases for few layers MoS$_2$ as shown in **Figure 5.4d**. The considerable increase of $\boldsymbol{d_2}$ with temperature shows SHG quenching. Thus, the calculated results of 1L and few layers for temperature dependent second order non-linear susceptibility show good agreement with our experimental findings.

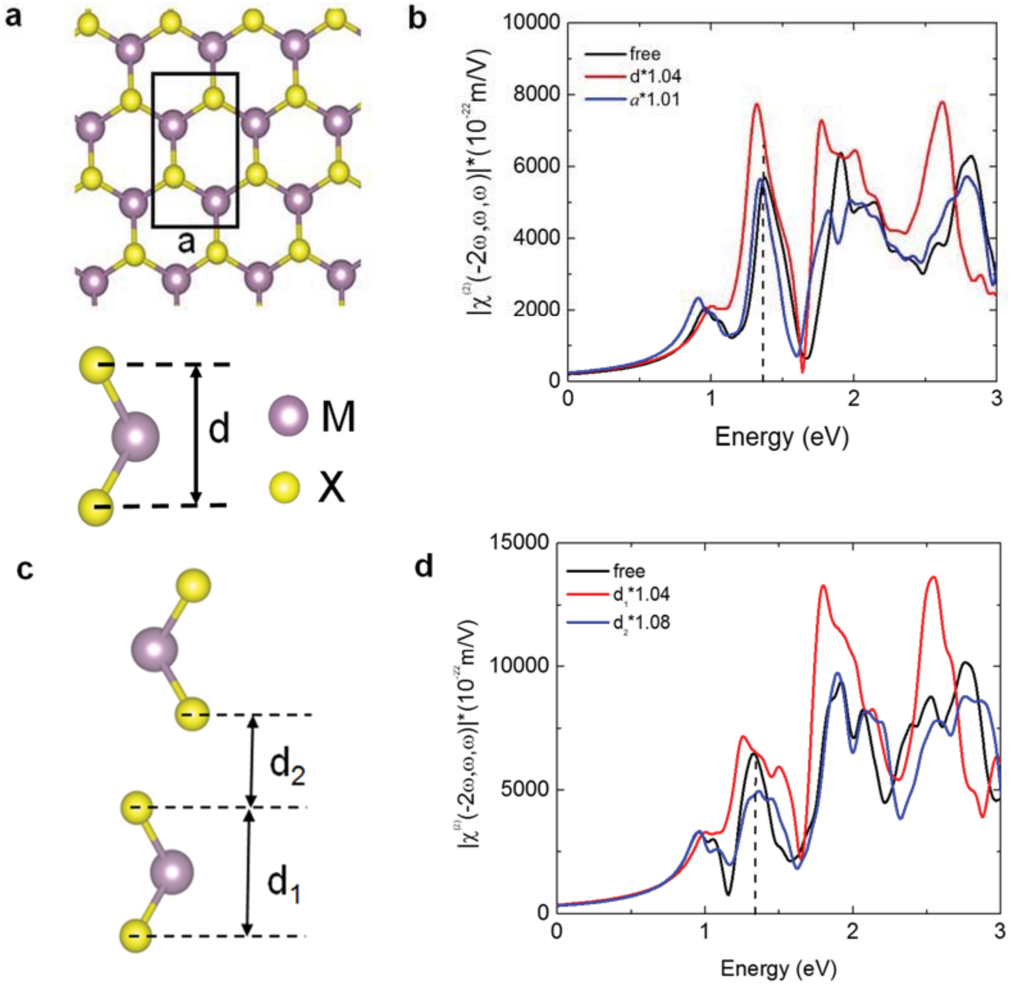

Figure 5.4 | Temperature dependent nonlinear susceptibilities in 1L and 3L of TMDs. (a) 1L MoS$_2$ (side view) showing intralayer attraction as represented by (S-M-S) bond length **d** (side view) and lattice constant **a** (top view). As temperature increases, **d** increases greater than **a**. **(b)** Second-order non-linear susceptibility calculation for 1L with 4% increase in **d** shows enhancement in non-linear susceptibility response as compared to free 1L. **(c)** Few layer MoS$_2$ showing intralayer attraction as represented by (S-M-S) bond length $\mathbf{d_1}$ and vander waal gap $\mathbf{d_2}$ between two layers. As temperature increases, $\mathbf{d_2}$ increases greater than $\mathbf{d_1}$. (d) Second-order non-linear susceptibility calculation for few layers with 8% increase in $\mathbf{d_2}$ shows quenching in non-linear susceptibility as compared to free few layers.

5.6 Chapter summary

In summary, we have shown SHG response is highly sensitive to temperature modulation in 2D TMD. Temperature variation in ultra-thin TMDs is found to tune SHG response which has variable trend for single layer and few odd layers (3L, 5L, 7L, etc) of TMDs. 1L $MoSe_2$ shows remarkable SHG enhancement (25.8%) in single layer $MoSe_2$ with temperature increase. On the other hand, few odd layers show considerable SHG quenching which is found to be -55.2%, -31.02% and -18.4% in case of 3L, 5L and 7L of $MoSe_2$. Other TMDs materials i.e. MoS_2, WS_2 and WSe_2 show the similar trend which reveals an important structural characteristic for TMDs. Second order non-linear susceptibility calculations considering weak Van der Waals forces during thermal expansion in ultrathin TMDs show good agreement with the experimental findings. Our results would pave the way to enable novel applications of TMDs in nonlinear optical devices.

Chapter 5 References

(1) Choi, B. K.; Kim, M.; Jung, K.-H.; Kim, J.; Yu, K.-S.; Chang, Y. J. Temperature Dependence of Band Gap in MoSe2 Grown by Molecular Beam Epitaxy. *Nanoscale Res. Lett.* **2017**, *12* (1), 492.

(2) Thripuranthaka, M.; Kashid, R. V.; Sekhar Rout, C.; Late, D. J. Temperature Dependent Raman Spectroscopy of Chemically Derived Few Layer MoS 2 and WS 2 Nanosheets. *Appl. Phys. Lett.* **2014**, *104* (8), 081911.

(3) Sahoo, S.; Gaur, A. P. S.; Ahmadi, M.; Guinel, M. J.-F.; Katiyar, R. S. Temperature-Dependent Raman Studies and Thermal Conductivity of Few-Layer MoS 2. *J. Phys. Chem. C* **2013**, *117* (17), 9042–9047.

(4) Sinha, S.; Sathe, V.; Arora, S. K. Temperature Dependent Raman Investigations of Few-Layered WS2 Nanosheets. *Solid State Commun.* **2019**, *298*, 113626.

(5) Mobaraki, A.; Sevik, C.; Yapicioglu, H.; Çakır, D.; Gülseren, O. Temperature-Dependent Phonon Spectrum of Transition Metal Dichalcogenides Calculated from the Spectral Energy Density: Lattice Thermal Conductivity as an Application. *Phys. Rev. B* **2019**, *100* (3), 035402.

(6) M, T.; Late, D. J. Temperature Dependent Phonon Shifts in Single-Layer WS 2. *ACS Appl. Mater. Interfaces* **2014**, *6* (2), 1158–1163.

(7) Li, Y.; Rao, Y.; Mak, K. F.; You, Y.; Wang, S.; Dean, C. R.; Heinz, T. F. Probing Symmetry Properties of Few-Layer MoS2 and h-BN by Optical Second-Harmonic Generation. *Nano Lett.* **2013**, *13*, 3329–3333.

(8) Zhao, M.; Ye, Z.; Suzuki, R.; Ye, Y.; Zhu, H.; Xiao, J.; Wang, Y.; Iwasa, Y.; Zhang, X. Atomically Phase-Matched Second-Harmonic Generation in a 2D Crystal. *Light Sci. Appl.* **2016**, *5* (8), e16131–e16131.

(9) Mennel, L.; Furchi, M. M.; Wachter, S.; Paur, M.; Polyushkin, D. K.; Mueller, T. Optical Imaging of Strain in Two-Dimensional Crystals. *Nat. Commun.* **2018**, *9* (1), 516.

(10) Liang, J.; Zhang, J.; Li, Z.; Hong, H.; Wang, J.; Zhang, Z.; Zhou, X.; Qiao, R.; Xu, J.; Gao, P.; et al. Monitoring Local Strain Vector in Atomic-Layered MoSe2 by Second-Harmonic Generation. *Nano Lett.* **2017**, *17* (12), 7539–7543.

(11) Khan, A. R.; Liu, B.; Ma, W.; Zhang, L.; Sharma, A.; Zhu, Y.; Lü, T.; Lu, Y. Direct Measurement of Folding Angle and Strain Vector in Atomically Thin WS$_2$ Using Second Harmonic Generation. **2020**.

(12) Novoselov, K. S.; Geim, A. K.; Morozov, S. V.; Jiang, D.; Katsnelson, M. I.; Grigorieva, I. V.; Dubonos, S. V.; Firsov, A. A. Two-Dimensional Gas of Massless Dirac Fermions in Graphene. *Nature* **2005**, *438* (7065), 197–200.

(13) Acyls, R. References and Notes (1). *Tetrahedron* **2007**, *3* (1), 1974–1976.

(14) Splendiani, A.; Sun, L.; Zhang, Y.; Li, T.; Kim, J.; Chim, C.-Y.; Galli, G.; Wang, F. Emerging Photoluminescence in Monolayer MoS 2. *Nano Lett.* **2010**, *10* (4), 1271–1275.

(15) Pei, J.; Yang, J.; Xu, R.; Zeng, Y.-H.; Myint, Y. W.; Zhang, S.; Zheng, J.-C.; Qin, Q.; Wang, X.; Jiang, W.; et al. Exciton and Trion Dynamics in Bilayer MoS 2. *Small* **2015**, *11* (48), 6384–6390.

(16) Yang, J.; Wang, Z.; Wang, F.; Xu, R.; Tao, J.; Zhang, S.; Qin, Q.; Luther-Davies, B.; Jagadish, C.; Yu, Z.; et al. Atomically Thin Optical Lenses and Gratings. *Light Sci. Appl.* **2016**, *5* (3), e16046–e16046.

(17) Wang, Y.; Cong, C.; Yang, W.; Shang, J.; Peimyoo, N.; Chen, Y.; Kang, J.; Wang, J.; Huang, W.; Yu, T. Strain-Induced Direct–Indirect Bandgap Transition and Phonon Modulation in Monolayer WS 2. *Nano Res.* **2015**, *8* (8), 2562–2572.

(18) Pei, J.; Gai, X.; Yang, J.; Wang, X.; Yu, Z.; Choi, D.-Y.; Luther-Davies, B.; Lu, Y. Producing Air-Stable Monolayers of Phosphorene and Their Defect Engineering. *Nat. Commun.* **2016**, *7* (1), 10450.

(19) Yang, J.; Wang, Z.; Yu, Z.; Lu, Y. Manipulating Optical Beam Flow Fronts in 2D Materials. *SPIE Newsroom* **2016**.

(20) Rose, A.; Smith, D. R. Overcoming Phase Mismatch in Nonlinear Metamaterials [Invited]. *Opt. Mater. Express* **2011**, *1* (7), 1232.

(21) Wu, W.; Wang, L.; Li, Y.; Zhang, F.; Lin, L.; Niu, S.; Chenet, D.; Zhang, X.; Hao, Y.; Heinz, T. F.; et al. Piezoelectricity of Single-Atomic-Layer MoS2 for Energy Conversion and Piezotronics. *Nature* **2014**, *514* (7523), 470–474.

(22) Wang, H.; Qian, X. Giant Optical Second Harmonic Generation in Two-Dimensional Multiferroics. *Nano Lett.* **2017**, *17* (8), 5027–5034.

(23) Malard, L. M.; Alencar, T. V.; Barboza, A. P. M.; Mak, K. F.; De Paula, A. M. Observation of Intense Second Harmonic Generation from MoS2atomic Crystals. *Phys. Rev. B - Condens. Matter Mater. Phys.* **2013**, *87* (20), 1–5.

(24) Xiao, J.; Ye, Z.; Wang, Y. Y.; Zhu, H.; Wang, Y. Y.; Zhang, X. Nonlinear Optical Selection Rule Based on Valley-Exciton Locking in Monolayer Ws2. *Light Sci. Appl.* **2015**, *4* (12), e366.

(25) Majumdar, A.; Fryett, T.; Liu, C.-H.; Zheng, J.; Wu, S.; Rivera, P.; Syler, K.; Clark, G.; Xu, X. Progress in 2D Semiconductor Optoelectronics; George, T., Dutta, A. K., Islam, M. S., Eds.; 2017; p 101940F.

(26) Säynätjoki, A.; Karvonen, L.; Rostami, H.; Autere, A.; Mehravar, S.; Lombardo, A.; Norwood, R. A.; Hasan, T.; Peyghambarian, N.; Lipsanen, H.; et al. Ultra-Strong Nonlinear Optical Processes and Trigonal Warping in MoS 2 Layers. *Nat. Commun.* **2017**, *8* (1), 2005–2009.

(27) Janisch, C.; Wang, Y.; Ma, D.; Mehta, N.; Elías, A. L.; Perea-López, N.; Terrones, M.; Crespi, V.; Liu, Z. Extraordinary Second Harmonic Generation in Tungsten Disulfide Monolayers. *Sci. Rep.* **2014**, *4* (c), 1–5.

(28) Seyler, K. L.; Schaibley, J. R.; Gong, P.; Rivera, P.; Jones, A. M.; Wu, S.; Yan, J.; Mandrus, D. G.; Yao, W.; Xu, X. Electrical Control of Second-Harmonic Generation in a WSe2 Monolayer Transistor. *Nat. Nanotechnol.* **2015**, *10* (5), 407–411.

(29) Kumar, N.; Najmaei, S.; Cui, Q.; Ceballos, F.; Ajayan, P. M.; Lou, J.; Zhao, H. Second Harmonic Microscopy of Monolayer MoS2. *Phys. Rev. B* **2013**, *87* (16), 161403.

(30) Kohn, W.; Sham, L. J. Self-Consistent Equations Including Exchange and Correlation Effects. *Phys. Rev.* **1965**, *140* (4A), A1133–A1138.

(31) Lee, B.; Wang, L. W.; Spataru, C. D.; Louie, S. G. Nonlocal Exchange Correlation in Screened-Exchange Density Functional Methods. *Phys. Rev. B - Condens. Matter Mater. Phys.* **2007**, *76* (24), 1–25.

(32) Gan, C. K.; Liu, Y. Y. F. Direct Calculation of the Linear Thermal Expansion Coefficients of <math> <msub> <mi>MoS</Mi> <mn>2</Mn> </Msub> </Math> via Symmetry-Preserving Deformations. *Phys. Rev. B* **2016**, *94* (13), 134303.

(33) El-Mahalawy, S. H.; Evans, B. L. The Thermal Expansion of 2 H -MoS 2 , 2 H -MoSe 2 and 2 H -WSe 2 between 20 and 800°C. *J. Appl. Crystallogr.* **1976**, *9* (5), 403–406.

(34) Aray, Y.; Vega, D.; Rodriguez, J.; Vidal, A. B.; Coll, D. S. Atoms in Molecules Theory for Exploring the Crystal Structure and Bond Nature of the MoS2 Bulk. *J. Comput. Methods Sci. Eng.* **2009**, *9* (4–6), 257–267.

(35) Li, C.; Fan, B.; Li, W.; Wen, L.; Liu, Y.; Wang, T.; Sheng, K.; Yin, Y. Bandgap Engineering of Monolayer MoS2 under Strain: A DFT Study. *J. Korean Phys. Soc.* **2015**, *66* (11), 1789–1793.

(36) Ostadhossein, A.; Rahnamoun, A.; Wang, Y.; Zhao, P.; Zhang, S.; Crespi, V. H.; Van Duin, A. C. T. ReaxFF Reactive Force-Field Study of Molybdenum Disulfide (MoS2). *J. Phys. Chem. Lett.* **2017**, *8* (3), 631–640.

(37) Addou, R.; Colombo, L.; Wallace, R. M. Surface Defects on Natural MoS2. *ACS Appl. Mater. Interfaces* **2015**, *7* (22), 11921–11929.

6 ADDITIONAL STUDY: LIGHT MATTER INTERACTIONS IN 1D NANOWIRES

6.1 Introduction

Zero phonon lines (ZPL)[1] are narrow sharp peak emission at low temperature which are purely electronic in nature. They have characteristic vibrational structure and hence can be used for determining photophysical, photochemical and physicochemical properties of complex compounds.[2] Hence, there has been a tremendous revival of interest in narrow line-width emissions due to their fundamental applications in single photon emission sources, which have key applications in linear optics quantum information processing.[3] ZPLs have also been established to be applied for nano lasers,[4] optical waveguides,[4a, 5] flexible/cost-effective optical devices[6] and tunable-wavelength emission displays.[7], optical data storage[8] and processing in the space-frequency domain and single impurity molecule spectroscopy.[9] Zero-phonon or quasi-line spectral emissions were reported by Shpol' skii[10] in 1962 at low temperature by inducing the molecules in a matrix or solution at low temperatures, thus confirming the phonon less nature of these emissions.

There have been several attempts to generate similar quasi-line or Shpol' skii spectra emissions. Recently, self-assembled InAs quantum dots[3] and trapped atoms have been demonstrated as such sources for highly indistinguishable single photons and quasi-line emissions. Several complex polyatomic organic molecules embedded in molecular crystals or solutions have been demonstrated in the past to obtain ZPL emissions (See

Table S1). But, all of them have been two-component systems which require the desired chromophore to be in a frozen solution or matrices in order to reduce the phonon sideband emissions. This dilutes the light emitting molecule concentration in the matrix and hence the light generation efficiency is considerably reduced.[2, 5-6] There have been no reports so far which show a single component and single-crystal molecule solid-state system generating Shpol' skii spectra. Broad phonon sideband emission arises due to different energy level of molecules in a system[11] and that is why they need to be put in matrices or solutions as discussed above, to confine their degree of freedom and achieve narrow quasi-line spectral emissions. In a single-crystal molecule system, high crystallinity is the key to observe Shpol' skii effect but until now it has been a challenge to grow highly crystalline solid states systems that generate ZPL emissions. One-dimensional (1D) nanostructures such as nanowires, nanoribbons/belts and nanotubes have gathered significant attention due to their two dimensional quantum confinement.[6a, 12] This makes them promising candidates for achieving quasi-line spectral emissions. But most those nanomaterials have been mostly externally doped conjugated polymers[13] or large two dimensional non-linear extended aromatic systems like hexabenzocoronene.[12, 14] That makes it difficult to achieve large scale high order crystalline and defect free growth of 1D structures, especially with molecules that show $\pi-\pi$ face stacking necessary to make 1D structures.[14-15] Most of the reported 1D organic structures have been demonstrated in liquid phase[16] grown by using self-assembly in liquid phase solutions, restricting their applications in solid state electronic devices.[17] Low molecular weight organic materials on the other hand offer a distinct advantage as compared to their inorganic counterparts in terms of their good processability,[18] large-scale/low-cost synthesis,[6a, 14] high photoluminescence (PL) efficiency[19] and molecular tenability of electronic properties.[20]

But, in solid state growth of organic molecules over a substrate, it is difficult to achieve dimensionality control and effectively control the width and length of the 1D nanostructure.[6a, 14] Moreover, it is well known that in organic crystalline structures the opto-electronic and electronic properties are a direct function of the molecular orientation, degree of crystallinity and defect states in the lattice.[21] For ensemble organic molecular systems in solution, the local arrangement of the molecules in the solution affects their ability to absorb light and hence affects their optoelectronic properties.[22] There have been recent reports on using physical vapor deposition (PVD)[7, 11, 23] techniques to grow solid states 1D crystalline organic structures. However, they still have not been able to control monodispersity of the organic molecules, especially with low-molecular weight organic molecules as deposition sources.[6a, 14]

Here, we present a single component, high crystalline organic 1D nanowire made from single-crystal low molecular weight oligoacene- pentacene (PEN) molecule deposited on hexagonal boron nitride (hBN) using a low temperature PVD process. We report interesting optical properties form the 1D nanowires at room and low temperature. The PL spectra from the nanowires are clearly resolvable into three vibronic peaks at room temperature as compared to the broad sideband emission from bulk thin film pentacene. We attribute this PL spectra to a high degree of crystallinity and reduced degrees of translational and rotational freedom[24] of molecules in 1D PEN wire. Hence, resulting in clearly resolvable vibronic energy levels and reduced charge-phonon coupling in the lattice. At cryogenic temperatures, due to further freezing of molecular degrees of freedom and reduction of thermal phononic coupling results in quasi-line spectra[25] from PEN wires. This emergence of these atomic-like quasi-line spectra is called Shpol' skii effect[10, 26] and was reported in frozen organic solutions at low temperatures by Shpol' skii in 1952. The reported quasi-line spectra have a linewidth of ~1-2 nm and are a resultant of the reduced phononic coupling with the excitons in the lattice[2]. The linewidth reported in our case is much lower as compared to the linewidth reported from similar organic 1D nanostructures[11] grown using similar PVD methods. These quasi line spectra arising at low temperatures are ZPLs[2] attributed to zero-phonon transitions between the electronic energy levels of the organic molecules, confirmed by a high value of the Debye-Waller factor (*DW*).[2, 25] We further establish the high crystallinity and higher degree of molecular orientation of the PEN molecules in the 1D nanowire structure using polarization-resolved PL emission spectra and time-resolved PL emission. We also demonstrate a metal oxide semiconductor (MOS) device incorporating the 1D PEN wire to effectively demonstrate an external electric control of the quasi line spectral emission at low temperatures. Our results effectively demonstrate the use of PEN 1D organic nanowires for future optoelectronic devices such as nanolasers[27], OFETs[28], multi-coloured light emitting diodes (LEDs)[7b], optically driven lasers[29], photodetectors, logic gates and construction of interconnects and functional units of next generation miniaturized optoelectronics.[6a]

6.2 Fabrication of 1D nanowires

Among light-weight oligoacenes, pentacene and its derivates have shown best performances in thin-film devices[30]. Thus, we chose pentacene for our 1D growth. Figure 6.1a shows the optical image of the PEN wires grown on hBN substrate. hBN provides a defect free and dangling bond free flat area for molecular deposition with high degree of molecular orientation[31]. Mechanically exfoliated few-layer hBN sheets were transferred onto a 285 nm SiO_2/Si substrate. The PEN was then deposited using a thermal vapor deposition process using a tube furnace (Figure A8.1). (See Appendices A4 and A8. Supplementary information Note 1). The grown PEN wires were characterized using

Raman spectroscopy (Figure A8.2). The growth of the PEN wires was optimized at various growth temperatures (Figure A8.3a) and time durations (Figure A8.3b) to achieve long length and high crystalline 1D nanowires. High resolution AFM imaging was used to characterize the physical thickness and diameter of the PEN wires (Figure 6.1b). Most of the PEN wires had a circular cross-section with an average width of ~300-400 nm and an average thickness of ~250-300 nm. The average length of the wires was ~14 µm, which is much higher than previously reported PVD grown 1D nanowires on substrates[6a, 7b, 11]. Figure 6.1c shows the schematic growth mechanism of 1D PEN nanowires on hBN substrates. First, the smaller PEN molecules are connected linearly by H-bonds forming long chains and depositing over hBN surface utilizing $\sigma-\pi$ interaction with the substrate[31]. The vertical deposition then is a result of Van der Waals interaction between pentacene molecules. At this juncture, as the deposition rate increases, $\pi-\pi$ interactions between PEN molecules cause the molecules to bend inwards facing each other[6a] leading to the formation of wire like 1D structures. We confirmed the same using high resolution SEM imaging (Figure 6.1d). The prepared samples were then excited using a 532 nm CW laser. The resultant PL emission spectra is shown in Figure 6.1e. The PL spectra from the 1D PEN wire is clearly resolved in to three peaks at 600 nm, 660 nm and 730 nm. The origin of the peaks is explained later. The spectrum from 1D PEN wires is in sharp contrast to the broad and much weaker PL emission from thin film pentacene grown on the same substrate and bulk pentacene samples.

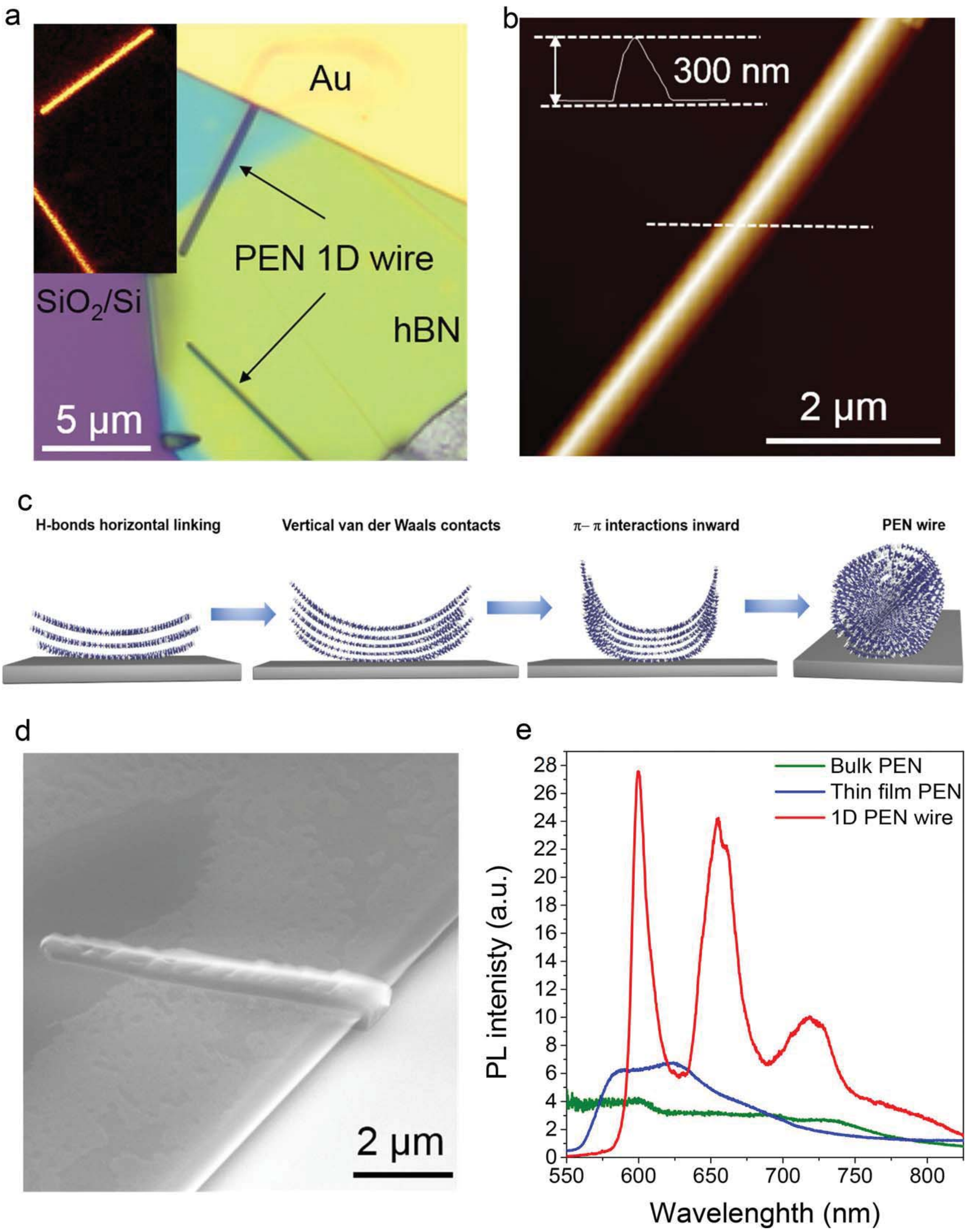

Figure 6.1 │Characterization of PEN wires
(a) Optical microscope image of the quasi 1D PEN wires used for measurements. The scale bar is 5 μm. Inset: PL mapping image of the PEN wires showing the strong emission from wires. (b) Zoomed Atomic force microscope (AFM) image of the PEN wires confirming the diameter to be ~ 300 nm. (c) Schematic representation of the growth mechanism of the PEN wires during the vapor deposition mechanism. See text for details. (d) SEM image of the PVD grown PEN wires on hBN substrate, showing the morphology of the wire. (e) PL emission spectra (red curve) from PEN wires at room temperature, showing three clear peaks at 600 nm, 660 nm and 730 nm. Broad sideband PL emission from bulk (green) and thin film crystalline pentacene grown on hBN (blue) is also shown for comparison.

The optical absorption and emission from organic molecular assemblies is a direct function of the molecular crystallinity and degree of orientation[21b]. Hence, well resolved and high-intensity PL emission from 1D wires is a resultant of the highly crystalline an ordered growth of PEN wires on a clean defect free flat hBN adsorption surface. To further confirm the role of hBN in achieving ordered growth, we ran the growth of PEN wires again using the same methods and conditions on a SiO_2/Si substrate. We observed tiny needle like 1D structures protruding out of micelle like nucleation sites (Figure A8.4). The growth of those 1D PEN structures on SiO_2 was highly disordered and the PL emission (Figure A8.4c) were much weaker and less resolved as compared to the wires grown on hBN. Thus, establishing the role of hBN as a template or adsorbent surface for the ordered high crystalline and dimensionality-controlled growth of 1D PEN wires.

6.3 Shpol' skii effect and quasi-line spectra

To further understand the optical properties of crystalline 1D PEN wires and substantiate their role for various optoelectronic applications, we performed temperature dependent PL spectroscopy down to 77 K. Figure 6.2a shows the PL spectra from 1D PEN wires at various temperatures. The spectra start to resolve into various sharp and narrow linewidth peaks as the temperature decreases. The first emergence of narrow peaks is spotted at 213 K (Figure A8.5). At 77 K, the spectrum is clearly resolved into sharp quasi-line emission peaks with an average line width of 2-3 nm (See Table S2 for fitted peak positions). In some optimal growth cases, we observed the linewidth to be ~ 1nm (Figure A8.6). Whereas, we did not observe such narrow linewidth PL peaks from 1D needles grown on SiO_2 (Figure 6.2b). The emergence of quasi-line spectra from 1D PEN wires is very different from the broad sideband PL emission from thin film PEN grown on similar hBN substrate (Figure A8.7).

The origin of quasi-line spectra from 1D PEN wires and the difference with thin film PEN be explained using the energy level band diagram in Figure 6.2c. In bulk thin films of organic molecules such as pentacene, the emission band broadening/dispersion results mainly from the fact that various molecules have different energy levels[32]. As a result, multiple vibronic band are formed (also called Davydov splitting[33]). The energy levels (in both ground and excited states) are roughly divided in vibronic sub-bands, defined by the number of quanta υ (=1,2…). Each vibronic band has further vibrational sub-bands induced due phononic coupling of charges (indicated by v̏=1,2...) The width of each vibronic band incorporating molecular interaction and vibrational frequency of molecules has been theoretically calculated by Spano et al.[34] Due to low crystallinity, the charges couple with phonons (vibrations) in the crystal lattice plane to form diffused vibronic/vibrational bands (as shown Figure 6.2c). Each vibrational band is spread due to this strong phononic coupling of rotational translational states of charges[2]. The interaction of molecules with lattice phonons is represented by spread of vibrational sublevels. Multiplicity of characteristic vibrational and vibronic bands of these molecules results in further diffusiveness of electronic-vibrational bands and causes a quasi-continuum spectrum as obtained from bulk thin films. The inhomogeneous spectral broadening arises from electronic transitions involving lattice phonons, giving rise to a comparatively broad phonon sideband emission (PSB)[2, 24].

In our single crystalline, 1D PEN wires due to flat h-BN substrate, the molecules are confined distinctly in the lattice with a specific geometric configuration and higher degree of orientation[4a, 5-6, 11] as compared to bulk organic thin films, with less defect and interfacial states. This limits the large rotational and translational degrees of freedom of molecules and this ordered environment drastically reduces the phonon coupling resulting in narrower optical transitions[2]. Even at room temperature narrowing of vibrational level occurs, simplifying the optical spectra into discrete narrower emissions (Figure 6.1e). The emergence and enhancement of vibrational structures can be attributed the increases of long-range order and higher degree of molecular orientation in PEN wires.

At low temperature all vibronic transitions can be further resolved (with FWHM ~ 2-3 nm), resulting in an almost quasi-line spectrum called the Shpol' skii effect. At low temperatures, the degrees of freedom for the molecules are further frozen resulting in further educed electron-phonon coupling. This causes the PL spectra to be resolved in to quasi-line peaks or the narrow zero-phonon lines[35] (ZPL) emissions from the vibronic/vibrational sub bands to ground state (as shown in Figure 6.1c). Such line-spectra only appears upon specific transitions in the band structure, which do not involve lattice phononic vibrations (analogous of Mössbauer[36] lines). The reduction in spread of vibronic/vibrational sub bands occurs due to high ordered growth of PEN molecules over hBN and further reduction in phonon-electron coupling at low temperature. It has been shown in the literature that Shpol' skii effect is affected by guest-host molecular interactions[23-24]. Hence, the emergence of Shpol 'skii spectrum can be attributed to these two factors: highly ordered molecular orientation (high crystallinity) and low temperature. ZPLs were not observed from the PEN needles on SiO_2 (Figure 6.2b). This further substantiates the role of high crystallinity in PEN wires in achieving ZPL spectral emissions at low temperature.

It has been shown theoretically that the electron-phonon coupling and change of temperature influences the FWHM and integrated PL emission from organic matrices[25, 30]. To further confirm the Shpol' skii effect and the role of ZPLs in the spectra obtained from 1D PEN wire, we performed temperature dependent FWHM and Integrated PL intensity analysis. The relation between the integrated intensity of the ZPL and total intensity of the (ZPL+PSB) band is determined by linear-electron phonon coupling and is called Debye-Waller factor (DW)[2, 37] and is defined by the following equation (1).

$$DW = \frac{I_{ZPL}}{I_{ZPL}+I_{PSB}} \tag{1}$$

where, I_{ZPL} is the integrated PL intensity from the sharp zero-phonon line peak and I_{PSB} is the total integrated area of the remaining broad sideband emissions. The I_{ZPL} and I_{PSB} were obtained by fitting the PL spectra from PEN wires using a Lorentzian fitting function (Figure A8.8) and then the integrated area under the curve under the sharp peak I_{ZPL} and under the nearest phonon sideband emission I_{PSB} were obtained to determine the DW factor

The variation of extracted DW factor from 1D PEN wire as a function of temperature is shown in Figure 6.2d. The high value of DW factor (0.72) at 77 K confirms the limited phonon coupling with the charges resulting in quasi-line spectra. As a comparison we have also shown calculated DW factor for an excitonic emission from 1L WSe_2 monolayer. The linewidth of PL emission peak is also a direct function of phonon coupling. Figure 6.2e (Figure A8.9) shows the variation in full-width half maximum (FWHM) from peak 1(peak 2, 3) emissions from 1D PEN wire and 1L WSe_2 monolayer. The FWHM from 1D PEN wire is much lower as compared to the excitonic peak width at 77 K from 1L WSe_2. The sharp reduction in FWHM (~ 2-3 nm at 77 K) from the PEN wire PL peak 1, confirms the reduced phonon coupling in the PEN crystal lattice[38] resulting in quasi-line spectral emissions, which is consistent with previously reported ZPL emissions from low dimensional organic materials[2] and other Shpol' skii matrices (See table S1). We further performed pumping power dependent PL measurements at 77 K (Figure A8.10), which confirmed the mission to be below lasing threshold.

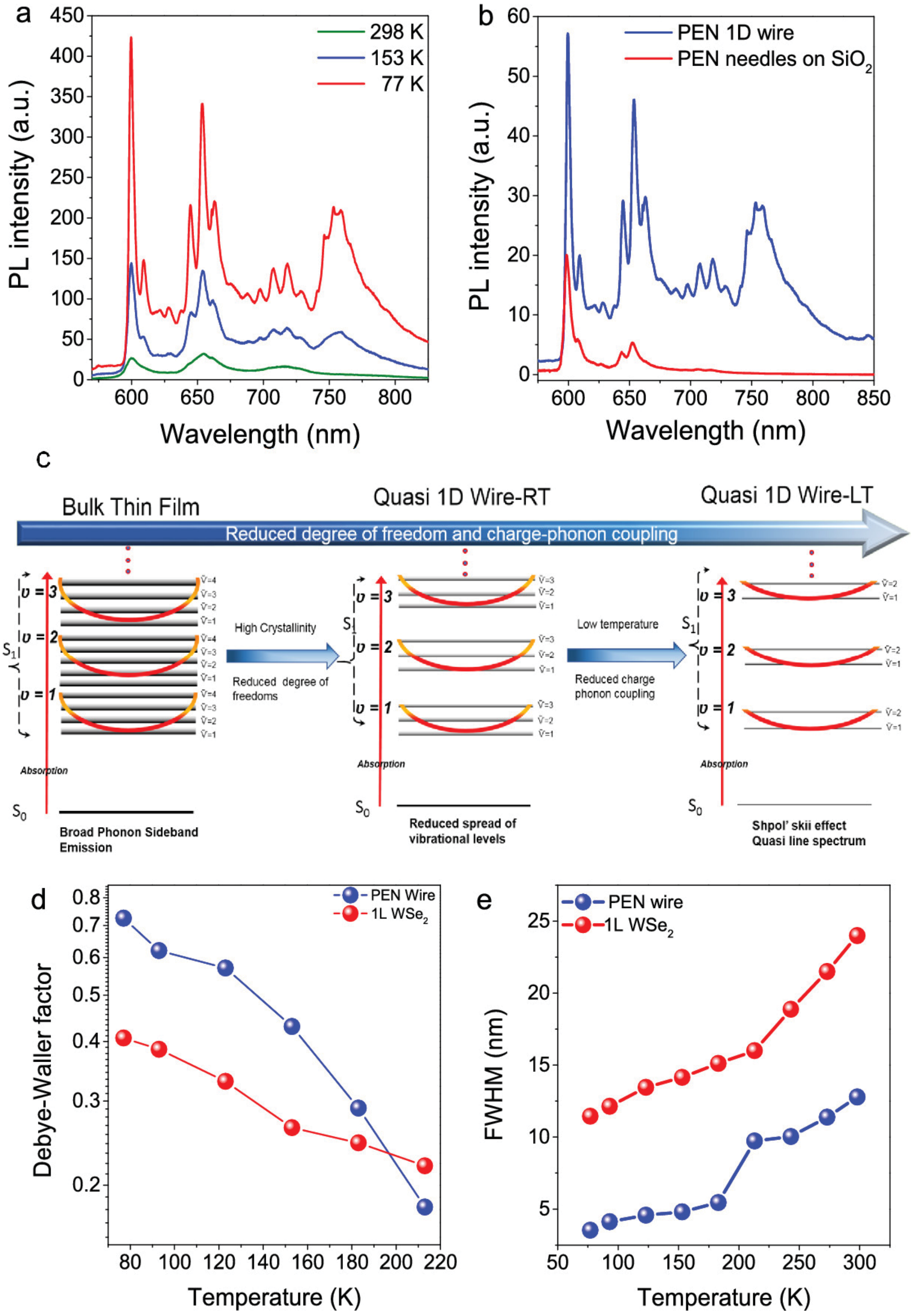

Figure 6.2 │Temperature dependent PL emission and Shpol' skii effect.
(a) Measured PL spectra at various temperatures from PEN wires. The vibronic levels are well resolvable at cryogenic temperatures as evident from quasi-line spectral emissions. (b) PL emission spectra comparison between PEN wires grown on hBN with PEN needles grown in SiO_2 at 77 K. The PEN needles

on SiO_2 do not show the clearly resolvable vibronic levels as shown from PEN wires grown on hBN. (c) Schematic showing the energy level diagram in pentacene. The exciton bands with vibrational coupling for pentacene thin film (left) are shown. Only first three vibronic bands are shown. The vibronic bands (red) are demonstrated by υ =1, 2, 3... and the vibrational bands (grey) formed due to strong coupling between the exciton and phonons are shown by v̏=1,2,3… The spread or thickness of vibrational levels accounts for the level of phononic coupling and degree of freedom in all cases. The molecules in bulk thin film case are at various energy levels leading to an emission band broadening and the PL emission is a broad sideband phononic emission as shown in Figure 6.1d. The vibronic levels in PEN wires at RT are further resolved due to confinement of molecules distinctly in the lattice with specific geometric configuration and high degree of orientation. In this case more neighbouring molecules have similar energy levels, leading to a degenerate PL emission spectrum as shown in Figure1d. At low temperature (right), the charge-phonon coupling, or vibrational coupling is further reduced leading to even further reduced thickness of vibrational levels at low temperature. As result the vibronic levels are well defined due to reduced degree of freedom of molecules and minimal charge-phonon coupling. This effect of observing quasi-line spectra at low temperature is called Shpol' skii effect as shown in Figure 6.2a. (d) Debye-Waller (*DW*) factor obtained from PEN wire (peak =600 nm) and 1L WSe_2 (peak =750nm) as a function of the temperature. At 77 K the D*W* factor is much higher in PEN wires as compared to TMDC monolayers confirming an almost zero phonon emission or a quasi-linear PL emission. (e) Variation of full-width half maximum (FWHM) of excitonic PL emission peaks from PEN wires (peak = 600nm) and WSe_2 (peak =750 nm). The FWHM from PEN wire excitonic emission is much lower as compared to TMD monolayer and the reduction in FWHM with temperature to ~ 3nm, confirms the zero-phonon line emission from PEN wires.

6.4 High order crystallinity and molecular orientation

To further understand the crystalline structure and orientation of pentacene molecule unit cells inside the 1D PEN wire, we performed polarization angle resolved PL emission spectroscopy at both room temperature and 77 K. Figure 6.3a shows the PL spectra at various emission polarization angles at room temperature. PL intensity from 1D PEN wires strongly depended on the emission polarization angle θ and showed a period of 180 degrees. Peak 1 (600 nm) showed opposite polarization dependence as compared to peaks 2 (660 nm) and 3 (730 nm). Based on the polarization data and theoretically predicted $\pi-\pi$[39] molecular packing in pentacene[30], we can identify the crystal faces in PEN wire as shown in Figure 6.3b. The wires grow along the 010 axis or the 100 face[14, 23] (see inset SEM image in Figure 6.3b and Figure A8.11).

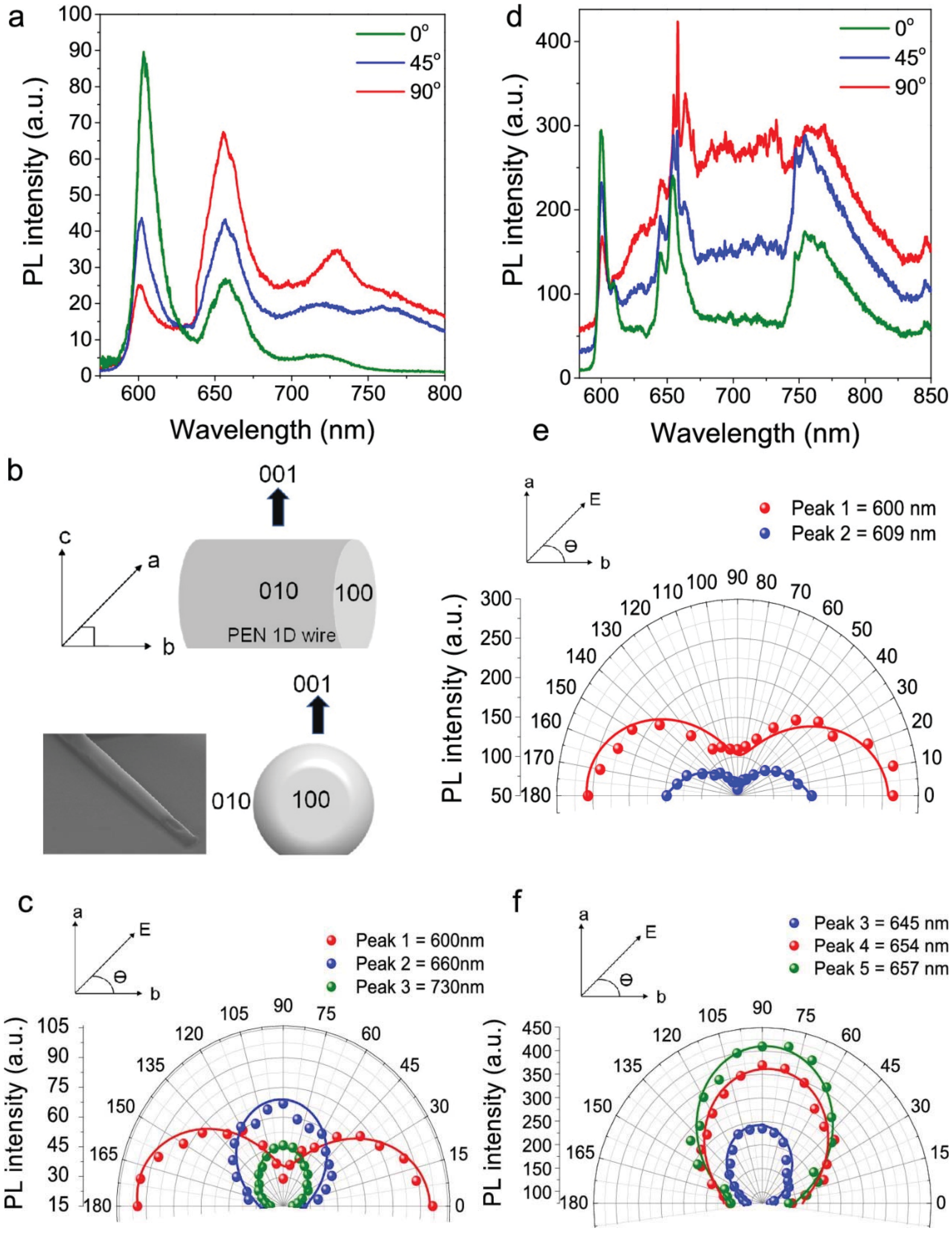

Figure 6.3 │Polarization angle-dependent PL measurements.

(a) Measured PL intensity as a function of emission polarization angle *θ* from PEN wire samples at room temperature, revealing the anisotropic excitonic nature of emission from the PEN wires. In experiment, the excitation polarization angle was fixed and the polarization angle of the emission θ was determined by using an angle-variable polarizer located in front of the detector. (b) Schematic diagram showing the growth morphology and crystalline structure molecular arrangement in PEN wires grown on hBN. The molecular axis as in a conventional triclinic pentacene crystal have been marked as a, b and c. The inset SEM image shows the 001 and 100 face of as grown PEN wires. (c) Measured polar plot of PL emission spectra peaks as a function of emission polarization angle *θ* from PEN wires at room temperature revealing the opposite anisotropic excitonic nature of PL emission peaks at 600 nm, 660 nm and 730 nm. E is the direction of selected emission polarization. 'a' and 'b' are pentacene molecular axis. (d) Measured PL intensity as a function of emission polarization angle θ from PEN wire samples at 77 K. (e-f) Measured polar plot of PL emission spectra peaks as a function of emission polarization angle θ from PEN wires at 77 K revealing the opposite anisotropic excitonic nature of PL emission peaks. For remaining polar plots see Figure A8.13.

Figure 6.3c shows the polar plot of PL intensities as a function of polarization angles. Peak 1 is clearly polarized along the long'b' axis of PEN unit cell, while peak 2 and 3 are aligned along the 'a' axis[23]. This clearly highlights anisotropy in 1D PEN wires originating due to high crystalline and ordered growth in the 1D wires. We performed similar polarization resolved (excitation and emission) measurements at 77 K (Figure 6.3d and Figure A8.12) to understand the anisotropic behaviour of the Shpol' skii spectra observed at 77 K. We observed the same trend as at room temperature. The quasi-line spectra peaks 1 and 2 (See Table S2) are aligned along the 'b' axis (Figure 6.3e). The remaining quasi-linear peaks were aligned along the 'a' axis of PEN unit cell as shown in Figure 6.3f and Figure A8.13. Increased crystallinity and order can also lead to enhanced lifetime of PL emission peaks in crystalline materials[40]. To substantiate the high crystallinity in our 1D nanowires, we also performed time-resolved PL (TRPL) measurements at room temperature and 77 K. Figure 6.4a shows the decay curve obtained from peaks 1,2 and 3 from PEN 1D wire at room temperature and the bulk thin film. The decay trace curves were deconvoluted with respect to the instrument response function (IRF) and then were fitted using the equation: $I = A\, exp(-\frac{t}{\tau_1}) + C$, where I is the PL intensity, A and C are constants, 't' is time, and τ_1 is decay rate indicating emission lifetime. The long single exponential lifetime represents radiative recombination time at room temperature.[41] An effective lifetime of τ_1 = 3.36 ± 0.6 ns, 3.07 ± 0.3 ns and 2.74 ± 0.4 ns (Figure 6.4c) was extracted for peaks 1, 2 and 3 respectively at room temperature, which is about three times higher than the extracted radiative lifetime form thin film pentacene of 1.24 ns. Similarly, at 77 K, effective radiative lifetime for 5 major peaks was extracted as shown in Figures 4b, d.

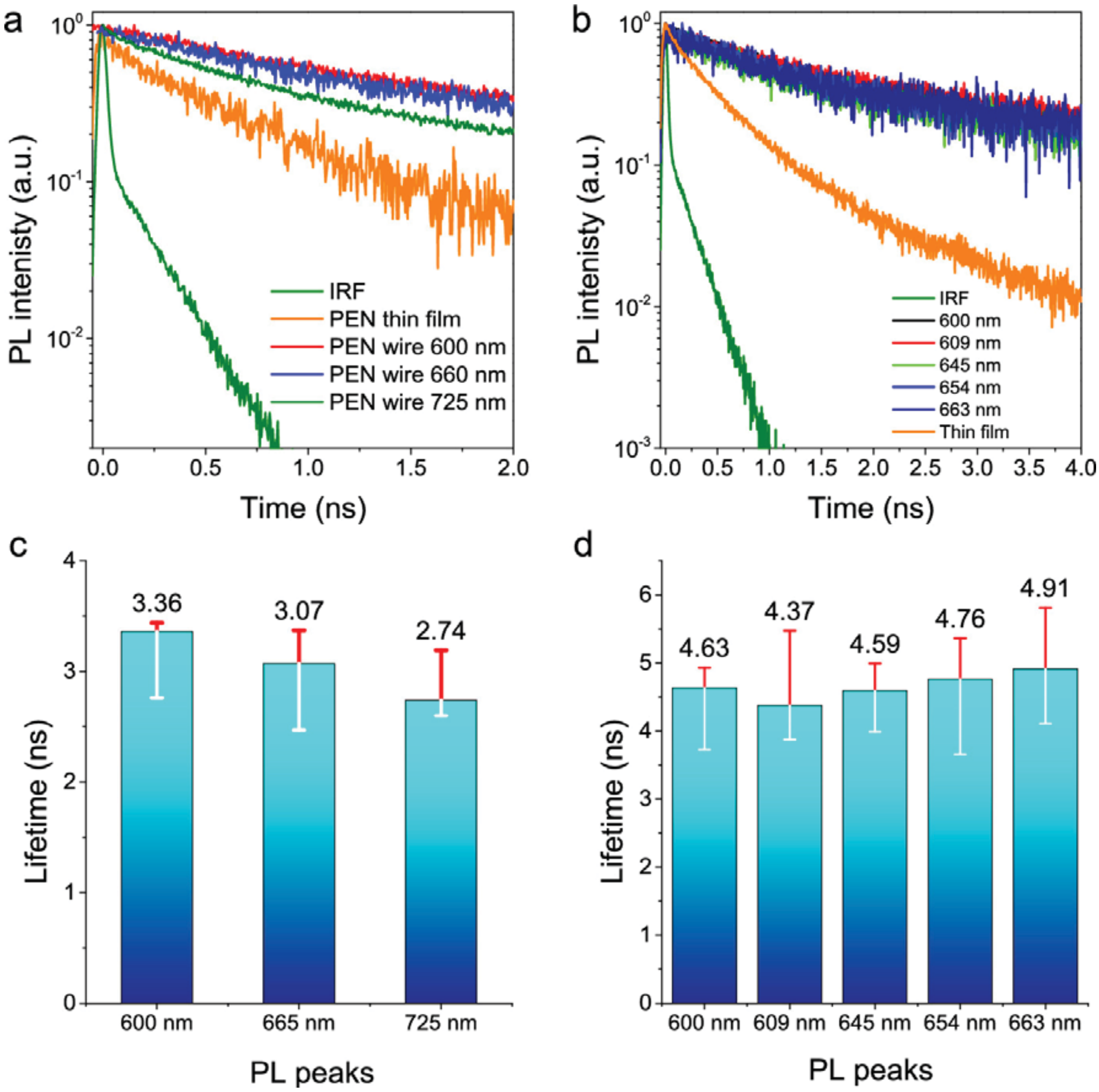

Figure 6.4 │Time-resolved PL emission from PEN wires.
(a-b) Time-resolved PL emission (normalized) from PEN wires at 298 K (a) and 77 K (b). The orange curve represents the decay curve from bulk thin film pentacene for comparison. An effective long lifetime of 1.24 ns (1.01 ns) was extracted from the orange decay curve at 298 K (77 K), by a fitting with deconvolution using the instrument response function (IRF) (green curve). The red/blue balls represent decay curve from 1L, which is from FR exciton emission. The red (600 nm), blue (660 nm) and green (730 nm) decay curves are from PEN wires PL emission spectra. The deconvolution using IRF, gives an effective lifetime value of 3.36 ns, 3.07 ns and 2.74 ns respectively at 298 K. Similarly, at 77 K, deconvolution with IRF has been used to extract a long lifetime from various peaks at 77 K. See text for values. (c-d) Graphical representation (with experimental errors bars) showing the distribution of extracted lifetime from various peaks of PL emission spectra from PEN wires. For peak positions refer to Table S2.

The error bar in Figure 6.4c, d shows the variation in the measured data from around 20 similar samples that were tested over a period of few weeks. The effective lifetime from 1D PEN wire increased to an average ~ 4.5 ns (Figure 6.4d) while the thin film lifetime was reported to be around 1.01 ns. It is important to note here that the prolonged lifetime in PEN wires as compared to thin film pentacene is due to the lower trap density and lower degree of non-radiative trap/defect assisted recombination of excitons as compared to the thin films. Similar effects have been observed in other crystalline low dimensional material such as TMDCs and perovskites[42]. Thus, establishing the high order crystallinity and high degree of molecular orientation in our 1D PEN nanowires.

6.5 MOS device based on 1D PEN nanowires

We further incorporated the 1D PEN nanowire into a metal-oxide semiconductor (MOS) device to use external static back gate voltage to manipulate the quasi-line spectra for various optoelectronic device applications. Figure 6.5a shows the schematic diagram of the MOS device used for back gate voltage dependent PL modulation. During the measurements, the gold electrode was grounded, and the p+ doped Si substrate was used as a back gate providing a uniform electrostatic doping for the 1D PEN in this MOS device. The measured PL spectrum was very sensitive to the electrostatic doping and can be significantly modulated by the gate voltage. The PL intensity decreases when we inject negative charge into the samples, indicating that the 1D PEN has an initial n-type doping, Figure 6.5b-c show the variation in PL spectra at different back gate voltages at 298 K (77 K). The variation in PL intensities with back gate voltage is evident even for quasi-line spectra peaks at low temperature. The variation in PL intensity of peaks 1, 4 and 12 (See Table A8.22) as a function of back gate voltage is shown in Figure 6.5d. Electrostatic control of the quasi-line spectra is further demonstrated through change in *DW* factor as a function of back gate voltage (Figure A8.14 and A8.15). Thus, establishing the applications of 1D PEN nanowires in future optoelectronic device applications.

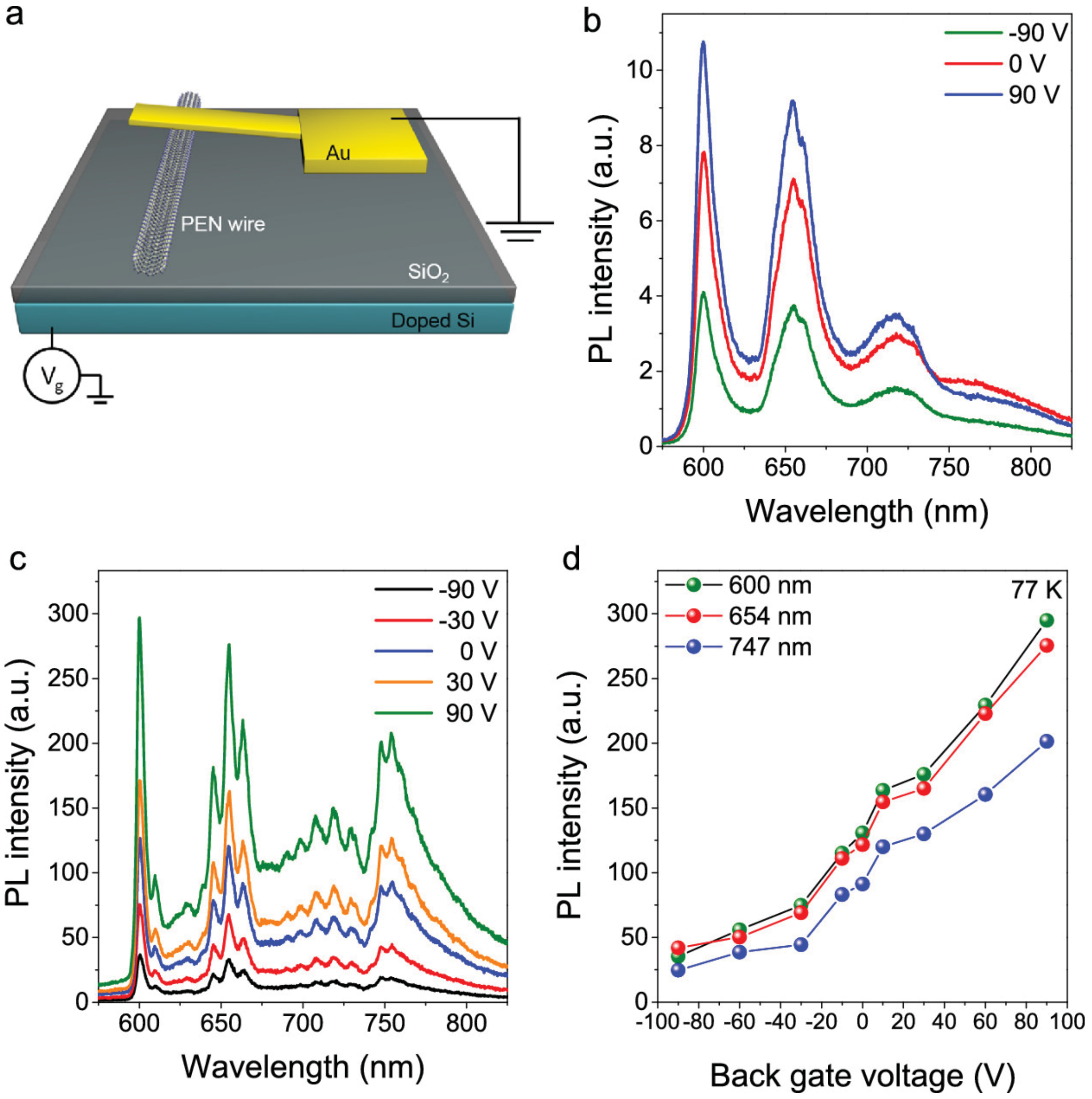

Figure 6.5 │Back gate dependent modulation of PL emission from PEN wire MOS device. (a) Schematic diagram of the MOS device used for static doping of charges into the PEN wire. (See optical image in Figure 6.1a). (b) Measured PL spectra from PEN wire sample at room temperature under various back gate voltages, showing clear modulation of all emission peaks. (c) Measured PL spectra from PEN wire sample at 77 K under various back gate voltages, showing similar modulation of all emission peaks as observed at room temperature. (d) Variation of peak =600 nm, 654 nm and 747 nm as a function of sweeping back gate voltage at 77 K, demonstrating a clear n-type doping in the PEN wire. The MOS device confirms the external control of the PL emission that can be achieved by modulating back gate voltage.

6.6 Chapter summary and future recommendations

In summary, we have demonstrated a quasi-line spectrum from a single component, solid state system of low-molecular weight single crystalline molecule organic material. We experimentally observed zero-phono lines in the PL emission spectra from 1D PEN nanowires originating due to Shpol' skii effect at cryogenic temperatures, which have not been reported before from single molecular crystalline solid-state systems. This was achieved due to a highly crystalline and ordered growth of PEN molecules in a 1D nanowire grown over an adsorbent defect free and flat hBN surface. Control of dimensionality and order in PVD process has been a challenge to grow similar 1D organic nanostructures for various optoelectronic applications. We demonstrated an optimized 1D nanowire which has high crystallinity and subsequently exciting optical properties for future optoelectronics. The restriction in degrees of freedom and reduced electron-phonon coupling in 1D nanowires led to vibronically well-resolved PL spectra. At low temperatures, further thermal phonon coupling is reduced, and the PL spectra is resolved in to quasi zero-phonon lines- the Shpol' skii spectra, as evident through extracted FWHM and *DW* factors form temperature dependent measurements. We further establish the high crystallinity through angle and time-resolved PL measurements. We finally demonstrate a MOS device based on 1D PEN nanowires, which shows an external control of quasi-line spectra using back gate voltage. Our results pave the way for use of organic 1D nanowires in nanolasers, OFETs, optical waveguides, chemical sensors, photodetectors and functional/interconnecting units of future nano optoelectronic and photonic devices. As high crystalline structures of 1D Pen nanowires offer amazing optical properties for industrial applications, we also speculate interesting nonlinear properties of 1D nanowires which is recommended for future research.

Chapter 6 References

1. Sild, O.; Haller, K., *Zero-Phonon Lines: And Spectral Hole Burning in Spectroscopy and Photochemistry*. Springer Science & Business Media: **2012**.

2. Naumov, A. V., Low-temperature spectroscopy of organic molecules in solid matrices: from the Shpol'skii effect to laser luminescent spectromicroscopy for all effectively emitting single molecules. *Physics-Uspekhi* **2013,** *56* (6), 605-622.

3. Kiraz, A.; Ehrl, M.; Mustecaplioglu, O.; Hellerer, T.; Brauchle, C.; Zumbusch, A. In *Zero-phonon-line emission of single molecules for applications in quantum information processing*, Photonic Materials, Devices, and Applications, International Society for Optics and Photonics: 2005; pp 584-592.

4. (a) Zhao, Y. S.; Peng, A.; Fu, H.; Ma, Y.; Yao, J., Nanowire waveguides and ultraviolet lasers based on small organic molecules. *Advanced Materials* **2008,** *20* (9), 1661-1665; (b) O'carroll, D.; Lieberwirth, I.; Redmond, G., Microcavity effects and optically pumped lasing in single conjugated polymer nanowires. *Nature nanotechnology* **2007,** *2* (3), 180.

5. Zhao, Y. S.; Xu, J.; Peng, A.; Fu, H.; Ma, Y.; Jiang, L.; Yao, J., Optical waveguide based on crystalline organic microtubes and microrods. *Angewandte Chemie International Edition* **2008,** *47* (38), 7301-7305.

6. (a) Zhao, Y. S.; Fu, H.; Peng, A.; Ma, Y.; Liao, Q.; Yao, J., Construction and optoelectronic properties of organic one-dimensional nanostructures. *Accounts of chemical research* **2009,** *43* (3), 409-418; (b) Law, M.; Sirbuly, D. J.; Johnson, J. C.; Goldberger, J.; Saykally, R. J.; Yang, P., Nanoribbon waveguides for subwavelength photonics integration. *Science* **2004,** *305* (5688), 1269-1273.

7. (a) Zhao, Y. S.; Fu, H.; Hu, F.; Peng, A.; Yang, W.; Yao, J., Tunable emission from binary organic one-dimensional nanomaterials: an alternative approach to white-light emission. *Advanced Materials* **2008,** *20* (1), 79-83; (b) Zhao, Y. S.; Fu, H.; Hu, F.; Peng, A. D.; Yao, J., Multicolor emission from ordered assemblies of organic 1D nanomaterials. *Advanced Materials* **2007,** *19* (21), 3554-3558.

8. Bree, P. d.; Wiersma, D. A., Application of Redfield theory to optical dephasing and line shape of electronic transitions in molecular mixed crystals. *The Journal of Chemical Physics* **1979,** *70* (2), 790-801.

9. Rebane, K. K., Zero-phonon line as the foundation stone of high-resolution matrix spectroscopy, persistent spectral hole burning, single impurity molecule spectroscopy. *Chemical Physics* **1994,** *189* (2), 139-148.

10. Shpol'skiĭ, É. V., LINE FLUORESCENCE SPECTRA OF ORGANIC COMPOUNDS AND THEIR APPLICATIONS. *Soviet Physics Uspekhi* **1960,** *3* (3), 372-389.

11. Zhao, Y. S.; Xiao, D.; Yang, W.; Peng, A.; Yao, J., 2, 4, 5-Triphenylimidazole nanowires with fluorescence narrowing spectra prepared through the adsorbent-assisted physical vapor deposition method. *Chemistry of materials* **2006,** *18* (9), 2302-2306.

12. Xiao, S.; Tang, J.; Beetz, T.; Guo, X.; Tremblay, N.; Siegrist, T.; Zhu, Y.; Steigerwald, M.; Nuckolls, C., Transferring self-assembled, nanoscale cables into electrical devices. *Journal of the American Chemical Society* **2006,** *128* (33), 10700-10701.

13. (a) Berson, S.; De Bettignies, R.; Bailly, S.; Guillerez, S., Poly (3-hexylthiophene) fibers for photovoltaic applications. *Advanced Functional Materials* **2007,** *17* (8), 1377-1384; (b) Merlo, J. A.; Frisbie, C. D., Field effect transport and trapping in regioregular polythiophene nanofibers. *The Journal of Physical Chemistry B* **2004,** *108* (50), 19169-19179; (c) Kim, D.; Han, J. T.; Park, Y.; Jang, Y.; Cho, J.; Hwang, M.; Cho, K., Single-crystal polythiophene microwires grown by self-assembly. *Advanced Materials* **2006,** *18* (6), 719-723.

14. Briseno, A. L.; Mannsfeld, S. C.; Jenekhe, S. A.; Bao, Z.; Xia, Y., Introducing organic nanowire transistors. *Materials Today* **2008,** *11* (4), 38-47.

15. Schenning, A. P.; Meijer, E., Supramolecular electronics; nanowires from self-assembled π-conjugated systems. *Chemical Communications* **2005,** (26), 3245-3258.

16. (a) Fu, H.; Xiao, D.; Yao, J.; Yang, G., Nanofibers of 1, 3-diphenyl-2-pyrazoline induced by cetyltrimethylammonium bromide micelles. *Angewandte Chemie International Edition* **2003,** *42* (25), 2883-2886; (b) Hu, J.-S.; Guo, Y.-G.; Liang, H.-P.; Wan, L.-J.; Jiang, L., Three-dimensional self-

organization of supramolecular self-assembled porphyrin hollow hexagonal nanoprisms. *Journal of the American Chemical Society* **2005,** *127* (48), 17090-17095.

17. Kang, L.; Chen, Y.; Xiao, D.; Peng, A.; Shen, F.; Kuang, X.; Fu, H.; Yao, J., Organic core/diffuse-shell nanorods: fabrication, characterization and energy transfer. *Chemical Communications* **2007,** (26), 2695-2697.

18. An, B. K.; Kwon, S. K.; Park, S. Y., Photopatterned arrays of fluorescent organic nanoparticles. *Angewandte Chemie* **2007,** *119* (12), 2024-2028.

19. An, B.-K.; Kwon, S.-K.; Jung, S.-D.; Park, S. Y., Enhanced emission and its switching in fluorescent organic nanoparticles. *Journal of the American Chemical Society* **2002,** *124* (48), 14410-14415.

20. (a) Lloyd, M. T.; Anthony, J. E.; Malliaras, G. G., Photovoltaics from soluble small molecules. *Materials Today* **2007,** *10* (11), 34-41; (b) Shin, T. J.; Yang, H.; Ling, M.-m.; Locklin, J.; Yang, L.; Lee, B.; Roberts, M. E.; Mallik, A. B.; Bao, Z., Tunable thin-film crystalline structures and field-effect mobility of oligofluorene–thiophene derivatives. *Chemistry of Materials* **2007,** *19* (24), 5882-5889.

21. (a) DeLongchamp, D. M.; Kline, R. J.; Lin, E. K.; Fischer, D. A.; Richter, L. J.; Lucas, L. A.; Heeney, M.; McCulloch, I.; Northrup, J. E., High carrier mobility polythiophene thin films: structure determination by experiment and theory. *Advanced Materials* **2007,** *19* (6), 833-837; (b) Spano, F. C., The Spectral Signatures of Frenkel Polarons in H- and J-Aggregates. *Accounts of Chemical Research* **2010,** *43* (3), 429-439.

22. Woo, H. Y.; Liu, B.; Kohler, B.; Korystov, D.; Mikhailovsky, A.; Bazan, G. C., Solvent Effects on the Two-Photon Absorption of Distyrylbenzene Chromophores. *Journal of the American Chemical Society* **2005,** *127* (42), 14721-14729.

23. Park, J. E.; Son, M.; Hong, M.; Lee, G.; Choi, H. C., Crystal-Plane-Dependent Photoluminescence of Pentacene 1D Wire and 2D Disk Crystals. *Angewandte Chemie* **2012,** *124* (26), 6489-6494.

24. Bloess, A.; Durand, Y.; Matsushita, M.; Verberk, R.; Groenen, E. J. J.; Schmidt, J., Microscopic Structure in a Shpol'skii System: A Single-Molecule Study of Dibenzanthanthrene in n-Tetradecane. *The Journal of Physical Chemistry A* **2001,** *105* (13), 3016-3021.

25. Kizel, V. A.; Sapozhnikov, M. N., The Interaction of Impurity Centres with the Surroundings and Quasi-Line Spectra. *physica status solidi (b)* **1970,** *41* (1), 207-216.

26. Tokousbalides, P., Observation of quasilinear fluorescence spectra (the "Shpol'skii effect") in matrix-isolated polycyclic aromatic hydrocarbons. *Journal of physical chemistry (1952) 81* (18), 1769-1772.

27. Zhang, W.; Yan, Y.; Gu, J.; Yao, J.; Zhao, Y. S., Low-Threshold Wavelength-Switchable Organic Nanowire Lasers Based on Excited-State Intramolecular Proton Transfer. *Angewandte Chemie International Edition* **2015,** *54* (24), 7125-7129.

28. Muccini, M., A bright future for organic field-effect transistors. *Nature Materials* **2006,** *5*, 605.

29. Duan, X.; Huang, Y.; Agarwal, R.; Lieber, C. M., Single-nanowire electrically driven lasers. *Nature* **2003,** *421*, 241.

30. Anthony, J. E., Functionalized Acenes and Heteroacenes for Organic Electronics. *Chemical Reviews* **2006,** *106* (12), 5028-5048.

31. Zhang, Y.; Qiao, J.; Gao, S.; Hu, F.; He, D.; Wu, B.; Yang, Z.; Xu, B.; Li, Y.; Shi, Y.; Ji, W.; Wang, P.; Wang, X.; Xiao, M.; Xu, H.; Xu, J.-B.; Wang, X., Probing Carrier Transport and Structure-Property Relationship of Highly Ordered Organic Semiconductors at the Two-Dimensional Limit. *Physical Review Letters* **2016,** *116* (1), 016602.

32. Spano, F. C., Optical microcavities enhance the exciton coherence length and eliminate vibronic coupling in J-aggregates. *The Journal of Chemical Physics* **2015,** *142* (18), 184707.

33. Beljonne, D.; Yamagata, H.; Brédas, J. L.; Spano, F. C.; Olivier, Y., Charge-Transfer Excitations Steer the Davydov Splitting and Mediate Singlet Exciton Fission in Pentacene. *Physical Review Letters* **2013,** *110* (22), 226402.

34. Yamagata, H.; Spano, F. C., Strong Photophysical Similarities between Conjugated Polymers and J-aggregates. *The Journal of Physical Chemistry Letters* **2014,** *5* (3), 622-632.

35. McCumber, D. E.; Sturge, M. D., Linewidth and Temperature Shift of the R Lines in Ruby. *Journal of Applied Physics* **1963,** *34* (6), 1682-1684.

36. Silsbee, R. H., Thermal Broadening of the M\"ossbauer Line and of Narrow-Line Electronic Spectra in Solids. *Physical Review* **1962,** *128* (4), 1726-1733.

37. Sears, V. F., Debye–Waller factor for elemental crystals. *Acta crystallographica. Section A, Foundations of crystallography 47* (4), 441-446.

38. Vainer, Y. G.; Kol'chenko, M. A.; Naumov, A. V.; Personov, R. I.; Zilker, S. J., Photon echoes in doped organic amorphous systems over a wide (0.35–50K) temperature range. *Journal of Luminescence* **2000,** *86* (3), 265-272.

39. Briseno, A. L.; Mannsfeld, S. C. B.; Reese, C.; Hancock, J. M.; Xiong, Y.; Jenekhe, S. A.; Bao, Z.; Xia, Y., Perylenediimide Nanowires and Their Use in Fabricating Field-Effect Transistors and Complementary Inverters. *Nano Letters* **2007,** *7* (9), 2847-2853.

40. (a) Debije, M. G.; Chen, Z.; Piris, J.; Neder, R. B.; Watson, M. M.; Müllen, K.; Würthner, F., Dramatic increase in charge carrier lifetime in a liquid crystalline perylene bisimide derivative upon bay substitution with chlorine. *Journal of Materials Chemistry* **2005,** *15* (12), 1270-1276; (b) Aghaei, E.; Haghighi, M., Enhancement of catalytic lifetime of nanostructured SAPO-34 in conversion of biomethanol to light olefins. *Microporous and Mesoporous Materials* **2014,** *196*, 179-190.

41. Palummo, M.; Bernardi, M.; Grossman, J. C., Exciton radiative lifetimes in two-dimensional transition metal dichalcogenides. *Nano letters* **2015,** *15* (5), 2794-2800.

42. (a) Liang, Q.; Liu, J.; Cheng, Z.; Li, Y.; Chen, L.; Zhang, R.; Zhang, J.; Han, Y., Enhancing the crystallization and optimizing the orientation of perovskite films via controlling nucleation dynamics. *Journal of Materials Chemistry A* **2016,** *4* (1), 223-232; (b) Shao, S.; Dong, J.; Duim, H.; Gert, H.; Blake, G. R.; Portale, G.; Loi, M. A., Enhancing the crystallinity and perfecting the orientation of formamidinium tin iodide for highly efficient Sn-based perovskite solar cells. *Nano Energy* **2019,** *60*, 810-816.

7 CONCLUSIONS AND PROSPECTS

7.1 Conclusions

In summary, this thesis has explored the extraordinary nonlinear light matter interactions through optical second harmonic generation (SHG) in low dimensional materials. 2D TMDs as the experimental platform are used to explore the nonlinear light matter interactions. Also, light matter interactions in 1D Pentacene nanowires are discussed as an additional study. We have used straining, folding, vapour deposition and thermal modulation to study extraordinary nonlinear light matter interactions in our samples.

Chapter 3 talks over the successful fabrication of folds and wrinkles in 1-3L WS_2 by controlling strain. Physical, electrical and optoelectronic characteristics of folds and wrinkles are investigated via atomic force microscopy (AFM), surface potential, current and photo-current measurements. Interlayer screening effect is found as the dominant factor causing layer dependent surface potential reduction for both perfect pack and twisted layers (folds) of ultrathin WS_2. Strain is found to tune semi conductive junction properties significantly which is ~12.5% reduction in Schottky barrier height per % strain where laser illumination causes further lowering of SBH due to photo generated carriers.

Chapter 4 discusses the investigation of extraordinary second harmonic generation in folds and strained wrinkles in ultrathin WS_2. SHG from twisted layers of folds follow vector superposition principle of SH wave vectors coming from individual folding layers, as a result, trilayer folds with 60^o folding angle show 9 times SHG enhancement due to the vector superposition of SH wave vectors coming from individual folding layers. Thus, polarization dependent SHG can be successfully used to determine the folding angle. Strain dependent SHG quenching and enhancement in the direction parallel and perpendicular respectively to the direction of the compressive strain vector is found in polarization dependent SHG. However, despite a variation in strain angle, total SHG remains constant which allows us to find the local strain vector using photoelastic approach. Band-nesting induced transition (C peak) is shown to highly enhance SHG, which can be significantly modulated by strain.

Chapter 5 is focused on temperature dependent SHG investigation in layered TMDs. SHG response is shown highly sensitive to temperature modulation in 2D TMDs using 900 nm laser excitation. Temperature dependent SHG is found to show opposite trends for single layer and few odd layers (3L, 5L, 7L, etc) of TMDs. A remarkable temperature dependent SHG enhancement (25.8%) is found in single layer $MoSe_2$ using 900 nm laser excitation whereas few odd layers show significant temperature dependent SHG quenching which is found to be -55.2%, -31.02% and -18.4% in case of 3L, 5L and 7L of $MoSe_2$. Temperature dependent SHG investigation with other TMDs i.e. MoS_2, WS_2 and WSe_2 shows the similar trend which reveals an important structural characteristic for TMDs. Second order non-linear susceptibility calculations considering weak Van der Waals forces in higher layer number (leading to variable symmetry for 1L and few odd layers) during thermal expansion in ultrathin TMDs show good agreement with the experimental findings.

Chapter 6 discusses light matter interactions in 1D Pentacene through optical PL spectroscopy as an additional study of light matter interactions in low dimensional materials. 1D Pentacene nanowires are grown on hBN (hexagonal Boron Nitride) using vapour deposition. 1D Pentacene is observed to show high crystalline features which are investigated through PL spectroscopy. High crystalline features are explained using Shpol' skii effect and we report the first experimental demonstration of Shpol' skii effect in a one-component organic solid-state system at low temperature. Zero phonon line (ZPL) emission is observed with width of ~1-2 nm and a high value of Debye-Waller factor (0.72) from our epitaxial grown high-crystalline and ordered 1D organic nanowire, which is attributed to specific molecular configuration and higher degree of orientation of molecules as compared to bulk thin film counterpart.

In sum, this thesis is focused on nonlinear light mater interaction in low dimensional materials for applications in next generation optoelectronic and nonlinear photonic devices.

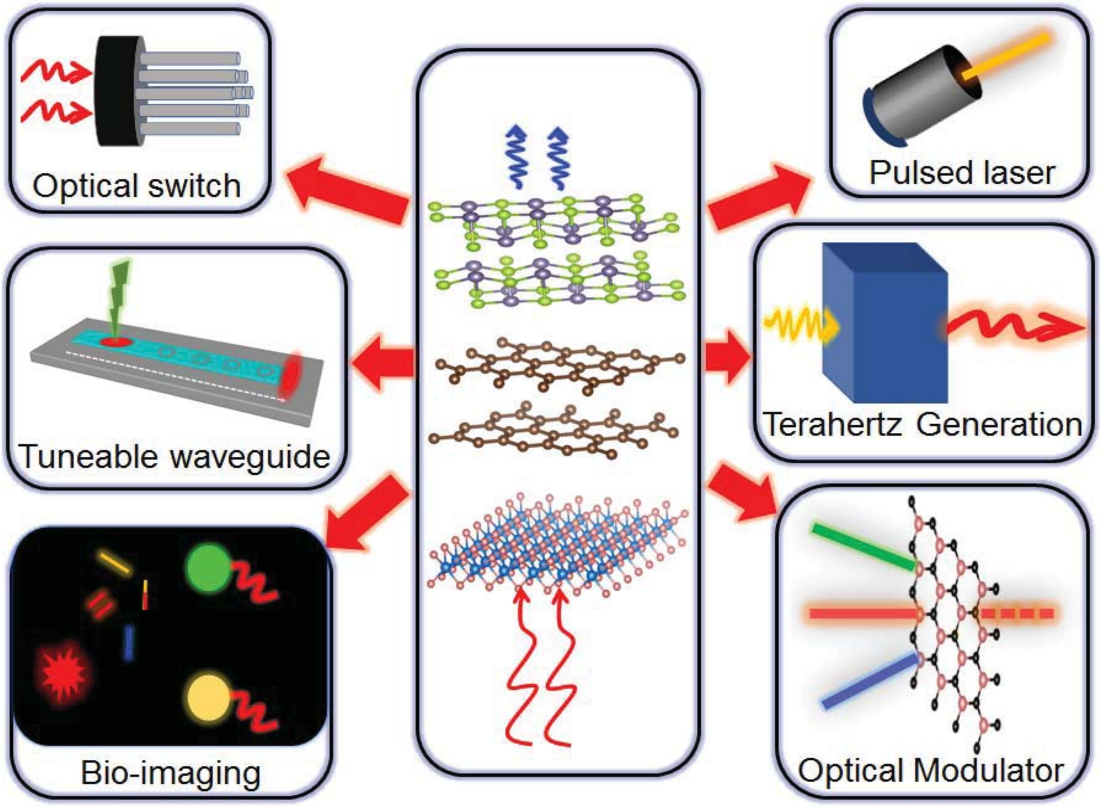

Figure 7.1 | Various prospects of optical harmonic generation for emerging applications in imaging and photonic devices

7.2 Applications and prospects

This thesis shows the extraordinary nonlinear responses achieved through folding, strain and thermal activity in low dimensional materials. This section will discuss about the device applications of nonlinear responses in low dimensional materials, their current progress, challenges and potential research directions ahead. Extraordinary light matter interactions in 2D materials can lead to numerous applications such as pulsed laser, bio-imaging and sensing, photonic devices and tera-hertz wave generation (Figure 7.1) which are stated as follow;

7.2.1 Ultrashort pulsed lasers

Ultrashort pulsed lasers have many applications in far-reaching fields, such as nonlinear imaging and microscopy, optical communications, military, micro- and nano-surgery, material processing, optical frequency comb and spectroscopy.[1] The optical harmonic generation gives the possibility of obtaining new frequencies when intensive pulsed laser radiation propagates through a non- linear environment which results in radiation generation with corresponding harmonics frequencies.[2] For example, green visible laser is achieved through the second harmonic generation when Nd:YAG laser (1064nm) is targeted on nonlinear KTP (potassium titanyl phosphate - $KTiOPO_4$) crystal. Similarly, Lithium Niobate ($LiNbO_3$) and LiB_3O_5 are also used to generate green laser (532nm) from Nd:YAG laser (1064nm).[2] The optical harmonic efficiency of a material is controlled by its saturable absorption which is the key factor for the optical harmonic conversion efficiency. Conventional materials show a limit to optical harmonic conversion which a minimal optical harmonic conversion efficiency.[3] Recently, researches on 2D materials have shown them as the suitable materials for ultra-short pulsed laser technology due to high absorption, ultrafast carrier recovery time, high optical harmonic conversion efficiency, and simple fabrication methods. Therefore, 2D materials are expected to be the potential materials for future laser technology. Various 2D materials are employed to check their potential for pulsed laser technology. For example, Graphene is found to generate coherent pulsed laser with good conversion efficiency from near IR to mid IR lasers.[4] The layer dependent optical harmonic generation in 2D TMDs and BP have been extensively studied for applications in laser technology. The bandgap at visible frequencies of TMDs shows efficient nonlinear conversion efficiency for visible pulsed lasers.[5–7] A series of 2D materials pulsed lasers have been developed in different configurations. The first TMDs based mode-locked laser with pulse duration of 800 ps was reported by Zhang et. al. using MoS_2 saturable absorber (SA) which was developed by depositing few-layered MoS_2 nanosheets.[8] The harmonic TMDs mode locked lasers are demonstrated to achieve high repetition rate fibre laser. A MoS_2 based mode-locked laser is reported with highest repetition rate of 2.5 GHz for 369*th* harmonic state with 3 ps pulse width.[9] Among the reported TMD mode-locked lasers, Tian et al. demonstrated the MoS_2 based laser with highest output power of 150 mW corresponding to a maximum pulse energy of 15.5 nJ and the shortest pulse duration was recorded as 935 fs.[10] A review on TMDs based pulse laser and graphene is reported by Chunyang et. al.[1] and Mohanraj et. al.[6] Our results show SHG tuning behaviour based on strain engineering, folding and thermal modulation. The strain dependent exciton peak shift allows us to get variable range of pulsed lasers.

7.2.2 Bio imaging

Optical harmonic generation has gained considerable popularity as an ideal method for imaging of live cells and tissues due to its large imaging depth, good resolution and reduction of photo damage in biological tissues.[11] For example, the use of near infrared excitation results in the ability to penetrate deeply into thick tissues because of reduced Rayleigh scattering, thus leading to the possibility of building a 3D image.[12] SHG, as a diagnostic tool, is used for the imaging of biological tissues such as membranes[13], collagen[14], myosin[11], microtubules, etc.

As the SHG microscope can selectively observe the non-inversion symmetric regions, therefore, non-symmetric structures, molecular ordering and structural organization in biological samples can be measured using SHG microscope. For example, SHG was successfully employed for the first time to observe the non-centrosymmetric structure of rat-tail tendon.[15] In another study SHG and THG were used to observe the Sebaceous gland and blood vessels in mouse.[16] The ordering of lipid molecules in the plasma membrane is estimated by comparing the SHG intensity coming from the polar dye molecules applied on membrane.[17,18] SHG, as a characterization tool for polar structures, is employed successfully for the imaging of polar structured proteins such as collagen myosin and microtubules in biological tissues.[19–24] As a result, various medical applications such as the diagnosis of collagen-related diseases and the detection of tumour-associated collagen as a cancer biomarker have been diagnosed using SHG microscopy due to their polar structures.[25–28] SHG, as affected by the electric field variation, can be employed to locate the sensitivity of neurons.[11,29] While some biological tissues show low intensity of SHG signal due to molecular symmetry, therefore, the membranes are stained with polar chromophores or amphiphilic polar dye molecules to enhance the SHG signal for imaging analysis.[30] SHG intensity comparison is beneficial to find the membrane and cell damage in biological tissues. In this context, a research is conducted on toxic material induced plasma membrane damage using SHG imaging. Amphiphilic dye molecules were introduced to enhance the quality of SHG imaging. An increasing degree of the disordering of membrane structure due to the concentration of the toxic material causes the SHG intensity (I_{SHG}) to drop. The fully destroyed membrane results in no SHG signal generation. Thus, the membrane damage would be able to be monitored by the I_{SHG} of the membrane. Similarly, positively charged micro-particles induced HeLa cells membrane were observed by the SHG microscope.[31] In a review[13], SHG microscopy was shown as a tool to investigate structural proteins from several tissue types i.e. tendon, bone, muscle, etc. Comparison of the SHG images provides the basis for identifying the molecular origin of biological tissues. Polarization anisotropy further probes the lateral and radial symmetry of the protein assemblies. Paul et. al. also highlighted optical second harmonic generation microscopy as an effective probe for the sensitive detection of cell membrane damage[26,32]

Recently, 2D materials are effectively used in various biomedical applications. For example, 2D MoS_2 was successfully used as a non-bleaching optical probe in biomedical diagnostics.[33] In addition, S6 ribonucleic acid aptamer conjugated graphene oxide was employed for selective two-photon imaging of SK-BR-3 breast tumour cell.[34] Even though research of 2D materials in bio-imaging applications is at the entry level, however, 2D materials are expected to open up new doors for biomedical imaging and sensing.

7.2.3 Photonic devices

A photonic integrated circuit (PIC) is a device that integrates multiple components to perform photonic functions or optical computing similar to an electronic integrated circuit.[35] Optical computing are proposed future techniques using photons which are expected to provide a fast speed, higher bandwidth data transfer with low power loss than the electrons used in conventional computers. Optical computing uses photonic logic, which is the use of photons in logic gates to implement logic functions (AND, OR, NOR, NAND, etc).[35–40] Optical harmonic generation along with other nonlinear optical processes such as sum frequency generation, difference frequency generation provide the main building blocks to implement photonic logic functions. However, a large obstacle for realizing photonic logic is the weak optical nonlinearity properties of the conventional materials causing large power consumption.[38] Here, we review the applications of nonlinear optics in some photonic devices such as frequency modulators, tuneable waveguides and optical switches, etc.

7.2.3.1 Optical modulators and tuneable waveguides

Optical modulators play an important role for various optical applications including signal processing, sensing and communication.[41]. Optical harmonic generation processes along with other nonlinear optical parametric processes such as sum-frequency generation(SFG), difference-frequency generation (DFG),etc are the important approaches to achieve tunable coherent radiation at optical frequencies that can hardly be obtained by lasers directly.[42] Low loss performance is vital for devices that operate in the terahertz regime (0.3–30 THz), because of the low efficiency offered by the available terahertz pulse generation methods. Low dimensional materials are expected to provide drastic improvements in both power-density and speed, which is able to overcome the limitations that have beset conventional photonic switches for decades.[43] In addition, 2D materials are expected to consume low power rates due to their low scale dimensions and phase matching.[44] In this regard, MXene, a graphene-like material, is successfully fabricated for optical modulation for an investigation in nonlinear optics which indicated that MXene could act as an information converter in an optical light-control-light system.[45]

A waveguide is a structure that guides waves, such as electromagnetic waves or sound, with minimal loss of energy by restricting the transmission of energy to one direction.[46]

Tunable waveguides are important building blocks of photonic circuits capable to tune and transmit the waves. The simplest and most fundamental tuneable waveguide is a waveguide second harmonic generation, where output frequency is doubled to the frequency of the input pump frequency. Optical harmonic generation waveguides offer coherent waves at wavelengths where no appropriate laser is available. Therefore, tuneable waveguide implementing high harmonic generation enables the generation of short wavelength beams.[47] Optical harmonic generation and other non-linear optical processes such as sum-frequency generation (SFG), and difference-frequency generation (DFG) are the most prominent approaches to obtain tuneable waves at optical frequencies hardly achievable by lasers directly.[42] 2D materials as compared to Conventional NLO crystals provide a more efficient way to provide tuneable waveguides due to phase matching and small scale.[44,48] For example, a WSe_2 monolayer based nonlinear plasmonic modulator is integrated on top of a lithographically defined metallic waveguide. The strong interaction between the surface plasmon polaritons (SPPs) and excitons in WSe_2 are reported to show 73 % change in transmission through the device. The nonlinear plasmonic modulator and waveguide mechanism showed an ultrafast response time of 290 fs.[49] Techniques such as thickness modulation, strain engineering, lattice variation, etc can be used to optimize the performance of 2D materials based optical modulators and tuneable waveguides.

7.2.3.2 Optical switches

All-optical switches are other interesting optical devices which are basic structures for optical logic gates and modulators.[50] An optical switch is a device that selectively switches optical signals on or off or from one channel to another, therefore, it provides a practical pathway for focusing and guiding light leading to next-generation power-efficient optical networks as controlling light with light is the key to fast optical processing. A demonstration is conducted to explore the photoactive properties of MoS_2 to find its suitability for fast response optical switching which shows 2D materials as efficient options for next generation optical switches.[44] Optical nonlinearity phenomena are expected to demonstrate efficient ways of photonic switching for 2D materials as well. Graphene, with an efficient THG conversion efficiency, is used to design a highly efficient and low power frequency-selective all-optical switch in terahertz range using Graphene.[50] Apart from that, MXene, a graphene-like material, is successfully fabricated for a novel all-optical switcher. Through modulation of the pump light, the "ON" and "OFF" modes in the all-optical switcher/modulator are designed to be achieved.[45]

Our results show SHG tuning behaviour based on strain engineering, folding and thermal modulation allows us to optimize the range, sensitivity and efficiency of the photonic devices.

7.2.4 Generation of terahertz radiation

There is a high demand of efficient function materials capable of supporting very high frequencies (i.e terahertz range ~10-12 Hz) for applications in modern ultrahigh-speed electronic. In addition, terahertz radiation has numerous applications in biomedical imaging, remote sensing, security and spectroscopy.[51,52] Traditional sources show lack of support for efficient THz technology at room temperature causing a limit to its practical applications. However, several theoretical proposals have shown efficient THz frequency generation in ultra-thin graphene at room-temperature using optical harmonic generation.[53,54] As Optical harmonic generation allows the conversion of optical or electronic signals into signals with much higher frequency, optical harmonic generation in graphene is predicted to be particularly efficient at the technologically important terahertz frequencies due to the unique electronic band structure of graphene.[53,54] The generation of terahertz harmonics up to the seventh order in single-layer graphene at room temperature was shown by Hafez et al.[51] with field conversion efficiencies in excess of 10^{-3}, 10^{-4} and 10^{-5} forthe third, fifth and seventh terahertz harmonics, respectively. These conversion efficiencies are remarkably high, given that the electromagnetic interaction occurs in a single atomic layer. In another study, the generation of coherent 0.1 to 4 THz via second-order nonlinear effect was experimentally demonstrated in graphene due to photon drag effect via femtosecond pulse excitation.[55] Various researches are reported on waves modulation in THz regime using Nonlinear optics in Graphene.[56,57] As THz relies on photon-drag effect, gating voltage modulated THz is experimentally achieved at room temperature.[58]Furthermore, an enhancement (~ three orders of magnitude) in THz generation is shown by Raeis-Zadeh et al.[59] using Plasmon drag effect. TMDs are predicted to display low absorption over broadband THz frequencies. Even though, there is a lack of experimental evidence on THz generation using optical HG in TMDs. Researchers reported MoS_2 coated metamaterials to modulate THz rays.[60] THz radiation is expected to be obtained in a large number of monolayers and few-layers leading to extend applications of 2D materials.[61] Tellurene, recently, is shown as a broad range multifunctional material for mid infrared range (150THz-500THz)[62] which needs to be explored further. Jinhui Shi et. al. reviewed 2D materials based emerging THz devices and highlighted nonlinear characteristics of 2D materials for THz regime.[63,64]

Our results show strain engineering, folding and thermal modulation based SHG tuning behaviour which allows us to optimize the efficiency of THz generation. Efficient THz generation need more 2D materials to be explored displaying strong nonlinear properties at THz ranges for efficient device making.

APPENDICES

APPENDIX A1: METHODS SECTION FOR CHAPTER 3

Sample Fabrication. WS_2 flakes were exfoliated onto buckled elastomeric substrate (Gel-Film® WF 6.0mil ×4 films) using scotch tape. Subsequently, the Gel film is suddenly released, generating well-aligned folds and wrinkles in WS_2 layers due to the application of compressive forces because of the sudden release. Sudden release of the pre-stress films was found to give a higher yield of folds and wrinkles in WS_2 layers. Strained WS_2 sample was transferred onto Au/SiO_2/Si electrode substrates followed by adhesively bonding an iron pad using copper tape to connect with AFM for further characterizations. AFM, PSI and Raman spectroscopy were used to detect the layer numbers.

Surface Potential Measurements. Surface potential measurements were done using AFM (Asylum Research, Cypheras) after carrying out the procedures described in the Sample Fabrication section. Pt/Ir coated Si tip (nanosensor PPP-EFM) with a calibrated spring constant ~ 1.9 N/m and radius of 28 ± 10 nm was used to conduct KFPM measurement. The tip was scan above ~ 10 nm higher than the surface in the noncontact mode with a drive frequency of 70 kHz and 1 V AC voltage. The SP mapping images by KPFM (scan size: 3μm ×3μm) were obtained, where the temperature was maintained at room temperature.

Dark and Photo-current Scanning. The Current and Photocurrent measurements were conducted on AFM in ambient conditions using Pt. tip, as illustrated in Figure 3a. Contact mode was used during the current scanning AFM. Topographic and Current images were obtained simultaneously so that topography and local currents can be compared directly. Most images were 512×512 pixels. For photo-current measurements, the illumination source was 532 nm laser. During certain measurements, neutral density filters were used to modulate the laser intensity. AFM images were analysed and plotted using the Gwyddion software package.

APPENDIX A2: METHODS SECTION FOR CHAPTER 4

Buckled Sample Fabrication. (i) WS_2 flakes are first exfoliated onto pre-buckled Gel-Film using scotch tape. (ii) Subsequently, the Gel film is released causing compressive forces on exfoliated WS_2 flakes generating well-aligned wrinkles perpendicular to the direction of the compressive forces; seem to cross the different layered samples. (iii-iv) The wrinkles fall down to form trilayer folds in 1-3L WS_2 whereas higher layered numbers (such as 5L) maintain their wrinkles' like curvature[1] (**Figure 4.1a)**. Strained WS_2 samples are transferred on a $Si/SiO_{2/}$ substrate.[2]

Experimental SHG setup. We perform SHG measurements on Zeiss 780 Confocal Microscopy. The fundamental laser field is provided tunable pulse laser Ti:sapphire laser with a pulse width of 150 fs and a repetition rate of 80 MHz. A 50× confocal objective lens (NA = 0.85) is used to excite the sample. SHG measurements are taken on fundamental laser wavelength 900nm. The reflected SH signal is collected by the same objective, separated by a beam splitter and filtered by suitable optical filters to block the reflected fundamental radiation. The SH character of the detected radiation is verified by its wavelength and quadratic power dependence on the pump intensity. Laser with tunability range (800nm-1040nm) is used for wavelength dependent SHG. For polarization resolved SHG, an analyzer (polarizer) is used to select the polarization component of the SH radiation parallel to the polarization of the pump beam. The sample is rotated by a rotational stage to obtain the orientation dependence of the SH response.

Simulations. In the present work, the plane-wave method in the framework of DFT using Abinit code is employed. Local density approximation is used for the exchange-correlation effect, and the energy cutoff of 52 Ry is chosen for the electron wave function expansion. A vacuum layer thicker of more than 10 Å is included to avoid interaction between periodic layers. The *k*-point sampling is 24×24×1 for the prime cell of 5L WS_2.

References for Annexure A1-A4

(1) Castellanos-Gomez, A.; Roldán, R.; Cappelluti, E.; Buscema, M.; Guinea, F.; Van Der Zant, H. S. J.; Steele, G. A. Local Strain Engineering in Atomically Thin MoS2. *Nano Lett.* **2013**, *23* (11), 534.

(2) Xu, R.; Yang, J.; Zhu, Y.; Yan, H.; Pei, J.; Myint, Y. W.; Zhang, S.; Lu, Y. Layer-Dependent Surface Potential of Phosphorene and Anisotropic/Layer-Dependent Charge Transfer in Phosphorene-Gold Hybrid Systems. *Nanoscale* **2016**, *8*, 129–135.

APPENDIX A3: METHODS SECTION FOR CHAPTER 5

Experimental SHG setup. The SHG measurements are performed on Zeiss 780 Confocal Microscopy with repetition rate ~ 80 MHz and 150 fs pulse width (Ti:sapphire) tuneable pulse. SHG measurements are taken at 900nm laser excitation. The reflected SH signal is collected by the same objective, separated by a beam splitter and filtered by suitable optical filters to block the reflected fundamental radiation. The SH character of the detected radiation is verified by its wavelength and quadratic power dependence on the pump intensity. For temperature dependent measurements, the sample is placed into a Linkam THMS 600 chamber. A temperature controller equipped with a heating source (thermos-couples) and cooling source (liquid nitrogen) is used to control the temperature of the sample.

APPENDIX A4: METHODS SECTION FOR CHAPTER 6

Material growth. h-BN flakes were mechanically exfoliated onto a thermally grown 285 nm thick SiO_2 layer deposited over silicon substrate. Before physical vapor deposition (PVD), optical microscope was used to characterize the topological information. The pentacene (purchased from Chem Supply: P0030-1G) was then deposited over the h-BN flakes, kept cantered in a vacuum tube in the furnace. h-BN sheet on SiO_2/Si substrate was placed around 15 cm downstream and a molecular pump was used to evacuate the quartz tube to ~10^{-4} mbar. The furnace was heated up to 135-185°C for various time intervals to grow PEN wires. (See S.I. Note 1). Then, the whole system was naturally cooled down to room temperature under vacuum. All the samples were characterized, and layer thickness were identified using the standard AFM measurements, which were collected in ambient atmosphere at room temperature with a Bruker Multi-Mode III AFM. For the MOS structure, used for back gate-dependent PL measurements, we transferred the 100 nm thick gold electrode to contact part of the 1D PEN nanowire as the probing pad. The voltage was supplied using a Kiethly 4200 semiconductor analyser.

Optical Characterization. PL measurements at room temperature and 77 K were conducted using a Horiba LabRAM system equipped with a confocal microscope, a charge-coupled device (CCD) Si detector, and a 532 nm diode-pumped solid-state (DPSS) laser as the excitation source. The laser excitation spot was 0.5 µm in size calibrated using pinhole and confirmed using direct CCD imaging technique. The laser power excitation density was 525.5 W/cm^2 unless otherwise specified. The laser beam was gaussian in nature and was focused on the middle cross-section of the wire for all measurements. For temperature-dependent (above 77 K) measurements, the sample was placed into a microscope-compatible chamber with a low temperature controller (using liquid nitrogen as the coolant). In the experiment, the incident polarization angle was controlled by an angle-variable half-wave plate and was fixed, and the polarization angle of the emission (θ) was determined by using an angle-variable polarizer located in front of the detector. Time resolved PL measurements were conducted in a setup which incorporates μ-PL spectroscopy and a time-correlated single photon counting (TCSPC) system. A linearly polarized pulse laser (frequency doubled to 522 nm, with 300 fs pulse width and 20.8 MHz repetition rate) was directed to a high numerical aperture (NA= 0.7) objective (Nikon S Plan 603). PL signal was collected by a grating spectrometer, thereby either recording the PL spectrum through a charge coupled device (CCD; Princeton Instruments, PIXIS) or detecting the PL intensity decay by a Si single-photon avalanche diode (SPAD) and the TCSPC (PicoHarp 300) system.

APPENDIX A5: SUPPLEMENTARY INFORMATION FOR CHAPTER 3

A5.1. Strained Sample Fabrication

Strained WS_2 flakes by exfoliating WS_2 nano-layers are fabricated onto buckled elastomeric substrate (Gel-Film® WF 6.0mil ×4 films) using scotch tape. Gel-Film® is Polyester based commercially available elastomeric film. Subsequently, the Gel film is released to generate compressive forces on WS_2 nano-layers as sudden release causes compression force generating well-aligned folds and wrinkles in WS_2 layers. It is found that sudden release of the pre-stress films gives a higher yield of folds and wrinkle nanostructures within WS_2 flakes. The mechanism behind the formation of these folds and wrinkles is buckling-induced delamination. Such strained WS_2 samples were then transferred onto Si/SiO_2/Gold electrode substrates for further characterization.

A5.2. Layer number identification of WS_2 on Si/SiO_2 substrate.

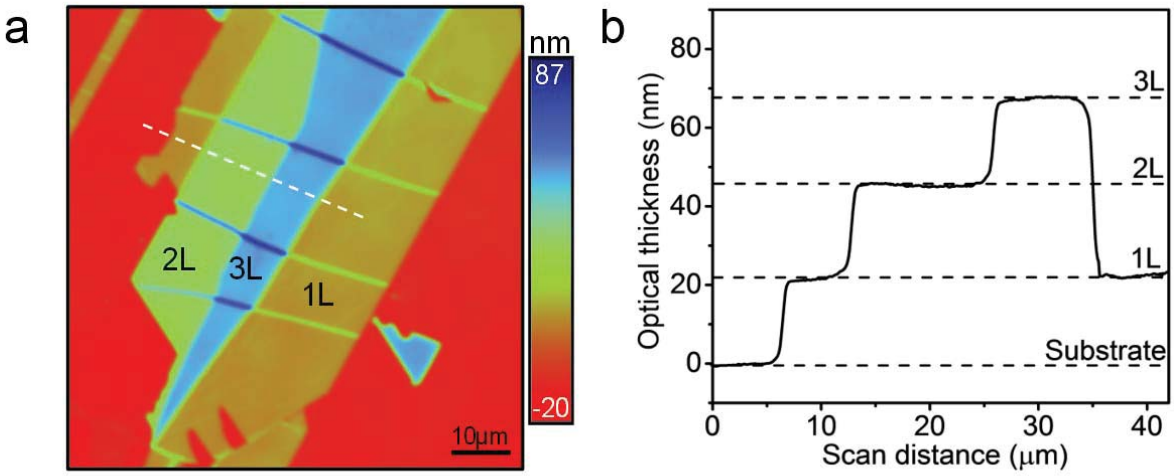

Figure A5.1 | Layer number identification of WS_2 on Si/SiO_2 substrate.
(a) PSI (Phase Shifting Interferometer) image of WS_2 flakes showing 1L, 2L and 3L. (b) PSI-measured *optical path length* (*OPL*) values showing layer number for 1-3L WS_2 along the white dashed line in (b) using the methods described in[1,2,3]

A5.3. Fold formation in 1-3L WS_2

This section describes the fold formation in 1-3L WS_2. Investigating the strained WS_2 sample, it is observed that the edges before and after big wrinkles (perpendicular to the direction of compressive forces) are not collinear (**Figure A5.2a**), instead are displaced by few tens of nanometres which showed the wrinkle to fold transition in ultra-thin WS_2.

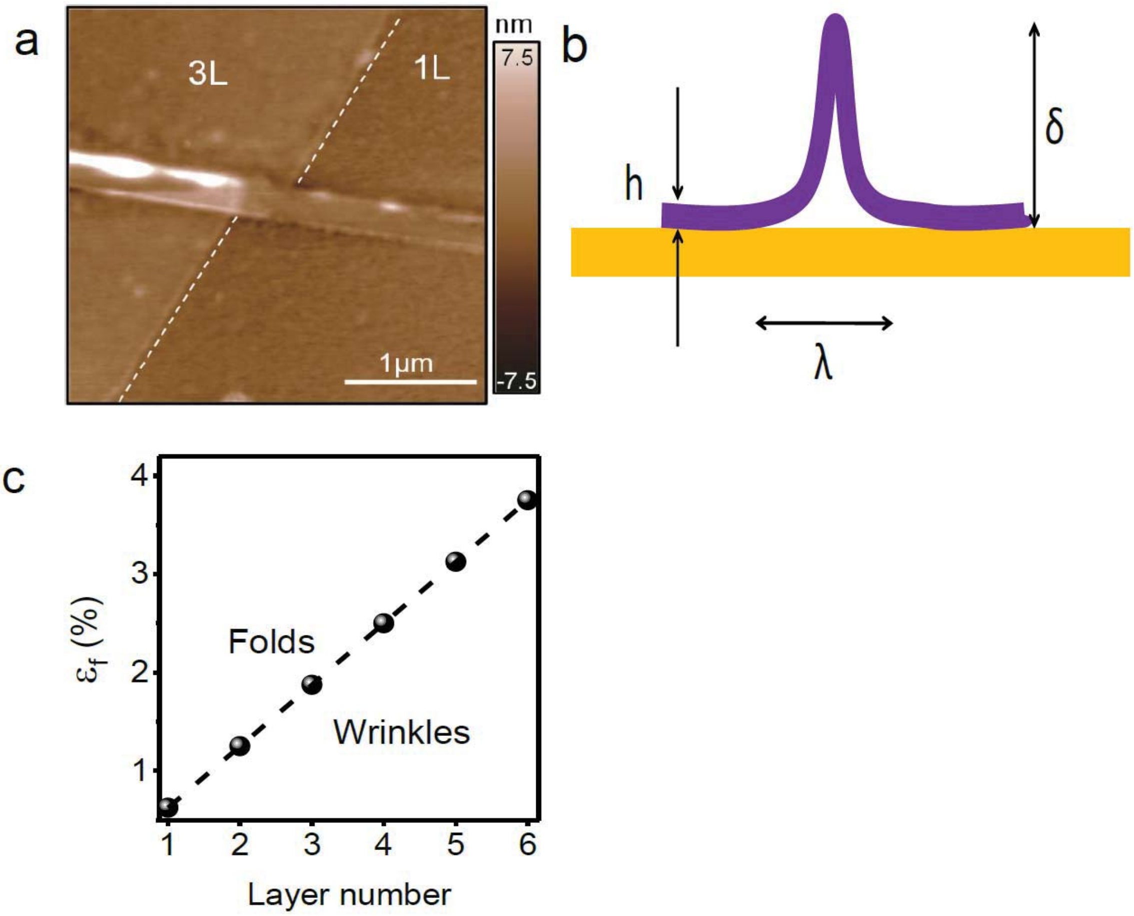

Figure A5.2 | Fold formation in 1-3L WS_2.
(a) AFM topography image of a strained WS_2. The white dashed lines indicate that the edges before and after the fold are not collinear, thus, showing the collapse of the wrinkles during the buckling-induced delamination process. (b) Analysis of the strain required for fold formation, h, λ and δ are thickness, width and height of WS_2 sheet. (c) Layer dependent folding strain (ε_f) calculation for 1-6L. Wrinkles maintain their curvature before $\varepsilon_{f\,(\%)}$ and become fold after $\varepsilon_{f\,(\%)}$

We found that big wrinkles cannot maintain their wrinkles' curvature and tend to collapse forming folds,^{4} and therefore, their height is found to be much smaller than tiny wrinkles. The total height measured on 1L, 2L and 3L samples match the height of 3L, 6L and 9L. We found tiny wrinkles' (formed parallel to the direction of compressive forces) height is greater than folds height, showing that they maintain their wrinkles' shape. The minimum strain required to start the wrinkling process is called the critical strain for wrinkling[5] The wrinkles height and density of wrinkles increases as the applied strain increases.[6–8] Eventually, after a strain level (ε_f), wrinkles cannot maintain its curvature and collapse. The opposite layers of wrinkles join each other to form folds. The folding process is dominant in small layer numbers which is greater in 1L than the 2L and 3L (1L > 2L > 3L) due to smaller value of elastic modulus in 1L as compared to 2L and 3L. As the layer number increases, critical strain for folding (ε_f) increases and fold formation becomes almost absent in higher number layers (5L and higher) due to high bending rigidity [9,10]. Here, we present the theoretical framework that we employ to find the layer dependent effect on the strain required for folding for WS_2.

The maximum uniaxial strain ε is accumulated on top of the winkles and can be estimated as [9]

$$\varepsilon \sim \pi^2 h\delta/(1-\nu^2)\lambda^2 \qquad (1)$$

where ν is the Poisson's ratio (ν =2.2 for WS_2[11]), h is the thickness of the flake, and δ and λ^2 are the height and width of the wrinkle which were measured using atomic force microscopy (AFM). Yuri et. al.[5] approximated the critical strain required for wrinkle to fold transition in thin films as;

$$\varepsilon_f \sim \left(\frac{h}{L}\right)\left(\frac{E_f}{3E_s}\right)^{\frac{1}{3}} \qquad (2)$$

where h is the thickness of the flake, E_f is the elastic modulus of the film (WS_2) and E_s is the elastic modulus of the substrate (Gel film). For E_f (WS2), we use the relation as under;

Elastic Modulus = E_{2D}/h [12] , where E_{2D} is 149 N/m[13] for 1L WS_2 and h=0.7nm for 1L give us $E_f(WS_2)$ = 198.6 GPa, As Gel-film is a polyester based elastomer material and E_s = 0.92 GPa.[14] L is the sample length to define the boundary of the region where folding is expected. In order to compare the folding strain among layer numbers, we calculate ε_f by taking L as the length of unit wrinkle along the direction of the force or average width of a wrinkle (500nm). **Figure A5.3** shows layer dependent folding strain (ε_f) calculation for 1-6L. Wrinkles maintain their curvature before $\varepsilon_{f\,(\%)}$ and become fold after $\varepsilon_{f\,(\%)}$. Taking an average 1L tiny wrinkle size with 150 nm width, 7 nm height gives us an approximated 0.05% which is below than 0.63% which is calculated critical folding strain for 1L. As layer number increases, folding strain increases linearly (**Figure A5.3**), therefore, we experience wrinkle to fold transition dominant in few layer numbers whereas higher layer numbers maintain their wrinkle like curvature.[4] [10]

A5.4. Layer dependent surface potential in 1-3L WS_2

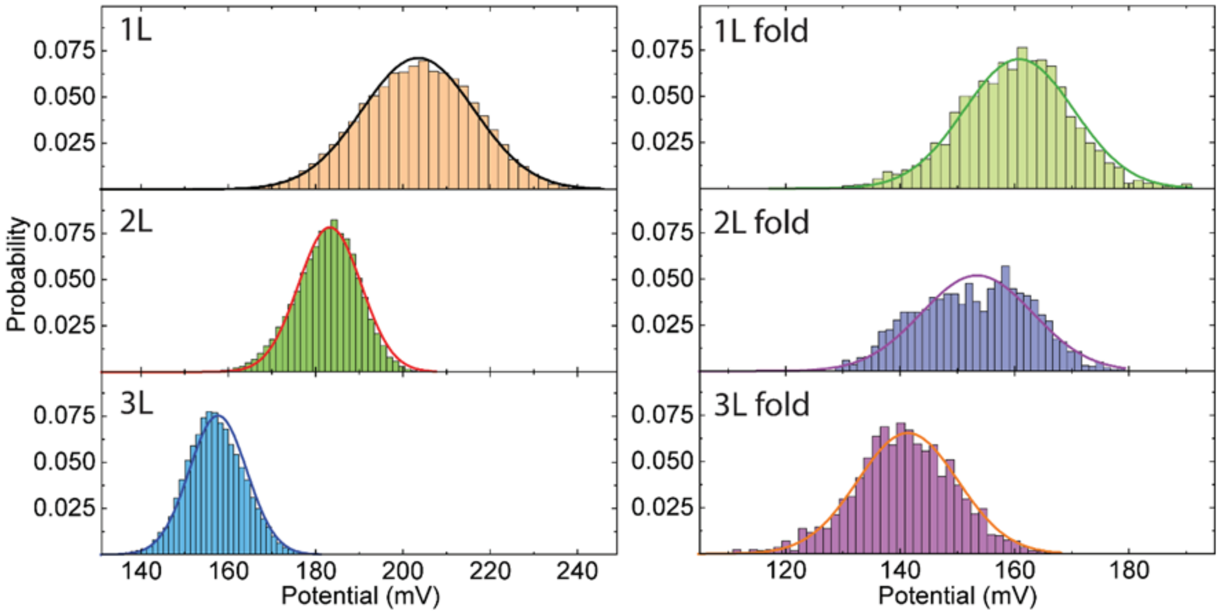

Figure A5.3. Histograms of the surface potential values collected at the 1-3L flat and folded regions

A5.5. Dependence of photocurrent on bias voltage in strained WS_2

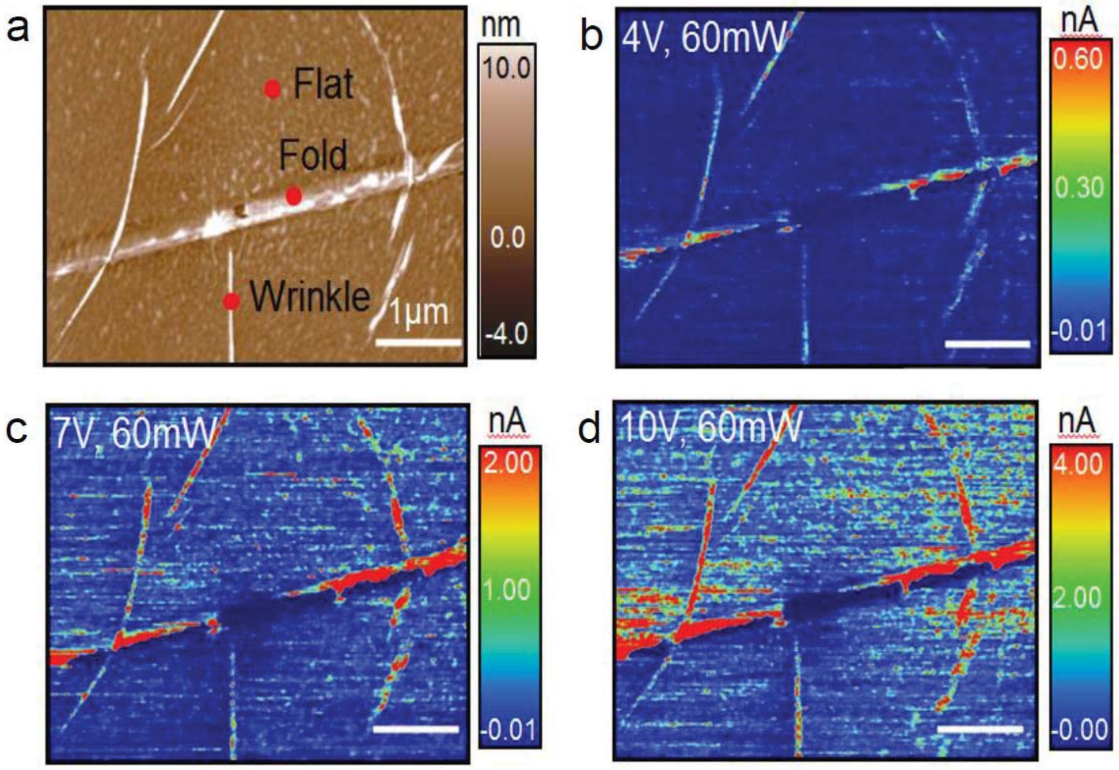

Figure A5.4 | Dependence of photocurrent on bias voltage in 1L WS_2.
(a) Topographical image of the sample using atomic force microscopy showing flat, fold and wrinkle regions. (b)-(d) PCAFM based photocurrent maps of the sample in (a) at forward bias voltages of (b) 4 V, (c) 7 V, and (d) 10 V, scale bars in figure b-d represent 1μm.

A5.6. Time-dependent photocurrent characteristics

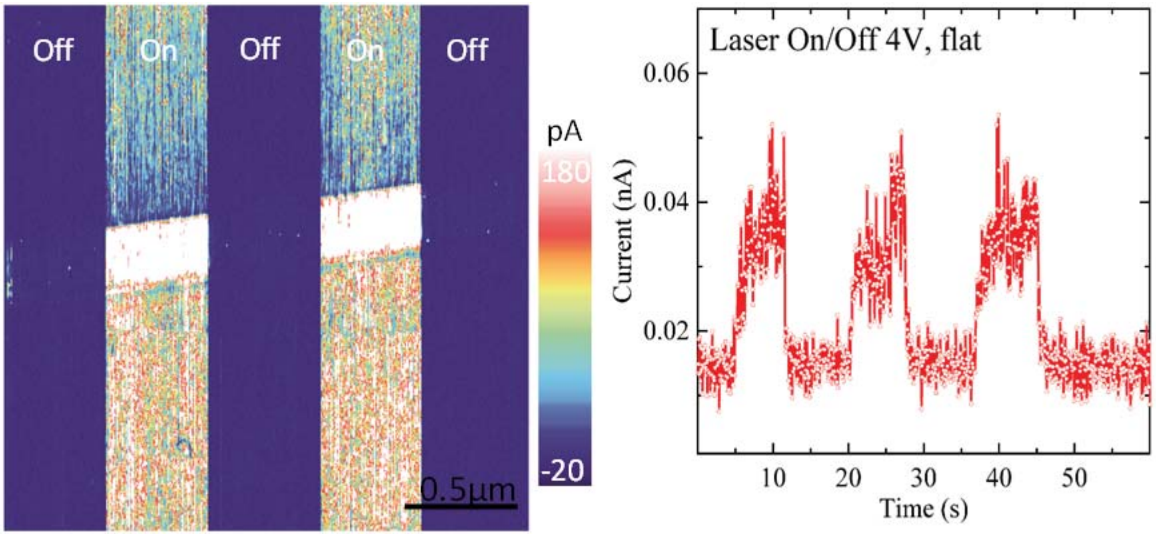

Figure A5.5. Time-dependent photocurrent characteristics obtained under bias of 4 V with periodically switching on/off incident laser.

A5.7. Dependence of surface potential on laser power

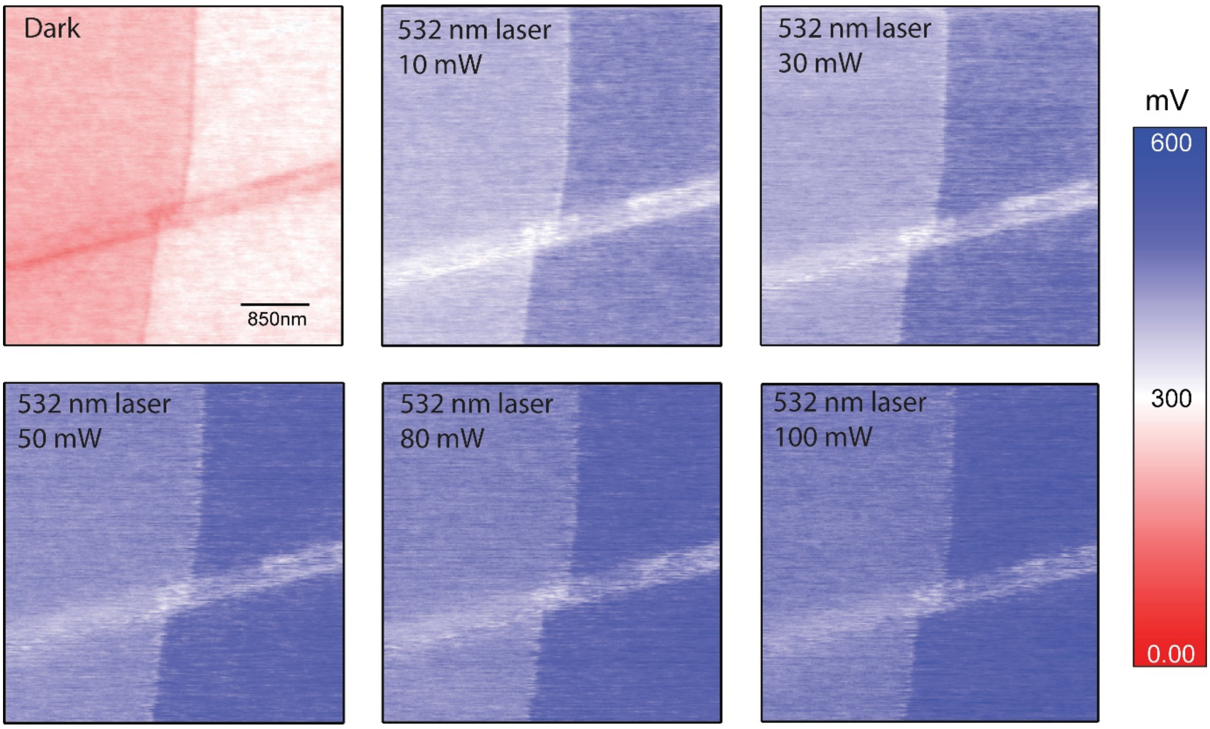

Figure A5.6 | Dependence of surface potential on laser power.
The surface potential mapping on both 1L and3L flat and wrinkled regions under different incident laser power.

A5. References

(1) Yang, J.; Wang, Z.; Wang, F.; Xu, R.; Tao, J.; Zhang, S.; Qin, Q.; Luther-Davies, B.; Jagadish, C.; Yu, Z.; et al. Atomically Thin Optical Lenses and Gratings. *Light Sci. Appl.* **2016**.

(2) Pei, J.; Yang, J.; Lu, Y. Elastic and Inelastic Light-Matter Interactions in 2D Materials. *IEEE J. Sel. Top. Quantum Electron.* **2017**, *23* (1).

(3) Pei, J.; Gai, X.; Yang, J.; Wang, X.; Yu, Z.; Choi, D. Y.; Luther-Davies, B.; Lu, Y. Producing Air-Stable Monolayers of Phosphorene and Their Defect Engineering. *Nat. Commun.* **2016**.

(4) Deng, S.; Berry, V. Wrinkled, Rippled and Crumpled Graphene: An Overview of Formation Mechanism, Electronic Properties, and Applications. *Mater. Today* **2016**, *19* (4), 197–212.

(5) Ebata, Y.; Croll, A. B.; Crosby, A. J. Wrinkling and Strain Localizations in Polymer Thin Films. *Soft Matter* **2012**, *8* (35), 9086–9091.

(6) Androulidakis, C.; Koukaras, E. N.; Pastore Carbone, M. G.; Hadjinicolaou, M.; Galiotis, C. Wrinkling Formation in Simply-Supported Graphenes under Tension and Compression Loadings. *Nanoscale* **2017**, *9* (46), 18180–18188.

(7) Pocivavsek, L.; Dellsy, R.; Kern, A.; Johnson, S.; Lin, B.; Lee, K. Y. C.; Cerda, E. Stress and Fold Localization in Thin Elastic Membranes. *Science (80-.).* **2008**, *320* (5878), 912–916.

(8) Auguste, A.; Yang, J.; Jin, L.; Chen, D.; Suo, Z.; Hayward, R. C. Formation of High Aspect Ratio Wrinkles and Ridges on Elastic Bilayers with Small Thickness Contrast. *Soft Matter* **2018**, *14* (42), 8545–8551.

(9) Castellanos-Gomez, A.; Roldán, R.; Cappelluti, E.; Buscema, M.; Guinea, F.; Van Der Zant, H. S. J.; Steele, G. A. Local Strain Engineering in Atomically Thin MoS2. *Nano Lett.* **2013**, *23* (11), 534.

(10) Castellanos-Gomez, A.; van der Zant, H. S. J.; Steele, G. A. Folded MoS2layers with Reduced Interlayer Coupling. *Nano Res.* **2014**, *7* (4), 1–7.

(11) Brau, F.; Damman, P.; Diamant, H.; Witten, T. A. Wrinkle to Fold Transition: Influence of the Substrate Response. *Soft Matter*. 2013, pp 8177–8186.

(12) Jiang, J.-W. Graphene versus MoS2: A Short Review. *Front. Phys.* **2015**.

(13) Hess, P. Prediction of Mechanical Properties of 2D Solids with Related Bonding Configuration. *RSC Adv.* **2017**, *7* (47), 29786–29793.

(14) Gündüz, G.; Erol, D.; Akkaş, N. Mechanical Properties of Unsaturated Polyester-Isocyanate Hybrid Polymer Network and Its E-Glass Fiber-Reinforced Composite. *J. Compos. Mater.* **2005**, *39* (17), 1577–1589.

APPENDIX A6: SUPPLEMENTARY INFORMATION FOR CHAPTER 4

A6.1. Strained samples fabrication

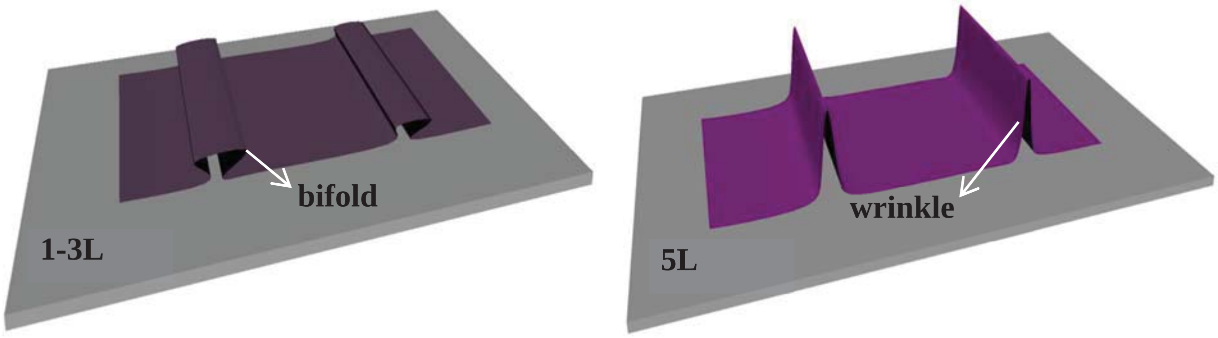

Figure A6.1 | Description of strained samples fabrication.
(a) Bifold formation in 1-3L. (b) Wrinkle formation in >3L respectively.

WS_2 flakes are first exfoliated onto pre-buckled Gel-Film using scotch tape. Subsequently, the Gel film is released causing compressive forces on exfoliated WS_2 flakes generating well-aligned wrinkles perpendicular to the direction of the compressive forces; seem to cross the different layered samples. The wrinkles fall down to form bifolds in 1-3L WS_2 whereas higher layered numbers (such as 5L) maintain their wrinkles' like curvature.[1] (**Figure A6.1a)** An isometric view of folds (1-3L) and wrinkles (>3L) is shown in **Figure A6.1**. Strained WS_2 samples are transferred on a Si/$SiO_{2/}$ substrate.[2]

A6.2. Power dependence on SHG intensity

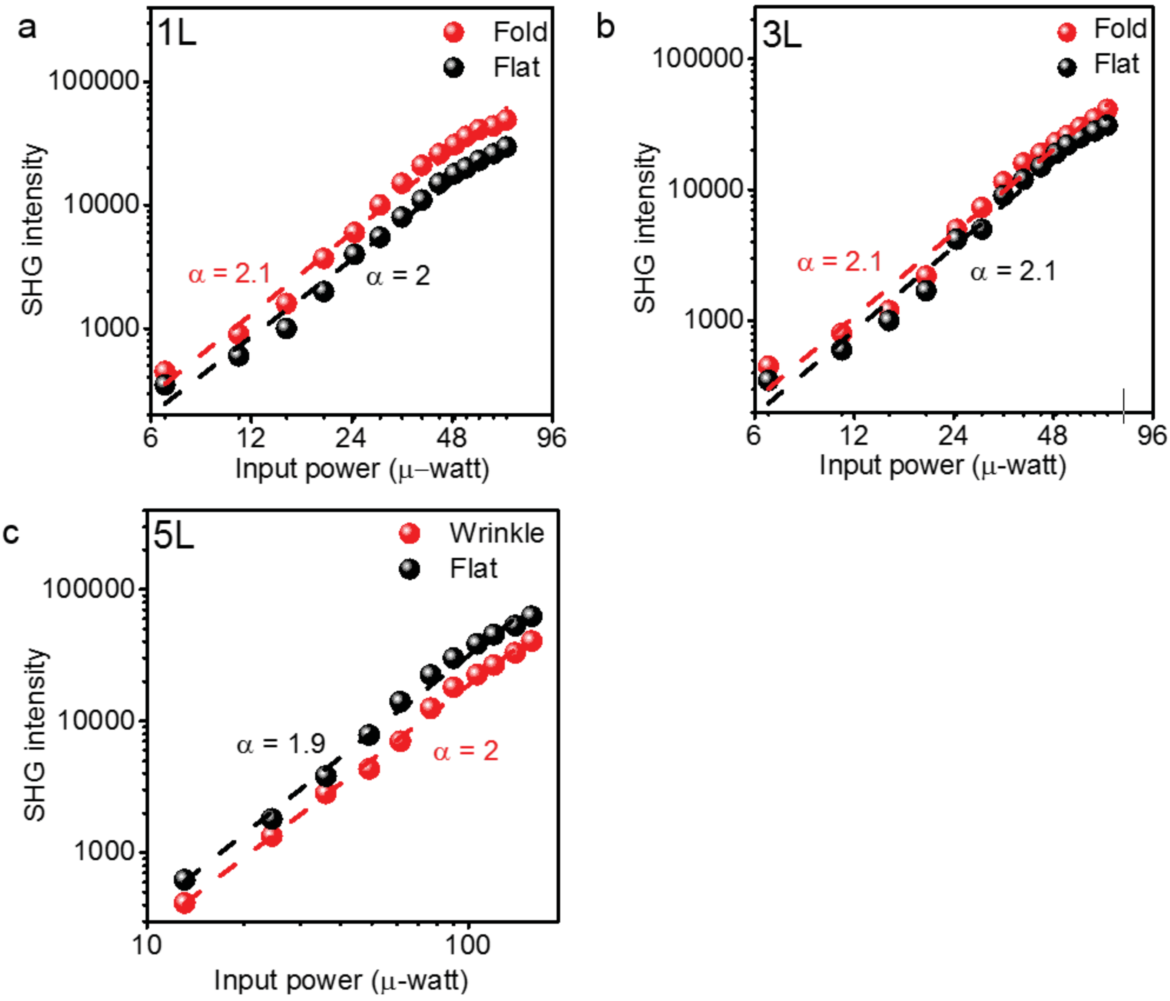

Figure A6.2 | Power dependence on SHG intensity
(a) Power dependent SHG intensity at 900nm pump laser in a logarithmic scale of folded/wrinkled and flat regions of 1L. (b) 3L. (c) 5L. The measured SHG intensity is shown as points and the dashed lines are the linear fits of the data.

A6.3. Layer dependent height of Folds/Wrinkles

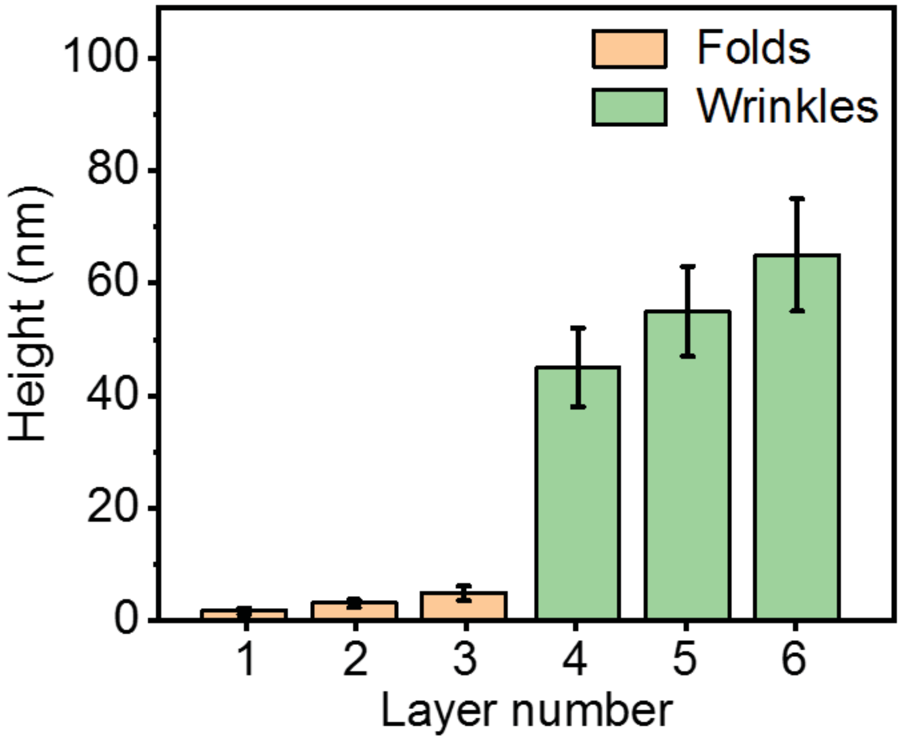

Figure A6.3 | Layer dependent height of Folds (1-3L) and Wrinkles (5-6L)

The height differences measured on wrinkle like protuberances in 1-3L buckled WS_2 are found to be 1.4 ± 0.5, 2.8 ± 0.5 and 4.2 ± 1 nm, respectively using Atomic Force Microscopy (AFM) measurements (**Figure A6. 2**). These values match the height of 2L, 4L and 6L samples very well as the thickness of single layer is evaluated around 0.7 nm[3], which agrees well with the reported value. Therefore, wrinkles like protuberances in 1-3L can be regarded as the trilayer folds. In a previous study on strain engineering, the formation of folds is also observed in ultrathin MoS_2 due to collapse of wrinkles which are attributed to reduced elastic modulus of ultrathin layers.[1,4] AFM investigations of wrinkles in 4-6L WS_2 show a rapid increase in the height (~40-75nm) which shows that >3L wrinkles in WS_2 maintain their curvature.

A6.4. Folding angle determination

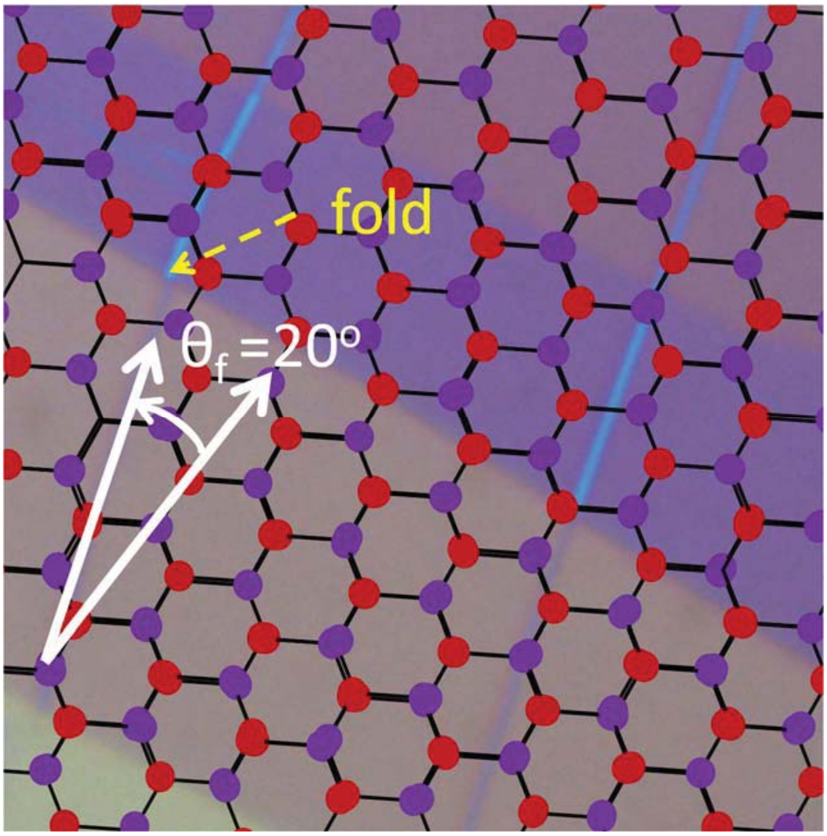

Figure A6.4 | Folding angle determination.

Folding angle (θ_f) is the angle between AC (armchair) direction and fold as shown in **Figure A6.4**. During parallel polarization SHG, maximum SHG signal is along AC direction.[5,6]

A6.5. Strain estimation on wrinkle nanostructures

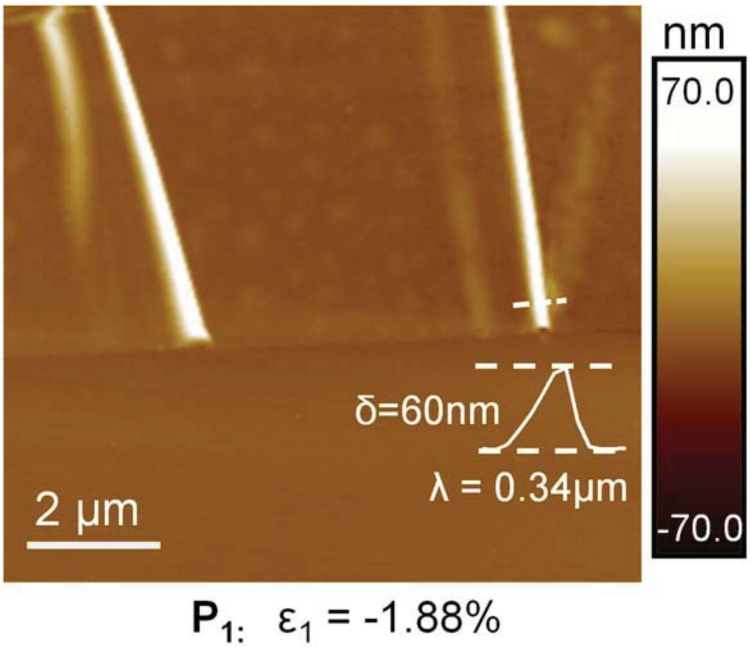

Figure A6.5 | Strain estimation on wrinkle.

Maximum strain on the wrinkle is produced at the top of the wrinkles and it can be estimated as under;[1]

$$\varepsilon \sim \pi^2 h\delta/(1-\nu^2)\lambda^2 \qquad (2)$$

where ν is the Poisson's ratio, h is the thickness of the flake, and δ and λ are the height and width of the wrinkle which were measured using atomic force microscopy (AFM). For P_1 point of the wrinkle $\delta = 60$nm, λ = 340nm, h = 3.5nm for 5L, ν = 0.22 for WS_2[7], strain is calculated ~ -1.88%. Negative sign is used due to compressive strain.

A6.6. Strain angle determination

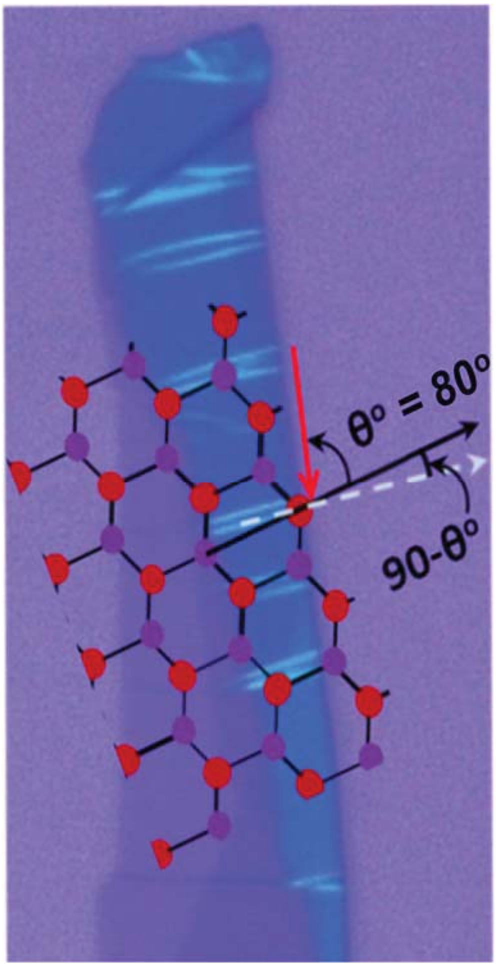

Figure A6.6 | Strain angle determination.

Strain angle (θ°) is the angle between strain direction (red arrow) and AC (armchair) direction. Parallel SHG polar plot is used to find the AC direction (black arrow). The compressive strain direction (red arrow) is perpendicular to the wrinkles. Thus, strain angle (θ°) is calculated ~ 80°.

A6.7. Wavelength dependent SHG of 3L fold

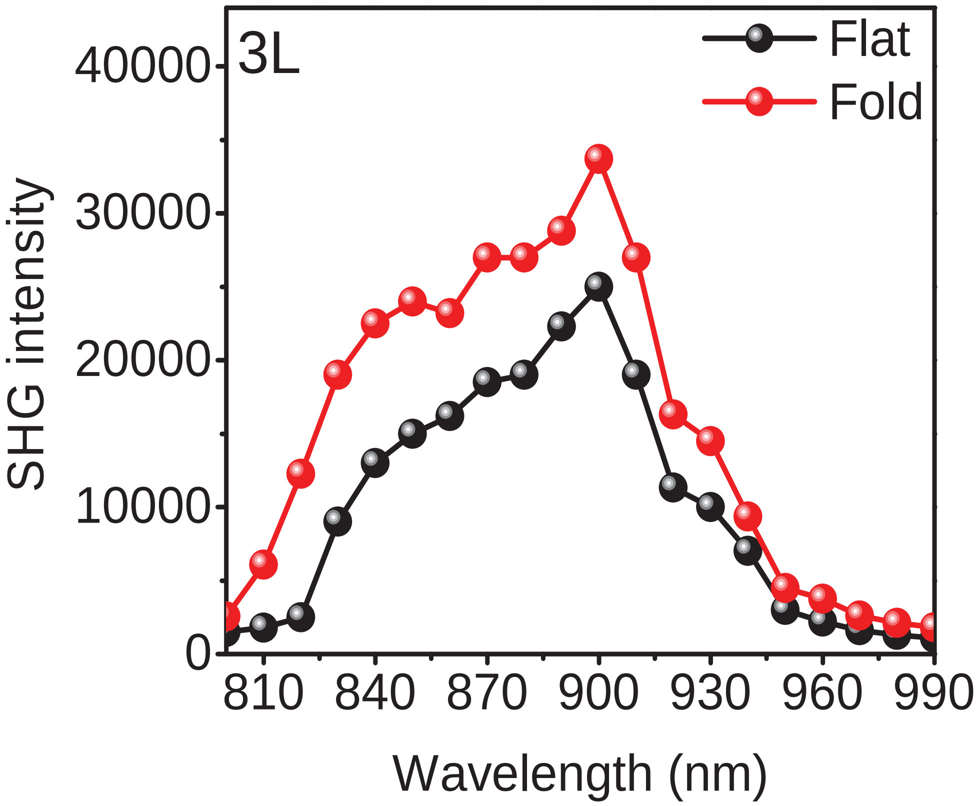

Figure A6.7 | Wavelength dependent SHG of 3L fold

A6. References

(1) Castellanos-Gomez, A.; Roldán, R.; Cappelluti, E.; Buscema, M.; Guinea, F.; Van Der Zant, H. S. J.; Steele, G. A. Local Strain Engineering in Atomically Thin MoS2. *Nano Lett.* **2013**, *23* (11), 534.

(2) Xu, R.; Yang, J.; Zhu, Y.; Yan, H.; Pei, J.; Myint, Y. W.; Zhang, S.; Lu, Y. Layer-Dependent Surface Potential of Phosphorene and Anisotropic/Layer-Dependent Charge Transfer in Phosphorene-Gold Hybrid Systems. *Nanoscale* **2016**, *8*, 129–135.

(3) Zhang, Y. Y.; Zhang, Y. Y.; Ji, Q.; Ju, J.; Yuan, H.; Shi, J.; Gao, T.; Ma, D.; Liu, M.; Chen, Y.; et al. Controlled Growth of High-Quality Monolayer WS 2 Layers on Sapphire. *ACS Nano* **2013**.

(4) Castellanos-Gomez, A.; van der Zant, H. S. J.; Steele, G. A. Folded MoS2layers with Reduced Interlayer Coupling. *Nano Res.* **2014**, *7* (4), 1–7.

(5) Li, Y.; Rao, Y.; Mak, K. F.; You, Y.; Wang, S.; Dean, C. R.; Heinz, T. F. Probing Symmetry Properties of Few-Layer MoS2 and h-BN by Optical Second-Harmonic Generation. *Nano Lett.* **2013**, *13*, 3329–3333.

(6) Wang, H.; Qian, X. Giant Optical Second Harmonic Generation in Two-Dimensional Multiferroics. *Nano Lett.* **2017**, *17* (8), 5027–5034.

(7) Liu, K.; Yan, Q.; Chen, M.; Fan, W.; Sun, Y.; Suh, J.; Fu, D.; Lee, S.; Zhou, J.; Tongay, S.; et al. Elastic Properties of Chemical-Vapor-Deposited Monolayer MoS 2 , WS 2 , and Their Bilayer Heterostructures. *Nano Lett.* **2014**, *14* (9), 5097–5103.

APPENDIX A7: SUPPLEMENTARY INFORMATION FOR CHAPTER 5

A7.1. Layer number identification of 1-8L $MoSe_2$

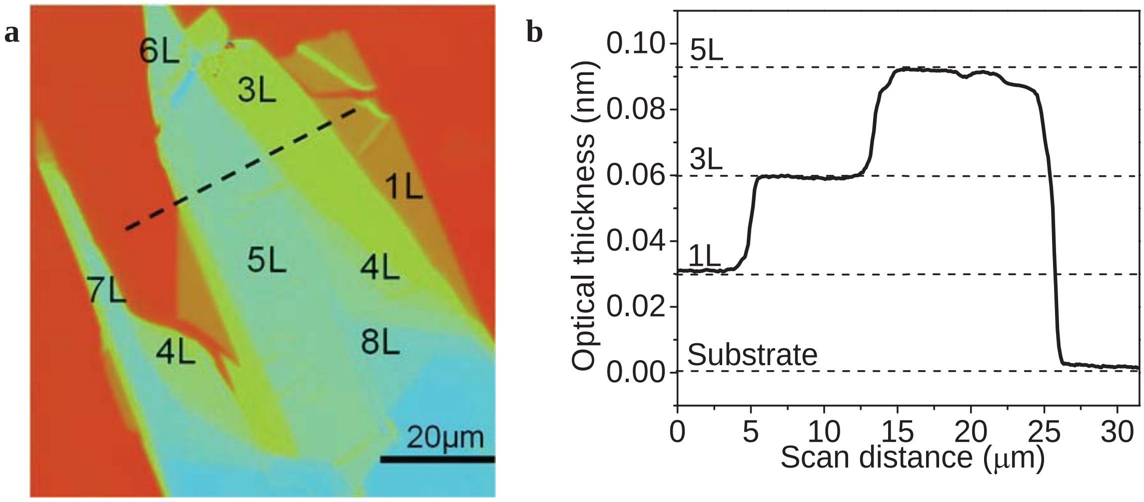

Figure A7.1 | Layer number identification of 1-8L $MoSe_2$ sample using Phase Shifting Interferometry. (a) PSI mapping of 1-8L $MoSe_2$ sample. (b) PSI-measured optical thickness values showing layer number for $MoSe_2$ sample along the black dashed line in (b) using the methods described in [1,2,3]

A7.2. Temperature dependent SHG of few layers WS_2

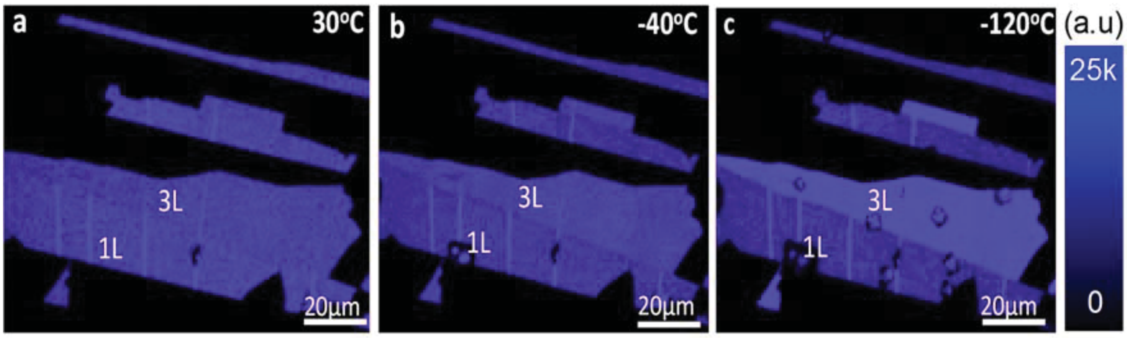

Figure A7.2 | Temperature Dependent SHG Mapping of 1-3L WS_2 at (a) 30°C. (b) -40°C. (c) -120°C.

A7. References

(1) Yang, J.; Wang, Z.; Wang, F.; Xu, R.; Tao, J.; Zhang, S.; Qin, Q.; Luther-Davies, B.; Jagadish, C.; Yu, Z.; et al. Atomically Thin Optical Lenses and Gratings. *Light Sci. Appl.* **2016**.

(2) Pei, J.; Yang, J.; Lu, Y. Elastic and Inelastic Light-Matter Interactions in 2D Materials. *IEEE J. Sel. Top. Quantum Electron.* **2017**, *23* (1).

(3) Pei, J.; Gai, X.; Yang, J.; Wang, X.; Yu, Z.; Choi, D. Y.; Luther-Davies, B.; Lu, Y. Producing Air-Stable Monolayers of Phosphorene and Their Defect Engineering. *Nat. Commun.* **2016**.

APPENDIX A8: SUPPLEMENTARY INFORMATION FOR CHAPTER 6

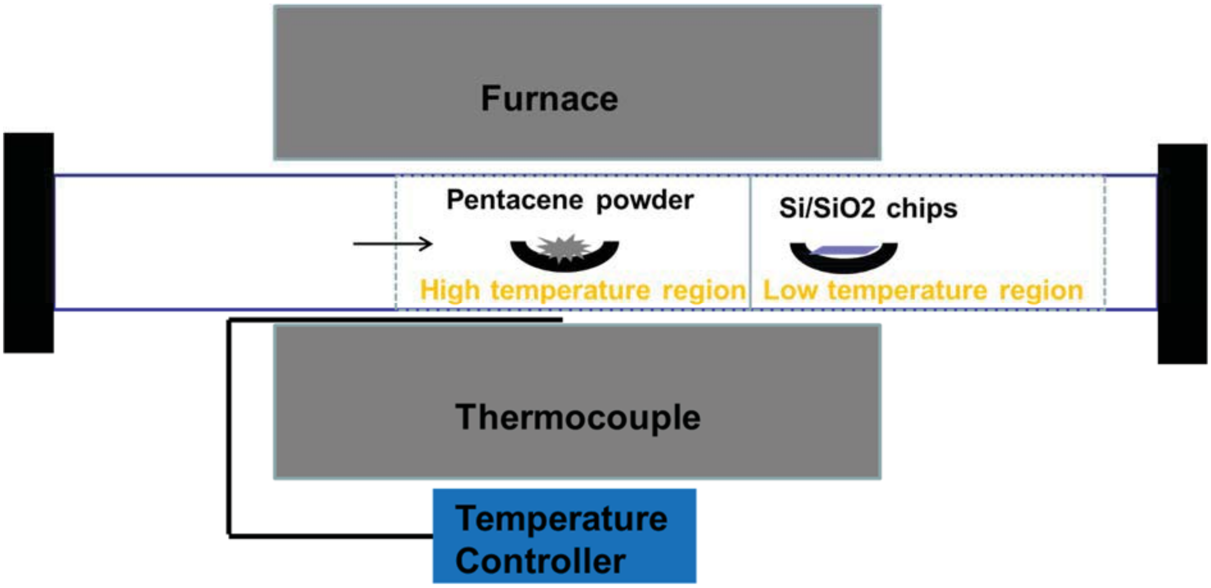

Figure A8.1 | Schematic diagram of the furnace used for growth of 1D pentacene (PEN) wires.

A8.1. Supplementary Information Note 1

1D Pentacene wires were realized on exfoliated h-BN over a Si/SiO2 substrate by thermal evaporation of Pentacene source. The **Figure A8.1** depicts the schematic experimental setup for physical vapor deposition (PVD) of 1D Pentacene. First, we used mechanically exfoliated few-layer hBN sheet on 285nm-thick SiO_2 on Si (SiO_2/Si) as the growth substrate without further annealing. Before growth, the hBN sheets were topographically examined using an optical microscope. The epitaxial growth of pentacene was carried out in a tube furnace. We put the pentacene powder at the centre of the furnace and the hBN sheets a few inches downstream and used a turbo molecular pump to evacuate the quartz tube to ~10^{-4} MPa. We then heated up the furnace to 135-180°C to grow pentacene wires. The length of the wires was controlled by the source temperature, the substrate position and growth time. When the growth was finished, we turned off the furnace and let the sample cool down to room temperature under vacuum.

We used 135-180°C temperature range in the growth process. We obtained pentacene wires growth on hBN which grew bigger to achieve the maximum average length around 15 microns at 155°C. The average length followed a reduction in value at higher temperature after 155 °C. **(Figure A8.3)**. In order to find out the most optimized growth time, we used 1 hr, 3hr, 4 hr and 24 hr growth time. 3 hrs growths were found to be the growth with highest yield including large sized pentacene wires. (**Figure A8.3**).

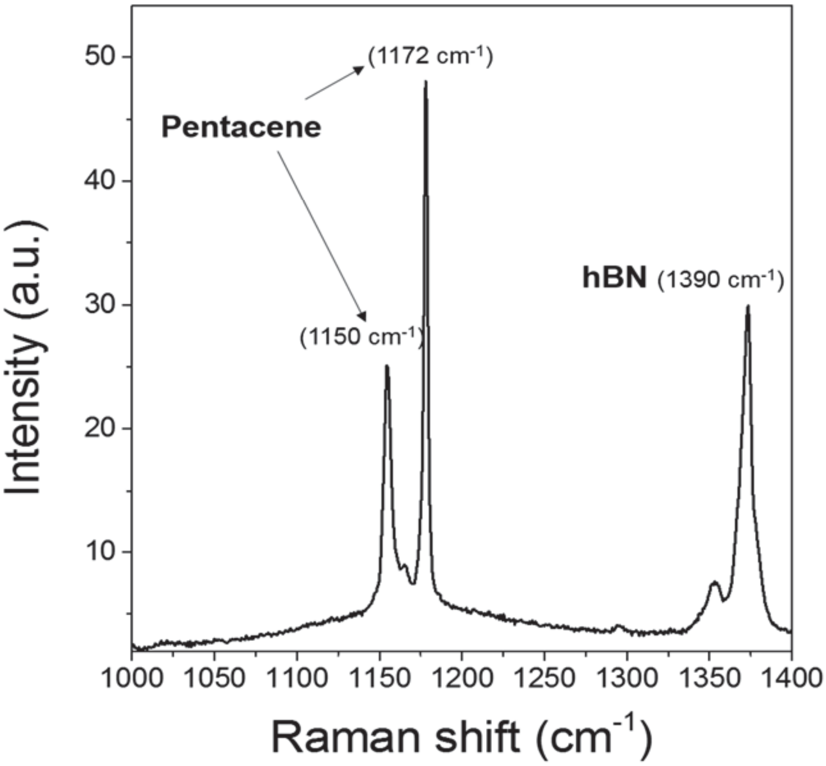

Figure A8.2 | Measured Raman spectrum from a 1D PEN wire sample grown on a h-BN flake. Peaks at 1150 cm^{-1} and 1172 cm^{-1} are for pentacene and peak at 1390 cm^{-1} is for h-BN.

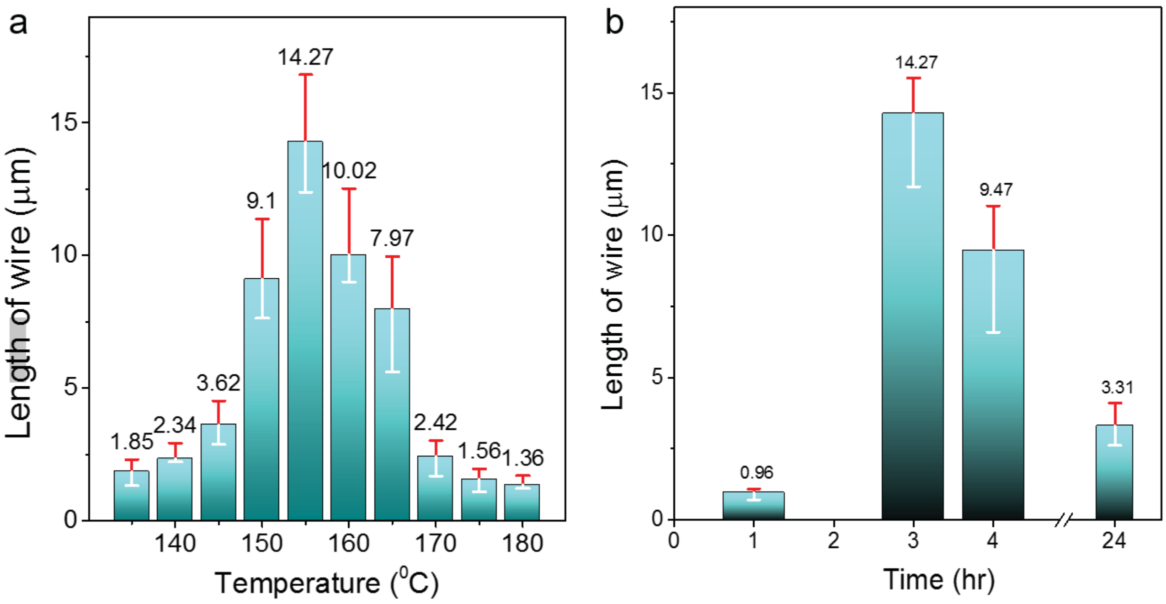

Figure A8.3 | Growth optimization of PEN wires.

(a) Length of PEN wires as a function of growth temperature in the furnace. The maximum length of the wires was obtained at 155 ^{0}C. The error bars demonstrate the experimental deviation as obtained after several optimization runs. (b) The length of PEN wires as a function of growth time in the PVD furnace. The longest wires with clear morphology were obtained at 3-hour growth mark.

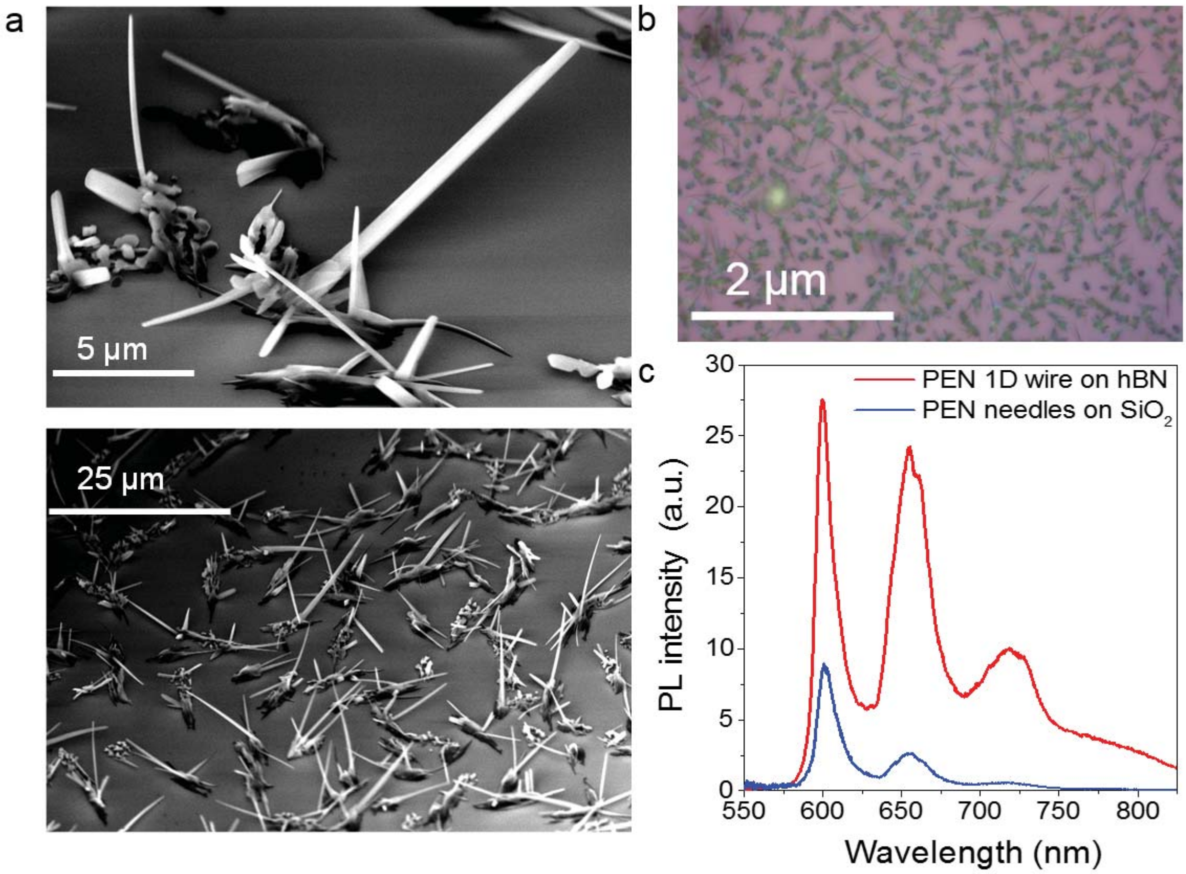

Figure A8.4 | Comparison between wires and needles
(a) SEM and optical (b) images of PEN needle like structures grown under same growth conditions as discussed in Figure A8.S1. The PEN needles on SiO$_2$ grow out of nucleation sites and diverge into needle-like structures as shown in Figure A8.2b. Whereas, on hBN the PEN wires follows higher degree of orientation and crystallinity and converge to form tube like wire structures (See Figure A8.1c). hBN serves as a stencil to help ordered growth of PEN H-bonded molecular chains in to wire like cylindrical quasi 1D structures. (c) PL spectra comparison from PEN wires grown on hBN as compared to the PEN needles grown on SiO$_2$. The PL emission from PEN wires is much stronger and vibronic levels are well resolved as compared to the needles on SiO$_2$.

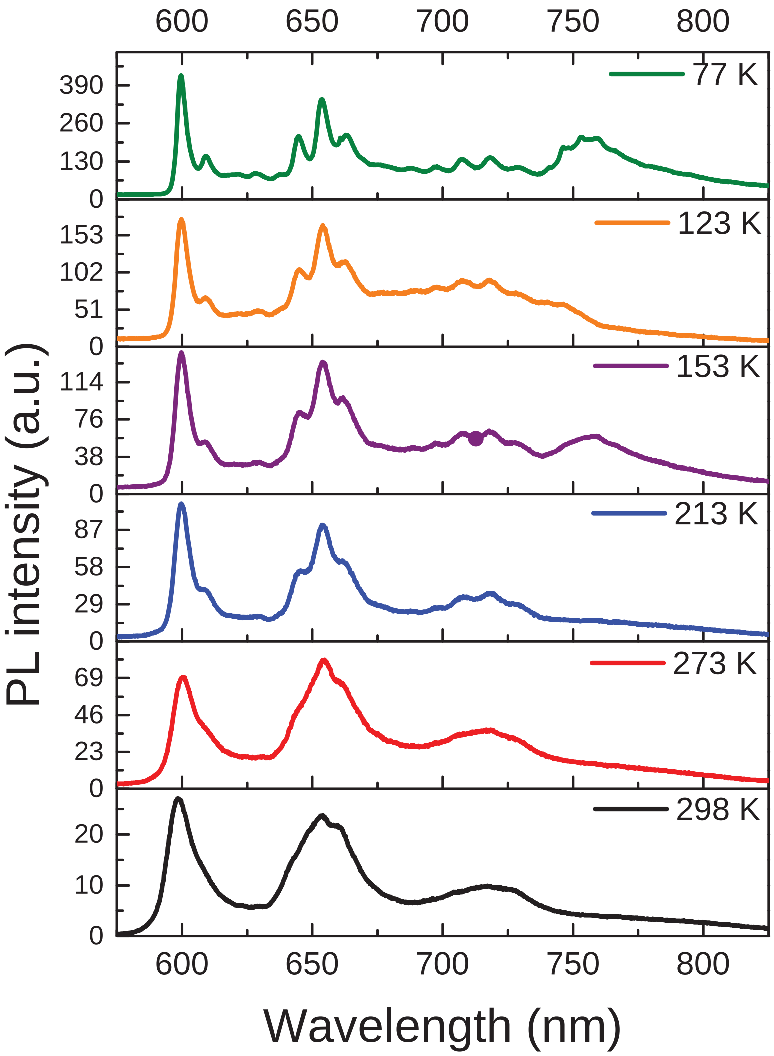

Figure A8.5 | Temperature dependent PL spectra from PEN wires.
PL emission spectra at various temperatures showing the clear resolvable vibronic levels as the temperature is reduced and the emergence of quasi-line Shpol' skii spectra t 77 K. The quasi line spectra start to emerge at 213 K and are fully resolvable as the temperature is further reduced.

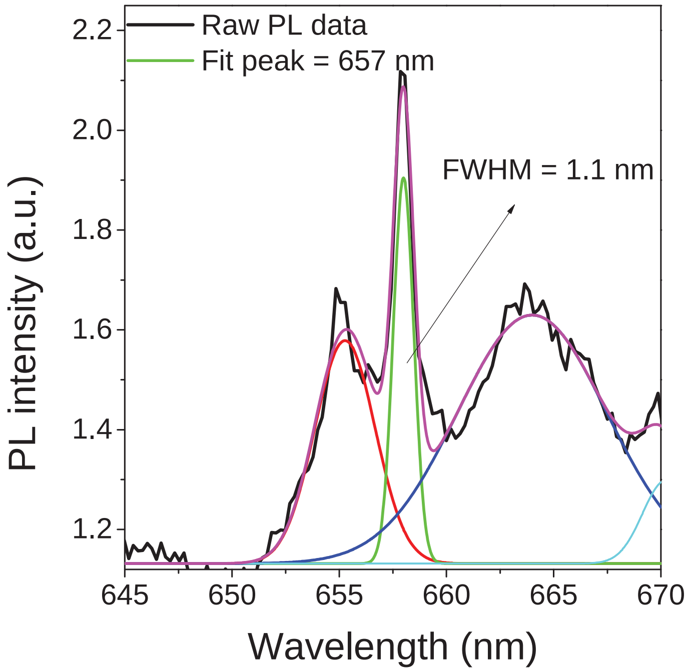

Figure A8.6 | Narrow line width emission.
PL emission from some of the optimal grown PEN wires, where the FWHM ≈ 1nm. Lorentzian fitting function has been used to fit the PL peaks.

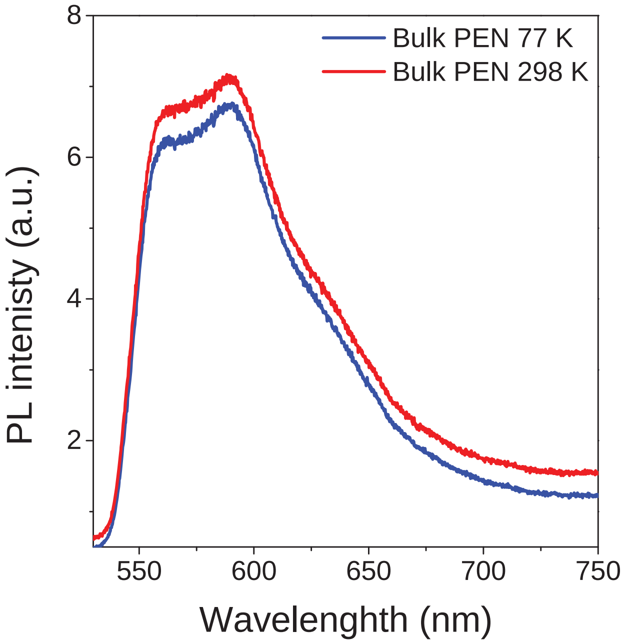

Figure A8.7 | PL emission from thin film PEN.
PL emission peak from thin film bulk crystalline PEN samples grown on hBN at room temperature and 77 K. The average thickness of the films around 70-100 nm.

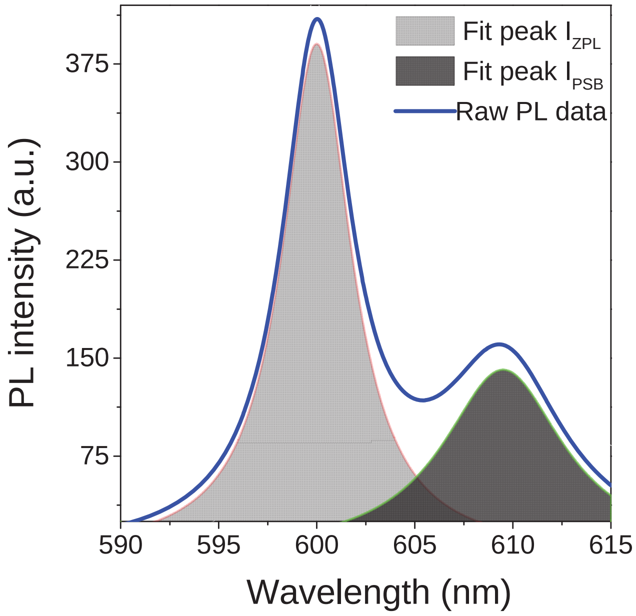

Figure A8.8 | Measured PL spectra from a 1D PEN wire sample at 77 K, fitted using a Lorentzian function to extract the I_{ZPL} and I_{PSB} necessary to determine the *DW* factor as shown in Figure 6.2e.

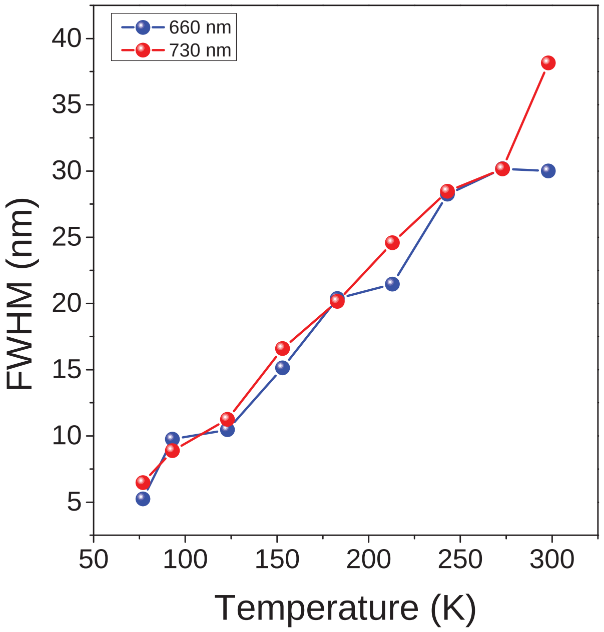

Figure A8.9 | FWHM vs temperature.

Variation of FWHM of peak = 660 nm and peak = 730 nm as a function of temperature. The variation of peak = 600 nm is shown in Figure 6.2e.

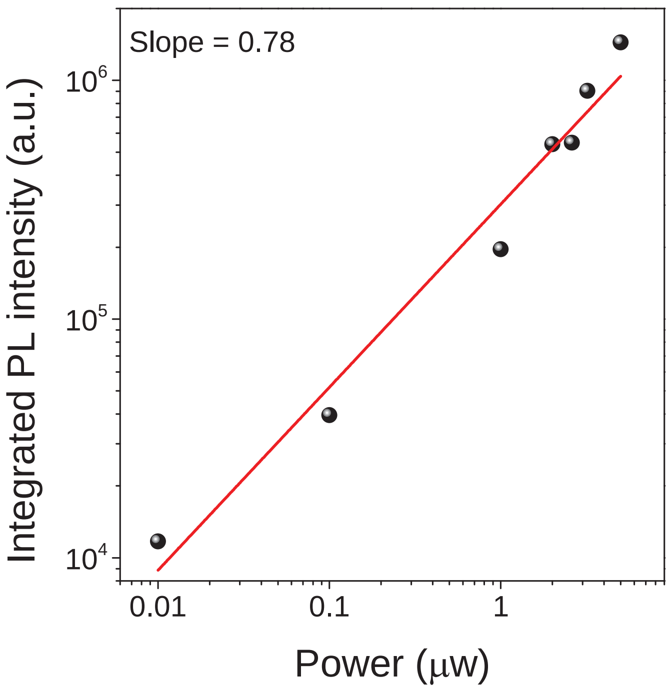

Figure A8.10 | Pumping power dependent PL measurement.
Variation of the 600 nm peak at 77 K with increasing pumping power. The sub-linear slope confirms that it is not lasing at this stage.

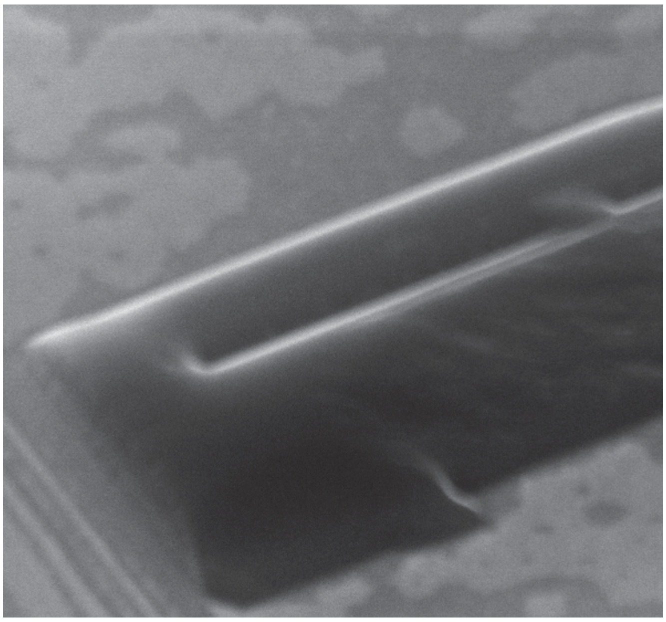

Figure A8. 11 | SEM image of PEN needle like structures grown under same growth conditions as discussed in Chapter 6.
The cross section clearly shows 100 face of the PEN wires.

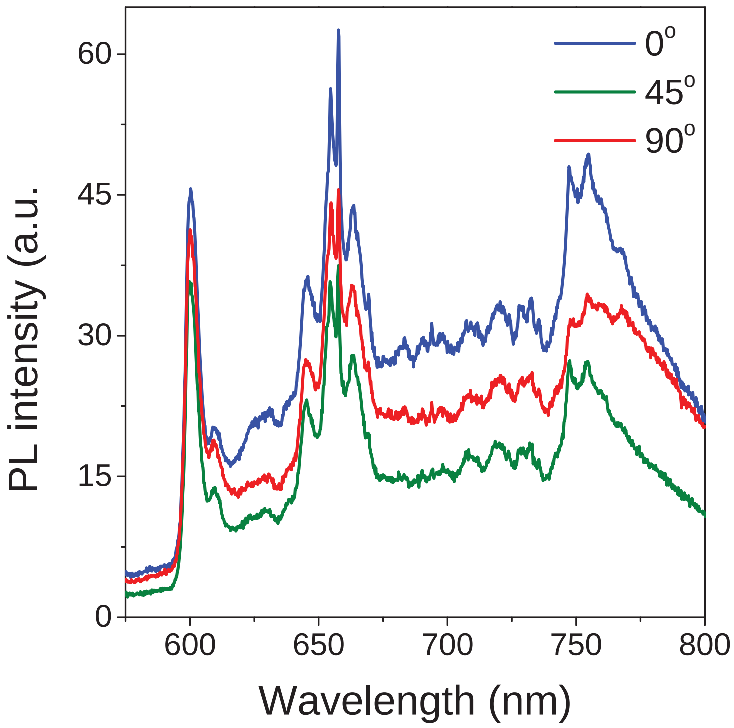

Figure A8.12 │ Excitation polarization angle-dependent PL measurements.
Measured PL intensity as a function of excitation polarization angle θ from PEN wire samples at 77 K, revealing the anisotropic excitonic nature of emission from the PEN wires. In experiment, the excitation polarization angle was determined by using an angle-variable half-wave plate polarizer in the excitation laser path.

b

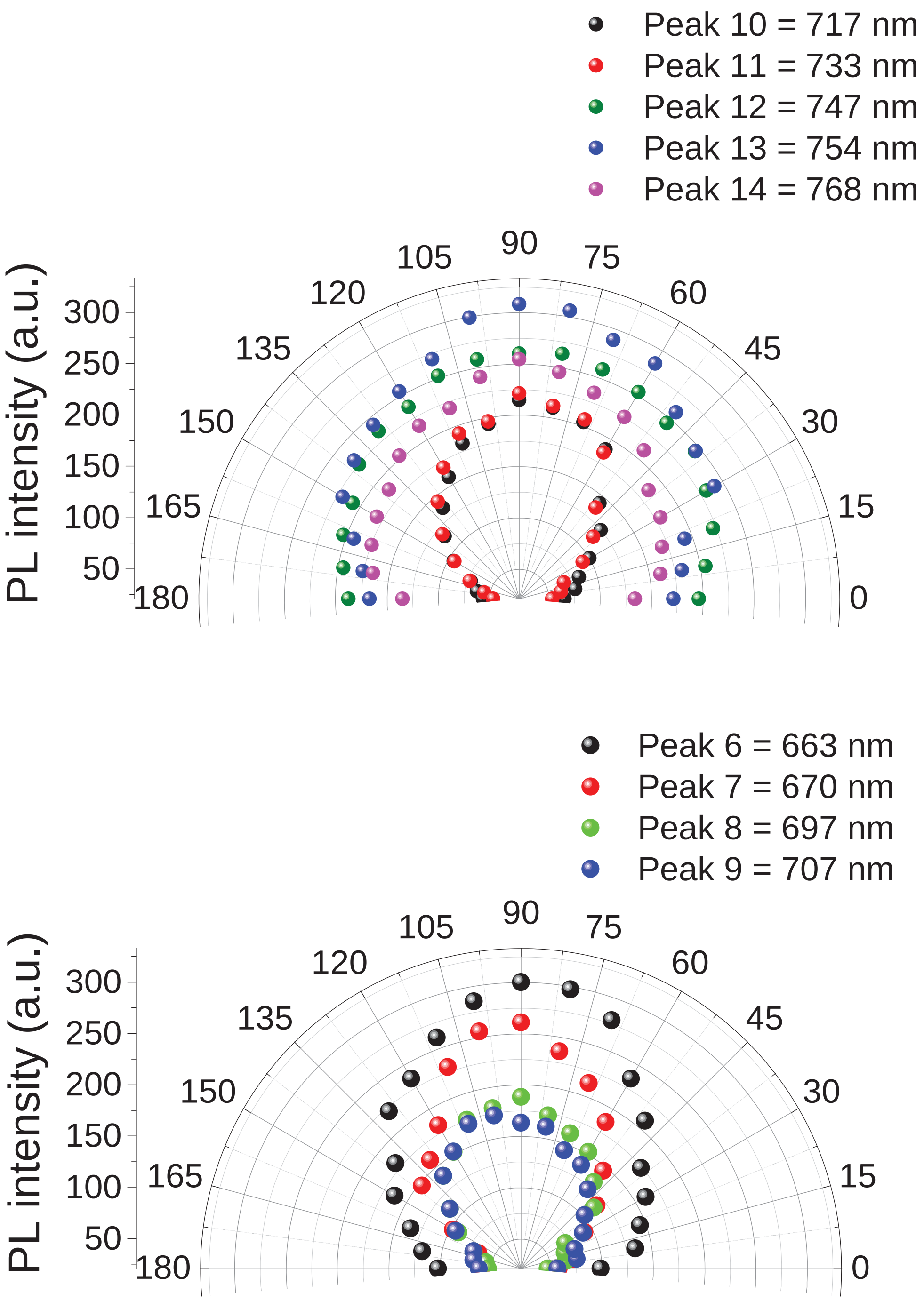

Figure A8.13 | Polarization angle-dependent PL measurements.
Measured polar plot of PL emission spectra peaks (6-14) as a function of emission polarization angle θ from PEN wires at 77 K revealing the opposite anisotropic excitonic nature of PL emission peaks. For polar plots of peaks 1-5, refer to Figure 6.3.

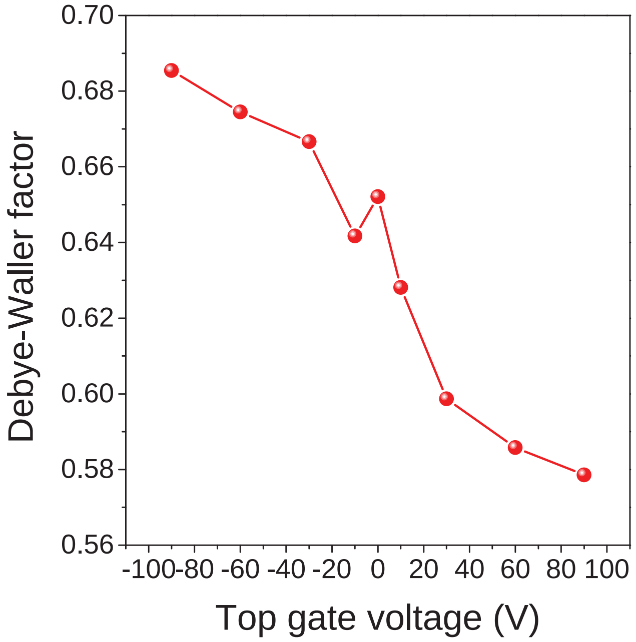

Figure A8.14│Debye-Waller factor as a function of back gate voltage.

The DW factor shows a clear modulation with change in back gate voltage which can be attributed to the change of doping levels with change in back gate voltage affecting the PL emission efficiency at different back gate voltages. This demonstrates the use of external voltage to control the quasi line spectra or zero-phonon line (ZPL) emissions from 1D PEN wires. The modulation in PL spectra with voltage is one of the fundamental characteristics of a semiconductor and has been used extensively to make functional transistors and devices from low dimensional materials. The application of electrostatic back gate voltage changes the doping concentration of charge carriers in the PEN wires and hence affects the recombination rate of excitons that combine radiatively to emit light. As shown in Figure 6.5d, at -90 V bias, the doping of the negative charges is maximum and much higher than the concentration of holes, which affects the recombination of excitons and hence the PL is suppressed. The opposite happens when the voltage is at +90V bias. The doping of negative charge carriers is suppressed and almost equal to the holes and hence results in higher recombination of excitons emitting more photons and a higher PL intensity

The *DW* factor is higher at negative bias and decreases as the bias reaches positive value. It can be attributed to the varying phonon excitonic coupling at various back gate voltages. As shown from temperature dependence of DW factor, lower phononic coupling leads to higher value of DW factor and vice-versa (See Figure 6.2e and associated text). Similarly, at negative back gate voltage bias the phononic coupling is minimal as shown from FWHM vs back gate voltage measurements in Figure A8.15. Lower FWHM value establishes that at negative bias the phononic interaction is minimum with the excitons and hence a higher value of DW factor. On the other hand, as shown in Figure 6.5, the PL intensity is maximum at positive bias due to doping concentration in the PEN wires is close to neutral at that bias.

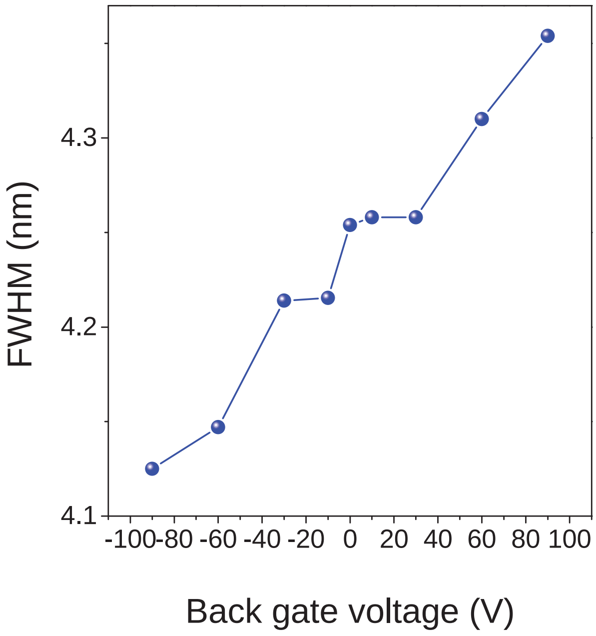

Figure A8.15 | Full width half maximum of exciton resonance peak at 600 nm as a function of back gate voltage.
The lower FWHM value at negative bias shows minimal phononic coupling with excitons and hence a higher DW factor value is observed at negative bias of the back-gate voltage.

Table A8.1: Full-width half maximum (FWHM) from other nanowire and Shpol skii matrix solutions

	System	Temperature (K)	FWHM (nm)
Nanowire Systems	GaN[1]	298	12
	CdS single crystal[2]	298	18-24*
	ZnO[3]	10	1.4
	InAsSb[4]	77	40-70
	Rubrene[5]	298	50
	DPBT single crystal[6]	77	2.9
	DMHP[7]	298	82*
	Organic-inorganic Perovskite[8]	298	10-32*
Shpol‘skii Matrices	Single perylene molecules in n-nonane[9]	1.7	1-2
	Terrylene in hexadecane[10]	1.7	0.3
	DBATT in n-tetradecane[11]	1.2	1.1-1.3
	TDI in hexadecane[12, 13]	1.7	1
	Pentacene in n-tetradecane[14]	1.2	0.5-1
	Single Crystal DCNP[15]	5	5

Table A8.2 | Peak positions at 77 K. PL emission spectra 77 K was fitted using a Lorentzian function and the resultant 14 peak positions have been tabulated in table above.

Peak Number	1	2	3	4	5	6	7	8	9	10	11	12	13	14
Peak Position (nm)	600	609	645	654	657	663	670	697	707	717	733	747	754	768

A8. References

1. Gradečak, S.; Qian, F.; Li, Y.; Park, H.-G.; Lieber, C. M., GaN nanowire lasers with low lasing thresholds. *Applied Physics Letters* **2005,** *87* (17), 173111.
2. Duan, X.; Huang, Y.; Agarwal, R.; Lieber, C. M., Single-nanowire electrically driven lasers. *Nature* **2003,** *421* (6920), 241-245.
3. Park, W. I.; Jun, Y. H.; Jung, S. W.; Yi, G.-C., Excitonic emissions observed in ZnO single crystal nanorods. *Applied Physics Letters* **2003,** *82* (6), 964-966.
4. Farrell, A. C.; Lee, W.-J.; Senanayake, P.; Haddad, M. A.; Prikhodko, S. V.; Huffaker, D. L., High-quality InAsSb nanowires grown by catalyst-free selective-area metal–organic chemical vapor deposition. *Nano letters* **2015,** *15* (10), 6614-6619.
5. Lee, J. W.; Kim, K.; Park, D. H.; Cho, M. Y.; Lee, Y. B.; Jung, J. S.; Kim, D.-C.; Kim, J.; Joo, J., Light-Emitting Rubrene Nanowire Arrays: A Comparison with Rubrene Single Crystals. *Advanced Functional Materials* **2009,** *19* (5), 704-710.
6. Zhang, C.; Zou, C.-L.; Yan, Y.; Hao, R.; Sun, F.-W.; Han, Z.-F.; Zhao, Y. S.; Yao, J., Two-Photon Pumped Lasing in Single-Crystal Organic Nanowire Exciton Polariton Resonators. *Journal of the American Chemical Society* **2011,** *133* (19), 7276-7279.
7. Wang, X.; Li, Z.-Z.; Zhuo, M.-P.; Wu, Y.; Chen, S.; Yao, J.; Fu, H., Tunable Near-Infrared Organic Nanowire Nanolasers. *Advanced Functional Materials* **2017,** *27* (45), 1703470.
8. Liu, P.; He, X.; Ren, J.; Liao, Q.; Yao, J.; Fu, H., Organic–Inorganic Hybrid Perovskite Nanowire Laser Arrays. *ACS Nano* **2017,** *11* (6), 5766-5773.
9. Pirotta, M.; Renn, A.; Werts, M. H.; Wild, U. P., Single molecule spectroscopy. Perylene in the Shpol'skii matrix n-nonane. *Chemical physics letters* **1996,** *250* (5-6), 576-582.
10. Moerner, W.; Plakhotnik, T.; Irngartinger, T.; Croci, M.; Palm, V.; Wild, U. P., Optical probing of single molecules of terrylene in a shpol'kii matrix: A two-state single-molecule switch. *The Journal of Physical Chemistry* **1994,** *98* (30), 7382-7389.
11. Bloess, A.; Durand, Y.; Matsushita, M.; Verberk, R.; Groenen, E. J.; Schmidt, J., Microscopic structure in a Shpol'skii system: A single-molecule study of Dibenzanthanthrene in n-Tetradecane. *The Journal of Physical Chemistry A* **2001,** *105* (13), 3016-3021.
12. Kiraz, A.; Ehrl, M.; Mustecaplioglu, O.; Hellerer, T.; Brauchle, C.; Zumbusch, A. In *Zero-phonon-line emission of single molecules for applications in quantum information processing*, Photonic Materials, Devices, and Applications, International Society for Optics and Photonics: 2005; pp 584-592.
13. Kiraz, A.; Ehrl, M.; Hellerer, T.; Müstecaplioğlu, Ö. E.; Bräuchle, C.; Zumbusch, A. In *Observation of Two-Photon Interference Using the Zero-Phonon-Line Emission of a Single Molecule*, Journal of Physics: Conference Series, IOP Publishing: 2006; p 67.
14. Durand, Y.; Bloeß, A.; van Oijen, A. M.; Köhler, J.; Groenen, E. J.; Schmidt, J., An optical study of single pentacene molecules in n-tetradecane. *Chemical Physics Letters* **2000,** *317* (3-5), 232-237.
15. Morawski, O.; Sobolewski, A. L.; Kozankiewicz, B.; Sznitko, L.; Miniewicz, A., On the origin of fluorescence emission in optically non-linear DCNP crystals. *Physical Chemistry Chemical Physics* **2014,** *16* (48), 26887-26892.